Universidad Autónoma de Madrid
Facultad de Ciencias
Departamento de la Materia Condensada

Dissipation in finite systems: Semiconductor NEMS, graphene NEMS, and metallic nanoparticles

A thesis presented by

César Óscar Seoánez Erkell

under the supervision of

Dr. Francisco Guinea López

Profesor de Investigación

Instituto de Ciencia de Materiales de Madrid (CSIC)

and tutored by

Prof. Guillermo Gómez Santos

Departamento de la Materia Condensada

Universidad Autónoma de Madrid

Madrid, 2007

To my parents and grandparents

Resumen

Los procesos de decoherencia y disipación en sistemas mesoscópicos han sido objeto en las últimas décadas de gran interés dado su papel clave en el estudio y utilización de fenómenos cuánticos a escalas cada vez mayores. Los espectaculares logros alcanzados en las técnicas de fabricación y medición han permitido el diseño de nanoestructuras móviles que hábilmente combinadas con otros protagonistas de la historia física reciente, tales como puntos cuánticos o gases electrónicos de baja dimensionalidad, otorgan la fascinante oportunidad de estudiar la interacción electrón-fonón cuanto a cuanto, con un potencial tecnológico prometedor. En la mayoría de las aplicaciones vislumbradas, así como para la observación de comportamiento cuántico en variables mecánicas macroscópicas tales como el centro de masas de resonadores micrométricos, es imprescindible una minimización de los procesos disipativos que perturban la dinámica vibracional de estos sistemas. En consecuencia se está llevando a cabo un gran esfuerzo actualmente en el análisis y modelización de los mismos, tanto desde un punto de vista experimental como teórico.

Esta tesis forma parte de dicho esfuerzo. En concreto, dos de las tres partes en que se divide están consagradas a la modelización de algunos de los principales mecanismos de fricción presentes en dos clases de sistemas nanoelectromecánicos (NEMS): nanoresonadores construidos a partir de heteroestructuras de semiconductor, y nanoresonadores en los que la parte móvil es un compuesto de carbono de baja dimensionalidad, bien sea una lámina de grafeno o un nanotubo.

En el primer caso nos hemos centrado en los procesos superficiales de absorción de energía mecánica asociados al acabado imperfecto, la presencia de impurezas y la estructura superficial parcialmente desordenada, invocando las similitudes existentes con los procesos de atenuamiento de ondas acústicas en materiales amorfos. El resultado es un modelo de espines acoplados al conjunto de modos vibracionales del resonador, analizado por medio de técnicas desarrolladas para el estudio del *Spin-Boson Model* y de procesos de relajación. Asimismo se modelizan los posibles efectos negativos que conlleva la deposición de electrodos metálicos sobre las estructuras de semiconductor.

Los osciladores de compuestos de carbono presentan una serie de peculiaridades que los diferencian de sus homólogos semiconductores, destacando su alto grado de cristalinidad y carácter metálico o semimetálico. Ello implica la prevalencia de mecanismos de fricción distintos, varios de los cuales se modelizan, destacando la excitación de pares electrón-hueco en el resonador debido a cargas distribuidas por la estructura, estudiada con métodos perturbativos autoconsistentes.

La tercera y última parte se dedica a otro tipo de sistema mesoscópico, las partículas nanometálicas, cuya respuesta óptica viene dominada por la excitación colectiva denominada *plasmón de superficie*. La presencia en el espectro de excitaciones electrónicas de pares electrón-hueco acoplados al plasmón provoca su progresivo atenuamiento tras ser excitado inicialmente por un campo eléctrico externo, por ejemplo un laser. Este proceso se puede considerar como ejemplo de entorno disipativo con un *número finito* de grados de libertad en interacción con el subsistema de interés, el plasmón. Los efectos que esta finitud conlleva en la modelización teórica de la dinámica electrónica son analizados en detalle, justificando la validez de ciertas aproximaciones asumidas hasta ahora sin demostración previa.

Conclusiones.

La fricción a bajas temperaturas asociada a los distintos procesos superficiales en resonadores de semiconductor ha sido modelizada adaptando el *Standard Tunneling Model* utilizado para explicar las propiedades acústicas de sólidos amorfos a $\sim 0.01 \lesssim T \lesssim 1$ K. El orden de magnitud así como la débil dependencia con la temperatura observada en los experimentos es cualitativamente reproducida. Sin embargo, llegar a un acuerdo cuantitativo se antoja difícil hasta que no se posea un conocimiento más detallado de los procesos y defectos estructurales presentes en el resonador.

Diversos mecanismos disipativos presentes en nanoresonadores de grafeno y nanotubos han sido analizados, obteniendo, al igual que en el caso previo, dependencias paramétricas de los mismos en función de las variables físicas relevantes del sistema, como la temperatura y dimensiones características. La importancia relativa de los mismos en función del régimen (amplitud de vibración, temperatura) ha sido establecida, predominando a bajas temperaturas la disipación óhmica debido a excitaciones electrónicas en el seno del resonador y a altas temperaturas la atenuación por procesos termoelásticos.

Se ha presentado un modelo muy utilizado en el estudio de la dinámica de plasmones superficiales y de la respuesta óptica de clusters metálicos, analizando la coherencia interna de dicho esquema teórico, justificando varios puntos clave del mismo que hasta ahora se habían tomado como válidos sin justificación rigurosa. De dicho análisis se obtiene asimismo información sobre los tiempos característicos de evolución del plasmón y del resto de excitaciones electrónicas acopladas al mismo, lo cual permite fundamentar una aproximación Markoviana a la hora de estudiar la dinámica del sistema acoplado plasmón - pares electrón-hueco.

Abstract

The physics of decoherence and dissipation in mesoscopic systems has attracted great interest, given its key role in the study and use of quantum phenomena at ever larger scales. The spectacular achievements in fabrication and measurement techniques have opened the doors to the design of mobile nanostructures which, combined in smart ways with other recent cornerstones like quantum dots or low-dimensional electron gases, grant the fascinating opportunity to study electron-phonon interactions at an individual level, with a promising technological potential. In most of the envisioned applications, as well as to observe quantum behavior in macroscopic mechanical variables like the center-of-mass of micrometric resonators, a minimization of the dissipative processes perturbing the vibrational dynamics of these systems is compulsory. Consequently strong efforts are being made to analyze and model them, both from the experimental as well as from the theoretical sides.

This thesis exemplifies these efforts. Specifically, two out of the three parts constituting it are consecrated to the modeling of some of the main friction mechanisms found in two kinds of nanoelectromechanical systems (NEMS): nanoresonators built from semiconductor heterostructures, and nanoresonators whose mobile part is a low-dimensional carbon compound, be it graphene or a nanotube.

In the first case we have focussed in the surface processes absorbing mechanical energy, related to the imperfect finish, presence of impurities and partially disordered surface structure. Similarities with acoustic wave damping in amorphous solids have been invoked to build an adaptation of the *Standard Tunneling Model* which aims to provide a low temperature description of such processes. The result is a model of spins coupled to the ensemble of vibrational eigenmodes of the resonator, which is analyzed by means of techniques developed for the study of the *Spin-Boson Model* and relaxation processes. Possible negative effects due to metallic electrodes deposited on top of the semiconductor structures are also modeled.

Oscillators made from carbon compounds, demonstrated for the first time this year, display a series of peculiarities distinguishing them from their semiconductor counterparts, specially their high degree of crystallinity and semimetal or metal character. The prevailing friction mechanisms thus differ, several out of which are modeled, with the excitation of electron-hole pairs in the resonator due to charges distributed throughout the device dominating at low temperatures and small vibrational amplitudes.

The third and last part is devoted to another kind of mesoscopic system, namely nanometallic clusters, whose optical response is dominated by the so-called *surface*

plasmon collective excitation. The presence in the electronic excitation spectrum of one-body electron-hole pairs coupled to the plasmon causes its progressive damping after its initial excitation by an external electric field, e.g. a laser pulse. This process may be considered as an example of finite dissipative environment interacting with the subsystem subject of our interest, the plasmon. The consequences of this finiteness on the theoretical modeling of the electronic dynamics are analyzed in detail, justifying the validity of several approximations assumed until now to hold without proof. This study will also shed some light on the characteristic times of the different electronic degrees of freedom, providing a basis for the use of a Markovian approximation in the analysis of the plasmon dynamics of nanometric clusters.

Acknowledgments

Looking back at these years of PhD, I really consider myself a very fortunate person. All the people next to me have always given their support and courage whenever I needed it. I have met many good, generous, idealistic and hardworking people, whose invaluable examples have been extremely stimulating, and a reason to reflect and rejoice. I start with my advisor, Paco Guinea. His efficacy, optimism and humility are simply impressive. Making use of his deep physical intuition and thorough knowledge of numerous fields he introduced me to fascinating research fields and also gave me the possibility to assist to several schools and workshops, where I could meet physicists and friends from many countries. Indeed, in some of them I met for the first time some of the people with whom I had the luck to collaborate, like Raj Mohanty and Rodolfo Jalabert.

Two stages abroad have been fundamental to get to this point, one with Antonio Castro-Neto in Boston and another with Rodolfo Jalabert in Strasbourg and Augsburg. In both cases they, together with their collaborators, made their best to help me in every issue to make me feel like at home, and with them I could also learn different ways of doing physics, a very enriching experience. Here go my thanks to Antonio, Raj, Silvia, Marco, Guiti, Alexei and Johan (BU), and to Rodolfo, Dietmar, Guillaume and Gert (IPCMS/U. Augsburg), and all the rest of nice and helping people I met there. I appreciate as well very much the effort made by Sebastián Vieira, Adrian Bachtold, Enrique Louis, Rodolfo Jalabert and Pablo Esquinazi to be part of the dissertation committee, and the work done by Guillermo Gómez-Santos as tutor.

In any case, most of the time was spent here in Madrid, in a wonderful group of the Condensed Matter Theory Department at the ICMM. I doubt I will ever again find a working place where I feel so comfortable. Moreover, there were many of us doing the PhD, so we could share this experience, having often great fun. If you are bored or feel depressed just knock on the door of offices 128 or 130, "mano de santo", as we say in spanish. Thank you so much for everything, Juan Luis, Alberto, Debb, Suzana, Javi, Rafas, Félix, Ramón, Geli, Luis, Virginia, Tobías, Leni, Belén, Berni, María, David, Fernando, Carlos, Samuel, Juan, Ana and Mª José. In the case of Geli, Ramón, Tobías, Pilar, Carlos, Alberto, Javi and Juan Luis thank you very much for helping me with my computer and physics-related doubts. Special thanks also to Sonia, Ángel, Antonio, Cayetana and Puri, thank you for your sympathy and attentions.

Some words of gratitude cannot be skipped for my friends outside the ICMM, your support is also very important to me: Javi, José, Héctor, Juan, Teo, Alfredo, Fátima, Nuria, Ana, Abelardo, Juan, Rocío, Izaskun, Ángela, Julio, Amadeo, Mario, Ful, Aurelio, Sabrina... I also thank my spanish and swedish family, which I know is always there in the good and bad circumstances: tío Mariano, tía Pili, Pilar, Esther, Aniana, Titti, Lars-Johan..., and my grandparents, who unfortunately are now gone.

And of course I am most indebted to my parents, your 28 years of love and care are impossible to balance, I cannot ask for more, tusen tack!

Citations to Previously Published Work

Parts of the contents of this work can be found in the following publications:

- C. Seoanez, F. Guinea and A. H. Castro-Neto (2007). *Dissipation due to two-level systems in nano-mechanical devices.* Europhysics Letters **78**, 60002, preprint archive cond-mat/0611153.

- C. Seoanez, F. Guinea and A. H. Castro-Neto (2007). *Surface dissipation in NEMS: Unified description with the Standard Tunneling Model, and effects of metallic electrodes.*. Sent to Physical Review B.

- C. Seoanez, G. Weick, R.A. Jalabert and D. Weinmann (2007). *Friction of the surface plasmon by high-energy particle-hole pairs: Are memory effects important?.* The European Physical Journal D **44**, 351, preprint archive cond-mat/0703720.

- C. Seoanez, F. Guinea and A. H. Castro-Neto (2007). *Dissipation in graphene and nanotube resonators.* Physical Review B **76**, 125427, preprint archive arXiv:07042225.

Contents

List of Figures

List of Tables

Part I

Dissipation in semiconductor NEMS

Chapter 1

NEMS

1.1 Introduction: current research topics

Nanoelectromechanical systems (NEMS) constitute a recent fascinating subject of current research, both from fundamental and application-oriented points of view [Cra00, Cle02, Ble04, ER05, SR05]. Inheritors of the bigger microelectromechanical systems (MEMS), they are mesoscopic solid-state devices with a special ingredient: one resonating component, with some of its characteristic dimensions lying in the submicron regime, whose mechanical motion is integrated into an electrical circuit. Typically this moving element can be a bridge, a pillar, or a cantilever, one of whose mechanical eigenmodes is excited and measured. Two features of these eigenmodes are essential to explain the potential of NEMS: First, due to its small dimensions, their modes vibrate at very high frequencies ω_0, currently from tens of MHz to GHz (microwave frequencies). This is desirable if one wishes to study the quantum regime where thermal fluctuations are smaller than the energy of a phonon, $kT < \hbar\omega_0$ (for GHz frequencies, milliKelvin suffice), and also for several high-speed signal processing components [Bli05, HFZ+05, BQKM07].

Second, and perhaps more important, they exhibit extremely low damping, measured in terms of the so-called *quality factor*

$$Q(\omega_0) = \frac{\omega_0}{\Delta\omega_0}\,, \tag{1.1}$$

where $\Delta\omega_0$ is the measured linewidth, reaching often $Q \sim 10^5$ or higher. This translates, for example in the case of NEMS-based single-electron transistors, into power dissipation rates several orders of magnitude below the ones of common CMOS-based transistors found in standard microprocessors operating at similar frequencies [BQKM07]. Thus, NEMS-based computing technology constitutes a very attractive alternative for applications demanding GHz or lower clock-speeds, robustness and/or operation at high temperatures ($T > 200^o$C).

Apart from nanoscale versions of Babbage's 18th-century mechanical computers, these two features open the scope for many other technological applications, among whom ultrasensitive sensors and actuators clearly outstand. Their working principle is easy: The interaction of the resonator with other elements of the circuitry, like charges if the vibrating element is charged, or with elements of the environment outside the device, cause measurable shifts in the frequency of the eigenmode. The sensitivity depends crucially on the small dimensions of the device and the linewidth $\Delta\omega_0$ of the mode, currently achieving sub-attonewton force detection [MR01] and mass sensing of individual molecules [KLER04]. Other successes include single-spin detection [RBMC04], study of Casimir forces at the nanometer scale [DLC$^+$05], high-precision thermometry [HKC$^+$07] or *in-vitro* single-molecule biomolecular recognition [DKEM06].

But leaving aside applications, they are also proving as very powerful tools in fundamental research:

- They allow for a study of electron-phonon interactions at a single quantum level, with setups prepared for the study of single electrons interacting with single phonons, or the analysis of single electrons shuttled via mechanical motion [EWZB01].
- At low enough temperatures several manifestations of a quantum behavior of the mechanical oscillator have been observed, or are expected to appear, like [Ble04]:
  - Zero-point motion detection and back-action forces due to the measurement process [LBCS04, NBL$^+$06]. A displacement sensitivity of 10^{-4}Åis needed, attainable with current cantilevers.
  - Avoiding back-action forces, quantum non-demolition measurements of energy eigenstates [SDC04, JLB07, MZ07, Jac07].
  - Quantization of thermal conductance [Ble99, SHWR00].
  - Quantum tunneling between macroscopically distinct mechanical states, with several proposals for applications in quantum computing [CLW01, GC05, SHN06, XWS$^+$06], see fig.(1.1).
  - Preparation of minimum-uncertainty quantum squeezed states with a position uncertainty below that of zero-point fluctuations [RSK05a, RSK05b].

Figure (1.2) shows some beautiful examples of setups for some of the applications mentioned above.

The study of quantum superpositions of mechanical degrees of freedom in NEMS is also a straight way to assess two important issues: i) The validity of quantum mechanics for ever larger systems [Leg02], and ii) The theoretical framework explaining environmentally-induced decoherence [LCD$^+$87, Wei99], a part of which we will use

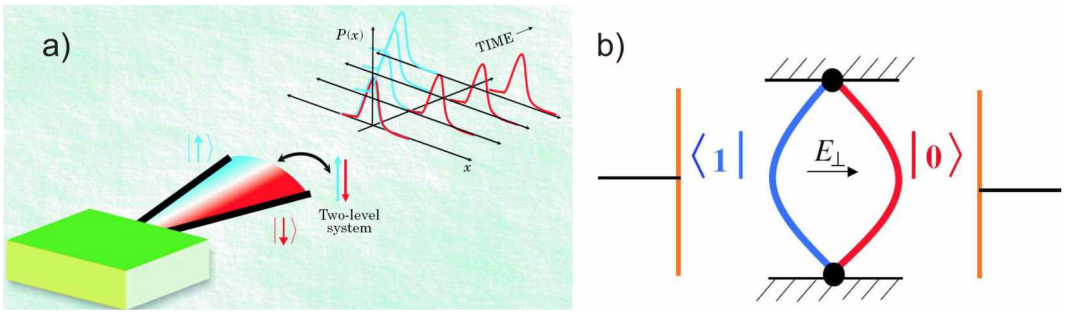

Figure 1.1: Preparation of quantum superpositions of macroscopically distinct resonator states. a) From [ER05]: the cantilever interacts with a two-level system (TLS) in such a way that the flexure depends on the TLS state, $|\uparrow\rangle$ or $|\downarrow\rangle$. If the TLS is prepared in a superposition state, the mechanical resonator state will be a linear combination of the two flexure states, with a probability distribution $P(x,t)$ as depicted to the right. b) When a doubly clamped bar is sufficiently compressed, it buckles, with two possible buckling positions. At low enough temperatures, tunneling through the energy barrier separating both states gives rise to eigenstates corresponding to superpositions of left and right buckled states, enabling its use as a qubit. From [SHN06]

.

in this thesis to analyze the mechanisms limiting the quality factors Q of the eigenmodes, and with them the observation of such quantum behavior.

As for most of these technological applications and fundamental science works low-dissipation, high-Q resonators are desirable, several works have been devoted to the analysis of the different sources of friction present in MEMS and NEMS [CR99, YSC+00, EOS+00, CR02, YOE02, MHE+02, AM03, HHP+03, ZGS+05, FZMR06, SCK+07], trying to determine the dominant damping mechanisms and ways to minimize them. In the first two parts of this thesis we will analyze them, both for the most common semiconductor-based resonators, with vibrating structures made of Si, GaAs, SiN, SiC... (part I), and also for carbon-materials based resonators, like nanotube [SYU+04] or graphene [BvdZV+07] devices (part II). But before we embark ourselves in such a task, it is convenient to learn a few basic facts about NEMS.

1.2 Semiconductor NEMS fabrication

The performance of a given nanomechanical oscillator depends to a great extent on its constituent materials and the manufacturing steps they have gone through, not to speak about reproducibility and scalability of results. A good review on MEMS and NEMS manufacturing techniques can be found in [Cle02]. We will focus on the

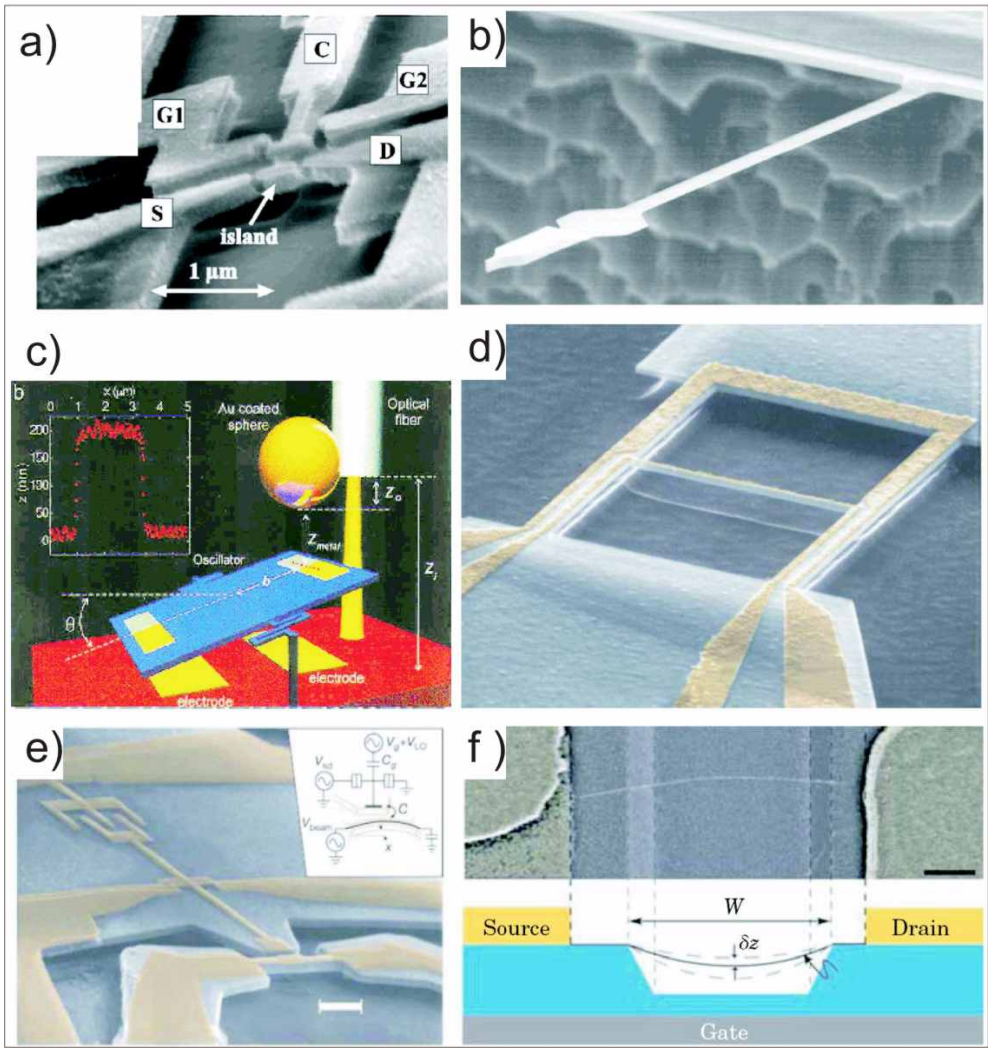

Figure 1.2: Several examples of nanoelectromechanical devices (NEMS). a) Mechanical single electron shuttle [EWZB01]. b) Ultrasensitive magnetic force detector used to detect a single electron spin [RBMC04]. c) Setup using a torsional oscillator used to study Casimir forces to check the validity of Newtonian gravitation at the nanometer scale [DLC+05]. d) Parametric radio-frequency amplifier providing a thousandfold boost of signal displacement at 17 MHz [SR05]. e) A 116-MHz nanomechanical resonator coupled to a single-electron transistor [KC03]. f) Tunable carbon nanotube resonator operating at 3-300 MHz [SYU+04].

most widely used technique for building NEMS, namely Epitaxial Heterostructure Nanomachining, applied to a (Si-SiO_2-Si) heterostructure, chosen frequently by experimentalists due to the high degree of crystallinity and perfection of the resulting

resonators, and more concretely in a study of dissipation with which we will compare our predictions [ZGS$^+$05, SGC07a, SGC07b, SCK$^+$07].

The starting heterostructure is fabricated by oxygen ion implantation in a crystalline Si wafer, followed by a high-temperature annealing of several hours, and is commonly known as SIMOX (Separation by IMplantation of OXigen) wafer. During the second step the previously formed mixed buried layer Si-SiO_2 becomes purified through oxygen migration, constituting a separated SiO_2 smooth buried layer, below a single-crystal recrystallized Si top layer. Typically, this single-crystal top layer, out of which our resonator will be carved, contains a relatively large number of defects, mostly threading dislocations running from the SiO_2 layer to this one, with typical defect densities of about $10^3 - 10^5/\text{cm}^2$. The top layer presents variations in thickness ~ 10 nm, as does the silicon oxide underneath.

To create the suspended structure, the wafer is subject to the nanomachining process depicted in fig.(1.3): first an etch mask is defined using lithography: a PMMA photoresist is coated over the wafer and then patterned using a nm-resolution electron beam, constituting a metal liftoff mask. Afterwards a layer resistant to Reactive Ion Etching (RIE) is deposited on top of it and lifted off, leaving behind a RIE-resistant mask, fig.(1.3b). Then the RIE is applied on the sample enough time to remove the top Si layer except where the protective mask lies, and remove also part of the underlying SiO_2 layer, fig.(1.3c). The suspended structure appears when the device is submerged in a selective wet etch which removes the SiO_2, like hydrofluoric acid, fig.(1.3d). Depending on the method to be used for the driving of the resonator, a top metallic coating can be deposited at will for example using lithography, before the RIE mask is created.

Even though spectacular, the final result is far from perfect: the SIMOX wafer defects, together with surface roughness and imperfections due to the resolution limitations of the different steps result in strong dissipation, as we will later see.

1.3 Motion transduction of mechanical eigenmodes in semiconductor NEMS

Well stablished transduction setups for the detection and driving of mechanical modes in MEMS, like optical methods as fiber-optic interferometry and reflection, or piezoresistive displacement transduction, cease to work properly for the submicrometer-sized NEMS. In the former case the light wavelengths exceed the resonator transverse dimensions and diffraction effects spoil the scheme, while in the latter dissipation heats the sample, precluding its use for low-temperature applications and studies.

For semiconductor NEMS, two other schemes have proved quite successful:

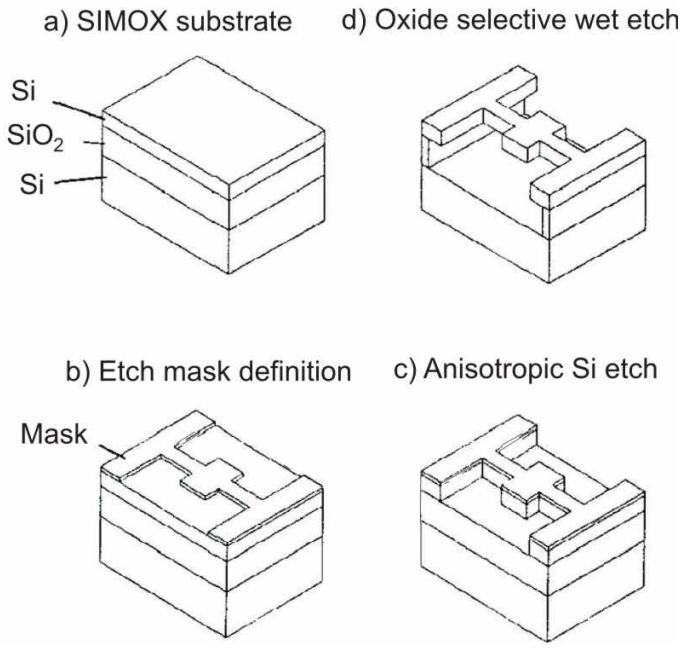

Figure 1.3: From [Cle02]. Building a nanoresonator using Epitaxial Heterostructure Nanomachining. (a) The process starts with a previously fabricated heterostructure, such as the SIMOX (Separation by IMplantation of OXigen) Si-SiO_2-Si shown. (b) Using electron beam lithography a mask is etched. (c) Anisotropic dry etch such as Reactive Ion Etching. (d) The oxide layer is removed using a selective SiO_2 wet etch, obtaining in this way the suspended structure. Metallization of the top layer can be performed lithographically before the process.

1.3.1 Magnetomotive scheme

As shown in fig.(1.4a), in this setup [MHE+02] the nanobridge is covered by a thin metallic layer, connected in turn to an external circuit whose AC current is controlled by the experimentalist, fixing its frequency ω at will. The whole circuit is embedded in a strong static magnetic field of several Tesla, perpendicular to the main axis of the bridge, as indicated in the figure. When the electrons of the AC current flow back and forth at frequency ω, they experience a Lorentz force due to the presence of the magnetic field perpendicular both to the field and the main axis, forcing the bridge to oscillate up and down. The area enclosed by the circuit is thus a function of time, and so the magnetic flux through it, therefore originating an induced electromotive force opposing the motion of the bridge, which is detected by a network analyzer. When the frequency is tuned to the one of a given mechanical eigenmode, the motion is strongly enhanced. With this scheme many modes can be excited, just by changing the circuit's frequency to the one of the mode of interest. The presence of the top

metallic layer adds extra dissipative sources which will be analyzed later.

1.3.2 Coupling to SETs and other sensitive electronic probes

The magnetomotive driving can be used in combination with more elements close to the resonator, to study electron-phonon interactions in a previously unexplored regime, with a single-electron single-phonon control. This can be achieved by coupling our magnetomotively driven charged resonator to a mesoscopic device whose conductance can be controlled and measured with great accuracy, like quantum dots, quantum point contacts or single-electron transistors (SETs) [KC03], as schematically depicted in fig.(1.4b). Using similar ideas but different geometries, fascinating devices like single-electron mechanical shuttles have been demonstrated [EWZB01, SB04].

1.4 Nanoscale elasticity theory: Vibrational eigenmodes of long and thin rods

Regarding the elastic properties of nanoresonators, it is clear that as size shrinks a point is reached when classical continuum mechanics ceases to be a good approximation. Nevertheless, for the sizes of current semiconductor nanorods and wavelengths of the modes excited ($\sim$ 50nm - 10μm), much bigger than typical interatomic spacing, continuum approximations continue to hold [SB98, LB99, SB02, SBNI02, LBT$^+$03, Ble04], and classical elasticity theory, using bulk concepts like Young's modulus E or Poisson's coefficient ν, predicts with reasonable accuracy the eigenmodes observed in experiments. In Appendix A.1 a brief review of continuum elasticity concepts and the derivation of the equations for the different modes present in quasi-1D resonators is given. Here we state the main results. For a long and thin rod, considering small deviations from equilibrium and wavelengths bigger than the transversal dimensions, three kinds of vibrational modes are found, namely longitudinal, flexural and torsional.

Longitudinal (or compressional) modes are as those found in bulk 3D solids but occur only along the direction of the main axis, chosen to be the Z axis, with the Z-component u_z of the local displacement field $u_i = x'_i - x_{i,eq}$ obeying the wave equation

$$\frac{\partial^2 u_z}{\partial z^2} = \frac{\rho}{E}\frac{\partial^2 u_z}{\partial t^2} \ , \tag{1.2}$$

ρ being the mass density. **Torsional** vibrations, like the one of fig.(1.5b), are parametrized in terms of the twisting angle $\phi(z)$, which obeys the wave equation

$$C\frac{\partial^2 \phi}{\partial z^2} = \rho I \frac{\partial^2 \phi}{\partial t^2} \tag{1.3}$$

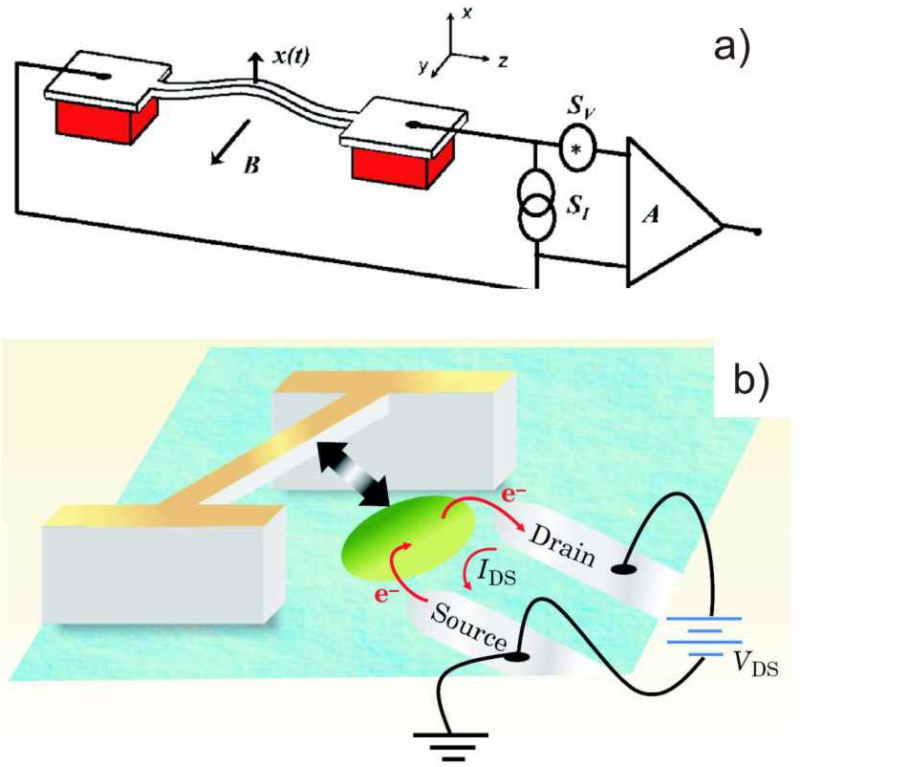

Figure 1.4: (a) Scheme of the magnetomotive driving and detection setup with a nanobridge. The electrons flowing back and forth through the bridge experience a Lorentz force which drives the motion of the bridge. Due to the oscillation the area of the loop formed by the circuit varies, and with it the magnetic flux enclosed by it, inducing an electromotive force according to Faraday's law, measured as a function of the AC electron current frequency by a vector network analyzer [MHE+02]. (b) The vibrating bridge interacts with the electrons flowing through a mesoscopic detector such as a quantum point contact or quantum dot placed nearby, altering the current I_{DS}, which is monitored with extremely high precision. Figures from [ER05, SR05].

where C is the so-called torsional rigidity. **Bending** (flexural) modes differ from the previous two in that they do not obey a standard wave equation. They correspond to transversal displacements $X(z,t), Y(z,t)$ following the equations of motion

$$\begin{aligned} EI_y \frac{\partial^4 X}{\partial z^4} &= -\rho S \frac{\partial^2 X}{\partial t^2} \\ EI_x \frac{\partial^4 Y}{\partial z^4} &= -\rho S \frac{\partial^2 Y}{\partial t^2} \ . \end{aligned} \tag{1.4}$$

Here I_j are the inertia moments of the X and Y axes, and S is the cross-section area of the rod. Even though these are not usual wave equations they admit plane wave-

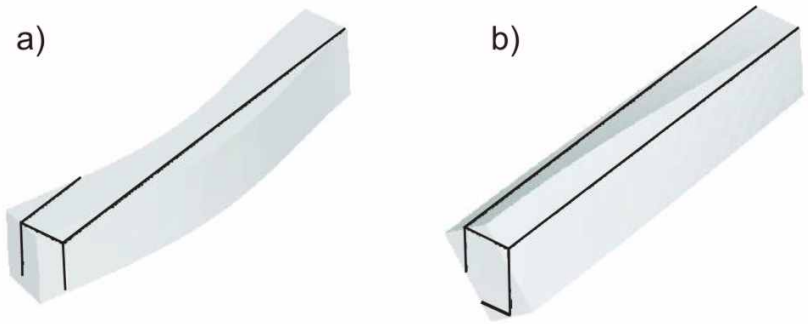

Figure 1.5: Examples of cantilever modes not present in a bulk solid, with the black lines indicating the beam in absence of movement serving as guide to the eye. a) Second flexural (bending) mode. b) Fundamental (first) torsional (twisting) mode.

kind of solutions $X(z,t), Y(z,t) \sim e^{i(kz-\omega t)}$, but with a *quadratic* dispersion relation, $\omega_j(k) = \sqrt{EI_j/(\rho S)}k^2$. An example of bending mode for a cantilever can be seen in fig.(1.5a).

1.5 Dissipative mechanisms damping the vibrational eigenmodes of semiconductor nanoresonators

Numerous dissipative sources limit the lifetime of an externally excited mechanical eigenmode, absorbing its energy irreversibly. Some of them, like surface impurities, clamping imperfections or gas friction can be reduced devising solutions like working in high vacuum conditions [MHE+02, MH07], annealing the samples at the right stage of the fabrication process [YSC+00, YOE02, WOE04, LVS+05] or engineering carefully the clamping points to minimize the coupling to bulk vibrational modes outside the resonator [HFZ+05]. They are thus *extrinsic* mechanisms, as opposed to *intrinsic* mechanisms, present even in a theoretically perfect sample, such as anharmonic coupling with other modes, electron-phonon or electron-electron interactions. A brief description of the most important mechanisms follows.

1.5.1 Extrinsic mechanisms

Gas or liquid friction

Collisions with surrounding gas molecules can impose severe limitations on the quality factor, specially in those setups designed to work in ambient conditions or in a liquid environment [BW04, DKEM06, MH07]. Depending on the fluid density

several regimes appear which have to be analyzed with different frameworks, ranging from free molecular to continuum limits. Q increases with decreasing pressure P, and for $P < 1$ mTorr it can be safely disregarded as the main frictional force for nanoresonators with $Q \geq 10^4$ [MHE+02, ER05].

Heating linked to the actuation or detection setup

In the magnetomotive scheme the flow of electrons through the metallic top layer is not ballistic, and heating of the layer is generated through their inelastic collisions, which in turn heats the semiconductor substrate underneath. Fortunately for the usual current densities this effect seems to be irrelevant compared to others [MHE+02]. In schemes using actuation and detection lasers illuminating the resonator, heating may play a more significant role, but we will not study it further in this thesis.

Noise introduced by the external electrical circuit

The external circuitry can be a source of extra damping and frequency shift, due to its finite impedance. This effect can be used for applications requiring an external control of linewidth, like signal processing [CR99, Sch02].

Clamping (attachment) losses

This mechanism corresponds to the transfer of energy from the resonator mode to acoustic modes at the contacts and beyond to the substrate through the anchorage areas [JI68, PJ04]. The motion of the resonator forces as well a motion of the atoms linking it to the rest of the device, irradiating in this way elastic energy to its surroundings. This mechanism can be of special relevance for short and thick beams, while for long and thin ones it plays a secondary role [HFZ+05, FZMR06].

Surface roughness and imperfections

As mentioned previously, the structures obtained through current methods present a certain degree of roughness of ~ 10 nm. On top of this, adsorbed impurities, dislocations and surface reconstruction processes are all coupled to the local atomic displacements linked to the resonator's motion, absorbing energy from the vibrational eigenmode and transmitting it irreversibly to the rest of degrees of freedom of the system. These imperfections and impurities also exist in the core of the resonator structure, but to a lesser degree as in the case of its surface, exposed to the environment and with atoms less bound than in the bulk, more susceptible to thermal rearrangements. Strong evidence has been accumulated of the increasing role played by surfaces as the resonator sizes shrink and surface-to-volume ratios grow, being the dominating friction source in thin nanobeams at low temperatures: i) The quality factor Q roughly scales linearly with the former ratio [YSC+00, ER05], as shown in

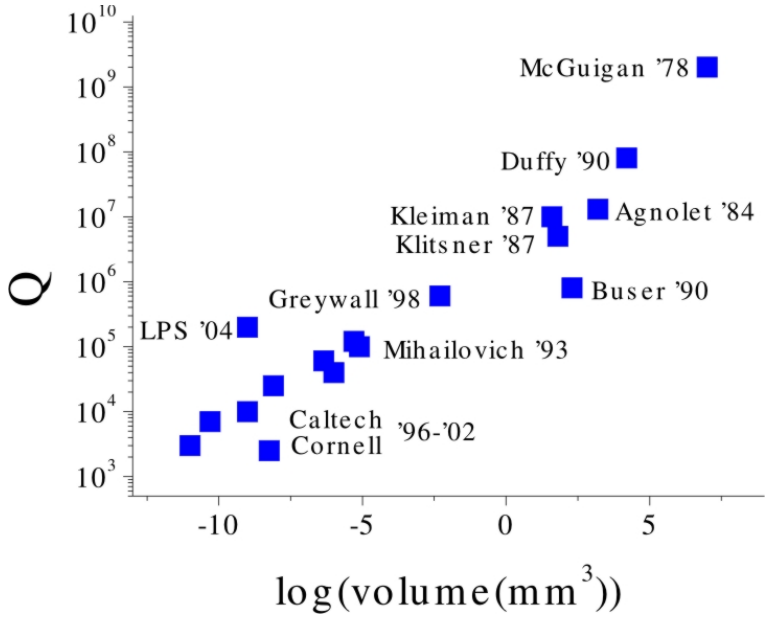

Figure 1.6: From ref. [ER05]. Evolution of reported quality factors in monocrystalline mechanical resonators with size, showing a decrease with linear dimension, i.e., with increasing surface-to-volume ratio, indicating a dominant role of surface-related losses.

fig.(1.6), ii) Q has been observed to increase up to an order of magnitude when the system went through a thermal treatment [YOE00, WOE04, LVS$^+$05] or the surface was deoxidized [YOE02]. In the next chapter we will study in depth these surface-related losses, dominant for thin beams at low temperatures, precisely the interesting regime where quantum effects show up if a very high Q is reached. Surface waves can be also excited by the vibrational eigenmode due to the roughness, but at low temperatures this process becomes strongly suppressed [MHE$^+$02], and thus will be ignored in our study.

Generation of e-h pairs in the metallic electrode due to electron-phonon coupling

In the magnetomotive scheme, where the semiconductor bridge is covered with a thin metallic top layer, the flowing electrons feel the Coulomb potential generated by static charges in the device and substrate. When the oscillating part is set into motion, this potential is time-dependent, and gives the chance to the electrons to absorb part of the mechanical energy stored in the eigenmode, creating e-h pairs. We will study this mechanism in the next chapter.

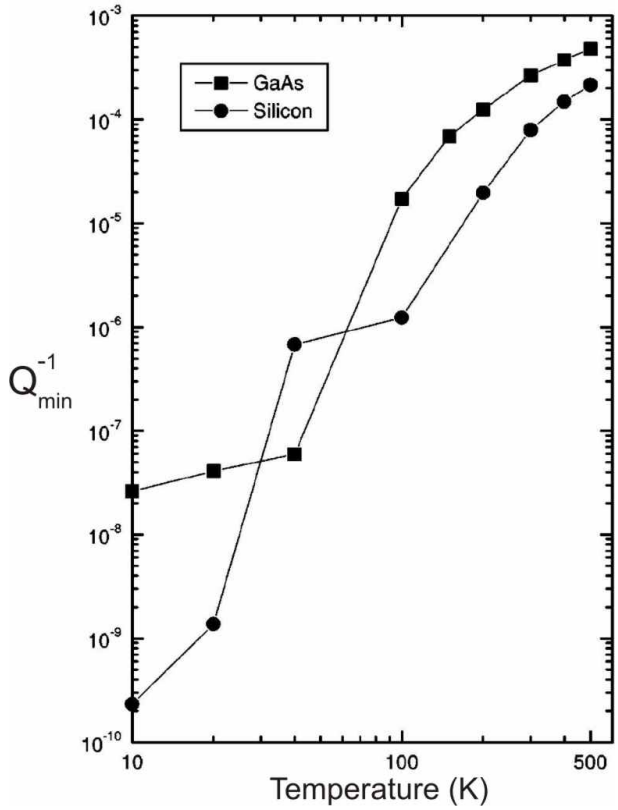

Figure 1.7: From ref. [LR00]. Minimum dissipation Q^{-1}_{min} imposed by the thermoelastic damping mechanism, as a function of temperature, for any resonator made from GaAs or Si.

1.5.2 Intrinsic mechanisms

Thermoelastic relaxation

The strain field generated by the excited eigenmode modifies the local thermal equilibrium, with the coupling to the local temperature field characterized by the linear expansion coefficient $\alpha = (1/L)dL/dT$. This translates into the local creation of thermal phonons by the long-wavelength eigenmode, which then diffuse to points with different temperatures leading to dissipation [Zen38, LR00, Cle02, Ü06]. This mechanism is strongly temperature dependent, being suppressed at low temperatures and dominating at high ones. In [LR00] a detailed study of this mechanism is carried out and the limits to the quality factor were established for any resonator made with Si or GaAs, two of the commonest materials, see fig.(1.7).

Anharmonic mode coupling (phonon-phonon interactions)

When the nanoresonator is strongly driven the harmonic approximation for the lattice potential breaks down, and higher order terms which couple the former vibrational eigenmodes have to be included, giving a finite lifetime to a given externally excited mode. At a temperature T, the externally excited mode will interact with thermal phonons, loosing its energy [Cle02, Ü06]. We will assume that the experiments are done at low excitations amplitudes, within the linear regime, where this effect can be neglected. Nevertheless, it is worth mentioning the exciting physics and potential applications of strongly driven nanoresonators, currently a subject of intensive research [KRSL07, SDC04, URA04, BM05, SHN06, SIM07].

Surface reconstruction and amorphization

Even if the fabrication processes and materials used were perfect, purely thermodynamic considerations imply that at a temperature $T > 0$ the sharp edges of a finite crystal begin to round off due to the increasing importance of entropy, in a process called creation of vicinal surfaces [Wei99]. The associated rearrangement of atoms and coupling of vibrational modes limit the maximum quality factor attainable.

After this brief overview of semiconductor nanoresonators and friction mechanisms affecting them, we will focus our attention in Chapter 2 on the theoretical modeling of surface-related dissipation at low temperatures, borrowing ideas from sound attenuation in amorphous glasses.

Chapter 2

Surface dissipation in semiconductor NEMS at low temperatures

2.1 Introduction

In this chapter we will try to provide a unified theoretical framework to describe the processes taking place at the surface of nanoresonators at low temperatures, which have been observed to dominate dissipation of their vibrational eigenmodes in this regime, see fig.(2.1). This is certainly a challenging task, since as we have seen many different dynamical processes and actors come into play (excitation of adsorbed molecules, movement of lattice defects or configurational rearrangements), some of whom are not yet well characterized, so simplifications need to be made. We will provide such a scheme, based on the following considerations:

- Experimental observations indicate that surfaces of otherwise monocrystalline resonators acquire a certain degree of roughness, impurities and disorder, resembling an amorphous structure [LTBP99, Wei99].
- In amorphous solids the damping of acoustic waves at low temperatures is successfully explained by the Standard Tunneling Model [AHV72, Phi72, Phi87, Esq98], which couples the acoustic phonons to a set of Two-Level Systems (TLSs) representing the low-energy spectrum of all the degrees of freedom able to exchange energy with the strain field associated to the vibration.

We will describe the attenuation of vibrations in nanoresonators due to their amorphous-like surfaces in terms of an adequate adaptation of the Standard Tunneling Model. We start reviewing such model, and some concepts and techniques used to analyze the spin-boson hamiltonian appearing in it. Then we proceed to apply in the proper way the Standard Tunneling Model to the non-bulk nanoresonator geometry.

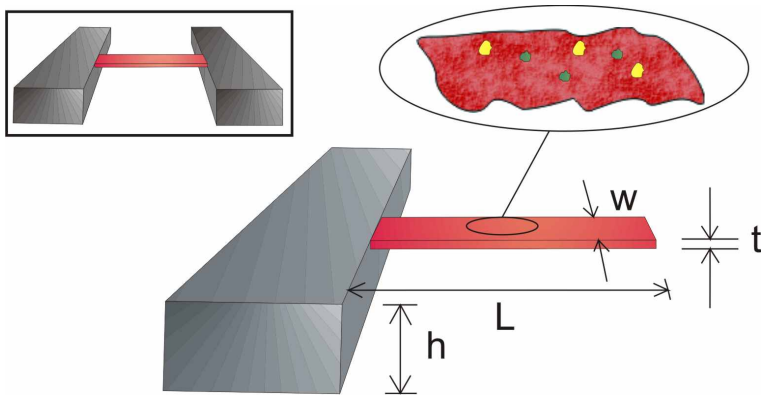

Figure 2.1: Sketch of the systems whose surface dissipation will be studied in this chapter. The inset shows a doubly clamped beam, while the main figure shows a cantilever characterized by its dimensions, width (w), thickness (t), and length, (L), where $w \sim t \ll L$. The height above the substrate is h. A schematic view of the surface is given, highlighting imperfections like roughness and adsorbates, which dominate dissipation at low temperatures.

Expressions for the frequency shift and dissipation in terms of the inverse quality factor Q^{-1} for flexural and torsional modes will be given, showing the scaling with dimensions, temperature and other relevant parameters of these systems. We will see that qualitative agreement with experimental observations is obtained, discussing limitations and possible modifications of the scheme to reach quantitative fitting to experiments. For NEMS covered with metallic electrodes the friction due to electrostatic interaction between the flowing electrons and static charges in the device and substrate will be also studied.

2.2 Damping of acoustic waves in amorphous solids: Standard Tunneling Model

The description and understanding of the properties of amorphous solids, where most of the simplifications linked to an infinite periodic structure are absent, has been full of unexpected results [Zal98]. In the low temperature regime, pioneering experiments by Zeller and Pohl [ZP71] revealed at $T < 1$ K striking differences between the thermal properties of dielectric amorphous solids as compared to those of crystalline solids. In a Debye dielectric crystalline solid it is well known that the heat capacity and the thermal conductivity due to phonons behave as $C \sim T^3$ and $\kappa \sim T^3$, but in the case of amorphous dielectrics none of them is true, instead a $C \sim T^{1.2}$ (and much bigger in value as compared to a crystalline form of the material) and $\kappa \sim T^{1.8}$

behavior is observed. Apart from this, a heat release as a function of time is observed on long time scales: after a sample is heated and then rapidly cooled down to some temperature T_0, in adiabatic conditions the sample begins gradually to heat itself afterwards. Moreover, measuring their acoustic properties at low temperatures, which a priori were expected to be similar to those found in crystalline solids due to the long-wavelength vibrations involved, the following dependence on the acoustic intensity was obtained [HAS$^+$72]: at low intensities, as the temperature is lowered the mean free path of the phonon decreases, while at high intensities a monotonous increase is observed.

Several theoretical scenarios were developed to explain these low-temperature features, the most successful of whom was the so-called *Standard Tunneling Model*, proposed simultaneously by Phillips and Anderson *et al.* [AHV72, Phi72].

The tunneling model claims the existence of the following states, intrinsic to glasses: an impurity, an atom or cluster of atoms within the disordered structure which present in their configurational space two energy minima separated by an energy barrier (similarly to the dextro/levo configurations of the ammonia molecule), as depicted schematically in fig.(2.2a). These states can be modeled as a degree of freedom tunneling between two potential wells. At low temperatures only the two lowest eigenstates have to be considered, characterized by the bias Δ_0^z between the wells and the tunneling rate Δ_0^x through the barrier, see fig.(2.2b). This corresponds to the Two-Level System (TLS) hamiltonian:

$$H_0 = \Delta_0^x \sigma_x + \Delta_0^z \sigma_z \ , \tag{2.1}$$

where σ_i are Pauli matrices. Due to the disorder of the structure, a broad range of values for the TLSs parameters Δ_0^z and Δ_0^x is expected to appear for the ensemble of TLSs present in the amorphous solid. In order to be operative, the Standard Tunneling Model has to specify the properties of this ensemble in terms of a probability distribution $P(\Delta_0^x, \Delta_0^z)$. The form of $P(\Delta_0^x, \Delta_0^z)$ can be inferred from general considerations [AHV72, Phi72], as detailed in Appendices B.1.1 and B.1.2, and is furthermore supported by experiments [Esq98]. The result is

$$P(\Delta_0^x, \Delta_0^z) = \frac{P_0}{\Delta_0^x} \, , \tag{2.2}$$

with $P_0 \sim 10^{44}\mathrm{J}^{-1}\mathrm{m}^{-3}$, $\Delta_0^x > \Delta_{min}$ (Δ_{min} fixed by the time needed to obtain a spectrum around the resonance frequency of the excited eigenmode), and $\varepsilon = \sqrt{(\Delta_0^x)^2 + (\Delta_0^z)^2} < \varepsilon_{max}$, estimated to be of the order of 5 K.

A last feature necessary to calculate the damping of acoustic waves caused by these low energy excitations is the coupling TLSs - phonons. As justified in Appendix B.1.3, the lattice distortions caused by the propagation of the wave affect mainly the TLSs asymmetry Δ_0^z, with the following final form for the hamiltonian describing the

coupled system TLSs + phonons:

$$H = \sum_{k,j} \hbar\omega_{k,j} b^\dagger_{k,j} b_{k,j} + \sum_{\Delta_0^x, \Delta_0^z} \left\{ \Delta_0^x \sigma_x + \left[\Delta_0^z + \sum_{k,j} \lambda_{k,j} (b^\dagger_{k,j} + b_{k,j}) \right] \sigma_z \right\} \tag{2.3}$$

Here $b^\dagger_{k,j}$ are the creation operators of the strain field waves $\mathbf{u}(\mathbf{r}, t)$ whose components $u_i(\mathbf{r}, t)$ obey the wave equations

$$E \frac{\partial^2 u_i}{\partial x_j^2} = \rho \frac{\partial^2 u_i}{\partial t^2} \tag{2.4}$$

The interaction hamiltonian is more specifically [Esq98]

$$H_{int} = \sigma_z \sum_{k_i,s} \lambda_{k_i,s} (b^\dagger_{k_{i,s}} + b_{k_{i,s}}) = \hbar\sigma_z \sum_{k_i,s} \left[\gamma \sqrt{\frac{1}{2\rho L^3 \hbar}} \frac{k_{i,s}}{\sqrt{\omega(k_{i,s})}} \right] (b^\dagger_{k_{i,s}} + b_{k_{i,s}}) \,, \tag{2.5}$$

where s is the polarization and i the component of the wavevector. L is the lateral size of the sample, while γ is the coupling constant, with an approximate value $\gamma \sim 1$ eV.

With the low energy TLS ensemble appearing in hamiltonian of eq.(2.3) characterized by a statistical distribution given by eq.(2.2), the strange thermal and acoustical properties of glasses at low temperatures mentioned in the beginning of this section can be satisfactorily explained [Phi87]: $C \sim T^1$ and $\kappa \sim T^2$ are obtained, close to the experimental ones, whose discrepancies can be corrected by modifying slightly the simplified probability distribution. The heat release experiments are as well explained, because there is a broad distribution of relaxation times for the initially thermally excited TLSs, and most of them will relax very slowly, transferring gradually their energy to the phonons of the solid, increasing its temperature. Concerning the dependence of the phonon mean free path behavior on acoustic intensity, it is explained by the saturation of the population of excited TLSs, that eliminates the scattering mechanism of resonant absorption and decay (to be explained later in this chapter) at high intensities. The scattering at higher temperatures is dominated by non-resonant relaxational processes, also to be described later, associated to the equilibration of the levels after a change in population, which occurs at a rate resulting in a mean free path for the phonon $l_{nres} \propto T^{-3}$.

The range of applicability of the Standard Tunneling Model is determined by the approximations involved. The first one concerns the assumption that the TLSs interact only indirectly via their interaction with the phonons. This is false below a certain temperature $T \sim 50$ mK, when interactions of dipolar character among TLSs cannot be disregarded [Esq98, YL88, AM03, ERK04]. The high temperature limit of applicability of the model is fixed by the moment when the TLS approximation, restricting the Hilbert space to the one spanned by the groundstates of the wells, see

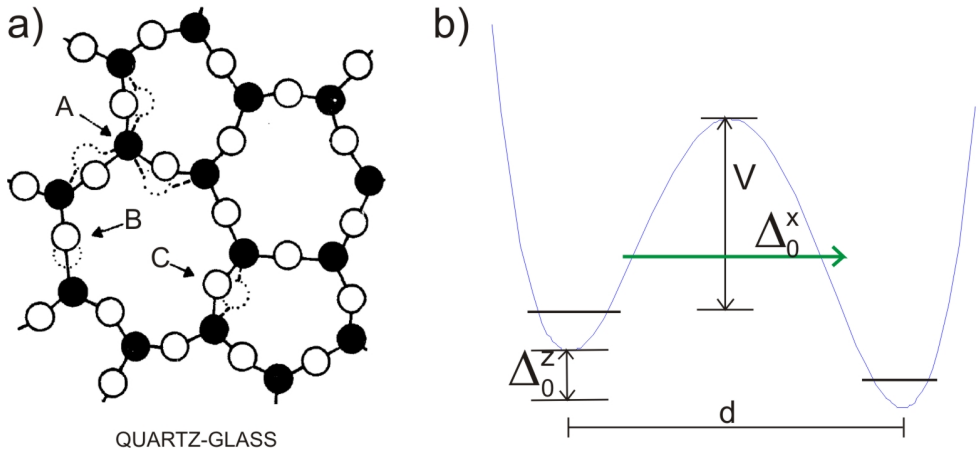

Figure 2.2: a) From [JPAH76]. Schematic view of an amorphous quartz structure, showing three possible types of two-state defects (A, B and C). b) Those two-states can be represented by a degree of freedom in a double well potential with an energy barrier of height V, width d, and asymmetry between wells Δ_0^z. At low temperatures only the ground states of both wells play a role in the dynamics, becoming mixed by the tunneling through the barrier (green arrow), of amplitude Δ_0^x. Thus the description is reduced to that of a Two-Level System.

fig.(2.2b), is not valid anymore, at about $T \sim 1$ K. The model also assumes weak intensities of the acoustic waves excited, or otherwise anharmonic coupling among vibrational modes and higher order terms coupling TLSs and phonons would become non-negligible.

2.3 Theoretical analysis of the damping of phonons due to TLSs

Given an externally pumped vibrational eigenmode of frequency ω_0, we will divide its dissipation due to the presence of TLSs into three parts: i) Resonant dissipation, ii) Friction caused by symmetric non-resonant TLSs, and iii) Relaxation processes due to the bias Δ_0^z.

For usual excitation amplitudes the first one can be ignored. To obtain the energy dissipation rate corresponding to the other two mechanisms, we will proceed for each of them in two steps: first we will study what is the effect of a *single* TLS, expressing the results in terms of its parameters Δ_0^z, Δ_0^x, and in a second step we will *sum* the individual contributions to dissipation *over all the TLS ensemble*, characterized by the distribution (2.2).

2.3.1 Resonant dissipation

Those TLSs with their unperturbed excitation energies close to ω_0 will resonate with the mode, exchanging energy quanta, with a rate proportional to the mode's phonon population n_{ω_0} to first order. For usual excitation amplitudes $\sim 0.1 - 1$Å the vibrational mode is so populated (as compared with the thermal population) that the resonant TLSs become saturated, and their contribution to the transverse (flexural) wave attenuation becomes negligible, proportional to $n_{\omega_0}^{-1/2}$ [AHSD74].

2.3.2 Dissipation of symmetric non-resonant TLSs

Dissipation caused by a single TLS

We will analyze here the dynamical behavior of one TLS coupled to the phonon ensemble:

$$H = \Delta_0^x \sigma_x + \Delta_0^z \sigma_z + \sum_{k,j} \lambda_{k,j}\ \sigma_z (b_{k,j}^\dagger + b_{k,j}) + \sum_{k,j} \hbar\omega_{k,j} b_{k,j}^\dagger b_{k,j} \tag{2.6}$$

This hamiltonian is nothing but the well-known *spin-boson model*, which applies to a great variety of physical phenomena related to open dissipative systems, and has been subject of intensive theoretical work [LCD+87, Wei99]. We will use some of this knowledge to describe the dynamics of the single TLS in terms of the spectral function

$$A(\omega) \equiv \sum_n |\langle 0 |\sigma_z| n\rangle|^2 \, \delta(\omega - \omega_n + \omega_0) \tag{2.7}$$

where $|n\rangle$ is an excited state of the total system TLS plus vibrations. We will see how this function describes the absorption properties of a symmetric TLS coupled to a vibrational ensemble through the operator σ_z.

The analysis of the spin-boson model for a TLS with asymmetry $\Delta_0^z \neq 0$ is much more cumbersome than the symmetric TLS case, if one tries to use the kind of techniques described in [LCD+87] that work for the symmetric case. Thus, to learn about the effect of the asymmetry Δ_0^z in the absorption spectrum of the TLS we will make a different kind of analysis, studying the delayed response of a TLS due to its bias Δ_0^z, and finally see its signatures in the absorption spectrum. A natural division of dissipative mechanisms will arrive as a consequence of this analysis: one contribution, the relaxation mechanism, will correspond to the presence of the bias, while the other will describe the dissipation occurring independently of the presence or absence of bias.

The techniques we will use for the analysis of the symmetric case are all described in [LCD+87], mainly i) Simple renormalization-group arguments to obtain effective or "dressed" values Δ_{eff}^x, Δ_{eff}^z of the TLS parameters from Δ_0^x, Δ_0^z due to

the interaction with high energy vibrational modes, ii) Characterization of the interaction with the different kinds of vibrational modes based on the criteria derived in the non-interacting blip approximation (NIBA, see Appendix B.2 for a brief review on the basic concepts and results), iii) Second-order perturbation theory in the interaction term of (2.6). These techniques are adequate for the regime where the Standard Tunneling Model holds, described just before the beginning of this section, and work better for very low vibration amplitudes of the externally excited vibrational mode. Even within the linear regime of the mode, above a certain amplitude other approaches designed to study strongly driven TLSs become more suited to describe the dynamics of at least part of the ensemble of TLSs, namely numerical methods as Quantum Monte Carlo [EW92, LWW98] or Numerical Renormalization Group [BTV03, BLTV05, ABV07, Wv07], or theoretical studies of the driven spin-boson model [GSSW93, GH98]. We will assume that the TLSs in resonance with the externally excited mode are saturated and thus do not contribute significantly to its dissipation, while for the rest of TLSs the vibration is assumed to be sufficiently weak for the techniques i), ii) and iii) to hold.

Spin-boson model for an almost symmetric TLS interacting with the nanoresonator modes

Now we take a TLS with $\Delta_0^z \ll \Delta_0^x$. In principle it is coupled to three kinds of vibrational modes, those described in section 1.4. The analysis of the resulting spectral function (2.7) would be greatly simplified if we could somehow compare the effect of the different kinds of modes and conclude that two of them have a negligible influence as compared with the third. Fortunately the path integral NIBA approach developed by Leggett *et al.* [LCD+87] (see Appendix B.2) reveals that the degree of influence of a given bosonic bath $\sum_k \hbar\omega_k b_k^\dagger b_k$ on the dynamics of a TLS coupled to it through $H_{\rm int} \equiv \sigma_z \sum_k \lambda_k \left(b_k^\dagger + b_k\right)$ for low temperatures and small enough coupling λ_k, is completely determined by the spectral density of the bath

$$J(\omega) \equiv \int_{-\infty}^{\infty} dt\, e^{i\omega t} \langle H_{int}(t) H_{int}(0)\rangle = \sum_k |\lambda_k|^2\, \delta(\omega - \omega_k) \tag{2.8}$$

This function corresponds to the spectral decomposition of the operator $H_{\rm int}$, telling us the rate at which transitions between the two eigenstates of the isolated TLS accompanied by excitation of a phonon happen, as a function of ω. The three kinds of modes coupled to our TLS are characterized by a $J(\omega) \sim \omega^s$. As explained in the end of Appendix B.2, this result, obtained for $T = 0$, changes at $T > 0$ because the thermal energy increases the number of possible initial and final states, and $J(\omega)$ changes to $J(\omega, T \gg \omega) \sim T^s$. Then, if temperature is lowered the modes with a $J(\omega)$ with the lowest power s (weakest T dependence) will affect the TLS dynamics more strongly than the others, which to a first approximation can be ignored.

Focussing on the case of a TLS coupled to the vibrations present in a rod, the starting hamiltonian is

$$H = \Delta_0^x \sigma_x + \Delta_0^z \sigma_z + \sigma_z F(\partial_i u_j) + H_{\text{elastic}} \tag{2.9}$$

where $\partial_i u_j$ is a component of the deformation gradient matrix, F is an arbitrary function, and H_{elastic} represents the elastic energy stored due to the atomic displacements, which will correspond in second quantization to the last term in eq.(2.6). Changing basis to the energy eigenstates of the TLS, eq.(2.9) becomes $H = \varepsilon\sigma_z + [(\Delta_0^x/\varepsilon)\sigma_x + (\Delta_0^z/\varepsilon)\sigma_z]F(\partial_i u_j) + H_{\text{elastic}}$. We are considering for the moment only slightly biased TLSs for whom $\Delta_0^z \ll \Delta_0$, so the last term can be ignored. A further expansion of F to lowest order in the displacement, together with a $\pi/4$ rotation of the eigenbasis, leads to:

$$H = \varepsilon\sigma_x + \gamma(\Delta_0^x/\varepsilon)\sigma_z \partial_i u_j + H_{\text{elastic}}\,, \tag{2.10}$$

where γ is the coupling constant, assumed to be as in amorphous 3D solids $\gamma \sim 1$ eV.

The atomic displacements can be decomposed into the normal vibrational modes, which for the cuasi-1D case of nanorods are the ones obeying eqs.(1.2-1.4). The vibrational modes of a beam with fixed ends have a discrete spectrum, but we will approximate them by a continuous distribution. This approximation will hold as long as many vibrational modes become thermally populated, $kT \gg \hbar\omega_{fund}$, where ω_{fund} is the frequency of the lowest mode. The condition is fulfilled in current experimental setups. The derivation of the second quantized version of the sort of eq.(2.6) for each of the modes and the corresponding spectral functions $J(\omega)$ are described in Appendix B.2.1. Here we state the main results:

The compression and twisting modes lead to an ohmic spectral function for $\omega \ll 2\pi c/R$ (R being a typical transversal dimension of the rod and c the sound velocity), when the rod is effectively 1D. In terms of the Young modulus of the material, E, and the mass density, ρ, we get: $J_{\text{comp}}(\omega) = \alpha_c|\omega|$, where,

$$\alpha_c = \gamma^2(2\pi^2\rho t w)^{-1}(E/\rho)^{-3/2}\,. \tag{2.11}$$

A factor $(\Delta_0^x/\varepsilon)^2$ has been thrown away, as we consider almost symmetric TLS with $\Delta_0^x \sim \varepsilon$. We will proceed similarly with the other modes. The twisting modes are defined by the torsional rigidity, $C = \mu t^3 w/3$ (μ is a Lande coefficient), and $I = \int dS x^2 = t^3 w/12$ (where S is the cross-section). The corresponding spectral function is given by: $J_{\text{torsion}}(\omega) = \alpha_t|\omega|$, where

$$\alpha_t = \gamma^2 C(8\pi^2\mu t w \rho I)^{-1}(\rho I/C)^{3/2}\,. \tag{2.12}$$

The analysis of the flexural (bending) modes differs substantially from the other ones, because they correspond to two fields that do not follow usual wave equations. The normal modes have a quadratic dispersion, $\omega_j(k) = \sqrt{EI_j/(\rho t w)}\,k^2$, leading to a *sub-ohmic* spectral function [LCD+87],

$$\boxed{J_{\text{flex}}(\omega) = \alpha_b\sqrt{\omega_{co}}\sqrt{\omega}}\,, \tag{2.13}$$

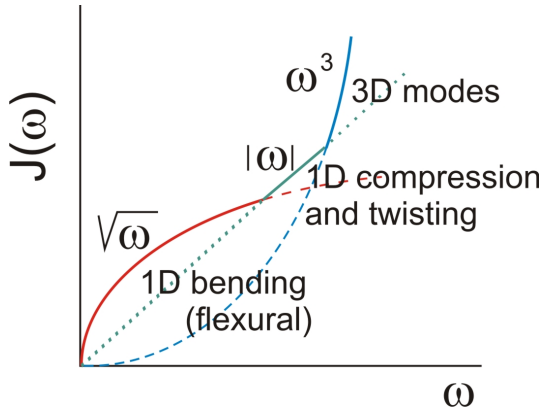

Figure 2.3: Sketch of the contributions to the spectral function which determines the dynamics of the TLS.

with,

$$\alpha_b\sqrt{\omega_{co}} = 0.3\frac{\gamma^2}{t^{3/2}w}\frac{(1+\nu)(1-2\nu)}{E(3-5\nu)}\left(\frac{\rho}{E}\right)^{1/4}, \tag{2.14}$$

where ν is Poisson's ratio and $\omega_{co} \simeq \sqrt{EI_y/(\rho tw)}(2\pi/t)^2$ is the high energy cut-off of the bending modes (frequency for whom the corresponding wavelength is of the order of t, thus indicating the onset of 3D behavior). This example of sub-ohmic spin-boson model is the first result of this thesis to be stressed, because the problem of a TLS interacting with a sub-ohmic environment is interesting in its own right [LCD+87, KM96, Wei99, Sta03, VTB05, GW88, SG06, CT06, Khv04, IN92], and the systems studied here provide a physical realization.

The bending modes prevail over the other, ohmic-like, modes as a dissipative channel at low energies. One may ask at what frequency do the torsional and compression modes begin to play a significant role, and a rough way to estimate it is to see at what frequency do the corresponding spectral functions have the same value, $J_{\rm flex}(\omega*) = J_{\rm comp,tors}(\omega*)$. The results are $\omega* \sim 30(1+\nu)^2(1-2\nu)^2(E/\rho)^{1/2}/[t(3-5\nu)^2]$ for the case of compression modes and $\omega* \sim 300(1-2\nu)^2(E/\rho)^{1/2}/[t(3-5\nu)^2(1+\nu)]$ for the torsional. Comparing these frequencies to the one of the onset of 3D behavior, ω_{co}, they are similar, justifying a simplified model where only flexural modes are considered. Collecting the previous results, we find the spectral function $J(\omega)$ plotted in Fig.[2.3].

TLS's dynamics

The interaction between the bending modes and the TLSs affects both of them. When a single mode is externally excited, as is done in experiments, the coupling

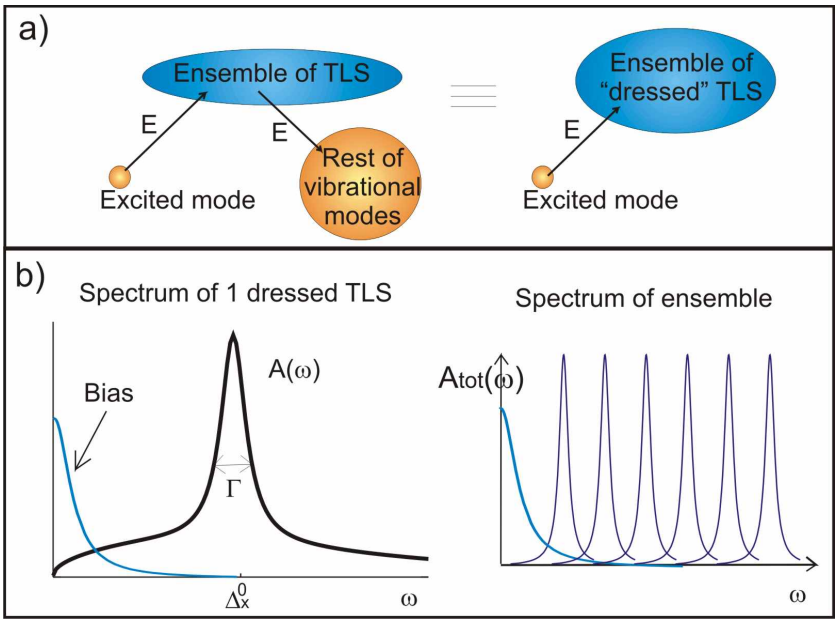

Figure 2.4: a) Schematic representation of the irreversible flow of energy from the externally excited mode to the TLS ensemble, and from the ensemble to the rest of vibrational modes. This process can be viewed as a flow of energy from the excited mode to an ensemble of "dressed" TLSs, with their dynamics modified by the presence of the vibrational modes. b) Left: Spectral function $A(\omega)$ of a single dressed TLS, weakly damped ($\Gamma < \Delta_0^x$). A peak around $\omega = 0$ arises if the system is biased, corresponding to the relaxational dissipation mechanism. Right: Total spectral function $A_{tot}(\omega)$ of the ensemble of dressed TLSs.

to the TLSs will cause an irreversible energy flow, from this mode to the rest of the modes through the TLSs, as depicted in fig.(2.4a). The dynamics of the TLSs in presence of the vibrational bath determines the efficiency of the energy flow and thus the quality factor of the excited mode. Taking a given TLS plus the phonons, its dynamics is characterized by the Fourier transform of the correlator $\langle\sigma_z(t)\sigma_z(0)\rangle$, the spectral function $A(\omega)$, eq.(2.7). We will see that, using second-order perturbation theory, the dissipation caused by an ensemble of TLSs on a given externally excited vibrational mode of frequency ω_0 is proportional to $\sum_j A_j(\omega_0)$, with the index j running over all the TLSs in the resonator, cf. eq.(2.18). We therefore study now $A(\omega)$.

High-energy oscillators with $\omega \gg \Delta_0^x$ adjust instantaneously to the value of σ_z, "dressing" the wells' eigenfunctions and decreasing the overlap between them, reducing accordingly the tunneling amplitude Δ_0^x [LCD+87]. This adiabatic renormalization of Δ_0^x can either reduce Δ_0^x to a finite value or suppress it completely. For

sub-ohmic coupling, eq.(2.14), the self-consistent equation for the renormalized value Δ_{ren} is:

$$\Delta_{ren} = \Delta_0^x \exp\{-\alpha_b \sqrt{\omega_{co}} \int_{\Delta_{ren}}^{\omega_{co}} d\omega J(\omega)/\omega^2\} \tag{2.15}$$

This equation has no solutions other than $\Delta_{ren} = 0$ if $\Delta_0^x \ll \alpha_b^2 \omega_{co}$, so that the tunneling amplitude of the low energy TLSs is strongly suppressed [SD85, LCD+87, Wei99, KM96]. The remaining TLSs experience a shift and a broadening of the spectral function function $A(\omega)$. For a typical Si nanoresonator with $L \sim 1\mu$m, $t \sim w \sim 100$ nm, $\alpha_b \ll 1$, and the shift is small, $\Delta_{ren} \sim \Delta_0^x$, and will be neglected in the following.

In addition, $A(\omega)$ acquires low and high energy tails, whose derivation can be found in Appendix B.3. At zero temperature the low energy tail is:

$$A(\omega) \propto \alpha_b \frac{\sqrt{\omega_{co}\omega}}{(\Delta_0^x)^2} \quad \omega \ll \Delta_0^x \ , \tag{2.16}$$

while the high energy part takes the form $A(\omega) \propto \alpha_b \sqrt{\omega_{co}} (\Delta_0^x)^2 \omega^{-7/2}$, for $\omega \gg \Delta_0^x$. The main features of $A(\omega)$ are shown in fig.(2.4b). Finally, we obtain the width of the resonant peak, $\Gamma(\Delta_0^x)$, using Fermi's golden rule, $\Gamma(\Delta_0^x) = 16\alpha_b \sqrt{\omega_{co}} \sqrt{\Delta_0^x}$. This description is valid for wavelengths such that $1/L \ll k \ll 1/\max(w,t)$. For a biased TLS, the value of Δ_0^z is not renormalized by the phonons.

As mentioned before, the coupled system TLSs + vibrations can be viewed, taking the coupling as a perturbation, from the point of view of the excited mode ω_0 as a set of TLSs with a modified absorption spectrum. The TLSs, dressed perturbatively by the modes, are entities capable of absorbing and emitting over a broad range of frequencies, transferring energy from the excited mode ω_0 to other modes. The contribution to the value of the inverse of the quality factor, $Q^{-1}(\omega_0)$, of all these non-resonant TLSs will be proportional to $A^{\rm tot}_{\rm off-res}(\omega_0) = \sum_{\Delta_0^x=0}^{\omega_0-\Gamma(\omega_0)} A(\Delta_0^x, \Delta_0^z, \omega_0) + \sum_{\omega_0+\Gamma(\omega_0)}^{\epsilon_{max}} A(\Delta_0^x, \Delta_0^z, \omega_0) \approx 2P\alpha_b \sqrt{\omega_{co}/\omega_0}$, a quantity measuring the density of states which can be excited through $H_{\rm int}$ at frequency ω_0, see Appendix B.3 for details.

For an excited mode ω_0 populated with n_{ω_0} phonons, $Q^{-1}(\omega_0)$ is given by

$$Q^{-1}(\omega_0) = \frac{\Delta E}{2\pi E_0} \ , \tag{2.17}$$

where E_0 is the energy stored in the mode per unit volume, $E_0 \simeq n_{\omega_0}\hbar\omega_0/twL$, and ΔE is the energy fluctuations per cycle and unit volume. ΔE can be obtained from Fermi's Golden Rule:

$$\Delta E^{\rm tot}_{\rm off-res} \simeq \frac{2\pi}{\omega_0} \times \hbar\omega_0 \times \frac{2\pi}{\hbar} n_{\omega_0} \left(\lambda \frac{k_0^2}{\sqrt{\omega_0}}\right)^2 A^{\rm tot}_{\rm off-res}(\omega_0) \, , \tag{2.18}$$

and the inverse quality factor of the vibration follows. For finite temperatures the calculation of $A^{\rm tot}_{\rm off-res}(\omega_0, T)$ is done in Appendix B.3. It has to be noted that in

experiments the *observed linewidth* is due to the total amount of *fluctuations*, so at a finite temperature it corresponds to the addition of emission and absorption processes. Thus in this context dissipation means fluctuations, and not net loss of energy. The combined contribution of these processes is

$$\boxed{(Q^{-1})^{\rm tot}_{\rm off-res}(\omega_0,T) \simeq 10 P_0 t^{3/2} w \left(\frac{E}{\rho}\right)^{1/4} \frac{\alpha_b^2 \omega_{co}}{\omega_0} \coth\left[\frac{\hbar\omega_0}{k_B T}\right]} \tag{2.19}$$

Before we continue with the third dissipative mechanism due to TLSs, a couple of words about the importance of multi-phonon processes is in order: Until now prevalence of one-phonon processes in the interaction among TLSs and vibrational modes has been assumed, but at temperatures much higher than the frequencies of the relevant phonons, multi-phonon processes should be taken into account. A useful indicator to estimate if one-phonon processes suffice to describe the interaction between the TLS and the bath is the Fermi's Golden Rule result for the linewidth: if the linewidth $\Gamma(\Delta_0^x, T)$ calculated in this way is much smaller than Δ_0^x, the approximation can be taken as good, while for $\Gamma(\Delta_0^x, T) \geq \Delta_0^x$ multiphonon processes have to be considered. The expression for the linewidth at a finite temperature is

$$\Gamma(\varepsilon, T) = 16\alpha_b \sqrt{\omega_{co}}\, \sqrt{\varepsilon} \coth\left[\frac{\varepsilon}{2k_B T}\right] \tag{2.20}$$

One can estimate, using the probability distribution (2.2), the total number of overdamped TLSs, $\Gamma(\varepsilon, T) \geq \Delta_0^x$, in the volume fraction of the resonator presenting amorphous features, V_{amorph}. With $V_{amorph} \sim V_{tot}/10$, and using $\Gamma(\varepsilon, T) \approx 2T\Gamma(\varepsilon, T = 0)/\varepsilon$, the number of overdamped TLSs, $\varepsilon \leq \Gamma(\varepsilon, T) \rightarrow \varepsilon \leq [30\alpha_b\sqrt{\omega_{co}}T]^{2/3}$, is $N \approx P_0 t w L [30\alpha_b\sqrt{\omega_{co}}T]^{2/3}$, which for typical resonator sizes $L \sim 1\mu$m, $t, w \sim 0.1\mu$m is less than one for $T < 1$ K. Therefore, unless the resonator is bigger and/or P_0 too, the TLSs can be assumed to be underdamped.

2.3.3 Contribution of biased TLSs to the linewidth: relaxation absorption

This very general friction mechanism arises due to the phase delay between stress and imposed strain rate. A detailed derivation for the case of TLSs in amorphous solids can be found in Appendix B.4. In our context, for a given TLS the populations of its levels take a finite time to readjust when a perturbation changes the energy difference between its eigenstates [J72̈, Esq98]. This time τ corresponds to the inverse of the linewidth (2.20). For a coupling as the one described by H_{int}, a component k of the deformation gradient matrix, $\partial u_k \sim \langle k, n_k | (k/\sqrt{\omega_k})(a_k^\dagger + a_k) | k, n_k \rangle$ associated to a vibrational mode $|k, n_k\rangle$ modifies the asymmetry Δ_0^z between the energy levels $\varepsilon_{1,2} = \mp\frac{1}{2}\sqrt{(\Delta_0^x)^2 + (\Delta_0^z + \xi_k \partial u_k)^2}$ (ξ_k the corresponding coupling constant with the

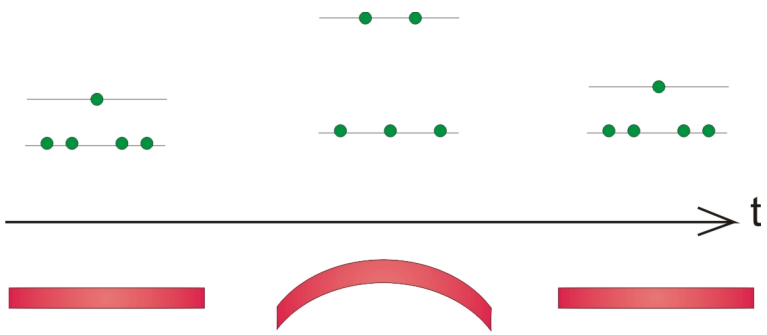

Figure 2.5: Schematic representation of the levels' population evolution of an ensemble of 5 identical TLSs with a response time $\tau \sim 1/\omega$, where ω is the frequency of the bending mode excited, whose evolution is also depicted in the lower part of the figure. The delay τ plus the bias Δ_0^z give rise to the relaxational energy loss mechanism of the mode, see text.

proper dimensions). So to first order the sensitivity of these energies to an applied strain is proportional to the bias

$$\frac{\partial \varepsilon^i}{\partial(\partial u_k)} = \frac{(\Delta_0^z \mp \xi_k \partial u_k)}{\varepsilon^i}\xi_k = \frac{\Delta_z^{tot}}{\varepsilon^i}\xi_k \ , \tag{2.21}$$

and the response of the TLS will be $\propto (\Delta_z^{tot}/\varepsilon)^2$. As derived in Appendix B.4, the imaginary part of the response, corresponding to Q^{-1} is also $\propto \tau/(1+\omega^2\tau^2)$, which in terms of $A(\omega)$ is the lorentzian peak at $\omega = 0$ of fig.(2.4b).

The mechanism is most effective when $\tau \sim 1/\omega$, where ω is the frequency of the vibrational mode; then, along a cycle of vibration, the following happens (see fig.(2.5)): When the TLS is under no stress the populations, due to the delay τ in their response, are still being adjusted as if the levels corresponded to a situation with maximum strain (and therefore of maximum energy separation between them, cf. $\varepsilon_{1,2}(u_k)$), so that the lower level becomes overpopulated. As the strain is increased to its maximum value the populations are still adjusting as if the levels corresponded to a situation with minimum strain, thus overpopulating the upper energy level. Therefore in each cycle there is a net absorption of energy from the mechanical energy pumped into the vibrational mode.

If on the other hand $\tau \gg 1/\omega$ the TLSs levels' populations are frozen with respect to that fast perturbation, while in the opposite limit $\tau \ll 1/\omega$ the levels' populations follow adiabatically the variations of $\varepsilon_{1,2}$ and there is neither a net absorption of energy.

For an ensemble of TLSs, the contribution to Q^{-1} is [Esq98]

$$Q_{\rm rel}^{-1}(\omega, T) = \frac{P_0\gamma^2}{ET}\int_0^{\varepsilon_{max}} d\varepsilon \int_{u_{min}}^1 du \frac{\sqrt{1-u^2}}{u}\frac{1}{\cosh^2(\varepsilon/2k_BT)}\frac{\omega\tau}{1+(\omega\tau)^2} \tag{2.22}$$

The derivation of eq.(B.43) only relies in the assumptions of an existence of well defined levels who need a finite time τ to reach thermal equilibrium when a perturbation is applied, and the existence of bias $|\Delta_0^z| > 0$. This implies that such a scheme is applicable also to our 1D vibrations, but is valid only if the perturbation induced by the bath on the TLSs is weak, so that the energy levels are still well defined. Therefore we will limit the ensemble to underdamped TLSs for whom $\hbar\Gamma(\varepsilon, T) < \varepsilon$. In eq.(B.43) the factor $\cosh^{-2}(\varepsilon/2k_BT)$ imposes an effective cutoff $\varepsilon < k_BT$, so that in eq.(2.20) one can approximate $\coth[\varepsilon/2k_BT] \sim 2k_BT/\varepsilon$, resulting in $\Gamma(\varepsilon) \sim 1/\sqrt{\varepsilon}$, and thus the underdamped TLSs will satisfy $\varepsilon \geq [30\alpha_b\sqrt{\omega_{co}}T]^{2/3}$. For $T \gg [32\alpha_b\sqrt{\omega_{co}}]^2$, which is fulfilled for typical sizes and temperatures (see Appendix B.5 for details):

$$Q_{\text{rel}}^{-1}(\omega_0, T) \approx \frac{20P_0\gamma^4}{t^{3/2}w}\frac{(1+\nu)(1-2\nu)}{E^2(3-5\nu)}\Big(\frac{\rho}{E}\Big)^{1/4}\frac{\sqrt{T}}{\omega_0} \tag{2.23}$$

Here $V_{amorph} \sim V_{tot}/10$ was assumed.

2.3.4 Comparison between contributions to Q^{-1}. Relaxation prevalence.

It is useful to compare the importance of the contributions to Q^{-1} coming from the last two mechanisms. For that sake, we particularize the comparison to the case of the fundamental flexural mode, which is the one usually excited and studied, of a doubly clamped beam, with frequency $\omega_0 \approx 6.5(E/\rho)^{1/2}t/L^2$ (for a cantilever these considerations hold, with only a slight modification of the numerical prefactors; the conclusions are the same). The result is:

$$\Big[\frac{Q_{\text{rel}}^{-1}(T)}{Q_{\text{off}-\text{res}}^{-1}(T)}\Big]_{\text{fund}} \approx \frac{300t^{1/2}}{L}\frac{(3-5\nu)}{(1+\nu)(1-2\nu)}\frac{E}{\rho}\frac{1}{T^{1/2}} \tag{2.24}$$

For a temperature $T = 1$K, the result is as big as 10^6 even for a favorable case $t = 1$nm, $L = 1\mu$m, $E = 50$GPa, $\nu = 0.2$, $\rho = 3\text{g/cm}^3$. Then it can be concluded that for any reasonable temperature and dimensions the dissipation is dominated by the relaxation mechanism, so that the prediction of the limit that surfaces set on the quality factor of nanoresonators is, within this model for the surface, eq.(2.23):

$$\boxed{Q_{\text{surface}}^{-1}(\omega_0, T) \approx Q_{\text{rel}}^{-1}(\omega_0, T) \sim \frac{T^{1/2}}{\omega_0}} \tag{2.25}$$

For typical values $L \sim 1\mu$m, $t, w \sim 0.1\mu$m, $\gamma \sim 5$ eV, $P_0V_{amorph}/V_{tot} \sim 10^{44}\text{J/m}^3$, and T in the range 1mK-0.5K the estimate for $Q_{\text{surface}}^{-1} \sim 10^{-4}$ gives the observed order of magnitude in experiments like [ZGS+05, SCK+07], and also predicts correctly a sublinear dependence, but with a slightly higher exponent, 1/2 versus the experimental fit 0.36 in [ZGS+05], or 0.32 in [SCK+07], see fig.(2.6).

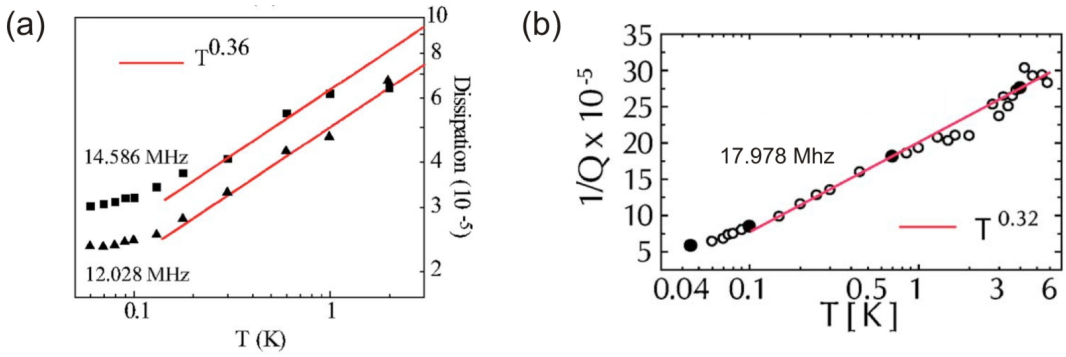

Figure 2.6: Experimental results for the dissipation of the fundamental flexural (bending) mode of three different doubly-clamped resonators. The dissipation is expressed in terms of Q^{-1}, the inverse of the quality factor.(a) Results obtained in ref. [ZGS+05] for two silicon doubly clamped beams of dimensions $0.2\times0.3\times6\mu$m and $0.2\times0.3\times7\mu$m. Their fundamental bending modes, 14.586 and 12.028 MHz respectively, show a $Q^{-1}(T) \sim T^{0.36}$ optimum fit for $0.1 < T < 1$ K. (b) Results of ref. [SCK+07] for a similar type of beam made of GaAs, of dimensions $0.5 \times 0.5 \times 15\mu$m, exhibiting an power law dependence $Q^{-1}(T) \sim T^{0.32}$ for $0.08 < T < 3$ K. These behaviors have to be compared with our model, who predicts $Q^{-1}(T) \sim T^{1/2}$, see text for details.

2.4 Extensions to other devices

2.4.1 Cantilevers, nanopillars and torsional oscillators

The extrapolation from doubly clamped beams to cantilevers [MSL+05] and nanopillars [SB04] is immediate, the only difference between them being the allowed (k,ω(k)) values due to the different boundary conditions at the free end (and even this difference disappears as one considers high frequency modes, where in both cases one has $k_n \approx (2n+1)\pi/2L$). All previous results apply, and one has just to take care in the expressions corresponding to the Q^{-1} of the fundamental mode, for whom there is more difference between the frequencies of both cases, the cantilever one being $\omega_0^{cant} \approx (E/\rho)^{1/2}t/L^2$ as compared to the doubly clamped case, $\omega_0^{clamped} \approx 6.5(E/\rho)^{1/2}t/L^2$.

2.4.2 Effect of the flexural modes on the dissipation of torsional modes

The contribution from the TLSs + subohmic bending mode environment to the dissipation of a torsional mode of a given oscillator can be also estimated. We will study the easiest (and experimentally relevant [SRCR04]) case of a cantilever. For paddle and double paddle oscillators the geometry is more involved, modifying the moment of inertia and other quantities. When these changes are included, the analysis

follows the same steps we will show.

Relaxation absorption. We assume, based on the previous considerations on the predominant influence of the flexural modes on the TLSs dynamics, as compared with the influence of the other modes, that the lifetime $\tau = \Gamma^{-1}$ of the TLSs is given by eq.(2.20). The change in the derivation of the expression for Q^{-1} comes in eq.(2.21), where the coupling constant $\xi_k^{\rm tors}$ is different, which translates simply, in eq.(B.43), into substituting $\gamma^2 \leftrightarrow \gamma_{\rm tors}^2$, and the corresponding prediction for $Q_{\rm rel}^{-1}$

$$\boxed{Q_{\rm rel}^{-1}(\omega_0, T) \approx \frac{20 P_0 \gamma_{\rm tors}^2 \gamma^2}{t^{3/2} w} \frac{(1+\nu)(1-2\nu)}{E^2(3-5\nu)} \Big(\frac{\rho}{E}\Big)^{1/4} \frac{\sqrt{T}}{\omega_0}}, \tag{2.26}$$

where now ω_0 is the frequency of the corresponding flexural mode. The range of temperatures and sizes for which this result applies is the same as in the case of an excited bending mode.

Dissipation of symmetric non-resonant TLSs The modified excitation spectrum of the TLS's ensemble, $A_{\rm off-res}^{\rm tot}(\omega_0, T)$, remains the same, and the change happens in the matrix element of the transition probability of a mode $|k_0, n_0\rangle$ appearing in eq.(2.18), $(\lambda k_0^2/\sqrt{\omega_0})^2$. The operator yielding the coupling of the bath to the torsional mode which causes its attenuation is the interaction term of the hamiltonian, which for twisting modes is given by eq.(B.30). In Appendix B.6 a detailed derivation of eq.(2.27) is shown. The main results are stated here. Again, $Q^{-1}(\omega_j) = \Delta E/2\pi E_0$, where the energy E_0 stored in a torsional mode $\phi_j(z,t) = A \sin[(2j-1)\pi z/(2L)] \sin(\omega_j t)$ per unit volume is $E_0 = A^2 \omega_j^2 \rho (t^2 + w^2)/48$ (z is the coordinate along the main axis of the rod). Expressing the amplitude A in terms of phonon number n_j, the energy stored in mode $|k_j, n_j\rangle$ is

$$E_0(k_j, n) = \frac{1}{2} \frac{\hbar \omega_j}{(t^3 w + w^3 t) L} (t^2 + w^2)(2n_j + 1)\,, \tag{2.27}$$

the energy fluctuations in a cycle of such a mode is

$$\Delta E = \frac{2\pi}{\omega_j} \times \hbar \omega_j \times \frac{2\pi}{\hbar} \frac{\gamma^2 \hbar \omega_j}{16 L t w \mu} n_j A_{\rm off-res}^{\rm tot}(\omega_j, T)\,, \tag{2.28}$$

and the inverse quality factor

$$(Q^{-1})_{\rm off-res}^{\rm tot}(\omega_0, T) \approx 0.04 \frac{\gamma^4 P}{t^{3/2} w} \frac{\rho^{1/4}(1+\nu)^2(1-2\nu)}{E^{9/4}(3-5\nu)} \frac{1}{\sqrt{\omega_0}} \coth\Big[\frac{\omega_0}{T}\Big] \tag{2.29}$$

For sizes and temperatures as the ones used for previous estimates the relaxation contribution dominates dissipation.

2.5 Frequency shift

Once the quality factor is known the relative frequency shift can be obtained via a Kramers-Kronig relation (valid in the linear regime), because both are related to the imaginary and real part, respectively, of the acoustic susceptibility. First we will demonstrate this, and afterwards expressions for beam and cantilever will be derived and compared to experiments.

2.5.1 Relation to the acoustic susceptibility

In absence of dissipative mechanisms, the equation for the bending modes is given by $-(12\rho/t^2)\partial^2 X/\partial t^2 = E\partial^4 X/\partial z^4$. The generalization in presence of friction is

$$-\frac{12\rho}{t^2}\frac{\partial^2 X}{\partial t^2} = (E+\chi)\frac{\partial^4 X}{\partial z^4} \tag{2.30}$$

Where χ is a complex-valued susceptibility. Inserting a solution of the form $X(z,t) = Ae^{i(kx-\omega t)}$, where k is now a complex number, one gets the dispersion relation $\omega = \sqrt{t^2(E+\chi)/(12\rho)}k^2$. Now, assuming that the relative shift and dissipation are small, implying $\mathrm{Re}(\chi) << \mathrm{E}$, $\mathrm{Im(k)} << \mathrm{Re(k)}$, the following expressions for the frequency shift and inverse quality factor are obtained in terms of χ:

$$\begin{cases} Q^{-1} & = \Delta\omega/\omega = -\mathrm{Im}(\chi)/\mathrm{E} \\ \delta\omega/\omega & = \mathrm{Re}(\chi)/2\mathrm{E} \end{cases} \tag{2.31}$$

Therefore a Kramers-Kronig relation for the susceptibility can be used to obtain the relative frequency shift:

$$\frac{\delta\omega}{\omega}(\omega,T) = -\frac{1}{2\pi}P\int_{-\infty}^{\infty} d\omega' \frac{Q^{-1}(\omega',T)}{\omega'-\omega} \ , \tag{2.32}$$

where P means here the principal value of the integral.

2.5.2 Expressions for the frequency shift

Relaxation processes of biased, underdamped TLSs dominate the perturbations of the ideal response of the resonator, as we have already shown for the inverse quality factor. For most of the frequency range, $\omega \geq [30\alpha_b\sqrt{\omega_{co}}T]^{2/3}$, $Q^{-1}(\omega,T) \approx A\sqrt{T}/\omega$, with A defined by eq.(2.23). The associated predicted contribution to the frequency shift, using eq.(2.32), is

$$\boxed{\frac{\delta\omega}{\omega}(\omega,T) \approx -\frac{A}{2\pi}\frac{\sqrt{T}}{\omega}\log\Big[\Big|1-\frac{\omega}{[30\alpha_b\sqrt{\omega_{co}}T]^{2/3}}\Big|\Big]} \tag{2.33}$$

For low temperatures, $\omega \gg [30\alpha_b\sqrt{\omega_{co}}T]^{2/3}$, the negative shift grows towards zero as $\delta\omega/\omega(\omega,T) \sim -\sqrt{T}\log[\omega/T^{2/3}]$, reaching at some point a maximum value, and decreasing for high temperatures, $\omega < [30\alpha_b\sqrt{\omega_{co}}T]^{2/3}$, as $\delta\omega/\omega(\omega,T) \sim 1/T^{1/6}$. Even though the prediction of a peak in $\delta\omega/\omega(T)$ qualitatively matches the few experimental results currently available [ZGS+05, SCK+07], it does not fit them quantitatively.

2.6 Applicability and further extensions of the model. Discussion

As mentioned, the predictions obtained within this theoretical framework do match qualitatively experimental results in terms of observed orders of magnitude for $Q^{-1}(T)$, weak sublinear temperature dependence, and presence of a peak in the frequency shift temperature dependence. But quantitative fitting is still to be reached, while on the experimental side more experiments need to be done at low temperatures to confirm the, until now, few results [ZGS+05, SCK+07].

Applicability. The several simplifications involved in the model put certain constraints, some of which are susceptible of improvement. We enumerate them first and discuss some of them afterwards: i) The probability distribution $P(\Delta_0^x, \Delta_0^z)$, borrowed from amorphous bulk systems, may be different for the case of the resonator's surface, ii) The assumption of non-interacting TLSs, only coupled among them in an indirect way through their coupling to the vibrations, breaks down at low enough temperatures, where also the discreteness of the vibrational spectrum affects our predictions iii) When temperatures rise above a certain value, high energy phonons with 3D character dominate dissipation, the two-state description of the degrees of freedom coupled to the vibrations is not a good approximation, and thermoelastic losses begin to play an important role, iv) For strong driving, anharmonic coupling among modes has to be considered, and some steps in the derivation of the different mechanisms, which assumed small perturbations, must be modified. This will be the case of resonators driven to the nonlinear regime, where bistability and other phenomena take place.

The solution to issue i) is intimately related to a better knowledge of the surface and the different physical processes taking place there. Recent studies try to shed some light on this question [CRB07], and from their results a more realistic $P(\Delta_0^x, \Delta_0^z)$ could be derived, which remains for future work. Before that point, it is easier to wonder about the consequences of a dominant kind of dissipative process which corresponded to a set of TLSs with a well defined value of Δ_0^x and a narrow distribution of Δ_0^z's of width Δ_1, as was suggested for single-crystal silicon [Phi88]. Following [Phi88], a $Q^{-1}(T) \sim \sqrt{T}$ behavior is obtained for low temperatures $T < \Delta_1$ if $\Gamma(\Delta_0^x, T) < \omega$, and a $Q^{-1}(T) \sim 1/\sqrt{T}$ if $\Gamma(\Delta_0^x, T) > \omega$, while at high temperatures $T > \Delta_1$ a constant $Q^{-1}(T) \sim Q_0$ is predicted for both cases. These predictions do not

match better with experiments than the results obtained with $P(\Delta_0^x, \Delta_0^z) \sim P_0/\Delta_0^x$, so issue i) remains open.

We try now to have a first estimate of the temperature for which interactions between TLSs cannot be ignored. Following the ideas presented in [Esq98], we will estimate the temperature $T*$ at which the dephasing time $\tau_{\rm int}$ due to interactions is equal to the lifetime $\tau(T) = \Gamma^{-1}(T)$ defined in eq.(2.20), for the TLSs that contribute most to dissipation, which are those with $\epsilon \sim \Delta_0^x \sim T$. For them $\tau^{-1}(T) = \Gamma(T) \approx 40\alpha_b\sqrt{\omega_{co}}\sqrt{T}$. The interactions between the TLSs are dipolar, described by $H_{\rm int} = \sum_{i,j} U_{1,2}\sigma_1^z\sigma_2^z$, with $U_{1,2} = b_{12}/r_{12}^3$, b_{12} verifying $\langle b_{12}\rangle \approx 0$, $\langle |b_{12}|\rangle \equiv U_0 \approx \gamma^2/E$ [YL88, Esq98]. From the point of view of a given TLS the interaction affects its bias, $\Delta_j^z = (\Delta_0^z)_j + \sum_i U_{ij}\sigma_j^z$, causing fluctuations of its phase $\delta\epsilon_j(t)$, which have an associated $\tau_{\rm int}$ defined by $\delta\epsilon_j(\tau_{\rm int})\tau_{\rm int} \sim 1$. These fluctuations are caused by those TLSs which, within the time $\tau_{\rm int}$, have undergone a transition between their two eigenstates, affecting through the interaction $H_{\rm int}$ the value of the bias of our TLS. At a temperature T, the most fluctuating TLSs are those such that $\epsilon \sim \Delta_0^x \sim T$, and their density can be estimated, using $P(\Delta_0^x, \Delta_0^z)$, as $n_T \approx P_0 kT$. They will fluctuate with a characteristic time $\tau(T) \approx [40\alpha_b\sqrt{\omega_{co}}\sqrt{T}]^{-1}$, so for a time $t < \tau(T)$ the amount of these TLSs that have made a transition is roughly $n(t) \approx P_0 kTt/\tau(T)$. For a dipolar interaction like the one described above, the average energy shift is related to $n(t)$ by [BH77] $\delta\epsilon(t) \approx U_0 n(t)$. Substituting it in the equation defining $\tau_{\rm int}$, and imposing $\tau_{\rm int}(T*) = \tau(T*)$ gives the transition temperature $T* \approx [6\alpha_b\sqrt{\omega_{co}}/(U_0P_0)]^2$. For example, for a resonator like the silicon ones studied in [ZGS+05], $L = 6\mu$m, $t = 0.2\mu$m, $w = 0.3\mu$m, the estimated onset of interactions is at $T* \approx 10$mK.

An upper limit $T_{\rm high}$ of applicability of the model due to high energy 3D vibrational modes playing a significant role can be easily derived by imposing $T_{\rm high} = \omega_{\rm min}^{\rm 3D}$. The frequency $\omega_{\rm min}^{\rm 3D}$ corresponds to phonons with wavelength comparable to the thickness of the sample, $\omega_{\rm min}^{\rm 3D} = 2\pi\sqrt{E/\rho}/t$. The condition is very weak, as the value for example for silicon resonators reads $T_{\rm high} \approx 400/t$, with t given in nm. At much lower temperatures the two-state description of the degrees of freedom coupled to the vibrations ceases to be realistic, with a high temperature cutoff in the case of the model applied to amorphous bulk systems of $T \sim 5$K.

2.7 Dissipation in a metallic conductor

Many of the current realizations of nanomechanical devices monitor the system by means of currents applied through metallic conductors attached to the oscillators. The vibrations of the device couple to the electrons in the metallic part. This coupling is useful in order to drive and measure the oscillations, but it can also be a source of dissipation. We will apply here the techniques described in [GJS04, Gui05] (see also [WP95]) in order to analyze the energy loss processes due to the excitations in the conductor.

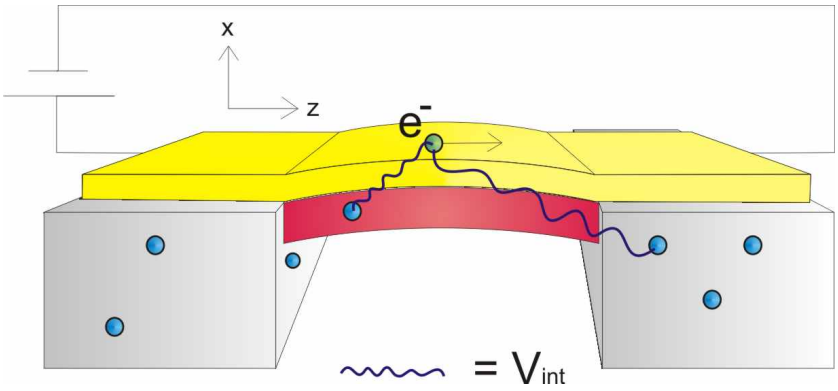

Figure 2.7: Sketch of the distribution of charges in the device. When the system oscillates, these charges induce time dependent potentials which create electron-hole pairs in the metallic layer deposited on top of the beam, absorbing part of the mechanical energy of the flexural mode. See text for details.

We assume that the leading perturbation acting on the electrons in the metal are offset charges randomly distributed throughout the device. A charge Q at position $\tilde{\mathbf{R}}$ creates a potential:

$$V(\tilde{\mathbf{r}},t) \equiv \frac{Q^2}{\epsilon_0|\tilde{\mathbf{R}}(t)-\tilde{\mathbf{r}}(t)|} \tag{2.34}$$

at a position $\tilde{\mathbf{r}}$ inside the metal, see Fig.[2.7]. As the bulk of the device is an insulator, this potential is only screened by a finite dielectric constant, ϵ_0. The oscillations of the system at frequency ω_0 modulate the relative distance $|\tilde{\mathbf{R}}(t)-\tilde{\mathbf{r}}(t)|$, leading to a time dependent potential acting on the electrons of the metal.

The probability per unit time of absorbing a quantum of energy ω_0 can be written, using second order perturbation theory, as [GJS04, Gui05]:

$$\Gamma = \int d\tilde{\mathbf{r}}d\tilde{\mathbf{r}}'dtdt'V(\tilde{\mathbf{r}},t)V(\tilde{\mathbf{r}}',t')\mathrm{Im}\chi[\tilde{\mathbf{r}}-\tilde{\mathbf{r}}',\mathrm{t}-\mathrm{t}']\mathrm{e}^{\mathrm{i}\omega_0(\mathrm{t}-\mathrm{t}')} \tag{2.35}$$

where $\mathrm{Im}\chi[\tilde{\mathbf{r}}-\tilde{\mathbf{r}}',\mathrm{t}-\mathrm{t}']$ is the imaginary part of the response function of the metal.

Charges in the oscillating part of the device. We write the relative distance as $\tilde{\mathbf{R}}(t)-\tilde{\mathbf{r}}(t) = \tilde{\mathbf{R}}_0-\tilde{\mathbf{r}}_0+\delta\tilde{\mathbf{R}}(t)-\delta\tilde{\mathbf{r}}(t)$ and expand the potential, whose time-dependent part is approximately

$$V(\tilde{\mathbf{r}},t) \approx \frac{Q^2\left[\tilde{\mathbf{R}}_0-\tilde{\mathbf{r}}_0\right]\cdot\left[\delta\tilde{\mathbf{R}}(t)-\delta\tilde{\mathbf{r}}(t)\right]}{\epsilon_0|\tilde{\mathbf{R}}_0-\tilde{\mathbf{r}}_0|^3} \tag{2.36}$$

For a flexural mode, we have that $\left[\tilde{\mathbf{R}}_0-\tilde{\mathbf{r}}_0\right]\cdot[\delta\tilde{\mathbf{R}}(t)-\delta\tilde{\mathbf{r}}(t)]$ has turned into $[X_0-x_0]\cdot[\delta X(t)-\delta x(t)] \sim t\cdot A\cdot\sin(\omega t)$, where $t = t_{\mathrm{ins}}+t_{\mathrm{metal}}$ is the thickness of the beam

and A is the amplitude of vibration of the mode. Thus the average estimate for this case for the correction of the potential is

$$\delta V(\tilde{\mathbf{r}},t) \sim \frac{Q^2}{\epsilon_0}\frac{t\cdot A\cdot\sin(\omega t)}{L^3}\ , \tag{2.37}$$

L being the resonator's length.

The integral over the region occupied by the metal in eq.(2.35) can be written as an integral over $\tilde{\mathbf{r}}_0$ and $\tilde{\mathbf{r}}'_0$. The RPA dielectric constant of a dirty metal is:

$$\mathrm{Im}\chi(\tilde{\mathbf{r}}-\tilde{\mathbf{r}}',t-t') = \int e^{i\tilde{\mathbf{q}}(\tilde{\mathbf{r}}-\tilde{\mathbf{r}}')}e^{i\omega(t-t')}\frac{|\omega|}{e^4 D\nu|\tilde{\mathbf{q}}|^2} \tag{2.38}$$

where e is the electronic charge, $D=\hbar v_{\mathrm{F}} l$ is the diffusion constant, v_{F} is the Fermi velocity, l is the mean free path, and $\nu\approx(k_{\mathrm{F}}t_{\mathrm{metal}})^2/(\hbar v_{\mathrm{F}})$ is the one dimensional density of states.

Combining eq.(2.35) and eq.(2.38), and assuming that the position of the charge, $\tilde{\mathbf{R}}_0$ is in a generic point inside the beam, and that the length scales are such that $k_{\mathrm{F}}^{-1}, t_{\mathrm{metal}}, t \ll L$, we can obtain the leading dependence of Γ in eq.(2.35) on L:

$$\Gamma \approx \frac{|\omega_0|A^2}{D\nu L}\left(\frac{t}{L}\right)^2 \approx \frac{|\omega_0|A^2}{l k_{\mathrm{F}}^2 L^3}\left(\frac{t}{t_{\mathrm{metal}}}\right)^2 \tag{2.39}$$

where we also assume that $|Q|=e$. The energy absorbed per cycle of oscillation and unit volume will be $\Delta E=(2\pi/\omega_0)\hbar\omega_0\Gamma_{\mathrm{ph}}/t^2L = 2\pi\hbar\Gamma_{\mathrm{ph}}/t^2L$, and the inverse quality factor $Q^{-1}_{\mathrm{ph}}(\omega_0)$ will correspond to

$$Q^{-1}_{\mathrm{ph}}(\omega_0) = \frac{1}{2\pi}\frac{\Delta E}{E_0} = \frac{\hbar\Gamma_{\mathrm{ph}}}{twL}\frac{1}{\frac{1}{2}\rho\omega_0^2A^2}\ , \tag{2.40}$$

where E_0 is the elastic energy stored in the vibration and A the amplitude of vibration. Substituting the result for Γ one obtains

$$Q^{-1} \approx \frac{2\hbar}{l k_{\mathrm{F}}^2 L^4 t^2 \rho\omega_0}\left(\frac{t}{t_{\mathrm{metal}}}\right)^2 \tag{2.41}$$

In a narrow metallic wire of width t_{metal}, we expect that $l\sim t_{\mathrm{metal}}$.

Typical values for the parameters in eq.(2.40) are $k_{\mathrm{F}}^{-1}\approx 1$Å, $A\approx 1$Å, $l\sim t_{\mathrm{metal}}\approx 10\mathrm{nm}\sim 10^2$Å, $t\approx 100\mathrm{nm}\approx 10^3$Åand $L\approx 1\mu\mathrm{m}\approx 10^4$Å. Hence, each charge in the device gives a contribution to Q^{-1} of order 10^{-20}. The effect of all charges is obtained by summing over all charges in the beam. If their density is n_Q, we obtain:

$$Q^{-1} \approx \frac{2\hbar n_Q}{l k_{\mathrm{F}}^2 L^3 \rho\omega_0}\left(\frac{t}{t_{\mathrm{metal}}}\right)^2 \tag{2.42}$$

For reasonable values of the density of charges, $n_Q = l_Q^{-3}, l_Q \gtrsim 10\text{nm}$, this contribution is negligible, $Q^{-1} \lesssim 10^{-16}$.

Charges in the substrate surrounding the device. Many resonators, however, are suspended, at distances much smaller than L, over an insulating substrate, which can also contain unscreened charges. As the Coulomb potential induced by these charges is long range, the analysis described above can be applied to all charges within a distance of order L from the beam. Moreover, the motion of these charges is not correlated with the vibrations of the beam, so that now the value of $\left|\delta\tilde{\mathbf{R}}(t) - \delta\tilde{\mathbf{r}}(t)\right|$ has to be replaced by:

$$\left|\delta\tilde{\mathbf{R}}(t) - \delta\tilde{\mathbf{r}}(t)\right| \approx A e^{i\omega_0 t} \ , \tag{2.43}$$

and the value of $|\tilde{\mathbf{R}}_0 - \tilde{\mathbf{r}}_0| \sim L$. Assuming, as before, a density of charges $n_Q = l_Q^3$, the effect of all charges in the substrate leads to:

$$Q^{-1} \approx \frac{2\hbar L}{l(k_{\mathrm{F}} t_{\mathrm{metal}})^2 l_Q^3 t^2 \rho\omega_0} \approx 0.3 \frac{\hbar L^3}{l(k_{\mathrm{F}} t_{\mathrm{metal}})^2 l_Q^3 t^3 \sqrt{E\rho}} \ , \tag{2.44}$$

where the second result corresponds to the fundamental mode, $\omega_0 \approx 6.5(t/L^2)\sqrt{E/\rho}$. For values $L \approx 1\mu\text{m}$, $A \approx 1\text{Å}$, $k_{\mathrm{F}}^{-1} \approx 1\text{Å}$, $l \sim t_{\mathrm{metal}} \approx 10\text{nm}$ and $l_Q \sim 10\text{nm}$, we obtain $Q^{-1} \sim 10^{-9}$. Thus, given the values of Q^{-1} reached experimentally until now this mechanism can be disregarded, although it sets a limit to Q^{-1} at the lowest temperatures. It also has to be noted that this estimate neglects cancelation effects between charges of opposite signs.

2.8 Conclusions

Disorder and configurational rearrangements of atoms and adsorbed impurities at surfaces of nanoresonators dominate dissipation of their vibrational eigenmodes at low temperatures. We have given a theoretical framework to describe in a unified way these processes. Based on the good description of low temperature properties of disordered bulk insulators provided by the Standard Tunneling Model [AHV72,Phi72, Esq98], and in particular of acoustic phonon attenuation in such systems, we adapt it to describe the damping of 1D flexural and torsional modes of NEMS associated to the amorphous-like nature of their surfaces.

We have explained the damping of the modes by the presence of an ensemble of independent Two-Level Systems (TLSs) coupled to the local deformation gradient field $\partial_i u_j$ created by vibrations. Flexural modes, with a high density of states at low energies, lead to sub-ohmic damping, which can modify significantly the distribution of TLSs. The problem of a TLS interacting with a sub-ohmic environment is interesting in its own right [LCD$^+$87,KM96,Wei99,Sta03,VTB05,GW88,CT06,Khv04,IN92], and the systems studied here provide a physical realization.

The different dissipation channels to which this ensemble gives rise have been described, focussing the attention on the two most important: relaxation dynamics of biased TLSs and dissipation due to symmetric non-resonant TLSs. The first one is caused by the finite time it takes for the TLSs to readjust their equilibrium populations when their bias Δ_0^z is modified by local strains, with biased TLSs playing the main role, as this effect is $\propto [\Delta_0^z/\sqrt{(\Delta_0^z)^2 + (\Delta_0^x)^2}]^2$. In terms of the excitation spectrum of the TLSs, it corresponds to a lorentzian peak around $\omega = 0$. The second effect is due to the modified absorption spectrum of the TLSs caused by their coupling to all the vibrations, specially the flexural modes. A broad incoherent spectral strength is generated, enabling the "dressed-by-the-modes" TLSs to absorb energy of an excited mode and deliver it to the rest of the modes when they decay.

We have given analytical expressions for the contributions of these mechanisms to the linewidth of flexural or torsional modes in terms of the inverse quality factor $Q^{-1}(\omega_0) = \Delta\omega_0/\omega_0$, showing the dependencies on the dimensions, temperature and other relevant parameters characterizing the device. We have compared the two mechanisms, concluding that relaxation dominates dissipation, with a predicted $Q^{-1}(\omega_0, T) \sim T^{1/2}/\omega_0$. Expressions have been provided for damping of flexural modes in cantilevers and doubly-clamped beams, as well as for damping of their torsional modes.

Analytical predictions for associated frequency shifts have been also calculated. Some important successes have been achieved, like the qualitative agreement with a sublinear temperature dependence of $Q^{-1}(T)$, the presence of a peak in the frequency shift temperature dependence $\delta\omega/\omega(T)$, or the observed order of magnitude of $Q^{-1}(T)$ in the existing experiments studying flexural phonon attenuation at low temperatures [ZGS$^+$05, SCK$^+$07]. Nevertheless, the lack of full quantitative agreement has led to a discussion on the assumptions of the model, its links with the physical processes occurring at the surfaces of NEMS, its range of applicability and improvements to reach the desired quantitative fit.

Finally, we have also considered the contributions to the dissipation due to the presence of metallic electrodes deposited on top of the resonators, which can couple to the electrostatic potential induced by random charges. We have shown that the coupling to charges within the vibrating parts does not contribute appreciably to the dissipation. Coupling to charges in the substrate, although more significant, still leads to small dissipation effects, imposing a limit at low temperatures $Q^{-1} \sim 10^{-9}$, very small compared to the values reached in current experiments [ZGS$^+$05,SCK$^+$07].

Part II

Friction mechanisms in graphene and carbon nanotube-based resonators

Chapter 3

Graphene-based structures: promising materials

3.1 From 3D to 0D, 1D and 2D

The versatility of carbon atoms to form all kinds of compounds with completely different properties can be hardly overemphasized [Pie93]. When carbon atoms combine to constitute a solid, they can form two types of bonds [MGM06, GMM06], see fig.(3.1): the very strong sp^3 bonds present in diamonds, where each atom has four first-neighbors located in the vertices of a tetrahedron whose center is occupied by that atom; and the more versatile sp^2 bonds, with three identical coplanar sp bonds forming 120^o angles between them, plus a fourth p-type orbital perpendicular to that plane. As a result an hexagonal honeycomb lattice with closest-neighbor distances of 1.4Å tends to form, with in-plane σ orbitals giving rigidity to the lattice and out-of-plane π orbitals providing delocalized charge carriers.

The stacking of these planes creates graphite, a highly anisotropic material thanks to the differences between the intra and inter plane bonds. The former are strong covalent bonds, whereas the latter are weak van der Waals forces, explaining the easiness with which the planes can slide one over the other, basis of the lubricant properties of graphite. Indeed, a band-structure calculation renders hopping amplitudes $t_{ab} = 2.4$ eV between nearest neighbors within a plane and $t_c = 0.3$ eV between atoms of consecutive planes, separated by 3.5Å. This anisotropy led Wallace already in 1947 [Wal47] to propose a simplified model where the interaction between planes is neglected, and a single graphite plane is studied to obtain approximately the electronic properties of graphite, viewing it as a 3D solid formed by the stacking of 2D independent hexagonal crystals.

Fortunately for the mesoscopics community this is not the end of the story of carbon compounds. The angles formed by the in-plane σ orbitals can be modified to a certain extent, so that not only hexagons but also pentagons or heptagons of

C atoms can be formed. This automatically leads to non-planar structures, some of whom may be energetically stable. This is the case of some closed structures, carbon fullerenes [DDE96], whose main representative is the C_{60}, a "football" $\sim$1 nm in diameter composed of carbon hexagons and pentagons, called buckminsterfullerene, see fig.(3.2d). The experimental discovery of this new class of 0-dimensional carbon allotropes in 1985 by a team leaded by Kroto, Curl and Smalley [KHO$^+$85] was a breakthrough awarded with the Noble Prize in Chemistry in 1996, opening several research lines in mesoscopics still active. Studies have focussed on the physical and chemical properties of such nano-objects, like heat conductance and high-temperature superconductivity [Had91], and applications have been proposed, for example in biomedics as vehicle for other molecules. They have been even used in double-slit experiments to test the validity of the wave-particle duality for such big molecules [ANVA$^+$99].

Some years later a second breakthrough took place: Ijima's paper on the synthesis of carbon nanotubes [Iji91] caught the attention of the scientific community and boosted research on these carbon structures, an example of whom is depicted in fig.(3.2h). This figure shows a single-walled nanotube, the result of the folding of a single graphite plane, but there are as well multiple-walled nanotubes, with several concentric folded graphite planes. Soon their amazing properties, with much more technological potential than 0D fullerenes, became apparent: depending on the way the carbon plane is cut and pasted when folding it to make the tube, it can be semiconductor or metal, and by doping them properly one can extend the scope to insulating and superconductor states; they are also good candidates for nanoelectronics, with extremely low scattering rates due to their high degree of crystallinity, allowing electrons to travel micrometers ballistically at room temperature [DDA01, FS01]. Coming to their mechanical properties, they are already used in the fabrication of high strength

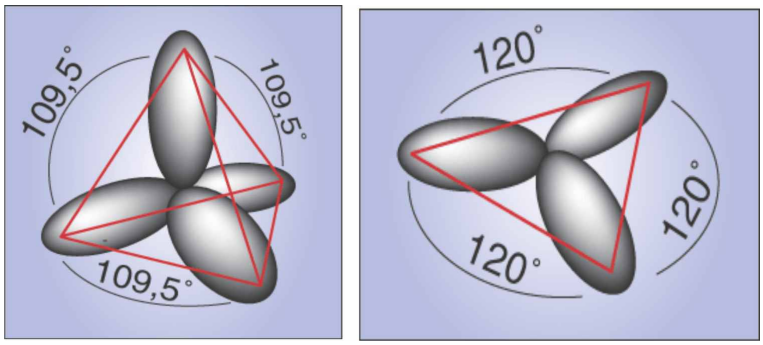

Figure 3.1: The two main types of hybrid orbitals formed by C atoms to create a solid. Left: sp^3 bonds. Right: sp^2, in plane, bonds. Image from http : //en.wikipedia.org/wiki/Orbital_hybridisation .

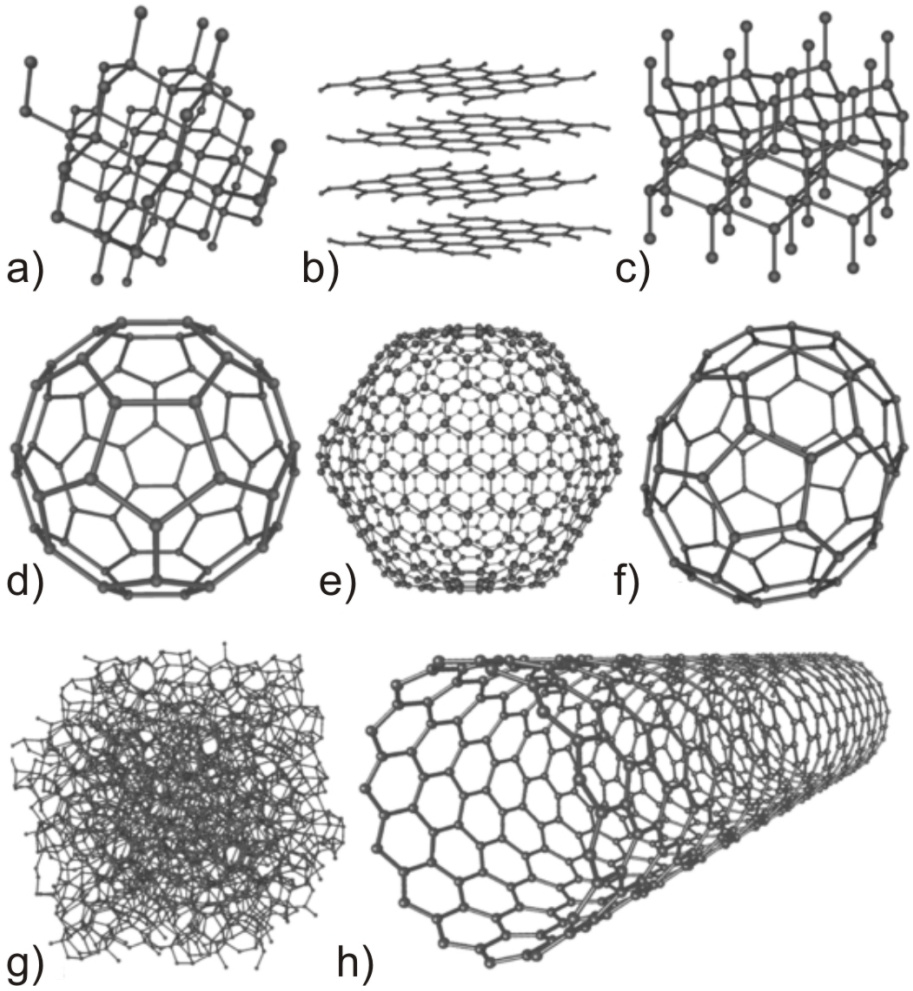

Figure 3.2: Eight examples of allotropes of carbon: a) Diamond, b) Graphite, c) Lonsdaleite, d) C_{60} (Buckminsterfullerene or buckyball), e) C_{540}, f) C_{70}, g) Amorphous carbon, and h) single-walled carbon nanotube or buckytube. Image from http : //en.wikipedia.org/wiki/Allotropes_of_carbon .

composites thanks to their ∼1 TPa (!) Young's Modulus and capacity to relax to their initial form after severe deformations. Their sharp-ending geometry makes them ideal field-emitters, with application in flat panel displays, and good nanotools, serving as tips in several kinds of microscopes (Atomic Force, Scanning Tunneling, Magnetic Resonance Force and Scanning Nearfield Optical, Chemical/Biological Force Microscope tips). Moreover, from the fundamental research point of view they are also very attractive: the propagation of electrons only along the axis makes them effective 1-dimensional systems where a Luttinger liquid picture substitutes the conventional Fermi liquid [EBF$^+$01] applicable to bulk metals [NP99], due to the lack of screening

of the Coulomb interaction, as compared to the 3D case. Quantum-mechanical interference effects, like the Aharonov-Bohm effect in presence of magnetic fields, have been also observed and studied [BSS+99].

The discovery of 0D fullerenes and 1D carbon nanotubes was believed to put an end to the quest for carbon allotropes, as there were convincing arguments and strong experimental evidence against the thermodynamic stability of 2D crystals [Pei35, Lan80, Mer68, ETB06]. The surprise came in 2004, when a single plane of graphite, the so-called graphene, was identified over a SiO_2 substrate [NGM+04]. Its existence over such an amorphous substrate or even suspended in a different setup [MGK+07] can be reconciled with the previous arguments by noting that the carbon monolayer shows a certain amount of corrugation, with "mountains" ("valleys") typically ~ 1 nm high (deep) and with a basis of ~ 30 nm diameter, fig.(3.3b). The associated total free energy is minimized, thanks to the strong reduction of thermal vibrations linked to the loss of planarity, which compensates the increase in elastic energy.

As depicted in fig.(3.3a), graphene can be considered the "mother" of 3D graphite, 0D fullerenes and 1D carbon nanotubes, increasing the attractiveness of its study. We will focus in this second part of the thesis mainly in graphene-based devices, so now a brief overview on its properties and virtues follows.

3.2 Graphene

Graphene is a remarkable material from many points of view. The first one refers to its exceptional electronic quality: in spite of the primitive methods employed to produce it, graphene crystals are extremely pure, able to carry huge current densities $\sim 10^8$ A/cm^2 (two orders of magnitude that of copper) [Wil06], with electron mobilities μ exceeding 15.000 cm^{2}V^{-1}s^{-1} under ambient conditions [NGM+04, NGM+05] and high carrier concentrations $n > 10^{12}$cm^2 in both electrically and chemically doped devices. In terms of mean free paths ballistic transport is observed on the submicrometer scale ($l_{\mathrm{mfp}} \approx 0.3\mu$m at $T = 300$K). For a recent comprehensive review on the electronic properties of graphene see [CGP+07].

A second remarkable property: it is stable down to nanometer sizes, where the confinement of electrons leads to the opening of semiconductor gaps, changing completely its electrical properties. Proceeding in this direction, Walt de Heer has proposed the use of electron-beam lithography to pattern a graphene sheet the proper way, carving in it nm ribbons serving as waveguides, and quantum dots to create, from a single starting sheet, a transistor. A semiconducting gap can be as well induced simply by growing epitaxially graphene on a SiC substrate, according to recent studies [ZGF+07]. Circuits using carbon nanotubes, however, need at some points to have them connected to the circuit through highly-resistive metal contacts, a major drawback also limiting the downscaling of silicon microchips, absent in graphene-

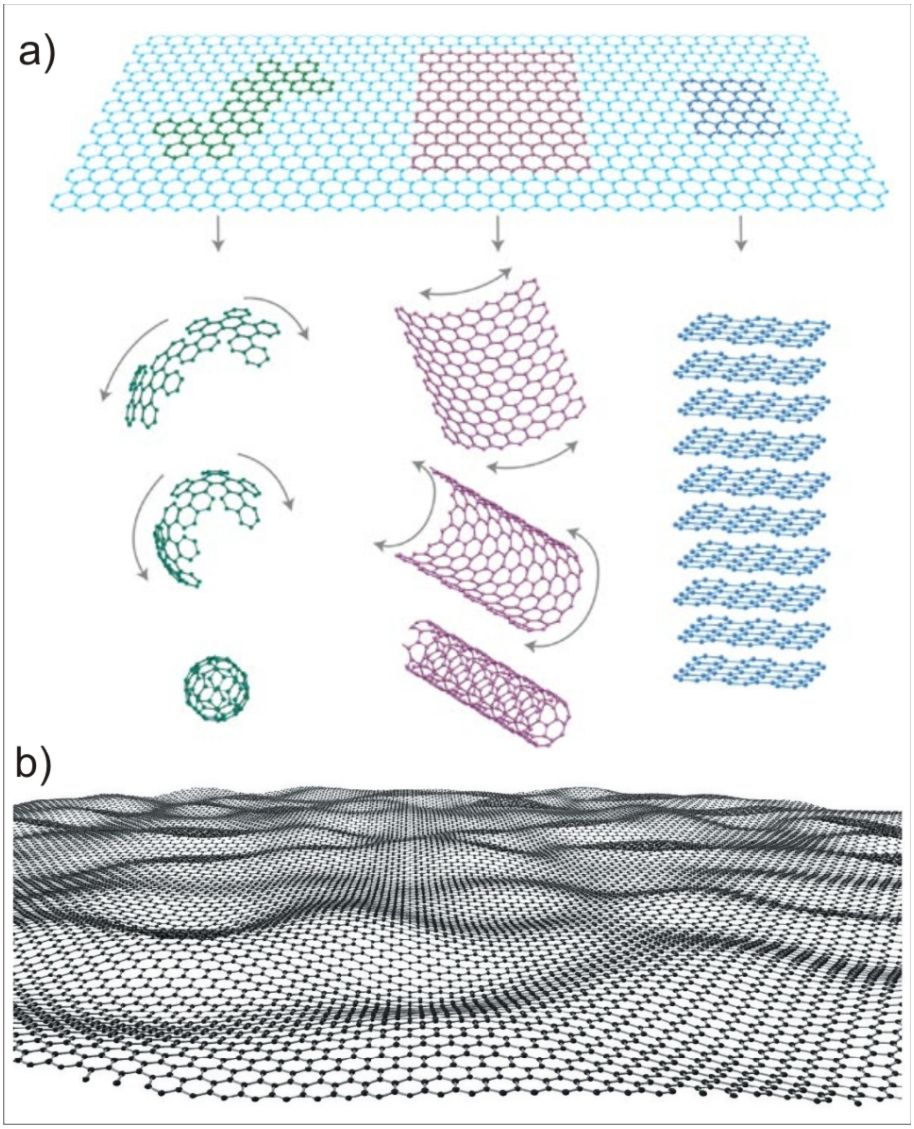

Figure 3.3: a) Image from [GN07]. The detailed understanding of graphene is important for the comprehension of the other carbon materials deriving from it: 0D buckyballs, 1D nanotubes and 3D graphite. b) Pictorial representation of the observed crumpling of graphene monolayers giving them thermodynamical stability. Extracted from [MGK$^+$07].

taylored circuits. These features raise hopes on graphene as a candidate for future electronics.

But even if those hopes were not fulfilled there is another aspect which justifies by itself research on graphene: Using the band-model of Wallace [Wal47] one can see

that the electrons in a honeycomb lattice can be described at low energies in terms of quasiparticles obeying the (2+1)-dimensional Dirac equation. This means that at low energies the charge carriers in graphene behave as though they were massless Dirac fermions, but with a "speed of light" reduced with respect to vacuum photons by a factor 300. This is clearly reflected in fig.(3.4b).

The main steps for its derivation go as follows: In the hexagonal lattice there are two inequivalent atoms per unit cell, so the lattice can be seen as composed of two interpenetrated triangular sublattices A and B, see fig.(3.4a). An atom of a given sublattice is surrounded by three nearest neighbors belonging to the other sublattice. Once the filled σ orbitals determine the honeycomb geometry, the properties of graphene can be calculated considering only the π orbitals with energies close to ε_F. Starting with a tight-binding hamiltonian with nearest-neighbor interactions

$$H = -t \sum_{<i,j>} a_i^\dagger a_j \,, \tag{3.1}$$

where $a_i^\dagger$ is the creation operator for site i, so that a generic wave function can be written in this localized basis as

$$\Psi = \sum_{i \in A} c_A e^{i\mathbf{k}\cdot\mathbf{r}_i} a_i^\dagger |0\rangle + \sum_{i \in B} c_B e^{i\mathbf{k}\cdot\mathbf{r}_i} a_i^\dagger |0\rangle \,, \tag{3.2}$$

one can find the eigenfunctions and eigenenergies of H by solving the matrix equation for the coefficients c_A and c_B

$$\begin{pmatrix} 0 & -t\sum_i e^{i\mathbf{k}\cdot\mathbf{u}_i} \\ -t\sum_i e^{i\mathbf{k}\cdot\mathbf{v}_i} & 0 \end{pmatrix} \begin{pmatrix} c_A \\ c_B \end{pmatrix} = E(\mathbf{k}) \begin{pmatrix} c_A \\ c_B \end{pmatrix} \tag{3.3}$$

The vectors $\mathbf{u}_i$ and $\mathbf{v}_i$ are defined in fig.(3.4a). Solving the equation one obtains the dispersion relation represented in fig.(3.4b), namely

$$E(\mathbf{k}) = \pm t \sqrt{1 + 4\cos^2\Big[\frac{\sqrt{3}}{2} a k_x\Big] + 4\cos\Big[\frac{\sqrt{3}}{2} a k_x\Big] \cos\Big[\frac{\sqrt{3}}{2} a k_y\Big]} \,, \tag{3.4}$$

with a lattice constant $a = 1.42$Å. With one electron per π orbital (half-filling) the Fermi level is located just where the Fermi surface collapses into 6 points, two of whom inequivalent. Expanding eq.(3.4) for low energies around these so-called Dirac points the dispersion relation is linear in $\mathbf{k}$

$$E(\mathbf{k}) = \hbar v_F |\mathbf{k}| \tag{3.5}$$

This is in stark contrast with the usual quadratic dispersion relation found in bulk metals or semiconductors. The fermi velocity v_F is given by $\hbar v_F = (3/2)ta$. Also

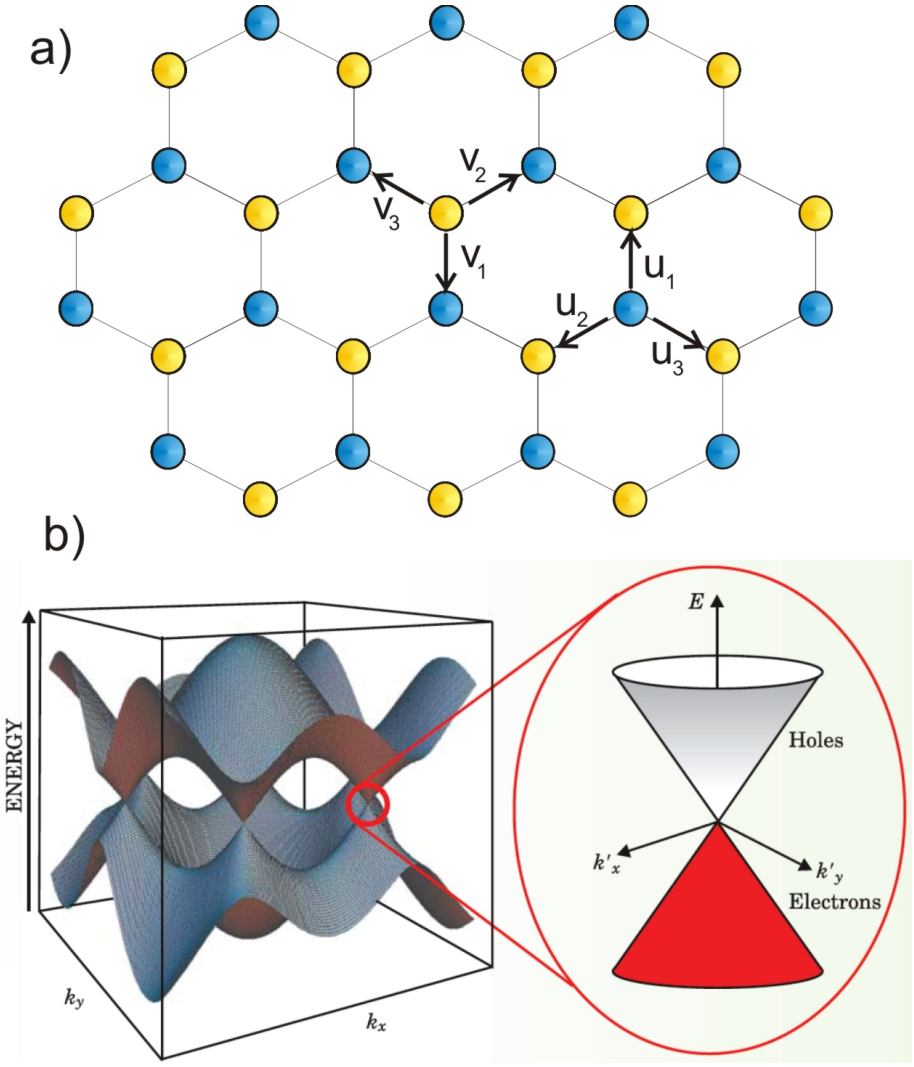

Figure 3.4: a) Graphene lattice can be seen as composed of two interpenetrated triangular sublattices A and B, with sublattice vectors $\mathbf{u}_i$ and $\mathbf{v}_i$. b) Plot of graphene's bandstructure as derived with a simple band-model for the honeycomb lattice [Wal47], eq.(3.4). When the graphene layer is neutral, the Fermi level is situated just at the 6 so-called Fermi points, one of whom is zoomed at the right. At low energies, the dispersion relation around those Fermi points is linear, relativistic-like, $E = \hbar v_F |\mathbf{k}|$. Image from [Wil06].

within this low energy subspace around the Dirac points, one can Taylor-expand and derive a low-energy effective model:

$$H \approx \frac{3}{2} ta \begin{pmatrix} 0 & \delta k_x + i\delta k_y \\ \delta k_x - i\delta k_y & 0 \end{pmatrix} = \hbar v_F (k_x \sigma_x + k_y \sigma_y) \ , \tag{3.6}$$

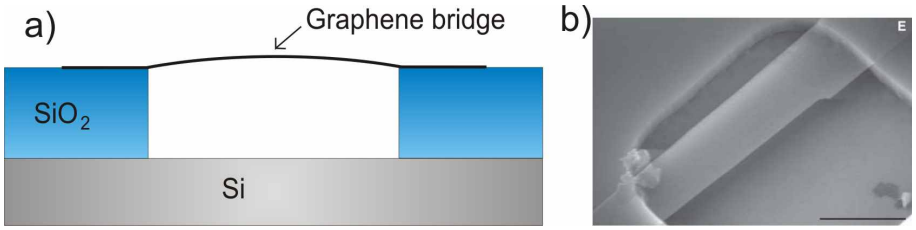

Figure 3.5: a) Schematic side view of the graphene-based resonator setup of ref. [BvdZV+07]. b) Scanning electron microscope image from [BvdZV+07], showing a few-layer ($N \sim 2$) graphene resonator. Scale bar, 1 μm.

arriving as anticipated at the Dirac hamiltonian in (2+1) dimensions, σ_j being the Pauli matrices. Experiments confirm this relativistic behavior of pseudoparticles close to the Fermi point, most clearly seen in recent ARPES results [BOS+07], which reproduce fig.(3.4b).

The vanishing density of states at the Fermi points means that in neutral graphene there are few quasiparticles to screen the Coulomb interaction. The resulting strong Coulomb interaction results, according to some works [GGV99, DHT07], into a marginal Fermi liquid behavior, with a quasiparticle lifetime $\tau(|\varepsilon - \varepsilon_F|) \sim |\varepsilon - \varepsilon_F|$, as compared to the quadratic dependence present in Fermi liquids. Nevertheless it has to be noted that this question is not yet fully settled. When the graphene layer is doped with carriers the Fermi level separates from the Dirac points and locates in a region where the density of states is no more vanishing, so that now the Coulomb interaction can be efficiently screened, and a standard Fermi liquid picture applies.

When one does not have a monolayer but a stack of them, the interlayer interaction modifies the dispersion relation, displacing slightly the conduction and valence bands creating the so-called electron and hole pockets, keeping a very low density of states (though no more vanishing) at neutrality. Numerous studies address the evolution of the physical properties as the number of layers of the system N is increased, starting from a single 2D graphene monolayer [NGM+04, NMM+06, Tho06, PP06]. It turns out that the 3D graphite electronic structure is very soon recovered, with about just 10 layers. Before that, the evolution of the electronic spectrum can be roughly classified into single layer, bilayer and $3 \leq N < 10$ cases, becoming increasingly complicated as N grows. We will not move further into this issue, and limit ourselves as well to mention that many other interesting phenomena occur in graphene as a consequence of the interplay of its peculiar bandstructure and finite size effects, like the observation of an anomalous quantum Hall effect [NGM+05, ZTSK05, NMM+06], a finite value of the electric conductivity at zero field [NGM+05, GN07], or unclear results about its magnetic response [MP06].

The extraordinary mechanical and electrical properties of graphene mono and

multilayers have not passed unnoticed to the NEMS community. Recently Bunch *et al* [BvdZV$^+$07] demonstrated the first example of electromechanical nanobridge where the vibrating bridge is a single or multilayer graphene sheet, see fig.(3.5). The advantages of the use of this material as compared with semiconductors like silicon or GaAs are clear: the strength of the σ bonds provides stability even to a single suspended carbon plane, as opposed to crystal Si or GaAs devices, allowing for much lighter resonators (the lightest one can think of) with thus higher mass or force sensitivity. Moreover, those bonds result in an extremely high Young's Modulus, which together with the large surface area of these devices enhances the detector's sensitivity as well. As to the friction mechanisms limiting the quality factor of the resonator's modes, the high degree of crystallinity of graphene minimizes the dissipative processes coming from impurities and imperfections, which as we saw dominate damping in semiconducting nanoresonators at low temperatures.

Graphene resonators of course present some drawbacks too, in the form of new dissipative mechanisms absent in semiconductor-based devices, or increased importance of some of the decoherence processes already described. The detailed description of these processes is the subject of the following chapter. As a final remark, we mention another interesting proposal for graphene as the basis for ultrasensitive gas sensors, based on the detection of local changes in the carrier concentration when a molecule is adsorbed [SGM$^+$07]. This is only possible thanks to the extremely low intrinsic electronic noise in graphene.

Chapter 4

Dissipative processes in graphene resonators

4.1 Introduction

In this chapter we will analyze several dissipative mechanisms affecting graphene resonators, both mono- and multilayer, like the ones fabricated by Bunch *et al* [BvdZV+07], comparing them with the semiconductor-based NEMS we have studied in the first part of the thesis. We start with a brief description of these devices.

4.1.1 Experimental setup

The heart of the setup consists of a mono- or multilayer graphene sheet exfoliated on top of a previously patterned trench etched in a SiO_2 surface, figs.(3.5) and (4.1a). This SiO_2 layer, $\sim$300 nm thick, is thermally grown from a starting underlying crystalline Si wafer. The movement of the sheet is detected with a fast photodiode by looking at variations in the intensity of the reflected light from a 632.8 nm He-Ne laser focussed on the resonator, which are due to the size variation of the interferometer formed by the suspended graphene sheet and the silicon back plane, see fig.(4.1b). Bunch *et al* use two different driving schemes to induce motion:

Electrical drive

As shown in Fig.(4.1a), a gate voltage V_g is applied between the graphene and the silicon layers, with both a static (DC) component and a small time-varying (AC) one, inducing a charge $q = C_g V_g$, where C_g is the capacitance between the two layers. The attraction between the charges of the two layers causes an electrostatic force downward on the graphene. The total electrostatic force on the sheet is

$$F_{el} = \frac{1}{2} C_g' V_g^2 \simeq \frac{1}{2} C_g' V_g^{DC} \left(V_g^{DC} + 2\delta V_g \right) = \frac{1}{2} C_g' \left(V_g^{DC} \right)^2 + C_g' V_g^{DC} \delta V_g \qquad (4.1)$$

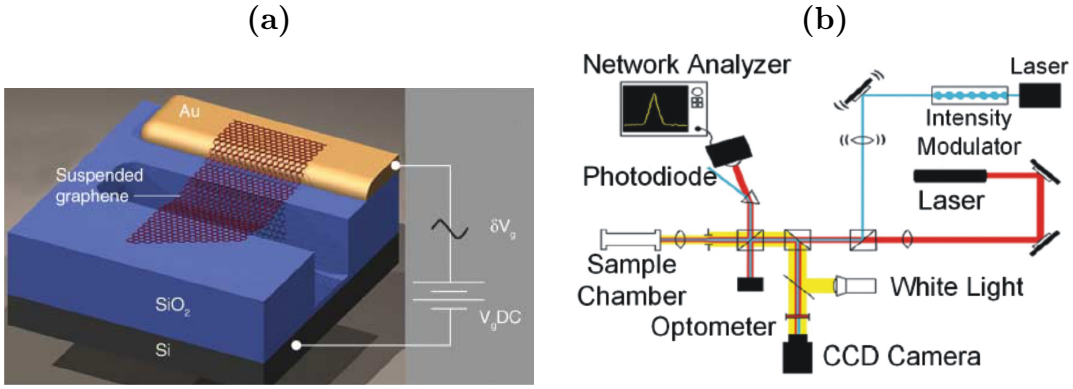

Figure 4.1: (a) Scheme of the resonator and the electrical actuation setup. (b) Optical actuation and detection scheme. From [BvdZV+07].

where $C'_g = dC_g/dz$ is the derivative of the capacitance with respect to the distance between the plates of the capacitor. The second term of the electrostatic force leads to the motion of the oscillator, with increased amplitude if the driving frequency ω is close to a resonance ω_0.

Optical drive

A 432 nm diode laser is intensity modulated at a frequency defined by the network analyzer and focussed on the suspended graphene, causing a periodic contraction/expansion of the layer that leads to motion (see Fig.(4.1b)).

4.1.2 Quality factors measured

The quality factors Q measured at room temperature for the fundamental mode of several resonators, with thicknesses ranging from the monolayer case to $\sim$ 100 layers, are shown in fig.(4.2a). The most prominent feature noted by the authors is a surprising lack of dependence of Q on the thickness of the resonators, leading them to suggest that the dominant dissipation mechanism is different from that of standard semiconductor NEMS. Comparing with results obtained for carbon nanotubes, they mention that the similarity of the structure and observed magnitude of Q perhaps points to a common dissipation mechanism, unknown until now for CNT resonators. They suggest also that an extrinsic mechanism such as clamping loss or fluctuating charge noise may dominate dissipation in graphene resonators. In a preliminary study of the temperature dependence of Q, they observe a sharp increase of the quality as T is lowered, as shown in fig.(4.2b).

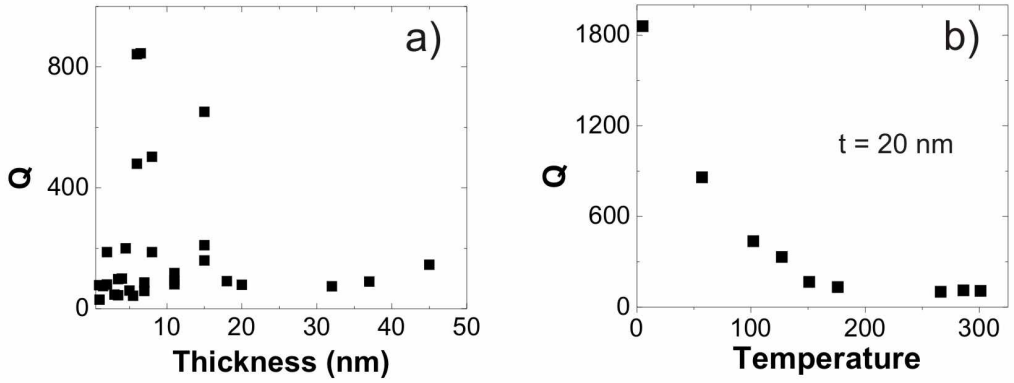

Figure 4.2: (a) The quality factor Q of the fundamental mode for all resonators studied in [BvdZV+07] does not show a clear increase with thickness, contrary to semiconductor NEMS. Thus surface processes like the ones described in previous chapters do not seem to dominate damping in these devices, in agreement with graphene's well-known high degree of crystallinity. (b) Temperature dependence of Q for a resonator 20 nm thick, showing a strong increase of the quality as the temperature is lowered. Courtesy from A. van der Zande (unpublished).

4.1.3 Damping mechanisms present in graphene resonators

Prior to analyzing in detail several of the mechanisms limiting the quality of the bending modes, we will briefly enumerate and describe the (known) most prominent ones, comparing them with the case of semiconductor NEMS:

Novel or enhanced mechanisms with respect to semiconductor resonators

The ability of graphene to sustain large carrier densities when an external voltage is applied is a feature distinguishing it from the NEMS studied in the first part of this thesis, and as we have seen is used in one driving scheme. When the oscillating graphene layer is charged, the presence of charge in the Si electrode gives rise to friction associated to the **excitation of electron-hole pairs in the graphene layer**. This is due to the time-dependent Coulomb potential that the charges in the graphene layer feel, created by the charges in the electrode.

And viceversa, when the Si electrode is charged, the time-dependent Coulomb potential due to the oscillating charged graphene layer causes **excitation of electron-hole pairs in the electrode**, absorbing mechanical energy. These processes are present in semiconductor devices only when the setup includes a metallic layer deposited on top of the resonator (magnetomotive technique), and play usually a secondary role due to the low charge density in the non-mobile part of the device.

Graphene resonators, on the contrary, have a higher charge density both in the graphene bridge and in the Si electrode in the setup with electrical drive, increasing the importance of this dissipative channel. Moreover, this mechanism is also present in the optical driving setup, as graphene is known to be, even in absence of applied voltages, locally charged, with so-called electron and hole puddles corresponding to the sheet corrugation [MAU+07], though its importance will be smaller as compared to the electrical drive setup case.

Apart from their presence in the graphene bridge and the Si electrode, **trapped charge** in the Si-SiO_2 interface, as well as charge distributed throughout the volume of the oxide is known to exist [Sze81, NB82], limiting for example the performance of MOS-based devices. In our case it will add an extra Coulomb potential to the one generated by the charge in the Si electrode, enhancing the **creation of e-h pairs in the graphene layer** with the corresponding damping of the vibration.

A process also missing in current semiconducting resonators which can damp the oscillation is the breaking and healing of bonds gluing the graphene sheet to the SiO_2 substrate, conveniently denominated **Velcro effect** [VZ0]. We will do some estimates based on the known chemical properties of SiO_2 surfaces and conclude that it may become a strong source of energy loss if the resonator is strongly driven into the non-linear regime, being otherwise negligible.

Other mechanisms a priori non-negligible in both kinds of resonators

Some of the trapped charged impurities throughout the device are not static entities, but have their own dynamics, coming frequently associated to the same defects causing surface dissipation in semiconductor NEMS. A clear example corresponds to charges switching between metastable trapping sites, which can be modeled by a set of two-level systems (TLSs). They generate the previously mentioned **fluctuating charge noise**, a real headache for the quantum computing community in need for long coherence qubit times [DH81, Wei88, PFFF02, BRS+04, SSMM07]. We will model the ones of the amorphous SiO_2 substrate with the usual TLS distribution employed in studies with amorphous materials [Phi88], concluding that this mechanism can be neglected.

Attachment losses due to the coupling of the bridge's oscillation to the phonons of the rest of the device through the anchorage areas will as well be estimated. Another source of dissipation which can be of importance, specially at high temperatures, is the **thermoelastic coupling** of the strain field of the excited resonator's bending mode to the rest of its modes, causing local variations in the temperature field. Its contribution will prove to be as well of secondary importance.

System properties	
Dimensions	
Thickness t	$10 \cdot 10^{-9}$ m
Width w	10^{-6} m
Length L	10^{-6} m
Height above substrate d	$300 \cdot 10^{-9}$ m
Frequency f_0	100 MHz
Amplitude A	0.5 nm
Carrier density ρ_C	10^{12}cm^{-2}
Properties of graphite	
Mass density ρ_M^C	2200 kg/m^3
Elastic constants	
E	10^{12} Pa
ν	0.16
Debye temperature θ_D	$\sim 570\,K$
Specific heat C_p	700 J / Kg. K
Thermal conductivity κ	390 W / m . K

Table 4.1: Parameters used in the estimates presented in the chapter, adapted to the systems studied in [BvdZV$^+$07]. Bulk data taken from [Pie93].

For all of the aforementioned mechanisms we will give a numerical estimate of their contribution to the quality factor at 300 K, and determine its temperature dependence, using a prototypical resonator characterized by the parameters given in table 4.1. The results are summarized in table 4.2.

Heating by the lasers

In the optical drive setup, the intense actuation laser induces a **local heating** of the resonator, reducing the quality factor. To a lesser extent this mechanism is also present in the electrical drive setup due to the weak He-Ne monitoring laser. We will not analyze in detail this effect, concentrating in the electric drive setup. The interesting study of this heating process is yet a task to be performed. Nevertheless, a first observation can be made, based on fig.(4.2b): in that experiment the intensity of the lasers used is not varied as T is lowered, so its effect on Q should be roughly independent of T, but as a drastic increase of Q is observed, it leads us to think that the heating by the lasers is not the dominant source of dissipation, in that temperature range at least.

	$Q^{-1}(T = 300K)$	Temperature dependence
Charges in the SiO_2	$10^{-7} - 10^{-6}$	T
Charges in graphene sheet and metallic gate	10^{-2}	T
Velcro effect	Absent	T^0
Two-level systems	10^{-22}	$A + BT$
Attachment losses	$10^{-6} - 10^{-5}$	T^0
Thermoelastic losses	10^{-7}	T

Table 4.2: Contribution of the mechanisms considered in section 4.2 to the inverse quality factor $Q^{-1}(T)$ of the systems studied in [BvdZV+07].

4.2 Estimates for the damping caused by the different mechanisms

4.2.1 Coupling to fixed charges in the SiO_2 substrate

We first calculate the dissipation induced in the graphene layer by a single fixed charge located in the SiO_2 substrate, and afterwards sum over all fixed charges.

The time dependent component of the unscreened potential induced by a charge separated by a distance d in the vertical direction from the graphene layer, acting on an electron at position $\tilde{\mathbf{r}}$ in the graphene layer is given, approximately, by:

$$V(\tilde{\mathbf{r}}, t) \approx \frac{e^2 d A e^{i\omega_0 t}}{(|\tilde{\mathbf{r}}|^2 + d^2)^{3/2}} \tag{4.2}$$

where A is the amplitude of the flexural mode, and ω_0 its frequency. Its Fourier transform is:

$$\begin{aligned} V(\tilde{\mathbf{q}}, \omega) &= \int d\tilde{\mathbf{r}} e^{i\tilde{\mathbf{q}}\tilde{\mathbf{r}}} V(\tilde{\mathbf{r}}, \omega) = -e^2 A \delta(\omega - \omega_0) \frac{\partial}{\partial d} \Big\{ \int_0^{2\pi} d\theta \int_0^{\infty} dr \frac{r e^{iqr\cos\theta}}{\sqrt{r^2 + d^2}} \Big\} \\ &= 2\pi e^2 A e^{-qd} \delta(\omega - \omega_0) \end{aligned} \tag{4.3}$$

This potential is screened by the polarizability of the graphene layer [WSSG06]. In an RPA self-consistent calculation (see Appendix C.1.2 and Section 6.4.2) the screening is expressed in terms of a renormalization of the charge, replacing e^2 as follows:

$$e^2 \to e^{*2} = \frac{e^2}{1 + (e^2/|\tilde{\mathbf{q}}|)\mathrm{Re}[\chi_0(|\tilde{\mathbf{q}}|, \omega)]} \approx \frac{|\tilde{\mathbf{q}}|}{\mathrm{Re}[\chi_0(|\tilde{\mathbf{q}}|, \omega)]} \tag{4.4}$$

where χ_0 is the susceptibility of the graphene layer. Rigorously this result is obtained only when 2D translational invariance is assumed, something we will do, ignoring

border effects. At low energy and momenta the value of the susceptibility tends to the compressibility (density of states) of the electrons in the layer. For the monolayer and multilayer cases we have:

$$\lim_{|\tilde{\mathbf{q}}|\to 0,\omega\to 0} \mathrm{Re}[\chi_0(|\tilde{\mathbf{q}}|,\omega)] = \begin{cases} \frac{k_\mathrm{F}}{\hbar v_\mathrm{F}} & N=1 \\ \frac{N\gamma}{\hbar^2 v_\mathrm{F}^2} & N\neq 1 \end{cases} \tag{4.5}$$

where N is the number of layers and γ is the interlayer hopping element. The result for the monolayer can be immediately obtained assuming a linear dispersion relation $\varepsilon(k) = \hbar v_\mathrm{F} k$, while for a stack with N layers, the model with one interlayer hopping element [GCP06] has been used, which gives rise to $2N$ low energy bands, most of which show a quadratic dispersion.

Using Fermi's golden rule applied to the perturbation potential of eq.(4.2) screened as described in eq.(4.4) one arrives at eq.(C.6) of Appendix C.1.1 for the width of the graphene mode. Fourier transforming to momentum space ($v(\tilde{\mathbf{q}},\omega) = v(-\tilde{\mathbf{q}},\omega)$):

$$\Gamma_\mathrm{ph} \approx \int d^2\tilde{\mathbf{q}} |v(\tilde{\mathbf{q}})|^2 \mathrm{Im}\chi_0(\tilde{\mathbf{q}},\omega_0)\,. \tag{4.6}$$

The low energy and momentum limit of graphene layers $\mathrm{Im}\chi_0(\tilde{\mathbf{q}},\omega_0)$ is given by [WSSG06, GCP06]

$$\mathrm{Im}\chi_0(\tilde{\mathbf{q}},\omega_0) \approx \begin{cases} \frac{|\omega| k_\mathrm{F}}{v_\mathrm{F}^2 |\tilde{\mathbf{q}}|} & N=1 \\ \frac{|\omega|\gamma^2 N^{3/2}}{v_\mathrm{F}^2 |\tilde{\mathbf{q}}|\sqrt{\rho}} & N\neq 1 \end{cases} \tag{4.7}$$

where, for $N \neq 1$, ρ is the total carrier density. This last expressions are valid for lengths bigger than the mean free path, $l \gg l_{mfp}$.

The energy absorbed per cycle of oscillation and unit volume will be $\Delta E = (2\pi/\omega_0)\hbar\omega_0\Gamma_\mathrm{ph}/twL = 2\pi\hbar\Gamma_\mathrm{ph}/twL$, and the inverse quality factor $Q_\mathrm{ph}^{-1}(\omega_0)$ will correspond to

$$Q_\mathrm{ph}^{-1}(\omega_0) = \frac{1}{2\pi}\frac{\Delta E}{E_0} = \frac{\hbar\Gamma_\mathrm{ph}}{twL}\frac{1}{\frac{1}{2}\rho\omega_0^2 A^2} = \frac{2\hbar\Gamma_\mathrm{ph}}{M\omega_0^2 A^2}\ , \tag{4.8}$$

where E_0 is the elastic energy stored in the vibration and M is the total mass of the resonator. Calculating eq.(4.6) and substituting in eq.(4.8) for a single graphene layer, a single charge turns out to give a contribution to the inverse quality factor of:

$$\boxed{Q^{-1} \sim \frac{1}{k_\mathrm{F} d}\frac{2\hbar}{M\omega_0 d^2}} \tag{4.9}$$

where $k_\mathrm{F} = \pi\sqrt{\rho_C}$, and ρ_C is the density of carriers in the graphene sheet. We can estimate this density as a function of the gate voltage V_g treating our system as a capacitor [NGM+04],

$$\rho_C = \frac{\epsilon_0\,\epsilon}{e}\frac{V_g}{d} \tag{4.10}$$

where ϵ_0 is the permittivity of free space, ϵ the relative permittivity of the material between the charged plates of the capacitor (in this case the graphene layer and the Si), and d the distance between the plates. In the region where the layer is suspended, $\epsilon = 1$, and for typical voltages applied $V_g \sim 100$ V the resulting carrier density turns out to be $\rho_C \sim 2 \cdot 10^{12}$ cm^{-2}. Thus $k_{\rm F} d \sim 10^2 - 10^3 \gg 1$. Eq.(4.9) can be generalized to a graphene sheet with N layers using eq.(4.7):

$$\boxed{Q^{-1} \sim \frac{1}{\sqrt{N\rho} d} \frac{2\hbar}{M\omega_0 d^2}} \tag{4.11}$$

The suppression with the number of layers is due to the increased screening in this system.

The total contribution to the inverse quality factor is obtained by multiplying eqs.(4.9) or (4.11) by the total number of charges $N_{\rm ch}$. An upper bound to the effective surface density of local charges, deduced from some models for the electric conductivity of graphene [NM07, HAS06], is $\rho_{\rm ch} \sim 10^{12}$cm^{-2}. In Appendix C.3 some facts about these charges are collected from the literature, and an independent estimate for $\rho_{\rm ch}$ is made, obtaining a smaller value, eq.(C.28). The reason for this discrepancy is still unclear to us. Using the first estimate for $\rho_{\rm ch}$ and the parameters in Table[4.1], we find $N_{\rm ch} \sim 10^4$ and $Q^{-1} \sim 10^{-11}$ at low temperatures.

This mechanism leads to ohmic dissipation, as the energy is dissipated into electron-hole pairs in the metallic graphene layer. Hence, as deduced in Appendix C.2.1, the temperature dependence of this mechanism is given by $Q^{-1}(T) \sim Q^{-1}(0) \times (kT/\hbar\omega_0)$, and $Q^{-1} \sim 10^{-6}$ at 300 K.

The analysis presented here does not consider the additional screening due to the presence of a metallic gate. In that case, one needs to add to the potential from a static charge, eq.(4.2), a contribution from the image charge induced by the gate. This effect will reduce the coupling between the graphene layer and charges in the vicinity of the gate.

4.2.2 Ohmic losses at the graphene sheet and the metallic gate.

The electrons in the vibrating graphene layer induce a time dependent potential on the metallic gate which is sometimes part of the experimental setup. The energy is transferred to electron-hole pairs created at the gate or at the graphene layer. These processes contribute to the energy loss and decoherence of electrons in metallic conductors near gates [GJS04, Gui05].

The coupling between charge fluctuations in the two metallic systems is due to

long range electrostatic interactions. The corresponding hamiltonian is

$$H = \frac{1}{2}\Big\{\int_C v_{scr}(z,\tilde{\mathbf{r}},t)\rho^C(z,\tilde{\mathbf{r}},t) \;+\; \int_G v_{scr}(0,\tilde{\mathbf{r}}',t)\rho^G(\tilde{\mathbf{r}}')\Big\} \qquad (4.12)$$
$$+ \int_C \frac{1}{2\rho_M t w}\Pi^2 + \frac{1}{2}\frac{Et^3 w}{12}\Big[\Big(\frac{\partial^2\phi}{\partial x^2}\Big)^2 + \Big(\frac{\partial^2\phi}{\partial y^2}\Big)^2\Big]$$

where the indices G and C stand for the gate and graphene layer, respectively. ρ_M is the mass density of the graphene sheet, and t, w, E its thickness, width and Young modulus, whereas $\phi(\tilde{\mathbf{r}},t)$ represents the vibrating amplitude field of bending modes and $\Pi = \partial L/\partial\dot{\phi}$ is its conjugate momentum (L is the Lagrangian). The self-consistent screened potentials $v_{scr}(z,\tilde{\mathbf{r}},t)$, $v_{scr}(0,\tilde{\mathbf{r}},t)$ are calculated as a function of the bare potentials $v_0(z,\tilde{\mathbf{r}},t)$, $v_0(0,\tilde{\mathbf{r}},t)$ in Appendix C.4.

As in the case of eq.(4.2), the time-dependent part of the bare potentials couples the electronic degrees of freedom and the mechanical ones through the charge $\rho(\tilde{\mathbf{r}})$ and amplitude of the vibrational mode, $A_{\tilde{\mathbf{q}}}$, and would give rise to a term in the quantized hamiltonian of the form

$$H_{int} \propto \rho(\tilde{\mathbf{r}})A_{\tilde{\mathbf{q}}} \propto (b^\dagger_{\tilde{\mathbf{q}}} + b_{\tilde{\mathbf{q}}})\sum_{\tilde{\mathbf{k}},\tilde{\mathbf{k}}'}[c^\dagger_{\tilde{\mathbf{k}}+\tilde{\mathbf{k}}'}c_{\tilde{\mathbf{k}}} + \text{h.c}] \qquad (4.13)$$

where $A_{\tilde{\mathbf{q}}}$ and $\rho(\tilde{\mathbf{r}})$ have been expressed in terms of creation and annihilation operators of phonons $(\tilde{\mathbf{q}},\omega_{\tilde{\mathbf{q}}})$ and electrons of a 2D Fermi gas, respectively.

But a realistic model requires taking into account the screening of the potential associated to these charge fluctuations. In terms of the screened potentials, the induced broadening of the mode $(\tilde{\mathbf{q}},\omega_{\tilde{\mathbf{q}}})$ of the graphene layer is, extrapolating eq.(C.6) of Appendix C.1.1 to this case, as [GJS04]

$$\Gamma(\omega_{\tilde{\mathbf{q}}}) = \sum_{\alpha=\mathrm{G,C}}\int d^3\tilde{\mathbf{r}}\int d^3\tilde{\mathbf{r}}'\Big\{\mathrm{ReV}^\alpha_{\mathrm{scr}}(\tilde{\mathbf{r}},\omega_{\tilde{\mathbf{q}}})\times\mathrm{ReV}^\alpha_{\mathrm{scr}}(\tilde{\mathbf{r}}',\omega_{\tilde{\mathbf{q}}})\times\mathrm{Im}\chi^\alpha[\tilde{\mathbf{r}}-\tilde{\mathbf{r}}',\omega_{\tilde{\mathbf{q}}}]\Big\} \qquad (4.14)$$

The static screening properties, $\lim_{\tilde{\mathbf{q}}\to 0}\mathrm{Re}\chi^\alpha(\tilde{\mathbf{q}},0)$, of the graphene layer and the gate are determined by their electronic compressibilities (densities of states), ν^C and ν^G respectively. We will assume that the distance between the graphene and the gate is much larger than the electronic elastic mean free path in either material, so that their polarizability is well approximated by the one of a diffusive dirty metal, see Appendices C.1.3 and C.1.4:

$$\chi^\alpha(\tilde{\mathbf{q}},\omega) \approx \frac{\nu^\alpha D^\alpha|\tilde{\mathbf{q}}|^2}{D^\alpha|\tilde{\mathbf{q}}|^2 + i\omega} \qquad (4.15)$$

where $D^\alpha = v^\alpha_{\mathrm{F}} l^\alpha$ is the diffusion constant, and l^α is the elastic mean free path. The two dimensional conductivity is $g^\alpha = k^\alpha_{\mathrm{F}} l^\alpha$.

We have assumed the gate to be quasi two dimensional. This approximation is justified when the distance between the gate and the graphene layer is much larger than the width of the gate. Appendix C.3.2 shows how for typical oxide thicknesses and voltages applied it is fulfilled. In this situation, the broadening of the mode, eq.(4.14), can be expressed, analogously to eq.(4.6), as

$$\Gamma(\omega_{\tilde{\mathbf{q}}}) \approx \int d^2\tilde{\mathbf{k}}\Big\{|v_{scr}(d,\tilde{\mathbf{k}},\omega_{\tilde{\mathbf{q}}})|^2 \mathrm{Im}\chi^{\mathrm{C}} + |\mathrm{v_{scr}}(0,\tilde{\mathbf{k}},\omega_{\tilde{\mathbf{q}}})|^2 \mathrm{Im}\chi^{\mathrm{G}}\Big\} \tag{4.16}$$

The screened potentials for a graphene layer oscillating in an eigenmode $(\tilde{\mathbf{q}},\omega_{\tilde{\mathbf{q}}})$ of amplitude $A_{\tilde{\mathbf{q}}}$, have in a first approximation only one momentum component, $v_{scr}(\tilde{\mathbf{k}},\omega_{\tilde{\mathbf{q}}}) = v_{scr}(\tilde{\mathbf{q}},\omega_{\tilde{\mathbf{q}}})\delta(\tilde{\mathbf{k}}-\tilde{\mathbf{q}})$, and these components are (see Appendix C.4)

$$\begin{cases} v_{scr}(d,\tilde{\mathbf{q}},\omega_{\tilde{\mathbf{q}}}) = \dfrac{q\left[\chi^C\left(e^{qd}+e^{-qd}\right)-2\chi^G e^{qd}\right]\rho_C A_{\tilde{\mathbf{q}}} e^{-qd}}{2\chi^C\chi^G\left(1-e^{-2qd}\right)} \\ v_{scr}(0,\tilde{\mathbf{q}},\omega_{\tilde{\mathbf{q}}}) = \dfrac{|\tilde{\mathbf{q}}|\left[-\nu^C\left(e^{2qd}+1\right)+2\nu^G\right]\rho_0 A_{\tilde{\mathbf{q}}} e^{-qd}}{2\nu^C\nu^G\left(1-e^{-2qd}\right)} \end{cases} \tag{4.17}$$

where $q = |\tilde{\mathbf{q}}|$ and ρ_C is the charge density in the graphene layer. The results for $\Gamma(\omega_{\tilde{\mathbf{q}}})$ and $Q^{-1}(\omega_{\tilde{\mathbf{q}}})$ can be formulated in terms of the total charge in the graphene layer, $Q_C = \int d^2\tilde{\mathbf{r}}\rho_C \approx L \times w \times \rho_C$.

In the limit of short separation between the layers, $d \ll L$, which is the situation present in current experimental setups, substitution of eq.(4.17) into eq.(4.16) leads to

$$\Gamma(\omega_0) \approx \frac{\omega_0 A^2 Q_C^2}{4d^2}\Big(\frac{1}{\nu^C D^C} + \Big(\frac{\nu^G}{\nu^C}\Big)^2 \frac{1}{\nu^G D^G}\Big) \tag{4.18}$$

The limit $D|\tilde{\mathbf{q}}|^2 \gg \omega$ for the imaginary part of the susceptibility of a dirty metal, $\mathrm{Im}\chi(\tilde{\mathbf{q}},\omega) \approx \omega\nu/\mathrm{D}|\tilde{\mathbf{q}}|^2$, has been used, and is justified in Appendix C.1.3. The first term in the summation describes losses at the graphene sheet, and the second at the gate. The associated inverse quality factor, according to eq.(4.8), is given by

$$\boxed{Q^{-1}(\omega_0) \approx \frac{\hbar Q_C^2}{2M\omega_0 d^2}\Big(\frac{1}{\nu^C D^C} + \Big(\frac{\nu^G}{\nu^C}\Big)^2 \frac{1}{\nu^G D^G}\Big)} \tag{4.19}$$

To make numerical estimates, we use the parameters in Table [4.1], with $\nu^C(E) = E/2\pi\hbar^2 v_F^2$, $v_F \approx 10^6$ m/s for a single layer of graphene, and $\nu^C(E) = (N\gamma)/\hbar^2 v_{\mathrm{F}}^2$ for a stack of N layers [GCP06]. Carriers in graphene stacks have large mobilities [NGM+04], and we take $D^C\nu^C \approx 10^3$. Typical charge densities for the graphene layer are, as discussed in the previous subsection, $\rho_C \sim 10^{12}\mathrm{cm}^{-2}$, leading to a total charge $Q_C \sim 10^4$. For these parameters, the contribution of the graphene sheet is $Q^{-1} \sim 10^{-8}$. The relative contribution from the gate depends on the distance

to the graphene sheet. For a Si layer with $D^G\nu^G \approx 10^3$ and at short distances, the contribution to the damping from the gate is of the same order as that of the graphene sheet.

Damping is associated to the creation of e-h pairs in a metal, which implies that this mechanism is ohmic. The inverse quality factor should thus increase linearly with temperature as described in Appendix C.2.1, leading to $Q^{-1} \sim 10^{-2}$ at 300 K.

4.2.3 Breaking and healing of surface bonds: Velcro effect.

In the fabrication process of the device, the graphene flake is deposited on the silica (SiO_2) substrate. The surface properties of silica are largely determined by the nature of silanol (SiOH) groups present there [MM90], due to the hydroxyl functional group that has chemical reactivity, as compared to the inert siloxane (Si-O-Si) surface [SG95]. In Appendix C.3.3 more information relevant to us is given on silica and its surface.

Graphene becomes linked to the silica surface through hydrogen bonds created by those silanol groups. When the flake is set into motion, some of this bonds may repeatedly break and heal (the Velcro effect [VZ0]), causing dissipation of the energy stored in the vibration. Numerical estimates are difficult to make, but nevertheless two qualitative arguments showing that its role in the damping is probably negligible can be presented:

i) This mechanism is expected to be temperature independent, in contrast with the strong decrease of friction observed as temperature is lowered [BvdZV$^+$07], fig.(4.2b).

ii) The elastic energy stored in a typical graphene oscillator of lateral dimensions $w \sim 1\mu$m is $E_0 = (1/2)\rho w^2 t \omega_0^2 A^2 \sim 10$eV, when the amplitude is $A \sim 1$nm. This means about $\sim 10^{-5}$eV per nm^2. On the other hand, the energy per hydrogen bond is about 10^{-1}eV, and typical radical densities at SiO_2 surfaces are [DPX98] ~ 1nm^{-2}. Hence the elastic energy available on average for each hydrogen bond is much less than the energy stored in the bond. Only rare fluctuations, where a significant amount of energy is concentrated in a small area will be able to break bonds, and in this way to induce energy dissipation. Note, however, that this argument ceases to be valid for very large amplitudes $\gtrsim 30$nm. For higher amplitudes, this mechanism can induce significant losses.

4.2.4 Fluctuating charge noise: Dissipation due to two-level systems.

As we have seen in Part I of this thesis, in an amorphous material an atom or a few atoms can have two nearly degenerate configurations. A vibration modifies the energy difference between these situations, and this coupling leads to the damping of acoustic phonons in amorphous SiO_2 [Esq98]. We have seen this mechanism is expected to

dominate friction in many semiconductor NEMS [MHE+02]. But with graphene resonators, we expect the graphene sheet to show a high degree of crystallinity, so we will only consider two-level systems (TLSs) in the rest of the structure.

The TLSs can only dissipate energy if they are coupled in some way to the vibrating graphene sheet. A possible mechanism is the existence of charge impurities associated to these defects (fluctuating charges), which are electrostatically coupled to the conducting electrons in the graphene.

We expect this mechanism to be less effective in the device considered here than in NEMs made of semiconducting materials, as now the TLSs reside in the SiO_2 substrate, not in the vibrating structure. The coupling, arising from long range forces, will be in comparison accordingly suppressed, by a factor of order $(a/d)^n$, where a is a length comparable to the interatomic separation, and n describes the decay of the coupling ($n = 1$ for the Coulomb potential between charged systems).

The temperature dependence of the contribution of TLSs to Q^{-1} is determined by the density of states of the modes coupled to the TLSs and the distribution of TLSs in terms of their paramenters (tunneling amplitude Δ_0^x and bias Δ_0^z) [SGC07a].The hamiltonian describing the coupling of the effective TLS's and the oscillating graphene sheet is given by [SGC07a]

$$H = \epsilon\,\sigma_x + \gamma\frac{\Delta_0^x}{\epsilon}\sigma_z\sum_{\mathbf{k}}\lambda_{\mathbf{k}}(b_{\mathbf{k}} + b_{\text{-}\mathbf{k}}^\dagger) + \sum_{\mathbf{k}}\hbar\omega_{\mathbf{k}}b_{\mathbf{k}}^\dagger b_{\mathbf{k}} \tag{4.20}$$

where $\epsilon = \sqrt{(\Delta_0^x)^2 + (\Delta_0^z)^2}$, γ is the coupling constant, which will be strongly suppressed in these devices as compared to attenuation of acoustic waves in amorphous materials, $\gamma \sim 1\text{eV} \times (\text{a/d})^{\text{n}}$, $b_{\mathbf{k}}^\dagger$ represent the phonon creation operators associated to the different vibrational modes of a sheet, and $\sum_{\mathbf{k}}\lambda_{\mathbf{k}}(b_{\mathbf{k}}+b_{\text{-}\mathbf{k}}^\dagger)$ represents the coupling to the strain tensor u_{ik}. There are two types, compression modes (longitudinal waves) and bending modes. The damping is due to the initial transfer of energy from the vibrational mode studied by the experimentalists to the TLSs, which in a second step transfer this energy to the rest of the modes. The properties of the spin-boson model, eq.(4.20), are fully determined by the power-law s of the spectral function [LCD+87], $J(\omega) \equiv \sum_k |\gamma\lambda_k\Delta_0^x/\epsilon|^2\,\delta(\omega-\omega_k) \sim \alpha\omega_{co}^{1-s}\omega^s$, where ω_k is the frequency of mode k, α is an adimensional constant and ω_{co} is the upper cutoff of the phonon bath. For this system, compression modes gives rise to a superohmic, $s = 2$, bath, while the bending modes constitute an ohmic bath, $s = 1$, and thus will prevail as a source of dissipation at low temperatures [LCD+87]. We will therefore restrict our analysis to the dissipation caused by the ohmic component of the vibrational spectrum.

A **detailed calculation** of the dissipation due to this mechanism is carried out in **Appendix C.5**. Here we state the main results. One arrives at $J(\omega) = \alpha\omega$, with

$$\alpha \approx 4\Big(\gamma\frac{\Delta_0^x}{\epsilon}\Big)^2\frac{\rho_M^{1/2}(1+\nu)^{3/2}(1-\nu)^{1/2}}{\hbar t^2 E^{3/2}(9+\frac{3\nu}{1-2\nu})} \tag{4.21}$$

Here ν is the Poisson ratio of graphene. Choosing fairly symmetrical TLSs, $\Delta_0^x/\epsilon \sim 1$, for the parameters in table 4.1, $\alpha \sim 10^{-5} \times (a/d)^{2n}$, very small. The relaxation of the TLSs dissipates the energy of the vibration, giving rise to the following expression for the inverse quality factor [Esq98],

$$Q^{-1}(\omega, T) = \frac{P\gamma^2}{EkT} \int_0^{\epsilon_{max}} d\epsilon \int_{u_{min}}^1 du \frac{\omega}{u\sqrt{1-u^2}}\, C(\omega, T) \tag{4.22}$$

where $u = \Delta_r/\epsilon$, $\epsilon_{max} \sim 5$ K, and $(u\sqrt{1-u^2})^{-1}$ comes from the probability density of TLS's in an amorphous solid, like SiO_2. $Q^{-1}(\omega, T)$ is a function of $C(\omega, T)$, the Fourier transform of the correlation function $C(t, T) = \langle \sigma_z(t)\sigma_z(0)\rangle_T$. For biased TLSs and $\alpha \ll 1$ an extensive analysis of $C(\omega, T)$ is performed in [Wei99], where several expressions are provided in different limits. Using them, the estimate for $Q^{-1}(\omega, T)$ follows:

$$\boxed{\begin{cases} Q^{-1}(\omega, T) \approx \frac{P\gamma^2}{E\hbar\omega}\left\{\frac{4\pi}{3}\alpha\epsilon_{max} + \frac{\pi^2}{3}\alpha^2 kT\right\}, & kT > \epsilon_{max} \\ Q^{-1}(\omega, T) \approx \frac{P\gamma^2\alpha}{E\hbar\omega}\frac{4\pi}{3}kT, & kT < \epsilon_{max} \end{cases}} \tag{4.23}$$

In the range of temperatures of current experiments (5K<T<300K), the dependence of dissipation with T is weak, and $Q^{-1} \sim 10^{-6} \times (a/d)^4 \sim 10^{-22}$. The main uncertainty of the calculation has been the use of the TLSs' distribution assumed for amorphous solids [Phi87], but due to the small value of α a weak dissipation is expected also with a modified distribution. Thus the conclusion is that the relative importance of TLSs damping is much smaller for graphene than for other NEMs devices [CR02, Ble04, ER05].

4.2.5 Other friction mechanisms

Attachment losses.

The main expressions needed are given in [PJ04]. When $d \gg t$, and d is much smaller than the wavelength of the radiated elastic waves in the SiO_2 substrate, the contribution to the inverse quality factor is given by

$$Q^{-1} \approx \frac{w}{L}\left(\frac{t}{d}\right)^2 \sqrt{\frac{\rho_M^C E^C (1-(\nu^O)^2)}{\rho_M^O E^O}} \tag{4.24}$$

where the superscript O applies to the silicon oxide, and ν^O stands for Poisson's ratio. The range of values of the quality factor varies from $Q^{-1} \approx 5 \cdot 10^{-6}$ for a graphene monolayer, to $Q^{-1} \approx 5 \cdot 10^{-3}$ for a stack with 30 layers and $t = 10$nm. These quantities probably overestimate the attachment losses, as they do not include the impedance at the SiO_2-graphene interface.

This damping process due to energy irradiated away from the resonator should not depend on temperature.

Thermoelastic effects.

When the phonon mean free path of the acoustic phonons is shorter than the wavelength of the mode under study, the acoustic phonons can be considered a dissipative environment coupled to the mode by anharmonic terms in the ionic potential [Zen38, LR00, Ü06]. These anharmonic effects are described by the expansion coefficient, α, and the thermal conductivity, κ. We follow the analysis in [Zen48]. For a rectangular beam vibrating at a frequency ω the inverse quality factor is

$$Q_Z^{-1}(T) = \frac{E\alpha^2 T}{C_p} \frac{\omega\tau_Z}{1+(\omega\tau_Z)^2} \tag{4.25}$$

where E is the Young Modulus, C_p is the specific heat at a constant pressure, and τ_Z is the thermal relaxation time associated with the mode, which in the case of a flexural vibration is given by $\tau_Z = t^2 C_p/(\pi^2\kappa)$. This estimate assumes that the graphene sheet is weakly deformed, and that the typical relaxation time is associated to the diffusion of phonons over distances comparable to the thickness of the sheet.

Although better approximations are available in the literature [LR00], eq.(4.25) is enough for an estimate of the order of magnitude of Q^{-1}. Using the parameters from table[4.1], for $t = 10$ nm and $f \sim 100$ MHz, we find that $\omega\tau_Z \ll 1$, and

$$Q_Z^{-1}(T = 300\mathrm{K}) \approx \frac{\mathrm{E}\alpha^2\mathrm{T}\omega\mathrm{t}^2}{\pi^2\kappa} \sim 5\cdot 10^{-7} \tag{4.26}$$

4.3 Extension to nanotube oscillators.

The analysis presented here can be extended, in a straightforward way, to systems where the oscillating part is a nanotube.

We expect in these devices a larger impedance between the modes of the nanotube and those of the substrate, so that attachment losses will be suppressed with respect to the estimate presented here for graphene.

The damping mechanisms which require long range forces between the moving charges in the nanotube and degrees of freedom of the substrate (fluctuating and static charges) will not be significantly changed. A nanotube of length L at distance d from the substrate will interact with a substrate area of order $(L+d)\times d$. A similar estimate for a graphene sheet of length L and width w gives an area $\sim (L+d)\times(w+d)$. As $L \sim w \sim d \sim 1\mu$m, the two areas are comparable.

On the other hand, ohmic losses induced in the nanotube will be reduced with respect to the two dimensional graphene sheet, as the number of carriers is lower in the nanotube.

Finally, we expect a longer phonon mean free path in the nanotube, which implies that thermoelastic effects will be reduced .

4.4 Conclusions.

We have considered six possible dissipation mechanisms which may lead to damping in a graphene mesoscopic oscillator. The main results are summarized in Table[4.2]. We expect that the calculations give the correct order of magnitude and dependence on external parameters.

We find that at high temperatures the leading damping mechanism is the ohmic losses in the metallic gate and the graphene sheet. This effect depends quadratically with the total charge at the graphene sheet, which can be controlled by the gate voltage.

When speaking about the room temperature prevailing damping source, however, a disturbing fact obtained in ref. ([BvdZV$^+$07]) has to be noted: the independence of the magnitude of Q at room temperatures for both the optical and electrical driving setups. Unless a mechanism like optical heating were of the order of the predicted dissipation due to ohmic losses, we are missing something. In principle optical heating does not seem to be an important friction source, as it should lead to an almost temperature independent $Q(T)$, contradicting results like the one shown in fig.(4.2b).

At low temperatures attachment losses limit the quality of the vibration. If the resonator is strongly driven, a new damping mechanism may come into play, the Velcro effect, which may limit substantially the quality factor as compared with the slightly driven case. The high crystallinity of the resonators eliminates the main source of dissipation in semiconducting resonators, namely surface-related effective TLSs coupled to the local strain field.

These conclusions apply with only slight modifications to carbon nanotube-based resonators.

A deeper knowledge on the charge distribution throughout the device as a function of the parameters characterizing the fabrication process and the operation of the resonator for the different setups would prove of great interest, as it may lead to substantial improvements in the quality factor through the design of charge minimization strategies, and shed some light on the prevailing damping mechanisms for these devices. More measurements of the quality factor as a function of temperature would be also desirable for these purposes.

Part III

Dissipation of collective excitations in metallic nanoparticles

Chapter 5

Metallic clusters: optical response and collective excitations

5.1 From atoms to bulk

[1] Nanometer-sized systems are the natural playground where the crossover from atomic-like to bulk behavior is observed. Among the simplest and most studied ones are clusters of alkaline or noble metal atoms, with radii a between 0.5 and several nm (few atoms to hundreds of thousands, respectively, see Fig. 5.1). The simpler electronic structure of alkaline atoms renders the theoretical modeling of alkaline clusters easier as compared to the case of noble metals (with both s and d electrons), but their high reactivity imposes stringent conditions on their production: clusters cannot be formed embedded in a solid matrix, so they are created, starting from an alkaline vapor at a high temperature, by expansion into vacuum within an inert carrier gas flux, a method called *seeded beam expansion* [KKS82]. Noble metals circumvent this problem, allowing for a more controlled fabrication and study by ion implantation in an inert matrix and subsequent high temperature annealing [DYN$^+$99, OKNS00]. Moreover, their chemical stability is required for their use as biological markers, one of their most promising applications [BTM$^+$02, CTB$^+$03]. We will comment further on this issue later.

The crossover size to observe bulk behavior depends on the physical property under study, and is moreover never clearcut. Two ingredients are the main responsibles of several new and interesting phenomena occurring in this *interregnum*. On the one hand, the spectrum of the electronic states remains discrete, with the energy levels broadened by the interactions with the environment. On the other, interferences and coherent behavior of electrons happen due to their coherent motion inside the system:

[1] For a very good and detailed review on the issues covered in this chapter see [Wei06]. It has been the main bibliographic source of this chapter and the beginning of the next.

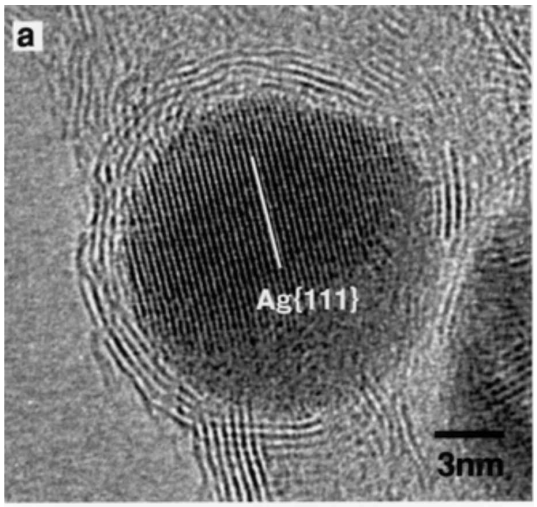

Figure 5.1: High resolution electron microscopy image of an Ag nanoparticle encapsulated within a boron nitride nanocage (from ref. [OKNS00]).

inelastic or phase-breaking scattering lengths are larger than the size of the cluster.

The strongest evidence of the quantization of the electronic spectrum in metallic nanoparticles is the so-called *electronic shell structure* observed for the first time in 1984 by Knight *et al.* [KCdH$^+$84]. In the nuclear shell-model [BB75, RS80] a given nucleon of a nucleus can be considered to a first approximation as confined by a mean-field potential created by the rest of nucleons. Analogously for clusters, the valence electrons originating metallic bands in the bulk can be thought of as dwelling in a mean-field potential created by the rest of valence electrons and all the ionic cores comprising the cluster. An immediate consequence of such a model is the existence of certain "magic numbers" of valence electrons (or correspondingly, atoms) for whom the system is energetically more stable, namely those filling angular-momentum shells, as in the nuclear shell-model. In [KCdH$^+$84], the histogram of clusters as a function of their size detected in a molecular beam of sodium seeded in argon showed a clear preference for $N = 8, 20, 40, 58$ and 92, which was explained with the use of such a shell model with a spherically symmetric potential $V(r)$ of the Woods-Saxon form [WS54]. It turns out that a sphere is a reasonable approximation for electronically closed-shell nanoparticles [dH93, Bra93], while for open-shell structures distortions occur due to the Jahn-Teller effect [dH93, JT37]. We will focus our attention in this thesis on the first, simpler case.

Bulk-like behavior is frequently observed for surprisingly small clusters. Furthermore, the size dependence of quantitative features can already be smooth for very

small systems. For instance, the binding energy of Na_9 clusters is quite close to that of Na_8, even if these two systems are very different from the molecular point of view [dH93]. Such a continuity points, together with the aforementioned evidence of electronic shells [KCdH$^+$84, KCdHS85], towards the relatively minor importance of the ionic cores and supports the descriptions based on the jellium model, where the conduction electrons are subject to a uniform neutralizing background [Bra93].

Electronic properties of metallic nanoclusters owe their uniqueness to two facts: first the already mentioned size range, where an evolution from discrete to continuum spectrum takes place, and second, the existence of a surface, a finite boundary that, due to the small size of these systems, has profound implications, the most relevant of which is the appearance of the so-called *surface plasmon*, a collective excitation that dominates the optical response for all clusters except the smallest ones, for whom transitions between single particle levels dictate the optical response. Indeed, the question of how large the size of the nanoparticle has to be in order to observe this collective excitation in such a finite system has the surprising answer that a very small cluster, like for instance Na_6, may already be enough [SKM$^+$91, YB91].

As we will see in next subsection, the surface plasmon corresponds to the excitation of a periodic displacement of the electronic center of mass with respect to the positive ionic background. The jellium approximation for this background allows to decompose the electronic Hamiltonian into a part associated with the electronic center of mass, a part describing the relative coordinates (treated in the mean-field approximation), and finally a coupling between the two subsystems. The coupling between the center of mass and the relative coordinates causes decoherence and dissipation of this collective state once it is excited.

The treatment of the surface plasmon as a quantum particle (the electronic center of mass degree of freedom) therefore provides a model system for the study of decoherence and quantum dissipation in confined nanoscopic systems, where the role of the electronic correlations is preponderant and the excitation spectrum arises from a *finite* number of particles. The finite number of electrons makes the term "environment" not completely justified in this situation, and leads us to the following question, which will be addressed in this thesis: How large in size do we need to go to be allowed to describe the relative coordinates of the electron gas as an environment damping the collective excitation? The existence of several experimental techniques to observe the surface plasmon dynamics, and the use of such excitation in biomedical applications add even more interest to the subject.

Based on the mentioned decomposition and mean-field approach an extensive and powerful analytical study of the plasmon dynamics is feasible, incorporating the effects of finite size, a dielectric material, or the finite temperature of the electron

gas. With the use of semiclassical expansions it allows to i) obtain the parametric dependence (in size, temperature, Fermi energy, etc) of the addressed quantities like the surface plasmon lifetime or its resonance frequency, ii) compute the optical properties of arbitrarily large clusters, and with some extensions also describe smaller ones, iii) be extended to nonlinear processes such as those resulting from the interaction with strong laser fields iv) address coherence and dissipation of the surface plasmon in both weak and strong laser field driving of the nanoparticle [YB91, YB92, MWJ02, MWJ03, WMWJ05, WIJW06, WIWJ07, WWIJ07].

Such a wealth of analytical results and gain of knowledge demands the use of certain approximations, some of which have been assumed until now to be valid without proof. In the context of this thesis we will first present the theoretical scheme and then justify its approximations, confirming the validity of previous results and putting the approach on a more firm basis. In particular, we will determine which are the energies of the electronic excitations that are active in the damping of the surface plasmon, and what is the characteristic response time of the large enough electronic environment. The latter is important in justifying the Markovian approximation that is assumed to describe the dynamics of the surface plasmon coupled to particle-hole excitations [WIWJ07]. Other complimentary techniques, like the time-dependent local density approximation (TDLDA), will not be analyzed. We will start by giving a first physical image of the surface plasmon, and summarizing available experimental techniques for its study and use in biomedical applications.

5.2 Surface plasmon excitation

The study of the response of metallic nanoparticles to externally applied electromagnetic fields reveals the main features of the electronic spectrum just outlined, with the optical response dominated by a collective resonance, the surface plasmon. What happens to the system when such a collective state is excited? For optical fields, the wavelength is bigger than the diameter $2a$ of the system and the frequency is such that the light electronic cloud is able to react to the variations of the field, whereas the ionic background, three orders of magnitude more massive, cannot follow the perturbation and remains approximately static. The result is the uniform relative displacement of electron and ionic clouds, creating unbalanced charges at the surface of the nanoparticle (a dipole) which try to restore the equilibrium situation in absence of an external field. The dipole is forced to oscillate with the frequency of the applied field (depicted in fig. 5.2), and its magnitude peaks at the so-called *surface plasmon frequency*, the natural frequency of the dipole, fixed by the electronic density, the spherical geometry, and the charge and mass of the electrons. So the surface plasmon is nothing but the self-sustained state of motion for which the center of mass of the negative charges oscillates with respect to the center of mass of the more massive

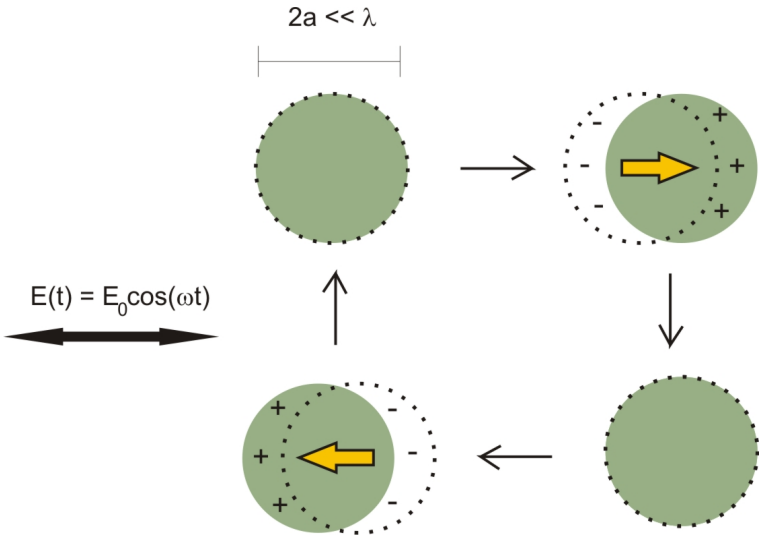

Figure 5.2: Schematic representation of the surface plasmon resonance in small metallic clusters. The wavelength λ of the exciting electrical field E(t) is much larger than the diameter $2a$ of the cluster. Thus, the electrical field throughout the nanoparticle is nearly uniform. The shaded regions symbolize the ionic background, while the dashed circles represent the electronic cloud. The "-" and "+" signs account for the uncompensated negative and positive charges. The electrical field exerts a force on the positively charged ions and an equal force on the electrons in the opposite direction, separating their centers of mass mainly due to the motion of the light electrons. The ions, being much more massive, remain almost at rest. The resulting surface charges create a dipolar restoring field (thick arrow) opposing E(t).

ionic cores.

Applying classical Maxwell's equations to the case of a dielectric metal sphere with appropiate boundary conditions, Mie obtained in 1908 [KV95, Mie08] a first estimate for this frequency, the classical Mie frequency $\omega_{\mathrm{M}} = \omega_{\mathrm{p}}/\sqrt{3}$, where $\omega_{\mathrm{p}} = (4\pi n_{\mathrm{e}} e^2/m_{\mathrm{e}})^{1/2}$ is the bulk plasma frequency and e, m_{e}, and n_{e} denote the electronic charge, mass, and density, respectively. In a real cluster surface effects lead to a small reduction of the surface plasmon frequency with respect to the Mie value ω_{M} [Bra93, GGI02, WIJW06]. Typical values for the surface plasmon energy are about several eV, belonging thus to the energy range corresponding to bound single-particle states [BB94].

5.2.1 Probing and using the surface plasmon

Several techniques show and use the existence of the surface plasmon to study electronic properties of metallic clusters. We will mention three of them:

Photoabsorption experiments

The cluster is illuminated by a light of a certain frequency, and the amount of absorbed photons is determined and given in terms of the photoabsorption cross section $\sigma(\omega)$, which is the probability that the system absorbs a photon times the area illuminated by the photon beam. The presence of the single-particle states derived in the electronic shell model should be signalled by several peaks in $\sigma(\omega)$, but they are usually overwhelmed by the peak of the collective excitation [BCLS93], thus indicating a substantial transfer of spectral weight to build the surface plasmon.

Noble metal nanoclusters as biological markers

An ideal optical label for large molecules should generate an intense optical signal; it should also be small, durable, chemically inert, and apt to bind to the molecule of interest in a controlled manner. Noble metal clusters meet all of these requirements when illuminated with a frequency close to the one of their surface plasmons. They overcome the main shortages present in other candidates like fluorescent dyes or nanocrystals of II-VI semiconductors, as they do not photobleach like the former and do neither optically saturate at reasonable exciting intensities like the latter. Several techniques take advantage of the excitation of the surface plasmon as a means to track the nanoparticle adhered to the molecule of interest: nanoparticles bigger than 40 nm in diameter can be imaged, based on Rayleigh scattering, in an optical microscope by illuminating in dark-field at the plasmon frequency [SSMS00], with differential interference contrast (DIC) and video enhancement [JG88], or with total internal reflection [SGH$^+$00]. For smaller nanoparticles, whose Rayleigh scattering is too small to be detected, local heating associated to its strong light absorption causes a temperature change which can be monitored by a sensitive interference method similar to DIC [BTM$^+$02], see fig. 5.3.

Pump-probe experiments: plasmon dynamics

The use of femtosecond pulsed lasers in time-resolved pump-probe spectroscopy has rendered possible to experimentally address the surface plasmon dynamics [BHMD00, FVF$^+$00, LKLA99, LUCS01]. An initial ultrashort laser pulse lasting around a hundred femtoseconds pumps energy into the nanoparticle by exciting the surface plasmon mode. After a certain time delay a second, much weaker, pulse, the probe laser, tests the absorption spectrum of the hot electron gas in the cluster. By repeating the experiment for several values of the delay an image of the time evolution of the

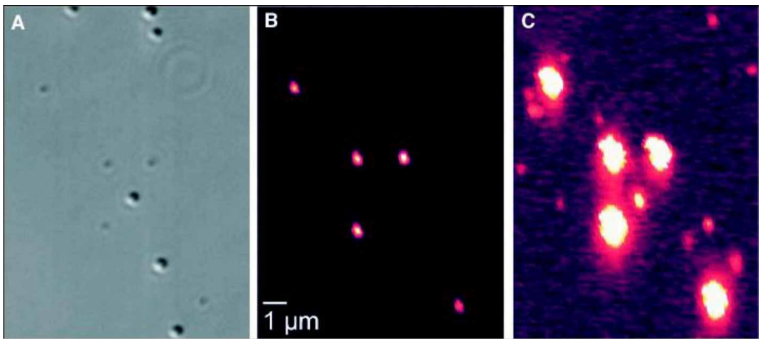

Figure 5.3: Noble metal nanoparticles can be used as biological tracers, thanks to their strong light scattering and absorption in the optical range due to the existence of the surface plasmon collective excitation. From ref. [BTM+02]. (A) Differential interference contrast (DIC) based on Rayleigh scattering of light and (B and C) photothermal images measuring local heating due to strong light absorption, of a sample containing 300-nm-diameter latex spheres, 80-nm-diameter gold spheres, and 10-nm-diameter gold spheres. The heating intensity was 30 kW/cm^2 (B) or 1.5 MW/cm^2 (C). The 80-nm gold spheres appear on all three images and allowed direct comparisons of the same imaged sample area. In the DIC image, the 10-nm particles are not visible, whereas the 300-nm latex spheres give very strong signals and the 80-nm gold spheres give weaker ones. In (B), a photothermal image at low power shows only the large metal particles. In (C), at high heating power, the 10-nm particles are clearly visible, whereas the 80-nm gold spheres saturate the detection capability. The strongly scattering latex spheres are completely absent in the photothermal images, as they do not absorb light as efficiently as a metallic cluster.

relaxation process is obtained.

Usually the experiments are performed on an ensemble of noble metal clusters embedded in an inert matrix, taking care that typical separations between clusters guarantee independence of their response. Several timescales are involved in the relaxation, linked to the different characteristic times of the degrees of freedom participating: surface plasmon, single-particle electron excitations, nanoparticle phonons, and embedding matrix phonons. As schematically depicted in fig. 5.4, the energy is initially stored in the surface plasmon collective mode, causing a non-thermal, highly-correlated, electronic distribution $f(\epsilon)$. In a femtosecond scale the surface plasmon decays through electron-electron and electron-surface scattering, transferring its energy to the rest of (single-particle) electronic degrees of freedom, which accordingly heat and reach a thermal equilibrium distribution with temperatures up to hundreds of degrees, depending on the intensity of the pump laser. Phonons of the nanoparticle, with typical frequencies $\sim 10^{12}$ Hz, come into play on a much longer timescale,

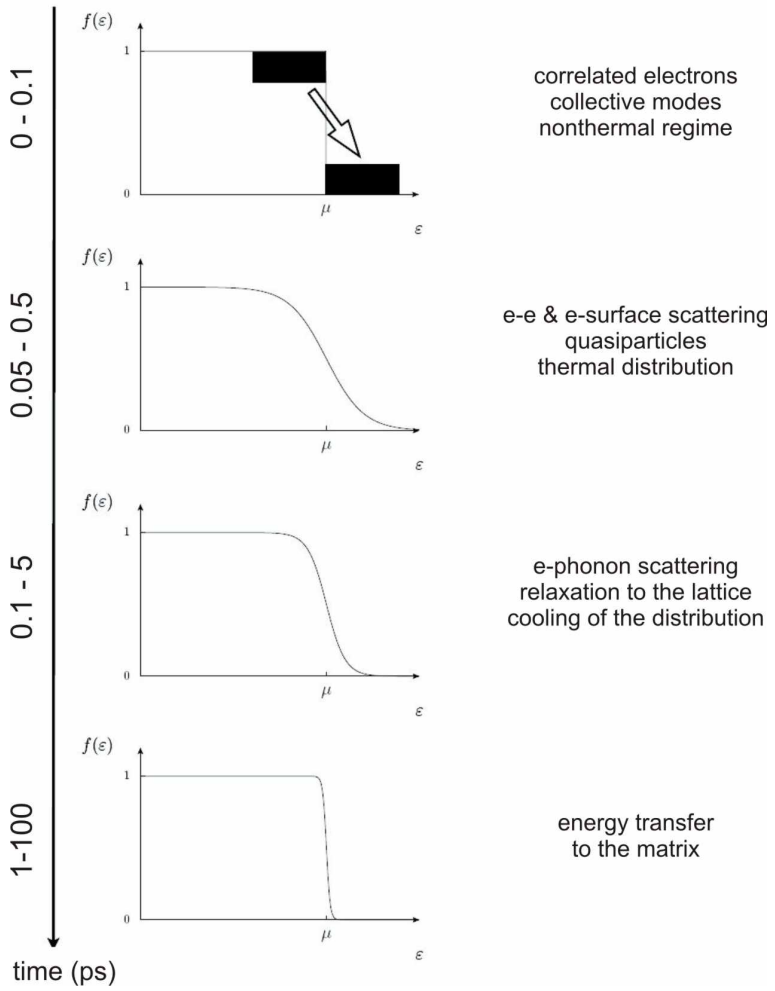

Figure 5.4: From ref. [Wei06]. Sketch of the relaxation processes in a metallic nanoparticle after an excitation by a strong and ultrashort femtosecond laser pump pulse. $f(\epsilon)$ is a sketch of the electronic distribution, while μ is the chemical potential. The arrow in the uppermost image symbolizes the effect of the pump laser on the electronic system.

of the order of a picosecond, and absorb part of the energy stored in the electronic distribution, cooling it. The relaxation process ends with the transfer of energy to the phonons of the matrix where the nanoparticle is embedded, on the timescale of several picoseconds, reaching the system as a whole thermal equilibrium.

In experiments, the normalized difference of transmission of the sample with and without the pump laser field, called differential transmission $\Delta\mathcal{T}/\mathcal{T}$, is the quantity measured to study the relaxation process: $\Delta\mathcal{T}/\mathcal{T} = (\mathcal{T}_{on} - \mathcal{T}_{off})/\mathcal{T}_{off}$. An example is

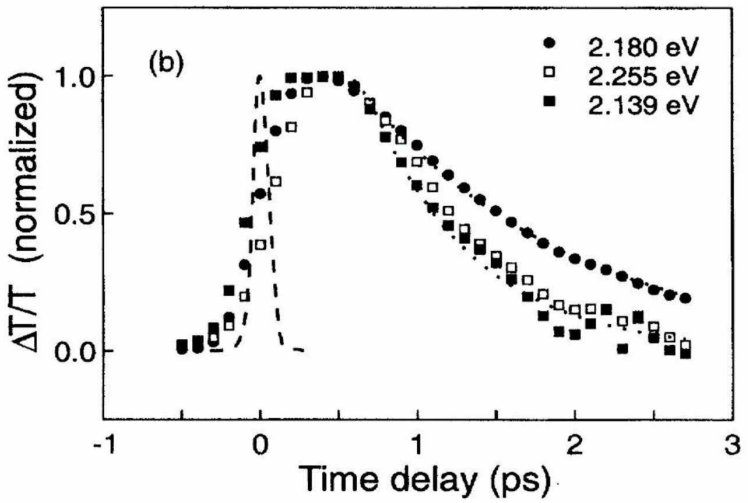

Figure 5.5: Experimental differential transmission $\Delta\mathcal{T}/\mathcal{T}$ as a function of the delay time between the pump and probe pulses, for different probe photon energies. The nanoparticles in this experiment are made of copper and embedded in a glass matrix. They have an average diameter of 10 nm. The plasmon resonance is located close to $\hbar\omega_{sp} \simeq 2.2$ eV. (Reproduced from Ref. [BMCD95])

given in fig. 5.5, showing the differential transmission as a function of the time delay between the pump and probe pulses, for different probe energies in the vicinity of the surface plasmon resonance. The decrease of $\Delta\mathcal{T}/\mathcal{T}$ as a function of time reflects the relaxation of the electronic energy to the lattice.

Chapter 6

Electronic dynamics in metallic nanoparticles: theoretical model

This chapter describes a very successful theoretical framework for the analytical description of the electron dynamics in metallic clusters, expressed in terms of two types of excited states, the single-particle e-h excitations, and the many-body surface plasmon collective state. In a basis of relative + center of mass electronic coordinates, e-h and surface plasmon excitations will correspond to the relative and center of mass coordinates, respectively. Some key assumptions needed for the conceptual soundness of the model will be underlined, whose justification will be provided in the final part of the chapter.

6.1 Electronic hamiltonian: relative and collective coordinates

The systems we will analyze are neutral, spherical, metallic nanoparticles of radius a containing N valence electrons. They thus have, as mentioned in the previous chapter, closed angular momentum shells ($N = 8, 20, 40, 58...$, the so-called "magic numbers" [Bra93]). We will work within the adiabatic Born-Oppenheimer approximation [AM76], treating the ions as static, compared with the lighter and faster valence electrons. Moreover, we will work within the jellium approximation, which neglects effects of the ionic structure and treats the ions as a continuous, homogeneous positively charged background of total charge $+Ne$, producing a charge density in the case of a spherical nanoparticle $\rho_i(r) = (Ne/V)\Theta(a-r)$, with $V = 4\pi a^3/3$ the volume of the cluster and $\Theta(x)$ the Heaviside step function. The subsequent model is simple enough to be applied for the description of big clusters containing up to several thousands of atoms, and the effects linked to the ionic structure turn out to be important only for the smallest cases, $N < 10$ [Bra93].

The electronic hamiltonian for an alkaline-metal nanoparticle in vacuum is in this context given by

$$H = \sum_{i=1}^{N} \Big[\frac{p_i^2}{2m_e} + U(r_i) \Big] + \frac{e^2}{2} \sum_{\substack{i,j=1 \\ (i \neq j)}} \frac{1}{|\mathbf{r}_i - \mathbf{r}_j|} \,, \tag{6.1}$$

where e and m_e are the electronic charge and mass, $\mathbf{r}_i$ is the position of the i^{th} conduction electron, $r_i = |\mathbf{r}_i|$, $\mathbf{p}_i$ is the associated momentum, and $U(r)$ represents the electrostatic interaction between the electrons and the ionic background.

For a noble metal cluster embedded in a dielectric medium, the electron-electron interaction in (6.1) is modified by the presence of the d-electrons and the matrix in terms of two dielectric constants ϵ_d and ϵ_m, and the expression for the Coulomb potential is much more cumbersome due to the loss of translational invariance. For a thorough study of this case see [Wei06, WMWJ05].

The shape of the confining potential $U(r)$ for a charged sphere of radius a and total charge $+Ne$, harmonic inside the nanoparticle with the Mie frequency $\omega_M = \sqrt{Ne^2/m_e a^3}$ and Coulomb-like outside, can be readily obtained using Gauss's theorem,

$$U(r) = \frac{Ne^2}{2a^3}(r^2 - 3a^2)\Theta(a - r) - \frac{Ne^2}{r}\Theta(r - a) \tag{6.2}$$

If the many-body eigenstates $|f\rangle$ and eigenenergies E_f of the hamiltonian (6.1) are known, the photoabsorption cross section $\sigma(\omega)$ can be calculated using Fermi's golden rule [Mer70]

$$\sigma(\omega) = \frac{4\pi e^2 \omega}{3c} \sum_f |\langle f|z|0\rangle|^2 \delta(\hbar\omega - E_f + E_0) \tag{6.3}$$

The ground state is $|0\rangle$, and the electric field is assumed to be along the z axis. From $\sigma(\omega)$ the frequency ω_{pl} and linewidth γ_{pl} of the surface plasmon are immediately obtained. But the calculation of the many-body eigenstates becomes exceedingly difficult for clusters bigger than a few electrons, and further approximation schemes have to be developed.

The most useful one starts by changing the electronic coordinate basis to the center of mass $\mathbf{R} = \sum_i \mathbf{r}_i/N$ and relative coordinates $\mathbf{r}'_i = \mathbf{r}_i - \mathbf{R}$. The corresponding conjugated momenta are $\mathbf{P} = \sum_i \mathbf{p}_i$ and $\mathbf{p}'_i = \mathbf{p}_i - \mathbf{P}/N$, respectively, and (6.1) becomes

$$H = \frac{\mathbf{P}^2}{2Nm_e} + H_{rel} + \sum_{i=1}^{N} [U(|\mathbf{r}'_i + \mathbf{R}|) - U(r'_i)] \tag{6.4}$$

where the hamiltonian for the relative-coordinate system reads

$$H_{rel} = \sum_{i=1}^{N} \Big[\frac{{p'_i}^2}{2m_e} + U(r'_i) \Big] + \frac{e^2}{2} \sum_{\substack{i,j=1 \\ (i \neq j)}} \frac{1}{|\mathbf{r'}_i - \mathbf{r'}_j|} \tag{6.5}$$

A first glance comparing eqs. (6.1) and (6.5) may make us wonder where is the difference between them, and what is our motivation to go from (6.1) to (6.4). Regarding the difference between hamiltonians, note that one of the relative coordinates is a function of the rest, as $\sum_i \mathbf{r}'_i = 0$. The change of variables, on the other hand, is justified as it is the right one if we are interested in the study of the surface plasmon collective excitation, which was shown in the previous chapter to correspond to electronic center-of-mass oscillations.

Assuming small displacements for the center of mass, $|\mathbf{R}| \ll a$, the dependence on the relative coordinates in the last term of (6.4) drops out, $U(|\mathbf{r}' + \mathbf{R}|) - U(r') \simeq \mathbf{R} \cdot \nabla U(r') + (1/2)(\mathbf{R} \cdot \nabla)^2 U(r')$, where derivatives are taken at $\mathbf{r}' = \mathbf{r}$. Choosing the oscillation axis of the center of mass in the z-direction, $\mathbf{R} = Z\mathbf{e}_z$, one obtains with (6.2)

$$\begin{aligned} \mathbf{R} \cdot \nabla U(r') &= Z m_e \omega_M^2 \Big[z' \Theta(a - r') + \frac{z' a^3}{r'^3} \Theta(r' - a) \Big] \qquad (6.6) \\ (\mathbf{R} \cdot \nabla)^2 U(r') &= Z^2 N e^2 \Big[\frac{1}{a^3} \Theta(a - r') + \frac{1 - 3\cos^2\theta'}{r'^3} \Theta(r' - a) \Big] \simeq Z^2 \frac{N e^2}{a^3} \Theta(a - r') \end{aligned}$$

where in the last line a second-order coupling in Z between the center-of-mass and the relative-coordinate system for $r' > a$ has been neglected as compared with the first-order one expressed in the second term of the right-hand side of the first line. Inserting (6.6) into (6.4),

$$H = \frac{\mathbf{P}^2}{2N m_e} + \frac{1}{2} \frac{N e^2}{a^3} \mathbf{R}^2 \sum_{i=1}^{N} \Theta(a - r_i) + H_{rel} + H_c = H_{cm} + H_{rel} + H_c \,, \tag{6.7}$$

where the coupling H_c between the center-of-mass and the relative coordinates is, to first order in the displacement $\mathbf{R}$ of the center of mass

$$H_c = \sum_{i=1}^{N} \mathbf{R} \cdot \nabla U(r'_i) \Big|_{\mathbf{R}=0} \,, \tag{6.8}$$

with $\mathbf{R} \cdot \nabla U(r'_i) \Big|_{\mathbf{R}=0}$ given in (6.6). Notice that due to the spread of the electrons' wavefunctions outside the geometrical boundary of the cluster, $r = a$, there is a finite probability for them to have $r_i > a$, which due to the sum over $\Theta(a - r_i)$ in (6.7), results in a reduction of the center-of-mass oscillation frequency from the classical

Mie value, $\tilde{\omega}_M = \omega_M\sqrt{1 - N_{out}/N} < \omega_M$. This quantum correction is the so-called *spill-out effect* [dH93, Bra93, KV95].

The structure of (6.7) is typical for quantum dissipative systems [Wei99]: The system under study (H_{cm}) is coupled via H_c to an environment or "heat bath" described by H_{rel}. The system-environment coupling results in dissipation and decoherence of the collective excitation.

6.2 Mean-field approximation and second quantization of the hamiltonian

The presence in H_{rel} of electronic interactions makes the problem still a formidable one and demands further simplifications. A mean-field approximation for the relative-coordinates' degrees of freedom, together with a second quantization procedure, will render a tractable hamiltonian suited for the study of collective excitations in metallic clusters.

The harmonic oscillator hamiltonian H_{cm} for the center-of-mass is quantized as usual with bosonic creation and annihilation operators [BF04],

$$\begin{cases} b = \sqrt{\frac{Nm_e\tilde{\omega}_M}{2\hbar}}Z + \frac{i}{\sqrt{2Nm_e\hbar\tilde{\omega}_M}}P_Z \\ b^\dagger = \sqrt{\frac{Nm_e\tilde{\omega}_M}{2\hbar}}Z - \frac{i}{\sqrt{2Nm_e\hbar\tilde{\omega}_M}}P_Z \end{cases} \tag{6.9}$$

where P_Z is the conjugated momentum to Z. Eigenstates $|n\rangle$ of H_{cm} satisfy $b|n\rangle = \sqrt{n}|n-1\rangle$ and $b^\dagger|n\rangle = \sqrt{n+1}|n+1\rangle$, and H_{cm} is expressed in terms of b and $b^\dagger$, subtracting the zero-point energy $\hbar\tilde{\omega}_M/2$, as

$$H_{cm} = \hbar\tilde{\omega}_M b^\dagger b \tag{6.10}$$

In the mean-field approximation for the hamiltonian H_{rel}, eq.(6.5), we forget the fact that one of the relative coordinates is not independent of the rest (hopefully causing $1/N$ errors which become negligible as the number of electrons N grows), and substitute H_{rel} by the mean-field approximation of eq.(6.1), mimicking the effect of the rest of electrons on a given one with an effective one-body potential $V(\mathbf{r})$ felt by the latter:

$$H_{rel} \approx \sum_{i=1}^{N} H_{sc}[r_i', p_i'] = \sum_{i=1}^{N}\Big[\frac{{p_i'}^2}{2m_e} + V(r_i')\Big] \tag{6.11}$$

We have used $V(\mathbf{r}) = V(r)$, valid for a spherical nanocluster. Numerical calculations using time-dependent local density approximation (TDLDA) within the spherical jellium model at zero temperature provide information about the shape of the potential

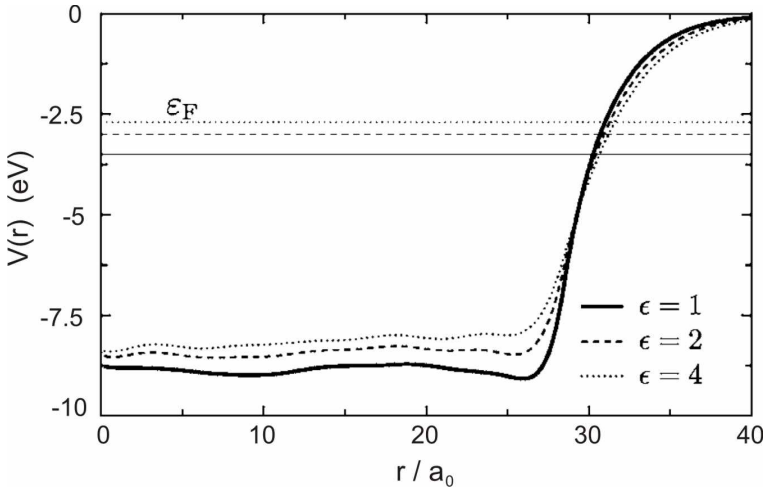

Figure 6.1: From [WMWJ05]. Self-consistent mean-field potential V as a function of the radial coordinate (in units of the Bohr radius $a_0 = 0.53\mathring{A}$) from TDLDA numerical calculations (at $T = 0$) for a nanoparticle with $N = 832$ valence electrons. The mean distance between electrons $r_s = (3/4\pi n_e)^{1/3} = 3.02a_0$ (silver), corresponding to $a \simeq 28.5a_0$; for Na $r_s = 3.93a_0$ [AM76], yielding similar results for $V(r)$, as the $\epsilon = 1$ case is equivalent to the one of an alkaline-metal cluster in vacuum. For most purposes in analytical calculations V can be approximated by a step function with discontinuity at $r = a$.

$V(r)$ [Eka84a, Eka84b, GK85, GDP96, CRSU00]. In this approach the original hamiltonian (6.1) is replaced by a self-consistent hamiltonian like (6.11) where $V(r)$ is a local function containing exchange and correlation terms. Results show that for most purposes $V(r)$ can be very well approximated in analytical calculations by a step function, with the jump located at $r = a$. An example of TDLDA result for $V(r)$ can be found in fig. 6.1.

From the self-consistent single-particle hamiltonian (6.11) a second-quantized version immediately follows in terms of fermionic creation and annihilation operators $c_\alpha^\dagger$ and c_α,

$$H_{rel} = \sum_\alpha \epsilon_\alpha c_\alpha^\dagger c_\alpha \ , \tag{6.12}$$

where $c_\alpha^\dagger$ creates the one-body state $|\alpha\rangle$ whose wavefunction in the coordinate representation satisfies $H_{sc}\psi_\alpha(\mathbf{r}) = \epsilon_\alpha \psi_\alpha(\mathbf{r})$.

The coupling term H_c between the center-of-mass and the relative coordinates

becomes in terms of the bosonic and fermionic operators $b^\dagger$ and $c^\dagger_\alpha$

$$H_c = \Lambda(b^\dagger + b)\sum_{\alpha\,\beta} d_{\alpha\beta} c^\dagger_\alpha c_\beta \ , \tag{6.13}$$

where $\Lambda = \sqrt{\hbar m_e \omega_M^3/2N}$, and

$$d_{\alpha\beta} = \langle\alpha|\Big[z\Theta(a-r) + \frac{za^3}{r^3}\Theta(r-a)\Big]|\beta\rangle \tag{6.14}$$

is the matrix element between two eigenstates of the unperturbed mean-field problem. In the constant Λ the approximation $\tilde{\omega}_M \approx \omega_M$ has been included, as it leads to $1/a^2$ negligible corrections in the quantities one wants to compute, like the lifetime of the surface plasmon, using the second quantized approximation for (6.1),

$$H = \hbar\tilde{\omega}_M b^\dagger b + \Lambda(b^\dagger + b)\sum_{\alpha\,\beta} d_{\alpha\beta} c^\dagger_\alpha c_\beta + \sum_\alpha \epsilon_\alpha c^\dagger_\alpha c_\alpha \tag{6.15}$$

6.3 Surface plasmon linewidth and finite size effects

6.3.1 Mechanisms causing the decay of the surface plasmon

The finite lifetime of the surface plasmon excitation can be related to several processes. When Mie performed his study of the optical response of metal clusters using Maxwell's equations, he used a simple free-electron Drude model [AM76] for the dielectric constant describing the metal. Within this approximation,

$$\epsilon(\omega) = \epsilon_d - \frac{\omega_p^2}{\omega(\omega + i\gamma_i)} \ , \tag{6.16}$$

where $\omega_p = \sqrt{4\pi n_e e^2/m_e}$ is the plasma frequency, γ_i^{-1} the relaxation or collision time, while e, m_e and n_e stand for the electron charge, mass and bulk density, respectively. ϵ_d is the dielectric constant of the metal without the free-carrier contribution. Inserting (6.16) in the expression he had derived for the photoabsorption cross section, he obtained

$$\sigma(\omega) = \frac{9\omega_p^2\mathcal{V}}{2c}\frac{\epsilon_m^{3/2}}{(\epsilon_d + 2\epsilon_m)^2}\frac{\gamma_i/2}{(\omega-\omega_M)^2 + (\gamma_i/2)^2} \ , \tag{6.17}$$

where ϵ_m is the dielectric constant of the medium in which the particle is embedded, and $\mathcal{V}$ the volume of the cluster. Expression (6.17) predicts the existence of the surface plasmon at the Mie frequency ω_M, with a linewidth γ_i. This value of γ_i accounts for the various processes leading to elastic or inelastic scattering in *bulk* metals, such

as interactions with phonons, electrons, impurities, etc. Experiments give, however, a much larger value for the linewidth, indicating that the plasmon lifetime is due mainly to quantum mechanical effects arising in such a confined system, absent in Mie's treatment. For example, for Sodium $\hbar\gamma_i \simeq 20$ meV, while the observed linewidth for Na clusters with $a = 2.5$ nm is more than 10 times this value.

We have already described one such finite-size effect, see eq.(6.15) and fig.(5.2): the motion of the electronic center of mass linked to the excitation of the surface plasmon results in a net surface charge creating a time-varying dipolar electric field inside the cluster, which couples to the mean-field one-particle states calculated in the absence of such a field. Through this coupling, represented by the second term of the right-hand side of (6.15), the one-particle states become excited, absorbing energy from the field, and thus damping the surface plasmon. This decay of the surface plasmon into one-particle one-hole (1p-1h) uncorrelated single-particle excitations which have the same energy as the collective mode is called *Landau damping*, just as the decay in bulk metals of the bulk plasmon into 1p-1h pairs [BB94, NP99]. The associated linewidth was first calculated using linear response theory [Kub57] and the fluctuation-dissipation theorem [CL00] in [KK66, BS89], and can also be obtained applying Fermi's Golden Rule with the coupling hamiltonian in (6.15), [WMWJ05]

$$\gamma = 2\pi\Lambda^2 \sum_{ph} |d_{ph}|^2 \delta(\hbar\omega_M - \varepsilon_p + \varepsilon_h)\,, \tag{6.18}$$

where $|p\rangle$ and $|h\rangle$ represent, respectively, particle and hole states of the mean-field problem. The result renders a plasmon linewidth with a characteristic $\gamma(a) \sim 1/a$ dependence, observed in experiments as shown in fig. (6.2):

$$\gamma(a) = \frac{3v_{\rm F}}{4a} g_0\left(\frac{\varepsilon_{\rm F}}{\hbar\omega_{\rm M}}\right)\,, \tag{6.19}$$

with $\varepsilon_{\rm F} = \hbar^2 k_{\rm F}^2/2m_{\rm e}$ and $v_{\rm F}$ the Fermi energy and velocity, respectively. The monotonically increasing function g_0 is defined as

$$\begin{aligned} g_0(x) = \frac{1}{12x^2}\Big\{ &\sqrt{x(x+1)}\big(4x(x+1)+3\big) - 3(2x+1)\ln\Big(\sqrt{x}+\sqrt{x+1}\Big) \\ &- \Big[\sqrt{x(x-1)}\big(4x(x-1)+3\big) - 3(2x-1)\ln\big(\sqrt{x}+\sqrt{x-1}\big)\Big]\Theta(x-1)\Big\}\,, \end{aligned} \tag{6.20}$$

$\Theta(x)$ being the Heaviside step function. It is very well approximated by

$$\tilde{g}_0(x) = (1 + (225x/64)^2)^{-1/4} \tag{6.21}$$

In the most interesting size range 0.5 nm$\leq a \leq$ 10 nm, where the transition from atomic to bulk behavior of physical properties takes place, the Landau damping mechanism dominates, limiting the lifetime of the collective excitation.

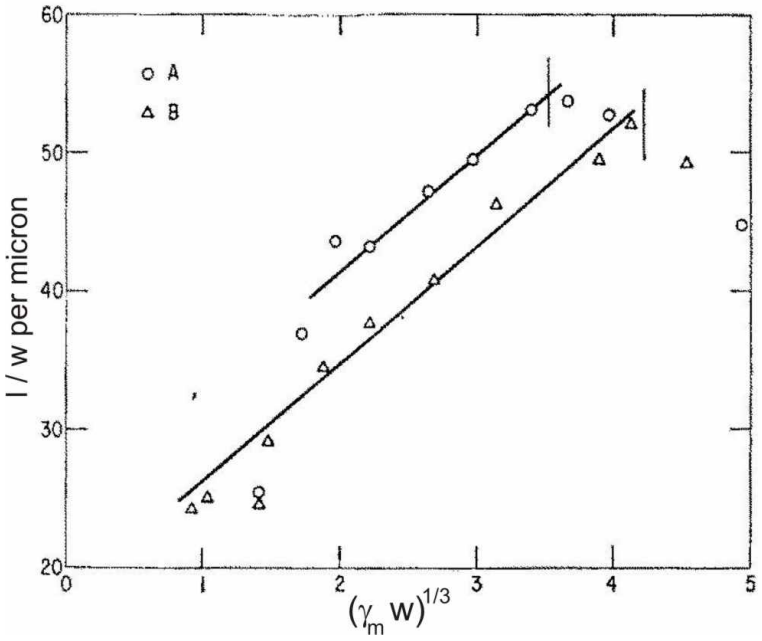

Figure 6.2: From [Dor65]. Experimental results for the inverse surface plasmon linewidth of silver nanoparticles embedded in a glass matrix. The quantity represented on the abscissa is proportional to the radius a of the nanoparticles (between $\sim$4 and 10 nm), while the vertical axis shows the inverse of the linewidth, $\tau = \gamma^{-1}$. It clearly demonstrates the linear size-scaling of the surface plasmon lifetime. The circles and triangles correspond to two different samples.

For large clusters, $a \geq 10$ nm, *radiation damping* due to the interaction of the surface plasmon with the external electromagnetic field dominates our mode's attenuation [KV95]. The lifetime associated to this mechanism can be shown to scale with size as $\gamma_{rad} \sim a^3$ [KK66], explaining why it is dominant for large clusters, becoming negligible for smaller ones in comparison with the Landau damping, who presents a weaker dependence of γ on a. For radii smaller than 0.5 nm the interaction with the ionic background becomes dominant, and the jellium model no longer provides a useful description. We will focus our attention in this thesis in the size range where Landau damping dominates.

6.3.2 Landau damping and the double-counting problem

The final form of the hamiltonian (6.15) is an *almost* perfect starting point for the description of the surface plasmon dynamics, in particular to address the Landau damping mechanism, with the plasmon (center-of-mass) degree of freedom coupled through H_c to the single-particle excitations, which can be viewed as a dissipative

environment for the plasmon. If the bosonic operator $b^\dagger$ and the fermionic operators $c_\alpha^\dagger$ corresponded to well-defined, independent degrees of freedom, one could proceed without further considerations to calculate for example perturbatively the effect of the relative coordinates on the plasmon lifetime, but as we have already noted, the final form of H_{rel} is obtained forgetting the fact that there are not N but $N-1$ independent relative coordinates. Thus, it seems that from N original degrees of freedom in (6.1) we have arrived at $N+1$ after the mean-field approximation and second quantization procedure, double-counting in some way the plasmon degree of freedom in H_{rel}. From the point of view of the study of the plasmon dissipative dynamics, this spoils the virtues of our approximate hamiltonian (6.15), as we have to guarantee that the environment to which we couple our system does not include our system.

Fortunately, previous knowledge coming from a related problem of nuclear physics, the description of the *giant dipolar resonance* of nuclei [RS80, YDG82], gives a hint on how to circumvent this inconsistency. This nuclear resonance corresponds to a collective motion of the (charged) protons with respect to the (neutral) neutrons, when an external electromagnetic field is applied, analogously to what happens in metallic clusters. Using a slightly different approach to obtain the approximate eigenstates of the nuclei, it was shown that the collective state is to a very good approximation a linear superposition of low-energy 1p-1h excitations of the Hartree-Fock ground state. The restriction to this kind of excitation, neglecting multiple p-h states, is a good approximation to describe the low energy physics of the system. The 1p-1h excitations are not true eigenstates due to the non-Hartree-Fock part of the Coulomb interaction, named residual interaction, which mixes them giving rise to more realistic eigenstates of the system, most of which are very similar to the ones obtained at the Hartree-Fock level, except for one linear combination, whose high energy lies *outside* the low-energy sector where its 1p-1h constituents are located, and which corresponds to the collective resonance. We will give a detailed derivation of these results in the following section.

The surface plasmon is thus basically originated from a combination of low-energy one-particle mean-field states, showing up when the Coulomb interaction is included in its full complexity. Coming back to the description of its dynamics, if we want to calculate its Landau damping, keeping a clear separation between the surface plasmon and the degrees of freedom constituting its dissipative environment, the previous results suggest the following two-step procedure [YDG82, YB92]:

1. Divide the Hilbert space spanned by the 1p-1h Hartree-Fock states into a low-energy (called restricted subspace, S_R) and a high energy (called additional subspace, S_A) subspaces. Introduce now the residual interaction in S_R, and obtain the eigenstates, one of whom will be the surface plasmon, having an energy lying in S_A.

2. To calculate the lifetime of the surface plasmon due to Landau damping, just

apply Fermi's Golden Rule using the residual interaction coupling the plasmon to the quasi-continuum of states in S_A degenerate with it.

In the context of the calculation of Landau damping using (6.1), the residual interaction is given by H_c, and to avoid the mixing of the surface plasmon and what we consider its environment, we just have to determine a safe energy cutoff $\Delta\epsilon_c$ below the surface plasmon frequency ω_{pl} such that (i) the value of ω_{pl} is insensitive to the increase of $\Delta\epsilon_c$, showing that the relevant low-energy Hartree-Fock 1p-1h excitations building up the surface plasmon lie below it, and (ii) only 1p-1h excitations above $\Delta\epsilon_c$, which can be thus regarded as belonging to a subspace independent of the surface plasmon, are included in Fermi's Golden Rule sum. The latter excitations are by definition S_A, so that the linewidth has an expression

$$\gamma \propto \sum_{ph\in S_A} |\langle p|z|h\rangle|^2 \delta(\hbar\omega_{pl} - \epsilon_p + \epsilon_h) \tag{6.22}$$

Here ph is a particle-hole excitation composed of a particle with energy ϵ_p and a hole with energy ϵ_h. In this calculation of γ the concrete estimate for the value of $\Delta\epsilon_c$ is irrelevant as long as $\Delta\epsilon_c < \omega_{pl}$ [YB92], but the approximate theoretical description of other physical quantities might depend on the cutoff. For example, if one uses (6.15) to study the decay and decoherence of the surface plasmon, the timescales that characterize the dynamics of the electronic environment in S_A [WIWJ07] depend on the cutoff energy. Moreover, it has been shown in [WIJW06] that the environment-induced redshift of the resonance frequency depends logarithmically on the cutoff.

We will in the following section derive an estimate for this cutoff based on sound physical arguments.

6.4 The surface plasmon as a superposition of low-energy particle-hole excitations

To show this fact and find an estimate for $\Delta\epsilon_c$ we will forget in this section about the model based in a separation of center-of-mass plus relative coordinates described in the beginning of previous section, whose main result was eq. (6.15), and use instead the approach borrowed from the description of giant dipolar resonances in nuclei which has already been briefly introduced.

6.4.1 Separable interaction ansatz

We now obtain the simplest model which starting from a mean-field approach includes the essential features of the Coulomb interaction originating the surface plasmon. The starting point is the simplest, mean-field approximation of the hamiltonian

(6.1), where the one-body electronic states obtained come from a self-consistent calculation like the TDLDA one (fig. 6.1). The problem with this naive approximation is that it fails to describe the ability of the Coulomb interaction to create self-sustained collective excitations, like the surface plasmon we want to study. We have to introduce an additional component $\delta V(r)$ to the self-consistent potential $V(r)$ which captures this feature of the Coulomb interaction. To obtain $\delta V(r)$, we recall the fact that the occurrence of collective vibrational modes in a system governed by independent-particle motion can be understood in terms of the variations in the average one-body potential produced by an oscillation in the nanoparticle electronic density. Such variations in the one-particle potential give rise to excitations in the electronic motion, and a self-sustained collective motion is obtained if the induced density variations are equal to those needed to generate the oscillating potential [BB75].

In our case, from the several collective modes susceptible of appearing in our system we focus our attention on the simplest, dipolar in character, surface plasmon. Starting from the knowledge of the existence of such a mode, the procedure to obtain the associated $\delta V(r)$ is then straightforward: calculate the variation in the average one-body potential $V(r)$ produced by an electronic density variation $\delta n(\mathbf{r})$ linked to the excitation of the collective mode. This was done in [WMWJ05], as follows:

Assuming that at equilibrium the electron density is uniform within a sphere of radius a, $n_e(r) = n_e\Theta(a-r)$, a rigid displacement with a magnitude Z along the z-direction changes the density at $\mathbf{r}$ from $n_e(\mathbf{r})$ to $n_e(\mathbf{r}-\mathbf{R}) = n_e(\mathbf{r}) + \delta n_e(\mathbf{r})$. To first order in the field $\mathbf{R} = Z\mathbf{e}_z$, $\delta n_e(\mathbf{r}) = -\mathbf{R}\cdot\nabla n_e(\mathbf{r}) = Zn_e\cos(\theta)\delta(r-a)$, where $\theta = \arccos(\mathbf{r}\cdot\mathbf{e}_z/|\mathbf{r}|)$. The related change in the mean-field potential seen by the electrons is thus

$$\delta V(\mathbf{r},\mathbf{R}) = \int d^3\mathbf{r}'\delta n_e(\mathbf{r}')V_C(\mathbf{r},\mathbf{r}') \tag{6.23}$$

where $V_C(\mathbf{r},\mathbf{r}')$ denotes the Coulomb interaction between electrons. The term δH which has to be added to the mean-field hamiltonian (6.11) is then

$$\delta H = \sum_{i=1}^{N}\delta V(\mathbf{R},\mathbf{r}_i') \tag{6.24}$$

A simple expression for $\delta V(\mathbf{r},\mathbf{R})$ can be obtained, given the spherical symmetry of the problem, using a multipolar decomposition for the Coulomb interaction [Jac75], namely

$$\delta V(\mathbf{r},\mathbf{R}) = Z\frac{4\pi n_e e^2}{3}\left[z\Theta(a-r) + \frac{za^3}{r^3}\Theta(r-a)\right], \tag{6.25}$$

so $\delta V(\mathbf{r},\mathbf{R})$ is actually the same as $\mathbf{R}\cdot\nabla U(r)$, eq.(6.4). A further simplification is obtained if we remember that, even though the electronic wavefunctions spread outside the geometrical boundaries of the nanocluster, giving rise to small quantum corrections like the spill-out effect, the expected influence of the exact form of $\delta V(\mathbf{r},\mathbf{R})$

for $r > a$ is very small. We can then simplify δV by extending its dipolar character also for $r > a$, $\delta V(\mathbf{r}, \mathbf{R}) \approx (4\pi n_e e^2/3) Z \cdot z$, with a resulting *separable form* for δH

$$\delta H \approx \frac{1}{2N} \frac{4\pi n_e e^2}{3} \sum_{ij}^{N} z_i z_j \tag{6.26}$$

where $Z = \sum_i^N z_i/N$ has been used. The term separable applies to those interactions satisfying $V(x_i, x_j) \sim f(x_i) \cdot f(x_j)$, $f(x)$ being a generic function of x, like (6.26). The results that would be obtained without the use of this approximation would include $1/N$ corrections to the ones we will present, like the estimate for $\Delta\epsilon_c$, so for our purposes we can work using the separable ansatz. Expressed in terms of the mean-field hamiltonian basis $|\alpha\rangle$, the second-quantized version of (6.26) reads

$$\delta H = \sum_{\alpha\beta\gamma\delta} \lambda d_{\alpha\gamma} d^*_{\delta\beta} c^\dagger_\alpha c^\dagger_\beta c_\delta c_\gamma \,, \tag{6.27}$$

where $d_{\alpha\gamma} = \langle\alpha|z|\gamma\rangle$ are dipole matrix elements and λ is a positive constant.

6.4.2 Linear response theory and Random Phase Approximation for the surface plasmon

We will analyze the response of the nanocluster to a time-dependent weak external perturbation, and obtain this response in a self-consistent way, leading to the RPA theory of response. The result will be written in terms of a response function, yet to be defined, whose poles determine the energies of the excited states. We will particularize to the separable potential of the dipolar field (6.27), and see what are its effects on the energies of the self-consistent mean-field states. We will obtain a secular equation for those RPA eigenenergies, and show how to solve it graphically.

We follow [BB94] and [RS80]. Suppose we know the stationary one-particle eigenstates $|i\rangle$ and eigenenergies e_i of the mean-field, time-independent hamiltonian (6.11), and now introduce a time-dependent external perturbation $V_x(\tilde{\mathbf{r}}, t) = V_x(\tilde{\mathbf{r}}) e^{i\omega t}$ of a given frequency ω, interacting with the system through its particle density $n(\tilde{\mathbf{r}})$,

$$H_{int}(t) = \int d\tilde{\mathbf{r}} V_x(\tilde{\mathbf{r}}, t) n(\tilde{\mathbf{r}}) \tag{6.28}$$

Then, the correction to the eigenstates of the system is, to first order in $H_{int}(t)$,

$$\phi'_i(t) = \Big[\phi_i + \frac{1}{2}\sum_j \langle j|V_x(\tilde{\mathbf{r}})|i\rangle \Big(\frac{e^{i\omega t}}{e_i - e_j - \hbar\omega} + \frac{e^{-i\omega t}}{e_i - e_j + \hbar\omega} \Big) \Big] e^{-ie_i t/\hbar} \,, \tag{6.29}$$

where ϕ_i is the single-particle wave function of state $|i\rangle$. The particle density becomes now $n(\tilde{\mathbf{r}},t)=\sum_i^{occ}|\phi_i'(\tilde{\mathbf{r}},t)|^2=n_0(\tilde{\mathbf{r}})+\delta n(\tilde{\mathbf{r}})e^{i\omega t}$, with

$$\delta n(\tilde{\mathbf{r}})=\sum_i^{occ}\sum_j\langle j|V_x(\tilde{\mathbf{r}})|i\rangle\langle i|n(\tilde{\mathbf{r}})|j\rangle\Big(\frac{1}{e_i-e_j-\hbar\omega}+\frac{1}{e_i-e_j+\hbar\omega}\Big). \tag{6.30}$$

We now define the independent particle retarded response function R^0 for the density change at $\tilde{\mathbf{r}}$ induced by a potential field at $\tilde{\mathbf{r}}'$, as

$$R^0(\tilde{\mathbf{r}},\tilde{\mathbf{r}}',\omega)=\sum_i^{occ}\sum_j\langle j|n(\tilde{\mathbf{r}})|i\rangle\langle i|n(\tilde{\mathbf{r}}')|j\rangle\Big(\frac{1}{e_i-e_j-\hbar\omega}+\frac{1}{e_i-e_j+\hbar\omega}\Big), \tag{6.31}$$

In terms of R^0, the response to an arbitrary perturbation potential can be calculated from the integral,

$$\delta n(\tilde{\mathbf{r}},\omega)=\int d\tilde{\mathbf{r}}'R^0(\tilde{\mathbf{r}},\tilde{\mathbf{r}}',\omega)V_x(\tilde{\mathbf{r}}'). \tag{6.32}$$

This is the independent particle response, but one more ingredient has to be included to construct the RPA theory of response. So far the only perturbation was the external field, but it is clear that the induced density oscillation $\delta n(\tilde{\mathbf{r}},\omega)$ will cause the self-consistent field to oscillate at the same frequency as well. We can define the change of the mean-field potential with respect to small density changes in terms of the functional derivative $\delta V(\tilde{\mathbf{r}})/\delta n(\tilde{\mathbf{r}}')$.In the case of an external long-wavelength field we have seen that the main modification to the mean-field potential is the presence of a dipolar electric field, described in (6.27). In terms of $\delta V(\tilde{\mathbf{r}})/\delta n(\tilde{\mathbf{r}}')$ the time-varying mean field is then

$$\delta V(\tilde{\mathbf{r}})=\int d\tilde{\mathbf{r}}'\frac{\delta V(\tilde{\mathbf{r}})}{\delta n(\tilde{\mathbf{r}}')}\delta n(\tilde{\mathbf{r}}') \tag{6.33}$$

Adding this potential to the external potential, we obtain the implicit equation for the self-consistent density,

$$\delta n_{RPA}(\tilde{\mathbf{r}},\omega)=\int d\tilde{\mathbf{r}}R^0(\tilde{\mathbf{r}},\tilde{\mathbf{r}}_2,\omega)\Big\{V_x(\tilde{\mathbf{r}}_2)+\int d\tilde{\mathbf{r}}'\frac{\delta V(\tilde{\mathbf{r}}_2)}{\delta n(\tilde{\mathbf{r}}')}\delta n_{RPA}(\tilde{\mathbf{r}}')\Big\} \tag{6.34}$$

It is more useful to express the self-consistent density in terms of the external field, defining in this way the RPA response function R^{RPA} (we will always work with retarded response functions, so it will be assumed in the following, and not mentioned explicitly as "retarded"),

$$\delta n_{RPA}(\tilde{\mathbf{r}},\omega)=\int d\tilde{\mathbf{r}}'R^{RPA}(\tilde{\mathbf{r}},\tilde{\mathbf{r}}',\omega)V_x(\tilde{\mathbf{r}}')\,. \tag{6.35}$$

From (6.34) and (6.35) follows the implicit equation that the RPA response function must satisfy:

$$R^{RPA}(\tilde{\mathbf{r}},\tilde{\mathbf{r}}',\omega)=R^0(\tilde{\mathbf{r}},\tilde{\mathbf{r}}',\omega)+\int d\tilde{\mathbf{r}}_2d\tilde{\mathbf{r}}_3R^0(\tilde{\mathbf{r}},\tilde{\mathbf{r}}_2,\omega)\frac{\delta V(\tilde{\mathbf{r}}_2)}{\delta n(\tilde{\mathbf{r}}_3)}R^{RPA}(\tilde{\mathbf{r}}_3,\tilde{\mathbf{r}}',\omega) \tag{6.36}$$

If the external perturbation were static, $\omega = 0$, equations (6.34) and (6.36) reduce simply to the Hartree-Fock self-consistent solution to the problem, where the occupied eigenstates contribute to the total effective one-body potential in the hamiltonian, which in turn changes the occupied wavefunctions, starting a cycle that ends when selfconsistency between eigenfunctions and total potential is reached. The RPA approximation is therefore nothing but the small amplitude limit of the time-dependent mean field approach.

The next step is to repeat the linear response calculations, imposing again (i)a self-consistent mean field approach for the total hamiltonian and (ii)small amplitude limit for the perturbation, but working in the basis and language in which (6.27) is written. The derivation of the response becomes much more tedious and lengthy (see e.g. [RS80, BB94]), so we will state here the main points and results, the latter being very similar in structure to those we have obtained:

Take the creation and destruction operators $c_\alpha^\dagger$ and c_α of the mean-field states of the unperturbed hamiltonian. The external perturbation is chosen to be a one-body operator, $V_x(t) = V_x e^{-i\omega t} + V_x^\dagger e^{i\omega t} = \sum_{kl} v_{kl}(t) c_k^\dagger c_l$. As also the rest of operators in the hamiltonian will be approximated to self-consistent one-body operators, one assumes

- First, that the ground state wavefunction $|\mathrm{RPA(t)}\rangle$ at any time is a Slater determinant, imposing in this way selfconsistency.
- Second, one assumes that the external field $V_x(t)$ is weak, introducing only small perturbations around the stationary Hartree-Fock ground state $|\mathrm{HF}\rangle$ of the unperturbed hamiltonian, $|\mathrm{RPA(t)}\rangle = |\mathrm{HF}\rangle + \delta|\psi(\mathrm{t})\rangle$.

The combination of Slater-determinant sort of solution plus small perturbations with respect to $|\mathrm{HF}\rangle$ limits automatically the Hilbert space out of which $|\mathrm{RPA(t)}\rangle$ is constructed, to the stationary Hartree-Fock ground state $|\mathrm{HF}\rangle$ plus the set of all its 1p-1h excitations $c_p^\dagger c_q|\mathrm{HF}\rangle$ (c_q annihilates an occupied one-particle state of $|\mathrm{HF}\rangle$, while $c_p^\dagger$ populates a previously empty one-particle state). This shows up in the so-called *spectral representation* of the RPA response function obtained

$$R^{RPA}_{pqp'q'}(\omega) = \sum_{i>0}\Big(\frac{\langle 0|c_q^\dagger c_p|i\rangle\langle i|c_{p'}^\dagger c_{q'}|0\rangle}{\hbar\omega - \epsilon_i + \epsilon_0} - \frac{\langle 0|c_{p'}^\dagger c_{q'}|i\rangle\langle i|c_q^\dagger c_p|0\rangle}{\hbar\omega + \epsilon_i - \epsilon_0}\Big)\,, \tag{6.37}$$

where the index pairs pq and $p'q'$ run only over particle-hole (ph) and hole-particle (hp) pairs, while all other matrix elements vanish in RPA order. Unsurprisingly, $R^{RPA}_{pqp'q'}$ satisfies an implicit equation analogous to (6.36),

$$R^{RPA}_{pqp'q'} = R^0_{pqp'q'} + \lambda \sum_{\substack{p_1q_1\\p_2q_2}} R^0_{pqp_1q_1} d_{p_1q_2} d^*_{p_2q_1} R^{RPA}_{p_2q_2p'q'} \tag{6.38}$$

In (6.38) we have introduced the spectral representation $R^0_{pqp'q'}$ of the response function of the free system,

$$R^0_{pqp'q'}(\omega) = \delta_{pp'}\delta_{qq'}\frac{\sum_{i>0}|\langle i|c_p^\dagger c_q|0\rangle|^2 - |\langle i|c_q^\dagger c_p|0\rangle|^2}{\hbar\omega - \epsilon_p + \epsilon_q}\,, \tag{6.39}$$

and we have also particularized to our case, where $V_x(t)$ is the dipolar field represented by the corresponding operator (6.27). Thanks to the separable form of the interaction, we can proceed further with (6.38) to get

$$R^{RPA}(\omega) = R^0(\omega)[1 + \lambda R^{RPA}(\omega)] \;\;\rightarrow\;\; R^{RPA}(\omega) = \frac{R^0(\omega)}{1 - \lambda R^0(\omega)} \tag{6.40}$$

with

$$R^0(\omega) = \sum_{pqp'q'} d^*_{pq} R^0_{pqp'q'} d_{p'q'} = \sum_{ph} |d_{ph}|^2 \Big(\frac{1}{\hbar\omega - \epsilon_p + \epsilon_h} - \frac{1}{\hbar\omega + \epsilon_p - \epsilon_h}\Big) \tag{6.41}$$

The last sum runs over 1p-1h states, $|ph\rangle$, whose energy with respect to the RPA ground state is $\Delta\varepsilon_{ph} = \epsilon_p - \epsilon_h$. The poles of $R^{RPA}(\omega)$ give the excitation energies E we are looking for, which are thus defined by the secular equation

$$\boxed{\frac{1}{\lambda} = \mathcal{S}(E)} \tag{6.42}$$

Here we have defined the RPA sum

$$\mathcal{S}(E) = \sum_{ph} \frac{2\Delta\varepsilon_{ph}|d_{ph}|^2}{E^2 - \Delta\varepsilon_{ph}^2}\,. \tag{6.43}$$

Nuclear physics textbooks (see, e.g., Ref. [RS80]) show how to solve the secular equation (6.42) graphically under the implicit assumption that the p-h spectrum is bounded in energy. Basically one plots $\mathcal{S}(E)$ and a horizontal line at the ordinate value $y = 1/\lambda$. The intersections of $\mathcal{S}(E)$ with the horizontal line give the solutions E, which turn out to be merely small renormalizations of the p-h energies $\Delta\varepsilon_{ph}$ except for the largest excitation energy ε_{pl} which corresponds to the collective mode, see fig.(6.3) for a schematic example. This state is nothing but the surface plasmon collective state. In fig.(6.3b-c) it shows how ε_{pl} is a function mostly of the initial low-energy 1p-1h excitations, depending only slightly on the high-energy ones, for a decaying dipole matrix element $d_{ph} \sim 1/\Delta\varepsilon_{ph}^2$. This decaying behavior will be demonstrated in next subsection, ensuring also the applicability of this schematic picture even though in a metallic cluster the p-h excitations are not bounded from above on the scale of the plasma energy.

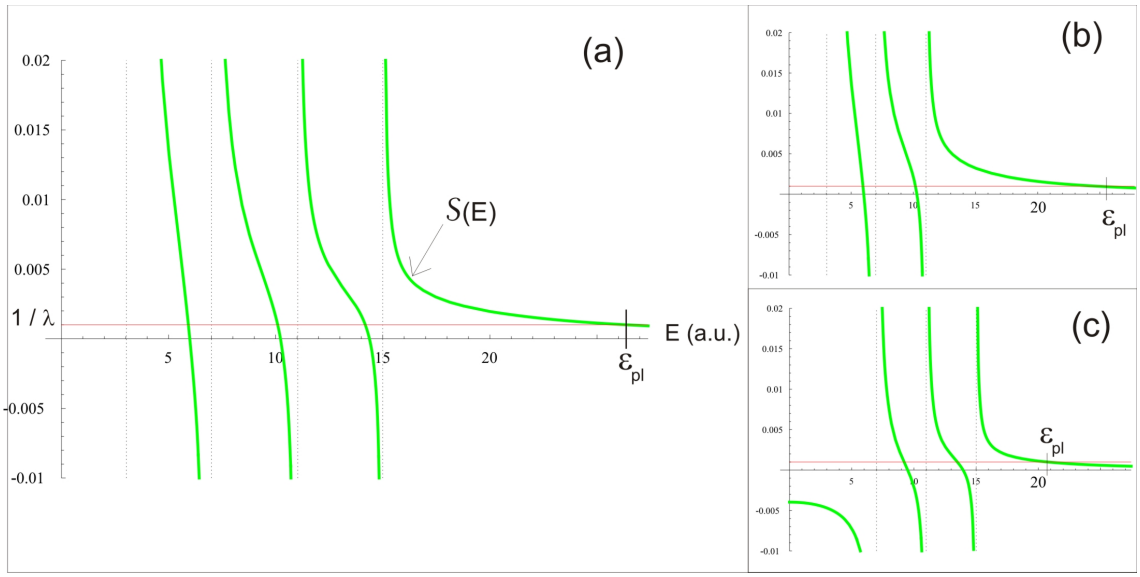

Figure 6.3: (a) Schematic example of the graphical solution of a secular equation of the kind (6.42). In this case the dipole matrix elements are assumed to have a dependence with $\Delta\varepsilon_{ph}$, $d_{ph} \sim 1/\Delta\varepsilon_{ph}^2$, which corresponds to the realistic case of metallic clusters. $1/\lambda$ is chosen to be $1/\lambda = 0.002$ (arbitrary units), while the sum includes only 4 1p-1h excitations, whose excitations energies in absence of the dipolar residual interaction (6.27) are $\Delta\varepsilon_{ph} = 3, 7, 11, 15$ (arbitrary units): $\mathcal{S}(E) = (1/3)/(E^2 - 3^2) + (1/7)/(E^2 - 7^2) + (1/11)/(E^2 - 11^2) + (1/15)/(E^2 - 15^2)$. Due to the residual interaction the eigenstates and eigenenergies change, with the new excitation eigenenergies E given by the crossing points where $\mathcal{S}(E) = 1/\lambda$. The highest excitation energy corresponds to the surface plasmon collective mode, ε_{pl}. (b) and (c) reflect the influence of high and low 1p-1h excitations in the value of ε_{pl}, respectively; in (b) $\Delta\varepsilon_{ph} = 15$ is absent, causing a slight shift of the surface plasmon energy ε_{pl}, while in (c) $\Delta\varepsilon_{ph} = 3$ is absent, resulting in a strong shift of ε_{pl}. This points to the predominant role of low-energy p-h excitations in the formation of the collective mode.

6.4.3 Fast decay of d_{ph}. Plasmon state built from low-energy p-h excitations

The secular equation (6.42) depends crucially on the form of the dipole matrix element d_{ph}. We will show now more rigorously that due to its fast decay $d_{ph}(\Delta\varepsilon) \sim 1/\Delta\varepsilon^2$, cf. eq. (6.57), the plasmon excitation energy depends only on the lowest 1p-1h excitations. Assuming that the p-h states are confined within a hard-wall sphere, one can calculate d_{ph}, see Appendix D.1 for a detailed derivation. d_{ph} is factorized into

radial and angular parts [YB92]

$$d_{ph} = \mathcal{A}_{l_p l_h}^{m_p m_h} \mathcal{R}_{l_p l_h}(\varepsilon_p, \varepsilon_h)\,. \tag{6.44}$$

The angular part is expressed in terms of Wigner-3j symbols as

$$\mathcal{A}_{l_p l_h}^{m_p m_h} = (-1)^{m_p}\sqrt{(2l_p+1)(2l_h+1)} \times \begin{pmatrix} l_p & l_h & 1 \\ 0 & 0 & 0 \end{pmatrix} \begin{pmatrix} l_p & l_h & 1 \\ -m_p & m_h & 0 \end{pmatrix} \tag{6.45}$$

and sets the selection rules for the total and azimuthal angular momenta, respectively:

$$l_p = l_h \pm 1 \quad , \quad m_p = m_h \tag{6.46}$$

The radial part depends on the energies of the p-h states as

$$\mathcal{R}_{l_p l_h}(\varepsilon_p, \varepsilon_h) = \frac{2\hbar^2}{m_{\mathrm{e}} a} \frac{\sqrt{\varepsilon_p \varepsilon_h}}{\Delta\varepsilon_{ph}^2}\,. \tag{6.47}$$

With the help of equations (6.44)–(6.47) and using the aforementioned dipole selection rules (6.46), we can write the RPA sum (6.43) as

$$\mathcal{S}(E) = \frac{32 k_{\mathrm{F}}^{-2}}{3} \left(\frac{\varepsilon_{\mathrm{F}}}{k_{\mathrm{F}} a}\right)^2 \sum_{\substack{n_h, l_h \\ n_p, l_p = l_h \pm 1}} f_{l_p} \frac{\varepsilon_p \varepsilon_h}{(E^2 - \Delta\varepsilon_{ph}^2)\Delta\varepsilon_{ph}^3}\,, \tag{6.48}$$

where n_h and n_p are radial quantum numbers. We have defined $f_{l_p} = l_h + 1$ if $l_p = l_h + 1$ and $f_{l_p} = l_h$ if $l_p = l_h - 1$. Using the semiclassical quantizations (D.24) and (D.25) of Appendix D.2, we finally obtain the result shown in Figure 6.4.

In the figure we show (solid black line) the resulting E-dependence of (6.48). The crossings of this curve with the horizontal dotted one with height $1/\lambda$ yield the excitation spectrum within the RPA. The lowest p-h energy estimated in Appendix D.2 is

$$\Delta\varepsilon_{\min} \simeq \frac{\varepsilon_{\mathrm{F}}}{k_{\mathrm{F}} a/\pi}\,. \tag{6.49}$$

The existence of a gap in the excitation spectrum of the dipole operator stems from the quantization of the states in a hard-wall sphere and the dipole selection rules. Whenever the energy E coincides with a p-h excitation energy $\Delta\varepsilon_{ph}$, we have a divergence in $\mathcal{S}(E)$ (see vertical grey lines in Fig. 6.4). For the lowest energies E of the interval considered the sum is dominated by the term associated with the divergence closest to E. On the other hand, for the largest energies E, the fast decay of d_{ph} with $\Delta\varepsilon_{ph}$ means that the divergences are only relevant for energies extremely close to them. Away from the divergences the sum is dominated by the contributions arising from the low-energy p-h excitations.

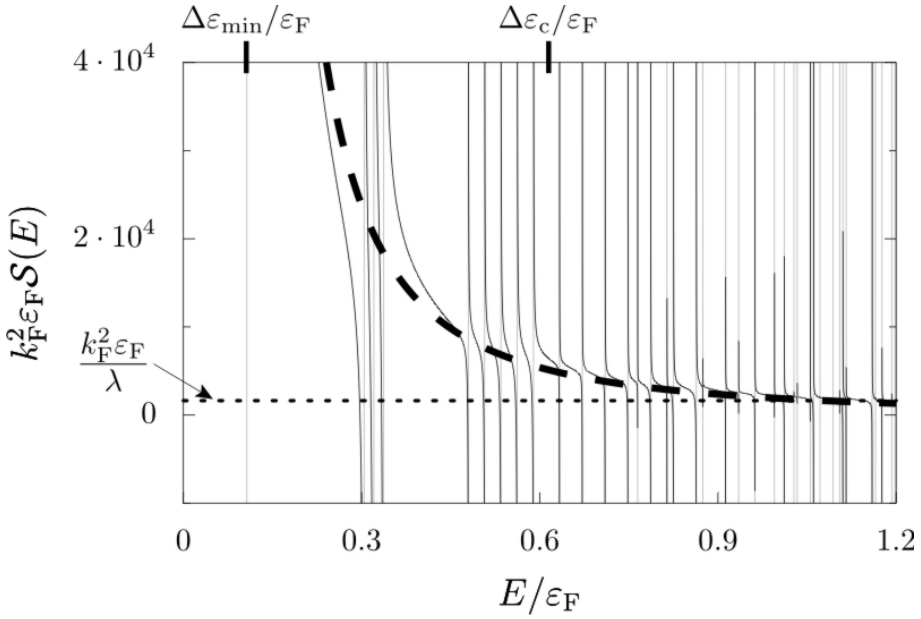

Figure 6.4: RPA sum (6.48) for a Na nanoparticle with $k_{\rm F}a = 30$ (solid black line). The p-h excitation energies $\Delta\varepsilon_{ph}$ (represented by vertical grey lines) have been obtained from the semiclassical spectrum (D.25). There are about 15000 degenerate excitations in the interval shown, and the smallest excitation $\Delta\varepsilon_{\rm min} \simeq \varepsilon_{\rm F}/10$ has a degeneracy $\mathcal{N} = 380$. The dashed line takes only into account the contribution of $\Delta\varepsilon_{\rm min}$ (see Eq. (6.60)). The cutoff energy $\Delta\varepsilon_{\rm c}$ separating the two RPA subspaces is also shown in the figure (see Eq. (6.66)). Above $\Delta\varepsilon_{\rm c}$ the two sums are close to each other, showing that for high energies the RPA sum is essentially given by the contributions coming from the low-energy p-h excitations. The horizontal dotted line indicates the position of the coupling constant λ entering the RPA secular equation (6.42), according to the estimate (6.61).

To gain physical insight and proceed further in the analysis of the electron dynamics in metallic nanoparticles, we introduce the typical dipole matrix element for states separated by a given energy difference $\Delta\varepsilon$,

$$d^{\text{p-h}}(\Delta\varepsilon) = \left[\frac{1}{\rho^{\text{p-h}}(\Delta\varepsilon)}\sum_{ph}|d_{ph}|^2\delta(\Delta\varepsilon-\Delta\varepsilon_{ph})\right]^{1/2} = \left[\frac{1}{\rho^{\text{p-h}}(\Delta\varepsilon)}\int_{\varepsilon_{\rm F}-\Delta\varepsilon}^{\varepsilon_{\rm F}}{\rm d}\varepsilon\,\mathcal{C}(\varepsilon,\Delta\varepsilon)\right]^{1/2}. \tag{6.50}$$

Here, we have introduced two quantities, $\rho^{\text{p-h}}(\Delta\varepsilon)$ and $\mathcal{C}(\varepsilon,\Delta\varepsilon)$. $\mathcal{C}(\varepsilon,\Delta\varepsilon)$ is the local density of dipole matrix elements

$$\mathcal{C}(\varepsilon,\Delta\varepsilon) = \sum_{ph}|d_{ph}|^2\delta(\varepsilon-\varepsilon_h)\delta(\varepsilon+\Delta\varepsilon-\varepsilon_p)\,. \tag{6.51}$$

As shown in Appendix D.4, this can be expressed as

$$\mathcal{C}(\varepsilon, \Delta\varepsilon) = \frac{1}{3\pi^2}\frac{a^2}{\Delta\varepsilon^2} F\left(\frac{\varepsilon}{\Delta\varepsilon}\right) , \tag{6.52}$$

where

$$F(x) = (2x+1)\sqrt{x(x+1)} - \ln\left(\sqrt{x} + \sqrt{x+1}\right) . \tag{6.53}$$

For $\Delta\varepsilon \ll \varepsilon$, equation (6.52) simplifies to

$$\mathcal{C}(\varepsilon, \Delta\varepsilon) \simeq \frac{2a^2}{3\pi^2}\frac{\varepsilon^2}{\Delta\varepsilon^4} . \tag{6.54}$$

In expression (6.50),

$$\rho^{\text{p-h}}(\Delta\varepsilon) = \sum_{ph} \delta(\Delta\varepsilon_{ph} - \Delta\varepsilon)\delta_{l_h, l_p \pm 1}\delta_{m_h, m_p} \tag{6.55}$$

is the density of p-h excitations with energy $\Delta\varepsilon$ respecting the dipole selection rules. In order to simplify the presentation, we do not consider spin degeneracy factors. In Appendix D.5 we show that for $\Delta\varepsilon \ll \varepsilon_{\text{F}}$ we have

$$\rho^{\text{p-h}}(\Delta\varepsilon) \simeq \frac{(k_{\text{F}}a)^4}{4\pi^2}\frac{\Delta\varepsilon}{\varepsilon_{\text{F}}^2} , \tag{6.56}$$

and therefore in such a limit the typical matrix element (6.50) can be approximated by

$$\boxed{d^{\text{p-h}}(\Delta\varepsilon) \simeq \frac{2\sqrt{2}k_{\text{F}}^{-1}}{\sqrt{3}k_{\text{F}}a}\left(\frac{\varepsilon_{\text{F}}}{\Delta\varepsilon}\right)^2} . \tag{6.57}$$

To check the validity of our estimate of the typical dipole matrix element, there is an *exact* sum rule $\sum_{ph}\Delta\varepsilon_{ph}|d^{\text{p-h}}|^2 = (3/4\pi)\hbar^2 N/2m_{\text{e}}$ [LS91, YB92], satisfied also in the presence of Coulomb interactions between electrons. Performing the sum using (6.57)

$$\sum_{ph}^{E_F} \Delta\varepsilon_{ph}|d^{\text{p-h}}(\Delta\varepsilon)|^2 \simeq \int_{\Delta\epsilon_{min}}^{E_F} d\Delta\varepsilon\Delta\varepsilon\Big[\int_{E_F-\Delta\varepsilon}^{E_F} d\varepsilon C(\varepsilon, \Delta\varepsilon)\Big] \tag{6.58}$$

one obtains about 70% of the exact result $(3/4\pi)\hbar^2 N/2m_{\text{e}}$ [Bra93]. This is quite reasonable regarding all the approximations we made to obtain (6.57).

In order to emphasize once more the importance of the low-energy p-h excitations, we present in Figure 6.4 (dashed line) the contribution to the RPA sum coming only from the infrared p-h excitation energy with the appropriate degeneracy factor $\mathcal{N}$ (see Eq. (D.27) in App. D.2). Indeed, we can estimate (6.43) as

$$\mathcal{S}(E) \approx \mathcal{N} \times \frac{2\Delta\varepsilon_{\min}\left[d^{\text{p-h}}(\Delta\varepsilon_{\min})\right]^2}{E^2 - \Delta\varepsilon_{\min}^2} . \tag{6.59}$$

With the results (6.49), (6.57), and (D.27), we obtain

$$\mathcal{S}(E) \approx \frac{64 k_{\mathrm{F}}^{-2}}{3\pi^5} (k_{\mathrm{F}} a)^3 \frac{\varepsilon_{\mathrm{F}}}{E^2 - (\varepsilon_{\mathrm{F}} \pi / k_{\mathrm{F}} a)^2} \,. \tag{6.60}$$

While in the lower part of the energy interval in Figure 6.4 the two curves exhibit considerable discrepancies, in the second half of the interval they are very close (except of course at the divergences). Since the collective excitation is found in this last interval, we see that it is mainly the low-energy p-h excitations that are relevant for the definition of the collective excitation.

Since the resonance energy is known from experiments, we can obtain the value of the coupling constant λ. Indeed, using the estimate (6.60) evaluated at $E = \hbar\omega_{\mathrm{M}}$ in the secular equation (6.42), we obtain

$$\frac{1}{\lambda} \simeq \frac{64 k_{\mathrm{F}}^{-2}}{3\pi^5} (k_{\mathrm{F}} a)^3 \frac{\varepsilon_{\mathrm{F}}}{(\hbar\omega_{\mathrm{M}})^2} \tag{6.61}$$

to leading order in $k_{\mathrm{F}} a \gg 1$. Notice that this result is consistent with the estimate obtained from the energy-weighted sum rule given in [YB92]. For the case studied in Figure 6.4, our estimate (6.61) yields $k_{\mathrm{F}}^2 \varepsilon_{\mathrm{F}} / \lambda \approx 1600$. As the radius a increases the lowest p-h energy decreases like $1/a$, the degeneracy at this value increases as a^2, and the density of p-h excitations contributing to (6.43), $\rho^{\text{p-h}}(\Delta\varepsilon)$, grows as a^4. This increase in the number of excitations contributing to the sum is partially cancelled by the $1/a$ behaviour of the typical dipole matrix element, resulting in a decrease of the coupling constant λ proportional to the number of particles in the cluster, $\lambda \sim 1/a^3$, and a value of the plasmon frequency which remains almost unaffected. Therefore, for a larger nanoparticle size, the divergences shown in Figure 6.4 would be more dense in energy, starting at a lower energy, and the vertical scale would increase as a^3, thus obtaining a similar value for the plasmon excitation energy $\hbar\omega_{\mathrm{M}}$.

6.4.4 Separation of the reduced and additional particle-hole subspaces

As we have shown in the last section, the high-energy part of the p-h spectrum is not crucial for the determination of the energy of the collective excitation. In what follows we make this statement more quantitative and estimate the upper-bound cutoff $\Delta\varepsilon_{\mathrm{c}}$ of the low-energy excitations that we need in order to obtain a stable position of the surface plasmon.

In order to obtain a quantitative estimate of the cutoff, we require that by changing it from $\Delta\varepsilon_{\mathrm{c}}$ to $(3/2)\Delta\varepsilon_{\mathrm{c}}$, the position of the plasmon changes only by a fraction of its linewidth γ, the smallest energy scale with experimental significance. Our criterion leads to the condition

$$\mathcal{S}_{\Delta\varepsilon_{\mathrm{c}}}(\hbar\omega_{\mathrm{M}}) = \mathcal{S}_{\frac{3}{2}\Delta\varepsilon_{\mathrm{c}}}(\hbar\omega_{\mathrm{M}} + \hbar\gamma) \,, \tag{6.62}$$

with the RPA sum $\mathcal{S}$ that has been defined in (6.43). The additional subscript refers to the upper bound of the p-h energies.

The left-hand side of (6.62) can be estimated according to

$$\mathcal{S}_{\Delta\varepsilon_{\rm c}}(\hbar\omega_{\rm M}) \simeq \int_{\Delta\varepsilon_{\rm min}}^{\Delta\varepsilon_{\rm c}} {\rm d}\Delta\varepsilon\, \rho^{\text{p-h}}(\Delta\varepsilon) \frac{2\Delta\varepsilon \left[d^{\text{p-h}}(\Delta\varepsilon)\right]^2}{(\hbar\omega_{\rm M})^2 - \Delta\varepsilon^2}\,, \tag{6.63}$$

with $d^{\text{p-h}}$ and $\rho^{\text{p-h}}$ as defined in (6.50) and (6.55), respectively. Using (6.56) and (6.57), we obtain

$$\mathcal{S}_{\Delta\varepsilon_{\rm c}}(\hbar\omega_{\rm M}) \simeq \frac{4k_{\rm F}^{-2}}{3\pi^2} \left(k_{\rm F}a \frac{\varepsilon_{\rm F}}{\hbar\omega_{\rm M}}\right)^2 \left(\frac{1}{\Delta\varepsilon_{\rm min}} - \frac{1}{\Delta\varepsilon_{\rm c}}\right) \tag{6.64}$$

to leading order in $k_{\rm F}a$. Similarly,

$$\mathcal{S}_{\frac{3}{2}\Delta\varepsilon_{\rm c}}(\hbar\omega_{\rm M} + \hbar\gamma) \simeq \frac{4k_{\rm F}^{-2}}{3\pi^2} \left(k_{\rm F}a \frac{\varepsilon_{\rm F}}{\hbar\omega_{\rm M}}\right)^2 \left(1 - \frac{2\gamma}{\omega_{\rm M}}\right) \left(\frac{1}{\Delta\varepsilon_{\rm min}} - \frac{2}{3\Delta\varepsilon_{\rm c}}\right). \tag{6.65}$$

Using the expressions (6.19) and (6.49) for γ and $\Delta\varepsilon_{\rm min}$, respectively, finally yields according to the criterion (6.62) the main result of this chapter, an estimate for the cutoff energy based on sound physical arguments

$$\boxed{\Delta\varepsilon_{\rm c} \simeq \frac{\pi}{9g_0(\varepsilon_{\rm F}/\hbar\omega_{\rm M})}\hbar\omega_{\rm M}}\,, \tag{6.66}$$

with the function g_0 defined in (6.20). For Na clusters, we have $\varepsilon_{\rm F}/\hbar\omega_{\rm M} = 0.93$ and our criterion yields a value $\Delta\varepsilon_{\rm c} \simeq (3/5)\varepsilon_{\rm F}$.

We have verified the robustness of our criterion (6.62) by exploring different physical parameters, like the size of the cluster. Indeed, it can be seen in Figure 6.4 that above $\Delta\varepsilon_{\rm c}$ the RPA sum evaluated from (6.48) (solid line) and the estimate (6.60) (dashed line) are close to each other, showing that for high energies the RPA sum is essentially given by the contributions coming from the low-energy p-h excitations. We have checked that this feature of $\Delta\varepsilon_{\rm c}$ is independent of the size a of the nanoparticle.

In order to have a well-defined collective excitation, the cutoff energy $\Delta\varepsilon_{\rm c}$ must obviously be larger than the minimal p-h excitation energy (6.49). For Na, we find that this condition is already verified with only $N = 20$ conduction electrons in the nanoparticle, in agreement with the experiments of reference [SKM$^+$91] and the numerical calculations of reference [YB91].

Eq. (6.66) is the key ingredient we needed to avoid the problem of the clear separation between the plasmon and its environment, as discussed in section 6.3.2. The splitting in low $\Delta\varepsilon_{ph} < \Delta\varepsilon_{\rm c}$ and high-energy $\Delta\varepsilon_{ph} > \Delta\varepsilon_{\rm c}$ p-h excitations gives physical soundness to the method based on the separation of the electronic degrees of freedom into centre-of-mass and relative coordinates [GGI02, WIJW06, WMWJ05,

WWIJ07] described in the first two sections of the chapter. Now that the Fermi's Golden Rule calculation of the Landau damping of the plasmon (6.18) is justified, provided one sums over p-h pairs with $\Delta\varepsilon_{ph} > \Delta\varepsilon_{\rm c}$, we will use the estimate (6.66) to compare in next section the characteristic time scales of the surface plasmon and its high-energy p-h environment. We will show that the memory of this environment is very short compared to the timescale characterizing the evolution of the plasmon, its decay time $\gamma(a)^{-1}$, justifying in this way a Markovian approach for the analysis of the plasmon dynamics in presence of such a dissipative bath, cf. [WIWJ07].

6.5 Dynamics of the relative-coordinate system

The decomposition (6.15) of H suggests to treat the collective coordinate as a simple system of one degree of freedom which is coupled to an environment with many degrees of freedom. The latter are the relative coordinates described by $H_{\rm rel}$. This is the approach taken in [WIWJ07]. In this picture, the time evolution of the center-of-mass system (i.e., the surface plasmon) strongly depends on the dynamics of the relative-coordinate system. Such a dynamics is characterized by a correlation function which can be written at zero temperature as [WIWJ07]

$$C(t) = \Lambda^2 \sum_{ph} |d_{ph}|^2 {\rm e}^{{\rm i}\Delta\varepsilon_{ph}t/\hbar}\Theta(\Delta\varepsilon_{ph} - \Delta\varepsilon_{\rm c})\,. \tag{6.67}$$

$C(t)$ is nothing but the Fourier transform of the spectral function of this dissipative bath [LCD+87, Wei99]

$$\Sigma(\Delta\varepsilon) = \frac{2\pi}{\hbar}\Lambda^2 \sum_{ph} |d_{ph}|^2 \delta(\Delta\varepsilon - \Delta\varepsilon_{ph})\Theta(\Delta\varepsilon_{ph} - \Delta\varepsilon_{\rm c}) \tag{6.68}$$

which has been calculated in [WIJW06]. Finite temperatures were shown to result in a small quadratic correction. Consistently with the results of the preceding sections, we employ our low energy estimates (6.56) and (6.57) to obtain

$$\Sigma(\Delta\varepsilon) \simeq \frac{3v_{\rm F}}{4a}\left(\frac{\hbar\omega_{\rm M}}{\Delta\varepsilon}\right)^3 \Theta(\Delta\varepsilon - \Delta\varepsilon_{\rm c})\,. \tag{6.69}$$

This result is consistent with the one of reference [WIJW06] (see Eq. (34) in there) in the limit $\Delta\varepsilon \ll \hbar\omega_{\rm M}$ and for zero temperature. A schematic plot is given in fig.(6.5), showing the dominant role that the p-h excitations with energies close to $\Delta\varepsilon_{\rm c}$ have in the properties of the environment, pointing to a correlation time $\tau_{\rm cor}$ of the bath of order $\sim \hbar/\Delta\varepsilon_{\rm c}$.

In principle we could calculate $C(t)$ by taking the inverse Fourier transform of (6.69). The decay of $C(t)$ *for very long times* is dominated by the discontinuity of Σ

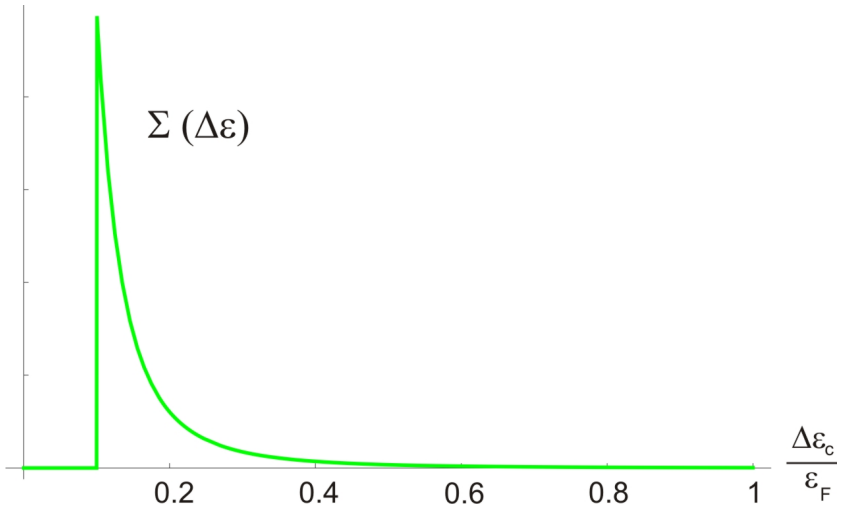

Figure 6.5: Schematic plot of the spectral function $\Sigma(\Delta\varepsilon)$, Fourier transform of $C(t)$, with $\Delta\varepsilon_{\rm c}$ taken to be $\Delta\varepsilon_{\rm c} = 0.1\varepsilon_F$. The sharp peak is a consequence of the fast decrease of $d^{\text{p-h}}(\Delta\varepsilon)$ with $\Delta\varepsilon$, eq. (6.57), which overwhelms the increase in the density of particle-hole excitations contributing to the damping of the plasmon, eq.(6.56), giving in this way a preponderant role in the dissipative bath to the particle-hole excitations with energies close to $\Delta\varepsilon_{\rm c}$.

at $\Delta\varepsilon_{\rm c}$. This is somehow problematic since $\Delta\varepsilon_{\rm c}$ can only be estimated as we did in Section 6.4.4, and since the functional form of the long time decay depends on how sharply the cutoff is implemented. However, it is important to realize that *it is not the very long time behavior that determines the relevant decay of the correlation function*, but rather the typical values at which $C(t)$ is reduced by an important factor from its initial value $C(0)$. We then estimate the correlation time as the mean decay time of $C(t)$,

$$\langle\tau_{\rm cor}\rangle = \left|\int_0^\infty {\rm d}t\, t\frac{\rm d}{{\rm d}t}\left(\frac{C(t)}{C(0)}\right)\right| = \frac{1}{C(0)}\left|\int_0^\infty {\rm d}t\, C(t)\right| . \tag{6.70}$$

If $C(t)$ were an exponentially decreasing function, $\langle\tau_{\rm cor}\rangle$ would simply reduce to the inverse of the decay rate. Using the definition (6.68), we get

$$\langle\tau_{\rm cor}\rangle = \frac{\hbar\displaystyle\int_{\Delta\varepsilon_{\rm c}}^\infty {\rm d}\Delta\varepsilon\Sigma(\Delta\varepsilon)/\Delta\varepsilon}{\displaystyle\int_{\Delta\varepsilon_{\rm c}}^\infty {\rm d}\Delta\varepsilon\Sigma(\Delta\varepsilon)} . \tag{6.71}$$

Given the fast decay of the function $\Sigma \sim 1/\Delta\varepsilon^3$, the above integrals are dominated

by their lower limit $\Delta\varepsilon_c$ and we have

$$\langle\tau_{\rm cor}\rangle \simeq \frac{2}{3}\frac{\hbar}{\Delta\varepsilon_c}\,. \tag{6.72}$$

Since $\Delta\varepsilon_c$ is of the order of $(3/5)\varepsilon_F$, we see that the response time (or correlation time) of the electronic environment is of the order of its inverse Fermi energy.

The estimate of the characteristic response time of the electronic environment is crucial in justifying the Markovian approximation used in [WIWJ07]. In that work, the degrees of freedom corresponding to the relative coordinates were integrated out and treated as an incoherent heat bath that acts on the collective coordinate. Such an approach relies on the fast response of the environment as compared to the time evolution of the surface plasmon. The typical scale for the latter is the inverse of the decay rate, $\tau_{\rm sp} = 1/\gamma$. Using (6.19) and (6.66), we therefore have

$$\boxed{\frac{\tau_{\rm sp}}{\langle\tau_{\rm cor}\rangle} = \frac{\pi}{9[g_0(\varepsilon_F/\hbar\omega_M)]^2}\frac{\hbar\omega_M}{\varepsilon_F}k_F a}\,. \tag{6.73}$$

For the example of Na nanoparticles worked in Section 6.4.3, we have $\tau_{\rm sp}/\langle\tau_{\rm cor}\rangle \simeq k_F a$. This is a safe limit since in not too small nanoparticles, $k_F a \gg 1$. As the size of the cluster increases, the applicability of the Markovian approximation is more justified. This is expected since the electronic bath has more and more degrees of freedom, approaching an "environment" in the sense of quantum dissipation. Since the physical parameters of alkaline nanoparticles entering (6.73) are close to that of noble-metal clusters, the dynamics of the surface plasmon can be expected to be Markovian in that case too.

6.6 Conclusions

We have studied the role of particle-hole excitations on the dynamics of the surface plasmon. A key concept in this analysis is the separation into low-energy excitations which lead to the collective excitation once they are mixed by the residual dipolar interaction, and high-energy excitations that act as an environment damping the resonance. Using the random phase approximation and assuming the separability of the residual interaction, we have established a criterion for estimating the cutoff energy separating the low- and high-energy subspaces. The resulting cutoff energy is approximately $(3/5)\varepsilon_F$ for the case of Na nanoparticles.

Since the number of electrons in the cluster is finite, the assumption that the high-energy particle-hole excitations act on the collective excitation as an environment, introducing friction in its dynamics, may be questionable. What settles this issue is the ratio between the typical evolution time of the collective excitation and the one of the high-energy particle-hole excitations. The former is given by the inverse of

the plasmon linewidth, while the latter is obtained from the decay of the correlation function of the environment. We have found that this ratio improves with increasing cluster size. Even for a small cluster with $a = 1\,\mathrm{nm}$, the ratio is approximately 10, justifying the use of the Markovian approximation which assumes a fast time evolution of the environment with respect to the one of the collective excitation.

The relevance of memory effects in the electronic dynamics of small clusters is of current interest, due to the advance in time-resolved experimental techniques [BHMD00, FVF$^+$00, LKLA99, LUCS01]. First-principle calculations have recently addressed this issue by comparing time-dependent density functional theories with and without memory effects for small gold clusters [KB06]. For very small clusters ($N < 8$) memory effects were shown to be important. It has to be noted, however, that the memory considered in [KB06] is that of the electron gas as a whole, while we are concerned in this work with the memory arising from the dynamical evolution of the relative-coordinate subsystem. It would be interesting to consider cluster sizes intermediate between the ones considered in the present work and those of reference [KB06] in order to study the emergence of memory effects.

Appendix A

Appendix to Chapter 1

A.1 Modes' equations of motion of quasi-1D resonators.

A.1.1 Elasticity basics.

We will follow ref. [LL59]. The starting point is to define the displacement vector of a given point x_i in the solid, $u_i = x_i' - x_i$, representing the difference between the coordinates of the same point before and after the deformation. The related magnitude that appears everywhere in the theory of elasticity is the so-called *strain tensor* (symmetric by definition):

$$u_{ik} = \frac{1}{2}\Big(\frac{\partial u_i}{\partial x_k} + \frac{\partial u_k}{\partial x_i} + \frac{\partial u_l}{\partial x_i}\frac{\partial u_l}{\partial x_k}\Big) \simeq \frac{1}{2}\Big(\frac{\partial u_i}{\partial x_k} + \frac{\partial u_k}{\partial x_i}\Big) \tag{A.1}$$

Then the *stress tensor* σ_{ik} is defined, considering the forces F_i exerted on a small volume dV due to the deformation of a body:

$$\int F_i dV = \int \frac{\partial \sigma_{ik}}{\partial x_k} dV = \oint \sigma_{ik} dS_k \;\rightarrow\; F_i = \frac{\partial \sigma_{ik}}{\partial x_k} \tag{A.2}$$

With these two quantities one can study the thermodynamics of the deformation: take a deformed body and suppose there is a small variation in the deformation, so that $u_i \rightarrow u_i + \delta u_i$, then the internal work done by the internal forces is given by

$$\int \frac{\partial \sigma_{ik}}{\partial x_k} \delta u_i dV \tag{A.3}$$

We will consider bodies at a fixed temperature T, so the thermodynamic potential we will use is the free energy $F = U - TS$, with a variation of F in a small deformation at a constant T given by $dF = \sigma_{ik} du_{ik}$, implying $\sigma_{ik} = \partial F / \partial u_{ik}\big|_T$. Now, for small deformations, choosing as non-deformed state the one in absence of external forces, we

can expand F as a function of u_{ik}, obtaining $F = \frac{1}{2}\lambda_{iklm}u_{ik}u_{lm}$, so that $\sigma_{ik} = \lambda_{iklm}u_{lm}$ (Hooke's law). For an isotropic body the expression reduces to $F = F_0 + (\lambda/2)u_{ii}^2 + \mu u_{ik}^2$ (λ and μ are the Lamé coefficients), which can be reexpressed as

$$F = \mu\Big(u_{ik} - \frac{1}{3}\delta_{ik}u_{ll}\Big)^2 + \frac{K}{2}u_{ll}^2 \qquad , \qquad K = \lambda + \frac{2}{3}\mu \tag{A.4}$$

defining the rigidity modulus K. If the deformation is homogeneous (the strain tensor is constant throughout the body), and more specifically a simple extension or compression along the z axis, one has

$$\sigma_{zz} = E \times u_{zz} \ , \tag{A.5}$$

defining the Young modulus,

$$E = \frac{9K\mu}{3K + \mu} \tag{A.6}$$

The ratio between transversal contraction u_{xx} and longitudinal elongation u_{zz} is Poisson's coefficient

$$\nu = -\frac{u_{xx}}{u_{zz}} = \frac{1}{2}\frac{3K - 2\mu}{3K + \mu} \, . \tag{A.7}$$

A.1.2 The case of a rod.

We start defining a local coordinate system (ξ, η, ζ), attached to the point, that coincides with (x, y, z) in the absence of deformation (the rod is then along the Z axis). Next we define $\vec{\Omega} = d\vec{\phi}/dl$, the rate of variation of the relative rotation angle between the local coordinate systems of two adjacent points (dl is taken along the bar's main axis). For example, a pure bending has $\vec{\Omega} = \Omega_\eta \vec{\eta}$. Now we define a coordinate system fixed in space, independent of the rod, with respect to whom a point in the rod will be given by a vector $\vec{r}$. The tangent vector at that point is given by $\vec{t} = d\vec{r}/dl$, and the curvature by $d\vec{t}/dl$, with modulus $1/R$, defining the curvature radius. For a slight bending one has

$$\vec{\Omega} = \vec{t} \wedge \frac{d\vec{t}}{dl} \simeq \vec{t} \wedge \frac{d^2\vec{r}}{dz^2} = \Big(- \frac{d^2Y}{dz^2}, \frac{d^2X}{dz^2}, 0\Big) \tag{A.8}$$

In terms of $\vec{\Omega}$ the free energy of a rod is deduced to be

$$F_{rod} = \frac{1}{2}\int \Big\{ I_1 E\Omega_\xi^2 + I_2 E\Omega_\eta^2 + C\Omega_\zeta^2 \Big\} dl \tag{A.9}$$

where I_1 and I_2 are the principal inertia moments of the section of the rod, and C is the so-called torsional rigidity. In the case of a slight bending the expression reduces to

$$F_{bending} = \frac{E}{2}\int \Big\{ I_1 \Big(\frac{d^2X}{dz^2}\Big)^2 + I_2 \Big(\frac{d^2Y}{dz^2}\Big)^2 \Big\} dz \tag{A.10}$$

Now we will deduce the equations for the modes as slight deviations from the equilibrium situation, and the first step towards our goal is the analysis of the equilibrium equations.

Equilibrium conditions.

If there are external forces $\vec{F}_{ext}$ applied to the rod, and external moments $\vec{M}_{ext}$ associated with them, the rod will suffer a deformation until the internal forces and moments compensate the external ones, so in equilibrium one must have

$$\begin{cases} \vec{F}_{ext} + \vec{F}_{int} = 0 \\ \vec{M}_{ext} + \vec{M}_{int} = 0 \end{cases}$$

Considering the case of slight bending, for which $\vec{\Omega}$ is given by eq.(A.8), the internal moment $\vec{M}_{int}$ associated to the internal stresses is $\vec{M}_{int\ bending} = (-EI_1Y'', EI_2X'', 0)$, where the double prime represents $\partial^2/\partial z^2$. Taking a small volume of length dl and supposing an external force per unit length along the rod $\vec{F}_{ext} = \vec{K} = (K_x, K_y, K_z)$, the first of the equilibrium equations results in $d\vec{F}/dl = -\vec{K}$, and the second in $d\vec{M}_{int} + [d\vec{l} \wedge \vec{K}] = 0 \rightarrow d\vec{M}_{int}/dl = \vec{F} \wedge \vec{t}$. Deriving the second equation with respect to l, and taking into account the small value of $d\vec{t}/dl$ (slight bending), one arrives at $d^2\vec{M}_{int}/dl^2 = \vec{t} \wedge \vec{K}$, so that

$$\begin{cases} EI_2\, \partial^4 X/\partial z^4 = K_x \\ EI_1\, \partial^4 Y/\partial z^4 = K_y \end{cases} \tag{A.11}$$

and the internal forces will be given by

$$\begin{cases} F_x = -EI_2X''' \\ F_y = -EI_1Y''' \end{cases}$$

Mode's equations.

To obtain the equations of motion of an elastic medium, we start from Newton's equation equating the product of mass and acceleration to the internal forces the mass is subject to

$$\rho\ddot{u}_i = \frac{\partial \sigma_{ik}}{\partial x_k} \tag{A.12}$$

In the simplest case of **longitudinal** vibrations we have, using eq.(A.5)

$$\rho\ddot{u}_z = \frac{\partial \sigma_{zk}}{\partial x_k} \rightarrow \frac{\partial^2 u_z}{\partial z^2} = \frac{\rho}{E}\frac{\partial^2 u_z}{\partial t^2} \tag{A.13}$$

This is the usual wave equation with linear dispersion relation. For the **bending** (flexural) case, the equations of motion are obtained just by substituting $-K_x$ and $-K_y$ in the equilibrium equations (A.11) by $\rho S\ddot{X}$ and $\rho S\ddot{Y}$ (S = transversal section of the rod):

$$\begin{aligned} EI_y\frac{\partial^4 X}{\partial z^4} &= -\rho S\frac{\partial^2 X}{\partial t^2} \\ EI_x\frac{\partial^4 Y}{\partial z^4} &= -\rho S\frac{\partial^2 Y}{\partial t^2}\ . \end{aligned} \tag{A.14}$$

These equations admit plane wave-kind of solutions $X(z,t), Y(z,t) \sim e^{i(kz-\omega t)}$, but with a quadratic dispersion relation, $\omega_j(k) = \sqrt{EI_j/(\rho S)}k^2$. In the case of **torsional** vibrations, the equations follow from equating the moment $C\,\partial\Omega_\zeta/\partial z$ to the temporal derivative of the angular momentum $\mathcal{L}$ per unit length, $\mathcal{L} = \rho I \partial\phi/\partial t$. In the last expression ϕ is the rotation angle of the considered section, so that $\partial\phi/\partial z = \Omega_\zeta$, and I is the inertia moment of the transversal section with respect to the center of mass, $I = \int (x^2+y^2)dS$, leading finally to

$$C\frac{\partial^2\phi}{\partial z^2} = \rho I \frac{\partial^2\phi}{\partial t^2} \tag{A.15}$$

Again a wave equation with linear dispersion relation for the variable ϕ.

Shape and frequency of the bending eigenmodes

Take a rod of length L, thickness t, width w, and mass density ρ. There are several possible configurations of a rod; we choose a doubly clamped beam, with both ends fixed. In the experiment the fundamental mode of transversal vibration in one of the directions, lets say X, is excited, and its frequency ω_0 is measured. Now we will solve the equation for $X(z,t)$ following [**?**] with fixed ends for the rod, and obtain a relation between ω_0 and the Young modulus E, from which we will calculate its value.
We try a solution of the form $X(z,t) = X_0(z) \times \cos(\omega t + \delta)$. Inserting it in the eq.(A.14) for $X(z,t)$, we obtain an equation that $X_0(z)$ has to verify:

$$\frac{d^4X_0(z)}{dz} = \omega^2\frac{\rho S}{EI_y}X_0(z) = \kappa^4 X_0(z) \tag{A.16}$$

The solution to this equation is of the form

$$X_0(z) = A\cos(\kappa z) + B\sin(\kappa z) + C\cosh(\kappa z) + D\sinh(\kappa z) \tag{A.17}$$

Now, the boundary conditions we have to impose in this solution are, for fixed ends, $X_0 = \frac{dX_0}{dz} = 0$ in $z = 0, L$. The final form of $X_0(z)$ in terms of κ, and the equation for the possible values of κ, are

$$\begin{aligned} X_0(z) &= A\Big\{(\sin\kappa L - \sinh\kappa L)(\cos\kappa z - \cosh\kappa z) - (\cos\kappa L - \cosh\kappa L)(\sin\kappa z - \sinh\kappa z)\Big\} \\ 1 &= \cos\kappa L\cosh\kappa L \end{aligned} \tag{A.18}$$

The possible values for κ can be estimated to be, for $\kappa L > 1$, $\kappa \simeq \frac{2n+1}{2}\frac{\pi}{L}$, because the $\cosh\kappa L$ takes big values that have to be "compensated" by the $\cos\kappa L$, for their product to be 1. Therefore the density of states in the k-space is approximately constant, $\frac{dN}{dk} \simeq \frac{L}{\pi}$. The first solution for κ is $\kappa_0 \simeq \frac{\sqrt{22.4}}{L}$, already close to $\frac{3}{2}\frac{\pi}{L}$, and from the relation between κ and ω ($\omega(\kappa) = \sqrt{\frac{EI_y}{\rho S}} \times \kappa^2$) we get

$$\omega_0 = \frac{22.4}{L^2}\sqrt{\frac{EI_y}{\rho S}} \tag{A.19}$$

Appendix B

Appendix to Chapter 2

B.1 Some details about the Standard Tunneling Model.

B.1.1 Distribution function of the TLSs

From ref. [Phi87]. The tunneling model proposes the existence of an ensemble of TLSs, each one characterized by a hamiltonian:

$$H_0 = \Delta_0^x \sigma_x + \Delta_0^z \sigma_z \tag{B.1}$$

The task is to determine the probability density distribution $P(\Delta_0^x, \Delta_0^z)$ of the TLSs in terms of Δ_0^x and Δ_0^z. A simplified expression for the tunneling amplitude as a function of the potential barrier height V and width d is

$$\Delta_0^x = \hbar\Omega e^{-\lambda} = \hbar\Omega e^{-d(2mV/\hbar^2)^{1/2}} \tag{B.2}$$

where $\hbar\Omega$ is approximately equal to the average of the ground states of both isolated wells, and m is the particle mass.
Typical values for λ can be estimated demanding that Δ_0^x must be approximately equal to kT if the tunneling state is to contribute to thermal properties at a temperature T. At 1 K this requires a tunnel splitting of 10^{-4} eV, which with $\hbar\Omega \sim 10^{-2}$ eV gives approximately $\lambda \sim 5$. This is equivalent to a bare proton tunneling across a barrier of 0.1 eV with $d = 0.7$ Å.
For Δ_0^z it is argued that the distribution function must be symmetric because both positive and negative values of Δ_0^z are equally likely. The scale of energy variation is determined by the thermal energy available at the glass-transition temperature T_g where the fluctuating local potentials of the liquid are frozen in the structure. Since T_g is between 200 and 1000 K for most glasses, this energy is about 0.05 eV, much larger than the thermal energy available at 1 K. The low temperature properties are

therefore sensitive to the center of a broad symmetric distribution, so that $P(\Delta_0^x, \Delta_0^z)$ can be taken as independent of Δ_0^z.
In the case of the dependence on Δ_0^x, due to the exponential dependence of Δ_0^x on λ, only a relatively small range of λ's is sampled for a large range of Δ_0^x and over this limited range the distribution of λ can be assumed constant. This leads immediately to $P(\Delta_0^x, \Delta_0^z) = P_0/\Delta_0^x$. This result is slightly modified by a logarithmic factor if the distribution of λ varies slowly with the energy, but we will ignore this dependence. The limits of the possible values for Δ_0^x and Δ_0^z, and the value of P_0, can be deduced from experiments (see next subsection).

B.1.2 Determination of values for P_0 and Δ^*

The value $P_0 \sim 10^{44}\mathrm{J}^{-1}\mathrm{m}^{-3}$ is obtained by the experimentalists through experiments of heat release in amorphous solids, as follows (the derivations in this appendix follow very closely the explanations appearing in ref. [Esq98]): An amorphous solid is taken which is at a temperature T_1, and cooled down very fast to a temperature T_0. The slower TLSs, which were, as all the rest, in thermal equilibrium at a temperature T_1, do not have time to follow the cooling of the system, so they equilibrate with the surroundings releasing part of their energy and heating up the rest of the solid, until it reaches another temperature $T_2 > T_0$. One can calculate the time dependence of the heat release as $\dot{Q}(t) = \dot{N}_\uparrow(t)\varepsilon = (1/2)\dot{\tilde{N}}(t)\varepsilon$, where $N_\updownarrow$ is the number of TLSs in the excited state, ε is the energy of such a state, and $\tilde{N} = N_\downarrow - N_\uparrow$. Then, assuming that the dynamical behavior of $\tilde{N}(t)$ can be described by the relaxation time approximation

$$\frac{d[\tilde{N}(t) - \tilde{N}_0(T)]}{dt} = -\frac{\tilde{N}(t) - \tilde{N}_0(T)}{\tau(T)} \tag{B.3}$$

where $\tau(T)$ is the relaxation time of a TLS with energy difference ε at a temperature T. Taking T =const., one arrives at

$$\dot{\tilde{N}}(t) = N\Big(\tanh\frac{\varepsilon}{2k_BT_0} - \tanh\frac{\varepsilon}{2k_BT_1}\Big)\frac{e^{-\frac{t}{\tau(T_0)}}}{\tau(T_0)} \tag{B.4}$$

so that the heat release is given by

$$\dot{Q}(t) = \frac{1}{2}\varepsilon N\Big(\tanh\frac{\varepsilon}{2k_BT_0} - \tanh\frac{\varepsilon}{2k_BT_1}\Big)\frac{e^{-\frac{t}{\tau(T_0)}}}{\tau(T_0)} \tag{B.5}$$

Replacing the total number N of TLSs by the distribution in terms of ε and u ($\varepsilon = \sqrt{\Delta_x^2 + \Delta_z^2}$ and $u = \Delta_x/\varepsilon$) and the volume V of the sample, the result is

$$\dot{Q}(t) = \frac{P_0V}{2}\int_0^{\varepsilon_{max}} d\varepsilon\varepsilon N\Big(\tanh\frac{\varepsilon}{2k_BT_0} - \tanh\frac{\varepsilon}{2k_BT_1}\Big)\cdot\int_{u_{min}}^1 du\frac{1}{u\sqrt{1-u^2}}\frac{e^{-\frac{t}{\tau(T_0)}}}{\tau(T_0)} \tag{B.6}$$

Notice that $\tau(T_0)$ is a function of ε and u. For low temperatures $\tau(T_0)$ can be approximated by the FGR result

$$\tau_{FGR}^{-1}(\varepsilon, \Delta_x, T) = \frac{4}{\pi}\frac{\gamma^2}{\rho\hbar^4}\frac{\Delta_x^2\varepsilon}{v^5}\coth\Big[\frac{\varepsilon}{2kT}\Big] \tag{B.7}$$

so that

$$\dot{Q}(t) = \frac{P_0 V}{2}\int_0^{\varepsilon_{max}} d\varepsilon\varepsilon N\Big(\tanh\frac{\varepsilon}{2k_B T_0} - \tanh\frac{\varepsilon}{2k_B T_1}\Big)\cdot\int_{\tau_{min}}^{\tau_{max}} d\tau_{FGR}\frac{P(\varepsilon,\tau_{FGR})e^{-t/\tau(T_0)}}{\tau_{FGR}(T_0)} \tag{B.8}$$

For usual experimental conditions and most glasses the last integral is insensitive to the limits of integration, and moreover, it can be shown that the main contribution to the heat release comes from TLSs with $\varepsilon \approx 2k_B T_1$ and $\tau \approx t$. For the case $\varepsilon \ll \varepsilon_{max}$, (B.8) leads to

$$\dot{Q}(t) = \frac{\pi^2 k_B^2}{24} P_0 V(T_1^2 - T_0^2)\frac{1}{t}e^{-t/\tau_{max}} \tag{B.9}$$

For $t < 0.1\,\tau_{max}$ the result is independent of τ_{max} and we obtain

$$\dot{Q}(t) = \frac{\pi^2 k_B^2}{24} P_0 V(T_1^2 - T_0^2)\frac{1}{t} \tag{B.10}$$

Fitting the heat release experiments to this formula determines P_0. There are other types of measurements that can be used for this purpose, but this is the most accurate one, as the coupling constant γ characterizing the coupling of the TLSs to the acoustic waves does not appear.

Regarding the upper cutoff of the distribution of TLSs, Δ^*, again the experiments, in this case sound velocity ones, fix a minimum of about 5 K for oxide glasses, reasoning as follows: The interaction of elastic waves with TLSs results in a relative change of the sound velocity

$$\frac{\delta v}{v} = -\frac{1}{V}\sum_{TLS}\frac{\gamma^2}{2\rho v^2\hbar}\chi'(\omega)\,, \tag{B.11}$$

where $\chi(\omega) = \chi'(\omega) + i\chi''(\omega)$ is the susceptibility of a single defect. At low temperatures the relaxation rates of thermal TLSs are much smaller than the external frequency ω, $\omega\tau \gg 1$; then only the 'resonant' part of the susceptibility, $\chi' = (\Delta_x^2/\varepsilon^3)\tanh\big[\varepsilon/2kT\big]$, is relevant. Summing according to the distribution $P(\Delta_x, \Delta_z) = P_0/\Delta_x$, the result is

$$\frac{\delta v}{v} = \frac{\gamma^2 P_0}{\rho v^2}\log(T/T_{ref}) \quad (\Gamma \ll \omega \ll k_B T/\hbar) \tag{B.12}$$

where T_{ref} is a reference temperature. This result is used to fit the experiments on the low-temperature sound velocity of various glasses. The logarithmic law arises from thermal TLSs with small bias Δ_z, i.e. with Δ_x close to temperature, and due to the fact that this behavior has been observed up to several K, it has been concluded that Δ_x^*/k_B is at least about 5 K.

B.1.3 Predominant coupling of the strain to the asymmetry

Given the energy of a TLS as $\varepsilon = (\Delta_x^2 + \Delta_z^2)^{1/2}$, the coupling to strain fields e may be represented by the deformation potential

$$D = \frac{d\varepsilon}{de} = \frac{\Delta_z}{\varepsilon}\frac{d\Delta_z}{de} + \frac{\Delta_x}{\varepsilon}\frac{d\Delta_x}{de}\,. \tag{B.13}$$

In the standard tunneling model the second term is neglected, with a resulting coupling

$$D = \frac{d\varepsilon}{de} \approx \frac{\Delta_z}{\varepsilon}\frac{d\Delta_z}{de}. \tag{B.14}$$

Experimental support is given in ref. [And86], where the following considerations are made: As there is a distribution of Δ_x and Δ_z, there will be a distribution $n(\varepsilon, D)$ in D. Due to the coupling D the TLSs influence the low-temperature behavior of the volume thermal-expansion coefficient β, $\beta \propto n_0\langle D\rangle$, and ultrasonic attenuation α, $\alpha \propto n_0\langle D^2\rangle$ (the averages are over the distribution of TLSs). From attenuation measurements $\langle D^2\rangle^{1/2} \approx 1$ eV, and from thermal expansion measurements $\langle D\rangle \approx 10^{-3}$ eV, so $n(D)$ is a very broad and almost symmetric distribution. Now, to justify eq.(B.14) the author first proves that $\langle D^2\rangle$ and n_0 are almost independent of pressure P, for values of P up to 1000 atm and more. This, together with the observed linear variation of α with temperature, indicates that the distribution $n(\varepsilon, D)$ is essentially independent of pressure. This is needed in order to get information from experiments of ultrasonic attenuation where a pressure is applied at low temperature (0.5 K). The TLSs affecting the propagation of sound are mainly those with energies close to 0.5 K, and as increasing pressure is applied, TLSs which were in this region get out from it, and others, which were originally out, replace them. Given the high pressures exerted (up to 1300 atm), and the value of $\langle D^2\rangle$, the lack of change observed in the population of TLSs around 0.5 K can only be explained if, for a TLS, when a pressure is applied (equivalent to a variation of local strain), the energy as a function of pressure first decreases and then increases, *id est*, D has to change sign at some point as P increases. The most natural explanation is to assume that the main effect of pressure is to change the relative positions of the two wells of the double-well potential (B.14), so that the product $\frac{\Delta_z}{\varepsilon}\frac{d\Delta_z}{de}$ changes sign at a certain moment (due to the change of sign of Δ_z), keeping the absolute value approximately constant. If D depended mainly on the second term of eq.(B.13), to explain the experiments the size of the tunneling barrier would have first to increase with P and then to decrease, which seems more unlikely.

B.2 Path integral description of the dissipative two-state system.

We will here remind the reader about the fundamental concepts underlying the derivation of some of the results stated in section 2.3.2. For a more detailed presentation of the basics see [FV63, Sim05, PIW], and for a detailed study of the spin-boson problem using a path integral approach see [LCD$^+$87, Wei99].

A formulation of Quantum Mechanics different from the canonical one developed by Schrödinger and Heisenberg but equivalent to it was developed by Richard Feynman in the fourties [Fey48], the Path Integral formulation, based on the following postulates [PIW]:

1. The probability for any fundamental event is given by the square modulus of a complex amplitude.

2. The amplitude for some event is given by adding together all the histories which include that event.

3. The amplitude a certain history contributes is proportional to $e^{iS/\hbar}$, where S is the action of that history, or time integral of the Lagrangian.

This approach is often used in semiclassical physics, where the transition from classical to quantum behavior of a system is studied. In terms of path integrals the classical behavior is obtained imposing $\hbar \to 0$, because in this way the interferences between the contributions $e^{iS[x(t)]/\hbar}$ of neighboring paths $x(t)$ will cancel out except for those close to the path for which $\delta S/\delta x(t) = 0$ (imposing of course the proper boundary conditions at the initial and final time), which is by definition the classical trajectory. The first quantum corrections will be obtained by considering also the contributions of the paths close to the classical solution, something usually done using stationary phase approximation calculations [Sim05], where the otherwise unmanageable integrals reduce to Gaussian integrals.

Feynman's ideas constitute also a very convenient framework to study the dynamics of open quantum systems, where a subsystem focus of our interest is not isolated but coupled to many external degrees of freedom (its "bath" or "environment") [FH65]. In the path integral approach, one starts with a generic path integral containing all the possible histories followed by all the variables of the composite "subsystem + environment" system. As we are only interested in the variables describing the subsystem, the second step is to integrate out the rest of variables as best as we can, analogously to what is done in studies involving reduced density matrices. Typically, the resulting integral, now containing only the variables of the subsystem, contains an action S composed of two parts, the action S_{isol} of the variables of the

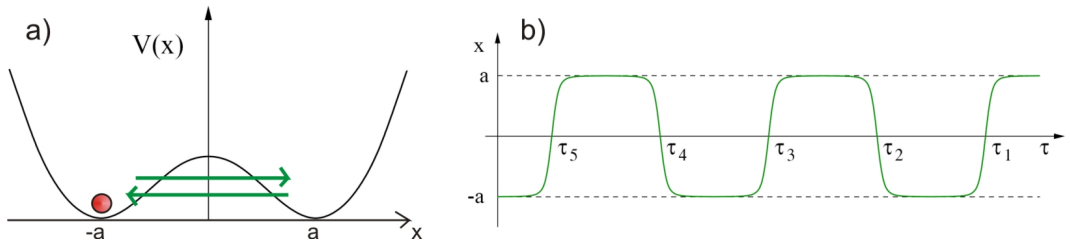

Figure B.1: a) Particle in a double well potential. The influence of purely quantum mechanical processes such as tunneling is included in the path integral semiclassical approach by considering the time as a general complex variable τ, and searching for stationary solutions $\delta S/\delta x(\tau) = 0$ whose contributions to the path integral are summed; after the solution in terms of τ is found, the real-time dynamics is obtained by performing an analytical continuation to real time. In a given history of the particle dynamics, each tunneling process is called "instanton", and in b) a prototypical multi-instanton stationary solution is represented. Image (b) from [Sim05].

subsystem in absence of other degrees of freedom, plus a second term containing the information about the effects due to the bath, the so-called influence-functional S_{infl} [FV63, FH65], where memory effects mediated by the bath are manifested in terms of "interactions" between the subsystem variables at different times. Fortunately a broad class of open systems can be considered to be coupled very weakly to each of the numerous degrees of freedom of their environment, allowing for a description of these environmental variables in terms of harmonic oscillators. The related path integrals are Gaussian and can be performed exactly [FV63]. Thus the approximations will start only when dealing with S_{infl}, not before.

The spin-boson model or dissipative two-state system [LCD$^+$87, Wei99], eq.(2.6), is perhaps the most successful and studied example using the previous ideas, due to its generality and applicability to many different systems, as well as due to its star role in the study of environment-induced phase transitions.

In absence of dissipation, the path integral method gives a good solution for the dynamics of the "tunneling particle", fig.(B.1a), by adding up the contributions of all the stationary solutions $\delta S/\delta x(\tau) = 0$ where τ is taken as a general complex variable, and performing in the final result an analytical continuation to real times. This allows to take into account quantum paths classically forbidden, including one or several tunneling processes. In the jargon of the field each tunneling process is called an "instanton" or "blip", and the solution is the result of summing all possible multi-instanton configurations, like the one in fig.(B.1b). The basic approximation involved in the calculation is to consider the tunneling processes as completely independent, with the total action of a multi-tunneling path with N tunneling events S_{N} being N

times the action of a single-tunneling path, $S_{\rm N} = N \times S_1$, or expressed in terms of blips, there is no interaction among them.

When a dissipative environment of harmonic oscillators is coupled to this system, the path integral resulting from integrating out the oscillators' degrees of freedom introduces, as previously told, an influence-functional $S_{\rm infl}[|x(\tau) - x(\tau')|]$ that provides memory to the dynamics. Now the result can be again expressed in terms of sums over multi-blip paths, but interactions play a role and complicate enormously the calculation. Leggett *et al.* introduced the so-called non-interacting blip approximation (NIBA), which basically limits the memory effects to the inclusion of the contribution to the action S corresponding to interaction between two consecutive periods separated by a tunneling process.

The success of this approximation lies in its numerous virtues, two out of which we highlight here for our purposes: i) It is a controlled approximation, with a clearly defined range of validity (basically low temperatures and weak tunneling amplitude as compared to the characteristic frequency of the ground states of the wells) and well defined expansion parameters, ii) It turns out to be a good description in a very broad range of cases, from baths leading to a weak damping to baths leading to a suppression of tunneling and localization of the particle.

Remember that the Hilbert space of the system described in fig.(B.1a) is reduced in the spin-boson model to the two ground states of the wells, represented by a spin up and spin down ($\langle\sigma_z\rangle = 1$ for the left well ground state and $\langle\sigma_z\rangle = -1$ for the right well ground state, for example). These two states become mixed by the tunneling amplitude Δ_0^x, introducing spin-flip processes in the dynamics. The basic result obtained within NIBA for the time evolution $P(t) = \langle\sigma_z(t)\rangle$ starting at $t = 0$ in a given well, $\langle\sigma_z(t=0)\rangle = 1$, is

$$P(t) = \frac{1}{2\pi i}\int_C e^{\lambda t}[\lambda + f(\lambda)]^{-1} d\lambda\,, \tag{B.15}$$

where C is the standard Bromwich contour, and

$$f(\lambda) \equiv \Delta_x^2 \int_0^\infty \cos\Big[Q_1(t)\Big] \exp -\Big[\lambda t + Q_2(t)\Big]\,, \tag{B.16}$$

with $Q_i(t)$ defined by

$$\begin{aligned} Q_1(t) &\equiv \int_0^\infty \frac{J(\omega)}{\omega^2}\sin[\omega t] d\omega \\ Q_2(t) &\equiv \int_0^\infty \frac{J(\omega)}{\omega^2}(1-\cos[\omega t])\coth[\hbar\omega/2k_BT] d\omega \end{aligned} \tag{B.17}$$

The function $J(\omega)$ appearing in the integrals is the spectral density of the bath,

$$J(\omega) = \int_{-\infty}^\infty dt\, e^{i\omega t}\langle H_{int}(t) H_{int}(0)\rangle\ . \tag{B.18}$$

At $T = 0$, up to second order in perturbation theory, it can be rewritten as

$$J(\omega) = \sum_k |\lambda_k|^2 \, \delta(\omega - \omega_k) \tag{B.19}$$

$J(\omega)$ reflects the evolution as a function of ω of the amount of possible transitions (fluctuations) from a starting initial state (at $T = 0$ the ground state) to all final states for whom an energy $\hbar\omega$ has been exchanged between our subsystem and the oscillators' bath.

Many of the oscillators' baths found in nature, like phonons in solids or e-h excitations in metals, display a spectral density $J(\omega) \sim \omega^s$ up to a certain cutoff (e.g. the Debye frequency in the case of phonons). A very important result states that whenever NIBA is applicable, the power s of $J(\omega)$ *is the crucial factor* determining the effect that the environment exerts on the TLS ($\langle\sigma_z(t)\rangle$) dynamics. As explained with an example in Appendices C.2.1 and C.2.3, at finite temperatures $T \gg \omega$ the amount of accessible transitions thanks to the thermal energy present in the system determines $J(\omega, T > 0)$, leading to $J(\omega, T) \sim T^s$.

B.2.1 Derivation of the spectral function for the case of the modes of a quasi-1D nanoresonator

The starting point is the hamiltonian (2.10), where $\partial_i u_j$ is a component of the deformation gradient matrix. In the case of the bending modes of a rod of dimensions L, t and w, and mass density ρ, there are two variables $X(z), Y(z)$ obeying eqs.(A.14). One can thus express $X(z), Y(z)$ in terms of bosonic operators, for example $X(0) = \sum_k \sqrt{\hbar/(2\rho t w L \omega_k)}(a_k^\dagger + a_k)$. We can relate this variables to the strain field $\partial_i u_j$ through the free energy F:

$$\begin{aligned} F_{rod} &= \frac{1}{2}\int dz EI_y\Big(\frac{\partial^2 X}{\partial z^2}\Big)^2 + EI_x\Big(\frac{\partial^2 Y}{\partial z^2}\Big)^2 = \frac{1}{2}\int dz \int dS \frac{1}{2}\lambda \sum_i u_{ii}^2 + \mu \sum_{i,k} u_{ik}^2 \\ &\approx \frac{1}{2}\int dz \int dS (\frac{3}{2}\lambda + 9\mu) u_{ij}^2 \end{aligned} \tag{B.20}$$

extracting an average equivalence for one component u_{ij}, $u_{ij} \approx 2\sqrt{EI_y/(3\lambda + 18\mu)tw}\,\partial^2 X/\partial z^2$. The interaction term in the hamiltonian is then

$$\begin{aligned} H_{\rm int} &= \hbar\sigma_z \sum_k \lambda \frac{k^2}{\sqrt{\omega_k}}(a_k^\dagger + a_k) \\ &= \hbar\sigma_z \sum_{ij}\sum_k \Big[2\gamma \frac{\Delta_0^x}{\varepsilon}\sqrt{\frac{EI_y}{(3\lambda + 18\mu)tw}}\sqrt{\frac{1}{2\rho t w \hbar L}}\Big] \frac{(k^{ij})^2}{\sqrt{\omega_k^{ij}}}(a_k^{ij\dagger} + a_k^{ij}) \end{aligned} \tag{B.21}$$

So we have approximately 9 times the same hamiltonian, once for each u_{ij}, and the corresponding spectral function $J(\omega)$ will be nine times the one calculated for

$$\begin{aligned} H_{\rm int} &= \hbar\sigma_z \sum_k \lambda \frac{k^2}{\sqrt{\omega_k}}(a_k^\dagger + a_k) \\ &\simeq \hbar\sigma_z \sum_k \Big[2\gamma \frac{\Delta_0^x}{\varepsilon}\sqrt{\frac{EI_y}{(3\lambda+18\mu)tw}}\sqrt{\frac{1}{2\rho tw\hbar L}}\Big]\frac{k^2}{\sqrt{\omega_k}}(a_k^\dagger + a_k) \end{aligned} \tag{B.22}$$

For this hamiltonian $J(\omega)$ is given by

$$J(\omega) = \frac{1}{2\pi}\sum_k \Big[2\gamma \frac{\Delta_0^x}{\varepsilon}\sqrt{\frac{EI_y}{(3\lambda+18\mu)tw}}\sqrt{\frac{1}{2\rho tw\hbar L}}\frac{k^2}{\sqrt{\omega_k}}\Big]^2 \delta(\omega-\omega_k) \tag{B.23}$$

Taking the continuum limit ($\frac{1}{L}\sum_k \to \frac{1}{\pi}\int dk$):

$$J(\omega) = \frac{2L}{(2\pi)^2}\int_{k_{min}}^{k_{max}} dk \Big[2\gamma \frac{\Delta_0^x}{\varepsilon}\sqrt{\frac{EI_y}{(3\lambda+18\mu)tw}}\sqrt{\frac{1}{2\rho tw\hbar L}}\Big]^2 \frac{k^4}{\omega_k}\delta(\omega-\omega_k) \tag{B.24}$$

Using the dispersion relation $\omega_j(k) = \sqrt{EI_j/(\rho ab)} \times k^2 = c \times k^2$ we express the integral in terms of the frequency:

$$\begin{aligned} J(\omega) &= \frac{L}{(2\pi)^2}\int_{\omega_{min}}^{\omega_{co}} \frac{d\omega_k}{\sqrt{c\,\omega_k}}\Big[2\gamma \frac{\Delta_0^x}{\varepsilon}\sqrt{\frac{EI_y}{(3\lambda+18\mu)tw}}\sqrt{\frac{1}{2\rho tw\hbar L}}\Big]^2 \frac{k^4}{\omega_k}\delta(\omega-\omega_k) \\ &= \frac{L}{(2\pi)^2}\Big[2\gamma \frac{\Delta_0^x}{\varepsilon}\sqrt{\frac{EI_y}{(3\lambda+18\mu)tw}}\sqrt{\frac{1}{2\rho tw\hbar L}}\Big]^2 \frac{\sqrt{\omega}}{c^{5/2}} \end{aligned} \tag{B.25}$$

$J_{\rm flex}(\omega)$ is just 9 times this, eq.(2.14).

For the compression and twisting modes the derivation follows analogous steps. Longitudinal or compression modes correspond to the displacement vector u_i obeying the wave equation (A.13). Hence, there are plane waves with linear dispersion relation $\omega_k = \sqrt{\frac{E}{\rho}}k$. The strain field ∂u appears in the hamiltonian coupled to a TLS located at $z=0$. The quantized $u(0)$ and $\partial u\,|_{z=0}$ are given by

$$u(0) = \sum_k \sqrt{\frac{\hbar}{2\rho twL\omega_k}}(a_k^\dagger + a_k) \quad , \quad \partial u\,|_{z=0} = \sqrt{\frac{\hbar}{2\rho twL}}\sum_k \frac{k}{\sqrt{\omega_k}}(a_k^\dagger + a_k) \tag{B.26}$$

The hamiltonian is:

$$\begin{aligned} H &= \varepsilon\sigma_x + \hbar\sigma_z \sum_k \Big[\gamma \frac{\Delta_0^x}{\varepsilon}\sqrt{\frac{1}{2\rho twL\hbar}}\frac{k}{\sqrt{\omega_k}}\Big](a_k^\dagger + a_k) + \sum_k \hbar\omega_k(a_k^\dagger a_k + \text{h.c.}) \\ &= \varepsilon\sigma_x + \hbar\sigma_z \sum_k \lambda_k(a_k^\dagger + a_k) + \sum_k \hbar\omega_k(a_k^\dagger a_k + \text{h.c.}) \end{aligned} \tag{B.27}$$

With such a form for the coupling the spectral function is given by eq.(2.11).

The twisting or torsional modes obey the wave equation (A.15). In analogy with the previous case we can quantize ϕ and get the same results for $\phi(0)$ and $\partial\phi\mid_{z=0}$ as for u(0) and $\partial u\mid_{z=0}$, just substituting ρ by ρI and E by C. But in our hamiltonian the coupling term involves $\partial u\mid_{z=0}$ and not $\partial\phi\mid_{z=0}$, so the latter has to be expressed in terms of the former. Proceeding as with the bending modes:

$$\begin{aligned} F_{rod} &= \frac{1}{2}\int dz C\left(\frac{\partial\phi}{\partial z}\right)^2 = \frac{1}{2}\int dz\int dS 4\mu\left[\left(\frac{\partial u_x}{\partial z}\right)^2+\left(\frac{\partial u_y}{\partial z}\right)^2\right] \\ &\approx \frac{1}{2}\int dz\int dS 8\mu\left(\frac{\partial u_x}{\partial z}\right)^2 \end{aligned} \tag{B.28}$$

Approximating further

$$\int dS 8\mu\left(\frac{\partial u_x}{\partial z}\right)^2 \approx 8\mu ab\left(\frac{\partial u_x}{\partial z}\right)^2 = C\left(\frac{\partial\phi}{\partial z}\right)^2 \tag{B.29}$$

the equivalence $\partial u\mid_{z=0}= \partial u_x/\partial z = \sqrt{C/(8\mu t w)}\partial\phi\mid_{z=0}$ is found. Therefore in this case one has an interaction term in the hamiltonian

$$H_{int} = \hbar\sigma_z\sum_k \gamma\frac{\Delta_0^x}{\varepsilon}\sqrt{\frac{C}{8\mu t w}}\sqrt{\frac{1}{2\rho I\hbar L}}\frac{k}{\sqrt{\omega_k}}(a_k^\dagger + a_k) \tag{B.30}$$

leading to an ohmic spectral function, eq.(2.11), as in the previous case.

B.3 Dissipation from symmetric non-resonant TLSs

B.3.1 Spectral function of a single TLS coupled to the subohmic bending modes

We follow the method of ref. [Gui85]. The form of $A(\omega)$, the spectral function of a single TLS, for frequencies $\omega \ll \varepsilon$ and $\omega \gg \varepsilon$ can be estimated using perturbation theory. Without the interaction, the ground state $|a\rangle$ of the TLS is the antisymmetric combination of the ground states of the two wells, and the excited state is the symmetric one, $|s\rangle$. We will use Fermi's Golden Rule applied to the subohmic spin-boson hamiltonian, $H = \varepsilon\sigma_x + \hbar\lambda\sigma_z\sum_k\left[\frac{k^2}{\sqrt{\omega_k}}\right](a_k^\dagger + a_k) + \sum_k \hbar\omega(k)a_k^\dagger a_k$, where a_k is the annihilation operator of a bending mode k. Considering only the low energy modes $\omega(k) \ll \varepsilon$, to first order the ground state and a state with energy $\omega(k)$ are given by

$$\begin{aligned} |g\rangle &\simeq |a\rangle - \frac{\frac{\lambda k^2}{\sqrt{\omega_k}}}{2\varepsilon}a_k^\dagger|s\rangle + \ldots \quad , \\ |k\rangle &\simeq a_k^\dagger|a\rangle - \frac{\frac{\lambda k^2}{\sqrt{\omega_k}}}{2\varepsilon}|s\rangle + \ldots \quad . \end{aligned} \tag{B.31}$$

We estimate the behavior of $A(\omega)$ by taking the matrix element of σ_z between these two states, obtaining (remember that $\omega(k) \propto k^2$)

$$A(\omega) \sim \frac{\hbar\alpha_b\sqrt{\omega_{co}}\sqrt{\omega}}{\varepsilon^2} + ... \quad , \quad \omega(k) \ll \varepsilon. \tag{B.32}$$

The expression in the numerator is proportional to the spectral function of the coupling, $J(\omega) = \alpha_b\sqrt{\omega_{co}}\sqrt{\omega}$. Now we turn our attention to the case $\omega(k) \gg \varepsilon$, where the ground state $|g\rangle$ and an excited state $|k\rangle$ can be written as

$$\begin{aligned} |g\rangle &\simeq |a\rangle - \frac{\lambda k^2/\sqrt{\omega_k}}{\hbar\omega_k + 2\varepsilon} a_k^\dagger |s\rangle + ... \quad , \\ |k\rangle &\simeq a_k^\dagger |a\rangle + \frac{\lambda k^2/\sqrt{\omega_k}}{\hbar\omega_k - 2\varepsilon} |s\rangle + ... \quad . \end{aligned} \tag{B.33}$$

The matrix element $\langle 0|\sigma_z|k\rangle$ is $\sim \frac{\lambda k^2}{\sqrt{\omega_k}} \frac{4\varepsilon}{(\hbar\omega_k)^2}$, leading to

$$A(\omega) \sim \frac{\alpha_b\sqrt{\omega_{co}}\varepsilon^2}{\hbar^3\omega^{7/2}} + ... \quad , \quad \omega(k) \gg \varepsilon. \tag{B.34}$$

B.3.2 Value of $A^{\rm tot}_{\rm off-res}(\omega_0)$

Now we will add the contributions of all the non-resonant TLSs using the probability distribution $P(\Delta_0^x, \Delta_0^z) = P_0/\Delta_0^x$ [AHV72, Phi72]. For the case of weak coupling, $\alpha_b < 1/2$ and $\omega_0 \geq (2\alpha_b)^2\omega_{co}$, which is the one found in experiments, one has

$$\begin{aligned} A^{\rm tot}_{\rm off}(\omega_0) \sim & \int_{\hbar[\omega_0+\Gamma(\omega_0)]}^{\epsilon_{max}} d\Delta_0^x \int_{-\Delta_0^x}^{\Delta_0^x} d\Delta_z \frac{P}{\Delta_0^x} \frac{\hbar\alpha_b\sqrt{\omega_{co}}\sqrt{\omega_0}}{(\Delta_0^x)^2} \\ & + \int_{\hbar(2\alpha_b)^2\omega_{co}}^{\hbar[\omega_0-\Gamma(\omega_0)]} d\Delta_0^x \int_{-\Delta_0^x}^{\Delta_0^x} d\Delta_z \frac{P}{\Delta_0^x} \frac{\alpha_b\sqrt{\omega_{co}}(\Delta_0^x)^2}{\hbar^3\omega_0^{7/2}} \end{aligned}$$

obtaining the result $A^{\rm tot}_{\rm off-res}(\omega_0) \approx 2P\alpha_b\sqrt{\omega_{co}/\omega_0}$.

B.3.3 The off-resonance contribution for T > 0

Using the same scheme, the modifications due to the temperature will appear in the density of states of absorption and emission of energy corresponding to a "dressed" TLS, $A(\varepsilon, \omega, T)$. Now there will be a probability for the TLS to be initially in the excited symmetric state, $|s\rangle$, proportional to $\exp[-\varepsilon/kT]$, and to emit energy $\hbar\omega$ giving it to our externally excited mode, $|k, n\rangle$, thus compensating the absorption of energy corresponding to the opposite case (transition from $|a\rangle|k, n\rangle$ to $|s\rangle|k, n-1\rangle$), but contributing in an additive manner to the total amount of fluctuations, which

are the ones defining the linewidth of the vibrational mode observed in experiments, fixing the value of $Q^{-1}(\omega, T)$. The expression for $A(\varepsilon, \omega, T)$ is given by

$$A(\omega, T) = \frac{1}{Z} \sum_i \sum_f |\langle i|\sigma_z|f\rangle|^2 e^{-\frac{E_i}{kT}} \delta[\hbar\omega - (E_f - E_i)] \tag{B.35}$$

We consider a generic state $|i_a\rangle = |a\rangle|k_1 n_1, ..., k_j n_j, ...\rangle$ or $|i_s\rangle = |s\rangle|k_1 n_1, ..., k_j n_j, ...\rangle$, and states that differ from it in $\hbar\omega_j$,

$$|f_{a\pm}\rangle = |a\rangle|k_1 n_1, ..., k_j n_j \pm 1, ...\rangle \qquad , \qquad |f_{s\pm}\rangle|s\rangle|k_1 n_1, ..., k_j n_j \pm 1, ...\rangle \tag{B.36}$$

As for $T = 0$, we will correct them to first order in the interaction hamiltonian $H_{int} = \hbar\lambda\sigma_z \sum_k \sqrt{\omega_k}(a_k^\dagger + a_k)$, and then calculate the square of the matrix element of σ_z, $|\langle i|\sigma_z|f\rangle|^2$.

Elements $|\langle i_{a,s}|\sigma_z|f_{a+,s+}\rangle|^2$ correspond to absorption by the "dressed" TLS of an energy $\hbar\omega_j$ from the mode k_j, while elements $|\langle i_{a,s}|\sigma_z|f_{a-,s-}\rangle|^2$ correspond to emission and "feeding" of the mode with a phonon $\hbar\omega_j$. The expressions for the initial states are

$$\begin{aligned}
|i_a\rangle = |a\rangle|k_1 n_1, ..., k_j n_j, ...\rangle \;\; &\rightarrow \;\; |a\rangle|k_1 n_1, ..., k_j n_j, ...\rangle + \sum_{k_i \ni n_i > 0} \frac{\hbar\lambda\sqrt{n_i\omega_i}}{\hbar\omega_i - 2\varepsilon}|s\rangle|...k_i n_i - 1...\rangle \\
&- \;\; \sum_{\forall k_i} \frac{\hbar\lambda\sqrt{(n_i+1)\omega_i}}{\hbar\omega_i + 2\varepsilon}|s\rangle|...k_i n_i + 1...\rangle \\
|i_s\rangle = |s\rangle|k_1 n_1, ..., k_j n_j, ...\rangle \;\; &\rightarrow \;\; |s\rangle|k_1 n_1, ..., k_j n_j, ...\rangle + \sum_{k_i \ni n_i > 0} \frac{\hbar\lambda\sqrt{n_i\omega_i}}{\hbar\omega_i + 2\varepsilon}|a\rangle|...k_i n_i - 1...\rangle \\
&- \;\; \sum_{\forall k_i} \frac{\hbar\lambda\sqrt{(n_i+1)\omega_i}}{\hbar\omega_i - 2\varepsilon}|a\rangle|...k_i n_i + 1...\rangle
\end{aligned} \tag{B.37}$$

and, for example, the state $|f_{a+}\rangle$ is given by

$$\begin{aligned}
|f_{a+}\rangle \;\; = \;\; & |a\rangle|k_1 n_1, ..., k_j n_j + 1, ...\rangle \rightarrow \\
& |a\rangle|k_1 n_1, ..., k_j n_j + 1, ...\rangle + \sum_{k_i \ni n_i > 0, i \neq j} \frac{\hbar\lambda\sqrt{n_i\omega_i}}{\hbar\omega_i - 2\varepsilon}|s\rangle|...k_i n_i - 1...k_j n_j + 1...\rangle \\
+ \;\; & \frac{\hbar\lambda\sqrt{(n_j+1)\omega_j}}{\hbar\omega_j - 2\varepsilon}|s\rangle|...k_j n_j...\rangle - \sum_{\forall k_i, i \neq j} \frac{\hbar\lambda\sqrt{(n_i+1)\omega_i}}{\hbar\omega_i + 2\varepsilon}|s\rangle|...k_i n_i + 1...k_j n_j + 1...\rangle \\
- \;\; & \frac{\hbar\lambda\sqrt{(n_j+2)\omega_j}}{\hbar\omega_j + 2\varepsilon}|s\rangle|...k_j n_j + 2...\rangle
\end{aligned} \tag{B.38}$$

with similar expression for the rest of states. The value of $|\langle i_{a,s}|\sigma_z|f_{a+,s+}\rangle|$ (absorption) is $|\langle i_{a,s}|\sigma_z|f_{a+,s+}\rangle| = \left|\frac{\lambda\sqrt{(n_j+1)\omega_j}4\varepsilon}{(\hbar\omega_j)^2 - 4\varepsilon^2}\right|$, with $n_j = 0, 1, ...$, while for emission the

result is $|\langle i_{a,s}|\sigma_z|f_{a-,s-}\rangle| = \left|\frac{\lambda\sqrt{n_j\omega_j}4\varepsilon}{(\hbar\omega_j)^2-4\varepsilon^2}\right|$, with $n_j = 1, ...$ Taking the limits we considered at T = 0 ($\hbar\omega_j \ll \varepsilon$ and $\hbar\omega_j \gg \varepsilon$) the results are the same as for T = 0 for absorption, except for a factor $(n_j + 1)$, and we also have now the possibility of emission, with the same matrix element but with the factor n_j:

$$\begin{array}{rl} \text{Absorption} & \left\{ \begin{array}{ll} \sim \frac{(n_j+1)\hbar\alpha_b\sqrt{\omega_{co}}\sqrt{\omega}}{\varepsilon^2} & \hbar\omega_j \ll \varepsilon \\ \sim \frac{(n_j+1)\alpha_b\sqrt{\omega_{co}}\varepsilon^2}{\hbar^3\omega^{7/2}}, & \hbar\omega_j \gg \varepsilon \end{array} \right. \\ \text{Emission} & \left\{ \begin{array}{ll} \sim \frac{n_j\hbar\alpha_b\sqrt{\omega_{co}}\sqrt{\omega}}{\varepsilon^2} & \hbar\omega_j \ll \varepsilon \\ \sim \frac{n_j\alpha_b\sqrt{\omega_{co}}\varepsilon^2}{\hbar^3\omega^{7/2}}, & \hbar\omega_j \gg \varepsilon \end{array} \right. \end{array} \tag{B.39}$$

Now we have to sum over all initial states, and noting that the first order correction to the energy of any eigenstate is 0, the partition function, Z, is easy to calculate, everything factorizes, and the result is, for example in the case $\hbar\omega_j \ll \varepsilon$:

$$\begin{aligned} A_{abs}(\varepsilon,\omega_j,T) &= \frac{1}{Z}\sum_{i\neq j,n_i=0}^{\infty}\sum_{n_j=0}^{\infty}\frac{\hbar\alpha_b\sqrt{\omega_{co}}\sqrt{\omega_j}}{\varepsilon^2}(n_j+1)e^{-\frac{\hbar\omega_j n_j}{kT}}e^{-\frac{\hbar\sum_i n_i\omega_i}{kT}} \\ &= \frac{\hbar\alpha_b\sqrt{\omega_{co}}}{\varepsilon^2}\frac{\sqrt{\omega_j}}{1-e^{-\frac{\hbar\omega_j}{kT}}} \\ A_{em}(\varepsilon,-\omega_j,T) &= \frac{1}{Z}\sum_{i\neq j,n_i=0}^{\infty}\sum_{n_j=1}^{\infty}\frac{\hbar\alpha_b\sqrt{\omega_{co}}\sqrt{\omega_j}}{\varepsilon^2}n_j e^{-\frac{\hbar\omega_j n_j}{kT}}e^{-\frac{\hbar\sum_i n_i\omega_i}{kT}} \\ &= \frac{\hbar\alpha_b\sqrt{\omega_{co}}}{\varepsilon^2}\frac{\sqrt{\omega_j}e^{-\frac{\hbar\omega_j}{kT}}}{1-e^{-\frac{\hbar\omega_j}{kT}}} \end{aligned} \tag{B.40}$$

In $A_{abs}(\varepsilon,\omega_j,T)$ we have added the contributions from the matrix elements

$$|\langle i_a|\sigma_z|f_{a+}\rangle|^2 e^{\frac{\varepsilon}{kT}} + |\langle i_s|\sigma_z|f_{s+}\rangle|^2 e^{\frac{-\varepsilon}{kT}} = |\langle i_a|\sigma_z|f_{a+}\rangle|^2[e^{\frac{\varepsilon}{kT}} + e^{\frac{-\varepsilon}{kT}}] \tag{B.41}$$

The sum of exponentials cancels with the partition function of the TLS (appearing as a factor in the total Z), leading in this way to the expression above (the same applies for $A_{em}(\varepsilon,-\omega_j,T)$). The total fluctuations will be proportional to their sum, which thus turns out to be at this level of approximation $\propto$ cotanh[$\hbar\omega_{\rm j}$/kT]:

$$A_{diss}(\varepsilon,\omega_j,T) = A_{abs}(\varepsilon,\omega_j,T) + A_{em}(\varepsilon,-\omega_j,T) = A_{diss}(\varepsilon,\omega_j,T=0)\text{cotanh}\Big[\frac{\hbar\omega_{\rm j}}{\rm kT}\Big] \tag{B.42}$$

In fact, this result applies for any other type of modes, independently of its dispersion relation, provided the coupling hamiltonian is linear in σ_z and $(a^\dagger_{-k} + a_k)$ and everything is treated at this level of perturbation theory. Moreover, it can be proven that if one has an externally excited mode with an average population $\langle n_j\rangle$, and fluctuations around that value are thermal-like, with a probability $\propto \exp[-|n_j - \langle n_j\rangle|/kT)]$, one recovers again the same temperature dependence, $\propto$ cotanh[$\hbar\omega_{\rm j}$/kT].

B.4 Q^{-1} due to the delayed response of biased TLSs (relaxation mechanism)

The derivation presented here is based mainly on pages 396-406 of ref. [Esq98]. We want to deduce the formula for the relaxation contribution to the attenuation of acoustic waves:

$$Q^{-1}(\omega,T)=\frac{P_0\gamma^2}{\rho v^2}\int_0^{\varepsilon_{max}}d\varepsilon\int_{u_{min}}^1 du\frac{\sqrt{1-u^2}}{u}\frac{1}{kT}\frac{1}{\cosh^2\left[\varepsilon/2kT\right]}\frac{\omega\tau}{1+(\omega\tau)^2} \tag{B.43}$$

Consider a set of TLSs with a difference of energy between their two eigenstates $\varepsilon=\varepsilon_2-\varepsilon_1$ and with instantaneous occupation fractions n_1 and n_2, that obey

$$\begin{cases} 1=n_1+n_2 \\ \dot{n}_1=-\nu_{21}n_1+\nu_{12}n_2 \end{cases} \tag{B.44}$$

where ν_{12} and ν_{21} are the transition rates due to the interaction of the TLS with the phonons, which reflect the finite response time of the TLS to a perturbation. This delayed response is responsible, together with the finite bias $\Delta_0^z>0$, of the dissipation (B.43), as we shall demonstrate. We will simplify the elasticity tensors and treat them as scalars. If we apply a periodic stress $\sigma(t)=\sigma_0 e^{-i\omega t}$ we perturb the energy levels, in the linear response approximation, according to

$$\varepsilon_\alpha(\sigma)=\varepsilon_\alpha(0)-v_0\lambda_{ij}^\alpha\sigma_{ij} \quad , \quad \varepsilon_\alpha(u)=\varepsilon_\alpha(0)-v_0 p_{ij}^\alpha u_{ij} \tag{B.45}$$

where

- v_0 is the unit cell volume,
- $\lambda_{ij}^\alpha=-(1/v_0)\partial\varepsilon_\alpha/\partial\sigma_{ij}$ is the elastic dipole of state α (also defined as the strain u_{ij} created by a homogeneous distribution of c defects per mole, $\lambda_{ij}^\alpha=\partial u_{ij}/\partial c^\alpha$),
- $p_{ij}^\alpha=-(1/v_0)\partial\varepsilon_\alpha/\partial u_{ij}$ is the so-called double force tensor (defined too as the stress σ_{ij} created by a homogeneous distribution of c defects per mole, $p_{ij}^\alpha=\partial\sigma_{ij}/\partial c^\alpha$)

Note that from the first definition of p_{ij}^α one can see that it is approximately proportional to the deformation potential γ_{ij}^α , $\gamma_{ij}^\alpha\simeq(1/2)\partial\Delta_z^\alpha/\partial u_{ij}=-v_0 p_{ij}^\alpha$. This last quantity is related to our coupling constant $\gamma_{ij}\sim\gamma$ of the interaction hamiltonian H_{int} through $\gamma_{ij}=2(\gamma_{ij}^2-\gamma_{ij}^1)$. So returning again to the applied periodic stress, it perturbs the energy levels, causing a variation in the TLS populations and the corresponding strain, according to $u_{ij}^{TLS}=c_\alpha\lambda_{ij}^\alpha$. We want to find an expression relating Δu_{ij}^{TLS} and $\sigma(t)$, from which we can deduce the associated dynamic compliance $\Delta S(\omega)=\Delta u/\sigma$. $S(\omega)$ is the inverse of the relative change of the elastic

stiffness, $\delta C(\omega) = \sigma/\Delta u$, the magnitude giving us the frequency shift and quality factor (eq.(B.43)) due to relaxational processes of TLSs.
We start dividing the instantaneous occupation fraction $n_1(t)$ as

$$n_1(t) = \bar{n}_1^0 + \Delta\bar{n}_1(t) + \delta n_1(t), \tag{B.46}$$

where $\bar{n}_1^0$ is the equilibrium value in the absence of stress, $\Delta\bar{n}_1(t)$ the perturbation to the equilibrium value due to the applied stress,

$$\Delta\bar{n}_1(t) = \frac{d\bar{n}_1}{d\varepsilon}\frac{\partial\varepsilon}{\partial\sigma}\sigma_0 e^{-i\omega t} = \Delta\bar{n}_1 e^{-i\omega t}, \tag{B.47}$$

$\bar{n}_1(t) = \bar{n}_1^0 + \Delta\bar{n}_1(t)$ is the instantaneous equilibrium value, $\delta n_1(t)$ is the deviation from the instantaneous equilibrium value due to the delayed response of the defects, and $\Delta n_1(t) = \Delta\bar{n}_1(t) + \delta n_1(t)$ is the deviation from the static equilibrium in the absence of applied stress,

$$\Delta n_1(t) = \Delta n_1 e^{-i\omega t}\,. \tag{B.48}$$

The definitions of $\Delta n_1(t)$ and $\delta n_1(t)$ imply that their amplitudes are complex, because they include a phase lag between the excitation and the response, due to the finite time needed for reaching the instantaneous equilibrium according to (B.44). The strain Δu_{ij}^{TLS} we need to compute $\Delta S(\omega)$ is that due to Δn_1, which is

$$\Delta u = \lambda_1\Delta n_1 + \lambda_2\Delta n_2 = \frac{c}{v_0}\frac{\partial\varepsilon}{\partial\sigma}\Delta n_1 \tag{B.49}$$

Now we want to extract the value of the complex phase appearing in eq.(B.48), and for that sake we have to manipulate a bit the rate equation (B.44): we begin using the condition for the equilibrium values of the populations (detailed balance condition),

$$\frac{d\bar{n}_1(t)}{dt} = 0 \quad\rightarrow\quad \bar{n}_1(t)\nu_{21} = \bar{n}_2(t)\nu_{12} \tag{B.50}$$

With this relation we transform (B.44) into

$$\frac{dn_1(t)}{dt} = -\frac{\delta n_1(t)}{\tau} \tag{B.51}$$

where $\tau^{-1} = \nu_{12} + \nu_{21}$. (B.51) indicates that the rate of change of the population is proportional to the deviation from the instantaneous equilibrium. Noting that

$$\frac{dn_1(t)}{dt} = \frac{d\Delta n_1(t)}{dt} = -i\omega\Delta n_1(t) \tag{B.52}$$

and

$$\delta n_1(t) = \Delta n_1(t) - \Delta\bar{n}_1(t) \tag{B.53}$$

and using (B.51), one obtains

$$\Delta n_1 = \frac{\Delta \bar{n}_1}{1 - i\omega\tau} = \Delta \bar{n}_1 \Big[\frac{1}{1 + (\omega\tau)^2} + i \frac{\omega\tau}{1 + (\omega\tau)^2} \Big] \tag{B.54}$$

So the dynamic compliance can be written as

$$\Delta S(\omega) = \frac{\Delta u}{\sigma} = \frac{c}{v_0} \frac{d\bar{n}_1}{d\varepsilon} \Big(\frac{\partial \varepsilon}{\partial \sigma} \Big)^2 \frac{1}{1 - i\omega\tau} \tag{B.55}$$

When one compares this result to the static compliance, it appears that the dynamic response function is obtained multiplying the static one by $(1 - i\omega\tau)^{-1}$. With the dynamic modulus $\delta C(\omega)$ an equivalent expression can be derived, with the roles of u and σ exchanged,

$$\delta C_{ijhk}(\omega) = \frac{\sigma}{\Delta u} = \frac{c}{v_0} \sum_{\alpha\beta} \frac{\partial n_\alpha}{\partial \varepsilon_\beta} \frac{\partial \varepsilon^\alpha}{\partial u_{ij}} \frac{\partial \varepsilon^\beta}{\partial u_{hk}} \frac{1}{1 - i\omega\tau} \tag{B.56}$$

Now, this can be rewritten observing that

$$\frac{\partial n_\alpha}{\partial \varepsilon_\beta} = \beta n_\alpha (n_\beta - \delta_{\alpha\beta}) \quad \text{and} \quad \sum_\alpha \mathrm{n}_\alpha = 1 \tag{B.57}$$

leading to

$$\delta C_{ijhk}(\omega) = \frac{c}{v_0} \beta n_\alpha n_\beta \Big(\frac{\partial \varepsilon^\beta}{\partial u_{ij}} - \frac{\partial \varepsilon^\alpha}{\partial u_{ij}} \Big) \Big(\frac{\partial \varepsilon^\beta}{\partial u_{hk}} - \frac{\partial \varepsilon^\alpha}{\partial u_{hk}} \Big) \frac{1}{1 - i\omega\tau} \tag{B.58}$$

To get to (B.43) we need a couple more transformations of this expression. First, if the energies of the eigenstates under strain u are given by

$$\varepsilon_{1,2}(u) = \mp \frac{1}{2} \sqrt{(\Delta_x)^2 + (\Delta_z + \sum_{ij} \gamma_{ij} u_{ij})^2}\,, \tag{B.59}$$

then eq.(2.21) is obtained, so that, together with the definition $\varepsilon = \varepsilon_2 - \varepsilon_1$, and the equivalence $n_1 n_2 = (1/4)\mathrm{sech}^2(\varepsilon/2\mathrm{k_B T})$, results in

$$\delta C_{ijhk}(\omega) = \frac{c}{v_0} \Big(\frac{\Delta_z}{\varepsilon} \Big)^2 \gamma_{ij} \gamma_{hk} \frac{\beta}{4} \mathrm{sech}^2(\varepsilon/2\mathrm{k_B T}) \frac{1}{1 - \mathrm{i}\omega\tau} \tag{B.60}$$

This is the result for a concentration of c defects per mole of TLSs with fixed ε and Δ_z. In the case of an amorphous solid one has instead a probability distribution in terms of the parameters Δ_x and Δ_z, $g(\Delta_x, \Delta_z) d\Delta_x d\Delta_z = P_0/\Delta_x d\Delta_x d\Delta_z$, which can be expressed with the variables $\varepsilon = \sqrt{(\Delta_x)^2 + (\Delta_z)^2}$ and $u = \Delta_z/\varepsilon$ as $g(\varepsilon, u) d\varepsilon du = P_0/(u\sqrt{1 - u^2}) d\varepsilon du$, with ε running from 0 to ε_{max} and u from u_{min} to 1. Writing

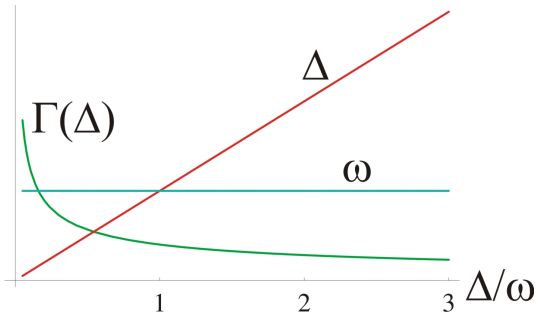

Figure B.2: Evolution with Δ_0^x of the different quantities determining the approximations to be taken in the integrand $\omega_0\tau/[1+(\omega_0\tau)^2]$ of eq.(B.43).

$\delta C_{ijhk}(\omega)$ in terms of ε and u, the inverse quality factor associated to the variations of the Young Modulus E, the component of C_{ijhk} entering the equations of motion of the vibration, is, as anticipated,

$$Q^{-1}(\omega,T) = \mathrm{Im}(\delta \mathrm{E})/\mathrm{E} = \frac{\mathrm{P}_0\gamma^2}{\rho \mathrm{v}^2}\int_0^{\varepsilon_{\max}} \mathrm{d}\varepsilon \int_{\mathrm{u}_{\min}}^1 \mathrm{du}\frac{\sqrt{1-\mathrm{u}^2}}{\mathrm{u}}\frac{1}{\mathrm{kT}}\frac{1}{\cosh^2\left[\varepsilon/2\mathrm{kT}\right]}\frac{\omega\tau}{1+(\omega\tau)^2} \tag{B.61}$$

B.5 Derivation of $Q^{-1}_{\rm rel}(\omega_0, T)$, eq.(2.23)

As discussed after eq.(B.43), we have to sum over underdamped TLSs, $\varepsilon \geq [30\alpha_b\sqrt{\omega_{co}}T]^{2/3}$, using the approximation for Γ, $\Gamma(\varepsilon,T) \sim 30\alpha_b\sqrt{\omega_{co}}T/\sqrt{\varepsilon}$. Moreover, if $\omega_0 \geq \Gamma(\epsilon = [30\alpha_b\sqrt{\omega_{co}}T]^{2/3}, T)$ then in the whole integration range $\omega_0 \gg \Gamma(\varepsilon,T) \Leftrightarrow \omega_0\tau(\varepsilon,T) \gg 1$, so that $\omega_0\tau/[1+(\omega_0\tau)^2] \approx 1/(\omega_0\tau)$, see fig.(B.2). $Q^{-1}_{\rm rel}(\omega_0,T)$ follows:

$$Q^{-1}_{\rm rel}(\omega_0,T) \approx \frac{P_0\gamma^2}{ET}\int_{[30\alpha_b\sqrt{\omega_{co}}T]^{2/3}}^{T} d\varepsilon \int_{u_{min}}^1 du\frac{\sqrt{1-u^2}}{u}\frac{\Gamma(\varepsilon,T)}{\omega_0} \tag{B.62}$$

For temperatures $T \gg [30\alpha_b\sqrt{\omega_{co}}T]^{2/3}$, which holds for reasonable T and sizes, the integral, which renders a result of the kind $Q^{-1}_{\rm rel}(\omega_0,T) \approx (1/\omega_0)(A\sqrt{T} - BT^{1/3})$, can be approximated by just the first term, obtaining eq.(2.23). In any case for completeness we give the expression for B:

$$B \approx \frac{500P_0\gamma^{14/3}}{t^2w^{4/3}}\frac{(1+\nu)^{4/3}(1-2\nu)^{4/3}}{E^{11/3}(3-5\nu)}\left(\frac{\rho}{E}\right)^{1/3} \tag{B.63}$$

Also for completeness we give the result for higher temperatures, although for current sizes the condition $\Gamma(\varepsilon = [30\alpha_b\sqrt{\omega_{co}}T]^{2/3}, T) > \omega_0$ implies values of T above the range of applicability of the Standard Tunneling Model. Now for some range of energies

$\Gamma(\varepsilon,T) > \omega_0$, and the range of integration is divided into two regions, one where $\omega_0\tau \gg 1$ and one where the opposite holds:

$$Q_{\rm rel}^{-1}(\omega_0,T) = \frac{P_0\gamma^2}{ET}\int_{u_{min}}^{1} du\frac{\sqrt{1-u^2}}{u}\times \left\{\int_{[30\alpha_b\sqrt{\omega_{co}}T]^{2/3}}^{[16\alpha_b\sqrt{\omega_{co}}2T/\sqrt{\omega_0}]^2} d\varepsilon\ \omega_0\tau(\varepsilon,T) + \int_{[16\alpha_b\sqrt{\omega_{co}}2T/\sqrt{\omega_0}]^2}^{T} d\varepsilon\frac{1}{\omega_0\tau(\varepsilon,T)}\right\} \tag{B.64}$$

The final result is $Q_{\rm rel}^{-1}(\omega_0,T) \approx -7P_0\gamma^2\omega_0/T + A\sqrt{T}/\omega_0 - CT/\omega_0^2$, with A defined by eq.(2.23) and C by:

$$C \approx \frac{1500P_0\gamma^6}{t^3w^2}\frac{(1+\nu)^2(1-2\nu)^2}{E^3(3-5\nu)^2}\Big(\frac{\rho}{E}\Big)^{1/2} \tag{B.65}$$

All the results for $Q_{\rm rel}^{-1}(\omega_0,T)$ have to be multiplied by the fraction of volume of the resonator presenting amorphous features, $V_{amorph}/(twL)$.

B.6 Derivation of eq.(2.27)

To calculate classically the energy stored of a torsional mode $\phi_j(z,t) = A\sin[(2j-1)\pi z/(2L)]\sin(\omega_j t)$ we just calculate the kinetic energy in a moment where the elastic energy is zero, for example at time $t=0$. If an element of mass is originally at position (x,y,z) (x,y transversal coordinates), with a torsion $\phi(z,t)$ it moves to

$$\mathbf{r}(t) = \Big(\sqrt{x^2+y^2}\cdot\cos\Big[\arccos\frac{x}{\sqrt{x^2+y^2}}+\phi\Big], \sqrt{x^2+y^2}\cdot\sin\Big[\arccos\frac{x}{\sqrt{x^2+y^2}}+\phi\Big], z\Big) \tag{B.66}$$

The kinetic energy at time $t=0$ is

$$E_0 = \int_0^L dz\int_{-t/2}^{t/2} dx\int_{-w/2}^{w/2} dy\cdot\frac{1}{2}\rho\Big|\frac{d\mathbf{r}}{dt}\Big|_{t=0}^2 \tag{B.67}$$

Substituting the expression for $\vec{r}(t)$ in the integrand, one arrives at

$$\begin{aligned} E_0 &= \int_0^L dz\int_{-t/2}^{t/2} dx\int_{-w/2}^{w/2} dy\cdot\frac{1}{2}\rho A^2\omega_j^2\sin^2\Big[\frac{(2j-1)\pi}{2L}z\Big](x^2+y^2) \\ &= \frac{1}{48}A^2\omega_j^2\rho L(t^3w+w^3t) \end{aligned} \tag{B.68}$$

In terms of the creation and annihilation operators

$$\phi_j(z,t) = \frac{\hbar}{2L\rho I\omega_j}(a_j^\dagger + a_j)e^{i(k_jz-\omega t)}\,, \tag{B.69}$$

so the mean square of its amplitude is $\langle\phi_j^2\rangle = A^2/2 = \hbar(2n+1)/[2L\rho I\omega_j]$. Substituting this in eq.(B.68) the eq.(2.27) for E_0 is obtained.

Appendix C

Appendix to Chapter 4

C.1 Electron-phonon coupling: friction in terms of the susceptibility χ

C.1.1 Damping of a phonon mode due to Coulomb interactions between charges in a device

We have seen in subsection 6.4.2 how the response of system to a given external perturbing field can be expressed, for weak perturbations, in terms of a susceptibility or response function. To be more concrete, we started from an interaction hamiltonian H_{int} acting as a perturbation on the initial one, H_0, and its eigenfunctions ϕ_i,

$$H_{int} = \int d\tilde{\mathbf{r}} V(\tilde{\mathbf{r}}, t)\rho(\tilde{\mathbf{r}}) \tag{C.1}$$

where $\rho(\tilde{\mathbf{r}}) = \sum_{\tilde{\mathbf{k}},\tilde{\mathbf{k}}'}[c^\dagger_{\tilde{\mathbf{k}}+\tilde{\mathbf{k}}'}c_{\tilde{\mathbf{k}}}e^{i\tilde{\mathbf{k}}'\tilde{\mathbf{r}}}+\text{h.c.}]$ is the charge operator, and the potential is an oscillating function of frequency ω, $V(\tilde{\mathbf{r}}, t) = V(\tilde{\mathbf{r}})e^{i\omega t}$. We saw in 6.4.2 that to linear order in H_{int} the variation in the particle density $n(\tilde{\mathbf{r}}, t) = \sum_i^{occ} |\phi_i'(\tilde{\mathbf{r}}, t)|^2$ with respect to the case in absence of perturbation can be expressed as

$$\delta n(\tilde{\mathbf{r}}) = \int d\tilde{\mathbf{r}}'\chi(\tilde{\mathbf{r}}, \tilde{\mathbf{r}}', \omega)V(\tilde{\mathbf{r}}'). \tag{C.2}$$

This can be taken as the definition of the *retarded density-density response function* χ for the charge density change at $\tilde{\mathbf{r}}$ induced by a potential field at $\tilde{\mathbf{r}}'$. In terms of a given approximation for the single-particle eigenstates $|i\rangle$ and eigenenergies e_i of the total hamiltonian $H_{tot} = H_0 + H_{int}$, it is expressed as

$$\chi(\tilde{\mathbf{r}}, \tilde{\mathbf{r}}', \omega) = \sum_i^{occ}\sum_j \langle j|n(\tilde{\mathbf{r}})|i\rangle\langle i|n(\tilde{\mathbf{r}}')|j\rangle\Big(\frac{1}{e_i - e_j - \hbar\omega} + \frac{1}{e_i - e_j + \hbar\omega}\Big). \tag{C.3}$$

The response frequencies of the system are given by the poles of the response function, which depend in turn on the approximation of the basis. For convenience we will generalize eq.(C.3) in terms of the N-body states $|\alpha\rangle$ of our system composed of N fermions. $|\alpha\rangle$ can be given, for example, by a Slater determinant of one-body states $|i\rangle$. We assume that the system starts in its ground state $|0\rangle$ (T=0 case). We define the fermionic creation operators $c_i^\dagger$ creating one-body states $|i\rangle$, so that

$$\chi(i,j,\omega) = \sum_\alpha \langle\alpha|c_i^\dagger c_j|0\rangle\langle 0|c_j^\dagger c_i|\alpha\rangle\Big(\frac{1}{\varepsilon_0-\varepsilon_\alpha-\hbar\omega}+\frac{1}{\varepsilon_0-\varepsilon_\alpha+\hbar\omega}\Big)\,. \tag{C.4}$$

Now we are interested in the probability per unit time that the field $V(\tilde{\mathbf{r}},t)$ transfers energy $\hbar\omega$ to the system. According to Fermi's Golden Rule of second-order perturbation theory the probability we are looking for is given by

$$\Gamma(V,\omega) = \frac{2\pi}{\hbar}\sum_\alpha |\langle\alpha|\hat{V}|0\rangle|^2\delta(\hbar\omega-\varepsilon_\alpha+\varepsilon_0) \tag{C.5}$$

Here $\hat{V} = \sum_{i,j}\langle j|V(\tilde{\mathbf{r}},t)|i\rangle c_i^\dagger c_j$ is the operator corresponding to $V(\tilde{\mathbf{r}},t)$ in the second-quantized basis $c_i^\dagger$. Eq.(C.5) can be expressed in terms of χ by providing the latter with an imaginary part through the addition of a small term $i\eta$ to ω, and then using the relation $\mathrm{Im}[1/(x-i\eta)] = \pi\delta(x)$. In this way we obtain the expression for Γ used in the thesis,

$$\Gamma(V,\omega) = \int d\tilde{\mathbf{r}}d\tilde{\mathbf{r}}' V(\tilde{\mathbf{r}})V(\tilde{\mathbf{r}}')\mathrm{Im}\chi(\tilde{\mathbf{r}},\tilde{\mathbf{r}}',\omega)\,. \tag{C.6}$$

Now the goal is to use a good approximation for the susceptibility function of our system.

C.1.2 Clean metal susceptibility

Suppose that our system is a metal. When the presence of impurities, electron-phonon collisions and electron-electron interactions is such that the collision frequency $\nu = 1/\tau$ of an electron is much less than the frequencies ω we are interested in, $\omega\tau \ll 1$, and/or the mean free path is much longer than the length scales L we study, $v_F\tau \gg L$, we are in the clean metal limit [NP99], where the susceptibility can be expressed in terms of elementary excitations. If one neglects electron-electron interactions (free electron gas), the retarded susceptibility is given by the bare bubble diagram:

$$\chi_0^R(\tilde{\mathbf{q}},\omega) = \frac{1}{V}\sum_{\tilde{\mathbf{k}},\sigma}\frac{n_F(\epsilon_{\tilde{\mathbf{k}}})-n_F(\epsilon_{\tilde{\mathbf{k}}+\tilde{\mathbf{q}}})}{\epsilon_{\tilde{\mathbf{k}}}-\epsilon_{\tilde{\mathbf{k}}+\tilde{\mathbf{q}}}+\hbar\omega+i\eta}, \tag{C.7}$$

where V is the volume of the system, $n_F(\epsilon)$ is the Fermi function, $\epsilon_{\tilde{\mathbf{k}}}-\epsilon_{\tilde{\mathbf{k}}+\tilde{\mathbf{q}}}$ are the excitation energies of the quasiparticles and $\eta\to 0$. The response of the system is

determined by the excitation of these one-body quasiparticle states, corresponding to zeroes of the real part of the denominator. The main effect of the inclusion of Coulomb interactions among electrons is the appearance of collective excitations, formed by a superposition of one-body states, called plasmons in the case of the electron gas. Their presence is manifested for example in an RPA calculation. RPA is the result of summing, for the interacting electron gas, the most important diagrams of each order [BF04], which turn out to be the ones of the bubbles, and these diagrams increase their importance as the density increases, so RPA is the high density limit of the interacting electron gas. The RPA result is the following:

$$\chi^R_{RPA}(\tilde{\mathbf{q}},\omega) = \frac{\chi^R_0(\tilde{\mathbf{q}},\omega)}{1 - V_{Coul}(\tilde{\mathbf{q}})\chi^R_0(\tilde{\mathbf{q}},\omega)}, \tag{C.8}$$

where V_{Coul} represents the Coulomb potential. The response will show peaks again in the zeroes of the real part of the denominator of $\chi^R_0(\tilde{\mathbf{q}},\omega)$, but now also when $1 - V_{Coul}(\tilde{\mathbf{q}})\chi^R_0(\tilde{\mathbf{q}},\omega) = 0$, which corresponds to collective excitations.

C.1.3 Dirty metal susceptibility

When due to the presence of impurities, electron-phonon collisions and electron-electron interactions the collision frequency $\nu = 1/\tau$ of an electron is higher than the frequencies ω we are interested in, $\omega\tau \gg 1$, and the mean free path is much shorter than the length scales L we study, $v_F\tau \ll L$, one enters the so-called hydrodynamic regime [NP99]. A given quasiparticle is subject to many collisions during one period of the exciting external field. It is thus completely "thermalized" well before it can sample the periodicity of the field. Therefore the best way to proceed is to assume that the collisions act to bring about everywhere a state of local thermodynamic equilibrium, and use just macroscopic "local" quantities (density, current, pressure, etc) to describe the state of the system; the response to the external field may be obtained by using the usual laws of thermodynamics and hydrodynamics. For high enough temperatures one arrives at an expression for the response function $\chi(\tilde{\mathbf{q}},\omega)$ which contains a peak corresponding to the plasmon and a continuous background arising from thermal diffusion. This background is the one described by eq.(4.15). Taking into account the plasmon contribution, eq.(4.15) becomes

$$\chi(\tilde{\mathbf{q}},\omega) = \frac{\nu D q^2}{Dq^2 - \omega^2\tau - i\omega}, \tag{C.9}$$

The plasmon contribution to the dissipation of the vibrational modes we study in this thesis can be safely neglected. Basically one has to see if $Dq^2 \gg \omega^2\tau$ in each of the layers (graphene and inversion layer in the Si-SiO_2 interface). In both cases one can take $D\nu \sim 10^3$, $\tau = l/v_F \sim 10^{-7}/10^6 \sim 10^{-13}$ s (assuming $l \sim 100$ nm), $q \sim 1/L \sim 10^6$ m^{-1}, $D = v_F l \sim 10^{11}$m^2/s. The density of states (DOS) of a stack

of N graphene layers is $\nu^C = N\gamma/\hbar^2 v_F^2$, being $\gamma \sim 0.3$ eV the interlayer hopping element. The DOS of the approximately two-dimensional electron gas lying in the inversion layer Si-SiO_2 is $\nu_{2DEG} \sim m*/\pi\hbar^2$, with $m* \sim 0.3m_{e^-}$ the effective mass of the electrons in Si. Using these values, $N \sim 10$, and for the frequencies of the oscillators analyzed, $\omega \sim 100$ MHz, one immediately verifies that indeed

$$Dq^2 \gg \omega,\, \omega^2\tau \quad \rightarrow \quad \mathrm{Im}\chi(\tilde{\mathbf{q}},\omega) \approx \frac{\nu\omega}{\mathrm{Dq}^2} \tag{C.10}$$

The inequalities are quite large, so there is place for substantial variations of l or N and they will still hold, justifying our use of eq.(4.15) and the limit $Dq^2 \gg \omega,\, \omega^2\tau$.

C.1.4 Microscopic derivation of eq.(4.15)

We sketch the analysis presented in [AS06]. This form of the susceptibility can be derived assuming a distribution of short-range scattering centers represented by potentials, creating an $V(\tilde{\mathbf{r}}) = \sum_i V_{imp}(\tilde{\mathbf{r}} - \tilde{\mathbf{r}}_i)$. To calculate propagators and physical magnitudes one has to perform in a final step a disorder average $\langle ... \rangle_{dis} = \int DV\ P[V](...)$, where the probability measure $P[V]$ describes the statistical properties of the potential V. In most applications it is sufficient to implement a Gaussian distribution, $P[V] = \exp\Big[-\frac{1}{2\gamma^2}\int d^dr d^dr' V(\tilde{\mathbf{r}})K^{-1}(\tilde{\mathbf{r}}-\tilde{\mathbf{r}}')V(\tilde{\mathbf{r}}')\Big]$, where γ measures the strength of the potential and K describes its spatial correlation profile, $\langle V(\tilde{\mathbf{r}})V(\tilde{\mathbf{r}}')\rangle_{dis} = \gamma^2 K(\tilde{\mathbf{r}} - \tilde{\mathbf{r}}')$. Very often one finds that the finite spatial correlation of V does not matter, in which case one may set $K(\tilde{\mathbf{r}}) = \delta(\tilde{\mathbf{r}})$, so that

$$\langle ... \rangle_{dis} = \int DV\ \exp\Big[-\frac{1}{2\gamma^2}\int d^dr V^2(\tilde{\mathbf{r}})\Big] \tag{C.11}$$

For length scales longer than the mean free path, so that the electrons experience multiple scattering, details of the form chosen for the potential $V(\tilde{\mathbf{r}})$ are quickly erased.

In practice, this average is very difficult to perform, and a series of techniques have been developed for mapping it into a different form. For example, in the replica field theory, the expectation value of an operator O is written in terms of a source J introduced conveniently in the action of the path integral representing the replicated partition function, $Z^R[J] = \int D(\Psi,\bar{\Psi})\exp\Big[-\sum_{a=1}^R S[\Psi^a,\bar{\Psi}^a,J]\Big]$,

$$\langle O\rangle = -(\partial/\partial J)\ln Z[J] = \lim_{R\to 0}\frac{1}{R}\frac{\partial Z^R[J]}{\partial J} = \lim_{R\to 0}\frac{1}{R}\sum_{a=1}^R\langle O(\Psi^a,\bar{\Psi}^a)\rangle_\Psi \tag{C.12}$$

When performing now the disorder average of the functional $Z^R[J]$ over the distribution $P[V]$, the result is the presence of a new effective interaction term in the action

of the system, with respect to the case without disorder:

$$\langle Z[J]\rangle_{dis} = \int D(\Psi,\bar{\Psi})\exp\Big[-\sum_{a=1}^{R} S|_{V=0}[\Psi^a,\bar{\Psi}^a\Big]+\sum_{a=1}^{R}]\frac{\gamma^2}{2}\sum_{mn}\int d^dr\bar{\Psi}^a_m(\tilde{\mathbf{r}})\Psi^a_m(\tilde{\mathbf{r}})\bar{\Psi}^b_n(\tilde{\mathbf{r}})\Psi^b_n(\tilde{\mathbf{r}}) \tag{C.13}$$

Then, one can apply perturbation theory to this interaction term to know what are the disorder averaged values of observables, or in our case of the susceptibility, using diagrammatic theory and an *ansatz* for the imaginary part of the self-energy correction to the fermion propagator, $\mathrm{Im}\Sigma(\omega_n) = -\mathrm{sgn}(\omega_n)/2\tau$, where τ is the so-called elastic scattering time, related to the elastic mean free path l by $\tau \equiv l/v_F$. One can see that this parameter is related to the potential strength γ^2 of the disorder potential by $\tau^{-1} = 2\pi\nu\gamma^2$, where ν is the density of states. Usually γ^2 is expressed through τ from the outset. The main results are

$$\begin{aligned}\langle G(\mathbf{x},\mathbf{y};\tau)\rangle_{dis} &= G(\mathbf{x},\mathbf{y};\tau)|_{V=0}e^{-|\mathbf{x}-\mathbf{y}|/2l}\\ \langle\chi(\mathbf{r},\tau)\rangle_{dis} &= \frac{T}{L^d}\sum_{\mathbf{q},\omega_m} e^{i\mathbf{q}\mathbf{r}+i\omega_m\tau}\frac{\nu Dq^2}{|\omega_m|+Dq^2}\end{aligned} \tag{C.14}$$

where $\chi(\mathbf{r},\tau)$ is the density-density correlation function (the susceptibility of a dirty metal).

C.2 Imχ, Q^{-1} and temperature dependence of friction

In order to make a connection between theory and experimental data a first point that has to be kept in mind is the following: Q^{-1}, the linewidth observed in the frequency domain of the response to an external driving force, does not correspond exclusively to an irreversible loss of energy of the mode (damping), but to all the processes which alter the phonon population of an excited mode of a certain frequency, including both increases and decreases of population. That is, Imχ, Q^{-1} correspond to the fluctuations of the given mode due to its coupling to other degrees of freedom of the system, giving a finite lifetime of the mode $(\mathbf{k}_0, n_{\mathbf{k}_0})$ subject of study due to any kind of process, including those increasing $n_{\mathbf{k}_0}$. Friction, instead, corresponds just to processes involving a decrease of $n_{\mathbf{k}_0}$.

C.2.1 Temperature dependence of Imχ, Q^{-1} due to excitation and relaxation of e-h pairs

Friction experienced by, for example, traveling charged particles through a host metal due to the excitation of e-h pairs has been subject of intensive research since a

long time [Gui84]. In the graphene resonator's case a similar effect produces absorption and fluctuations of energy, but there is an important difference with the previous example: we are studying the linewidth of a single bending mode of a well-defined wavevector $\tilde{\mathbf{q}}$ and frequency $\omega_{\tilde{\mathbf{q}}}$, so we will not sum over frequencies to calculate the total absorption and fluctuations of the resonator's vibrational modes due to this mechanism. More specifically, we want to calculate

$$\Gamma(\omega_{\tilde{\mathbf{q}}}, T) = \int d^3\tilde{\mathbf{r}} \int d^3\tilde{\mathbf{r}}' \mathrm{ReV}_{\mathrm{scr}}(\tilde{\mathbf{r}}, \omega_{\tilde{\mathbf{q}}}) \mathrm{ReV}_{\mathrm{scr}}(\tilde{\mathbf{r}}', \omega_{\tilde{\mathbf{q}}}) \mathrm{Im}\chi[\tilde{\mathbf{r}} - \tilde{\mathbf{r}}', \omega_{\tilde{\mathbf{q}}}, \mathrm{T}] \tag{C.15}$$

And for this we need $\mathrm{Im}\chi[\tilde{\mathbf{r}} - \tilde{\mathbf{r}}', \omega_{\tilde{\mathbf{q}}}, T]$. To obtain the dependence with T we can recall the fact that, embedded in $\mathrm{Im}\chi$, what we are looking for is the sum of e-h transitions that absorb an energy $\omega_{\tilde{\mathbf{q}}}$ from the vibrational mode $(\tilde{\mathbf{q}}, \omega_{\tilde{\mathbf{q}}})$ through H_{int} plus desexcitations that transfer an energy $\omega_{\tilde{\mathbf{q}}}$ to that mode. We will begin by analyzing the $T = 0$ case, where only the former can take place, so that dissipation and fluctuations are indistinguishable. We will see that for a given frequency $\omega \ll E_F/\hbar$, the e-h transitions available are proportional to ω, independently of the dimension of the fermionic bath. It is a direct consequence of the exclusion principle through the restrictions imposed by the Fermi distribution functions $n_F(E) = 1/[1 + \exp[(E - E_F)/k_B T]]$ appearing. Taking for example a 3D Fermi gas, with dispersion relation $E = \sum_i \frac{\hbar^2 k_i^2}{2m}$, the probability of exciting an e-h pair of frequency ω will be proportional to the number of such pairs available, $P(\omega)$,

$$P(\omega) = \int d^3\tilde{\mathbf{k}} \int d^3\tilde{\mathbf{k}}' n_F(E(\tilde{\mathbf{k}})) \Big[1 - n_F(E(\tilde{\mathbf{k}}'))\Big] \delta\Big(\omega - \frac{E(\tilde{\mathbf{k}}) - E(\tilde{\mathbf{k}}')}{\hbar}\Big) \tag{C.16}$$

Expressing the integrals in terms of energies and making the approximation $\hbar\omega \ll E_F$,

$$\begin{aligned} P(\omega) &\propto \int_0^\infty dE \sqrt{E(E + \hbar\omega)} n_F(E)[1 - n_F(E + \hbar\omega)] \\ &= \int_{E_F - \hbar\omega}^{E_F} dE \sqrt{E(E + \hbar\omega)} \simeq E_F \times \hbar\omega \sim \omega \end{aligned} \tag{C.17}$$

In the case we took a fermionic bath of a different dimension, the only difference in the calculation would arise in the factor which in the 3D case is $\sqrt{E(E + \hbar\omega)}$, which will be in general a function $f(E, \hbar\omega)$. But as long as this is a smooth function of E and $\hbar\omega$, for $\hbar\omega \ll E_F$ we can approximate $f(E, \hbar\omega) \approx f(E_F, 0)$ and arrive again at $P(\omega) \sim \omega$. At $T = 0$ only excitations of e-h pairs from the ground state can occur, so the net absorption rate involving excitations of frequency ω will be indeed proportional to ω.

At finite temperatures there will be absorption and emission processes. First we will calculate the number of e-h excitations of a certain frequency ω which will cause

energy absorption, as in the $T = 0$ case:

$$P(\omega,T) = \int d^n\tilde{\mathbf{k}} \int d^n\tilde{\mathbf{k}}' n_F(E(\tilde{\mathbf{k}})/k_BT)\Big[1 - n_F(E(\tilde{\mathbf{k}}')/k_BT)\Big]\delta\Big(\omega - \frac{E(\tilde{\mathbf{k}}) - E(\tilde{\mathbf{k}}')}{\hbar}\Big) \tag{C.18}$$

For frequencies and temperatures such that $\hbar\omega \ll k_BT \ll E_F$ one can approximate

$$\begin{aligned} P(\omega,T) &\propto \int_0^\infty dE f(E,\hbar\omega) n_F(E/k_BT)[1 - n_F([E+\hbar\omega]/k_BT)] \\ &\approx f(E_F,0)\int_0^\infty dE n_F(E/k_BT)[1 - n_F(E/k_BT)] \\ &= f(E_F,0) \times k_BT \times \int_0^\infty dx\, n_F(x)[1 - n_F(x)] \sim T \end{aligned} \tag{C.19}$$

So for excitation frequencies much smaller than the temperature the number of available excitations absorbing energy is proportional to T, and roughly independent of ω. The number of desexcitations compensating this absorption processes has a similar expression:

$$P'(\omega,T) \propto \int_0^\infty dE f(E,\hbar\omega) n_F([E+\hbar\omega]/k_BT)[1 - n_F(E/k_BT)], \tag{C.20}$$

and is also proportional to T, leading to $\mathrm{Im}\chi(T), Q^{-1}(T) \sim T$.

C.2.2 Temperature dependence of energy loss due to excitation and relaxation of e-h pairs

The net amount of energy absorbed by the fermionic environment of e-h pairs of frequency ω at a finite temperature, $A(\omega,T)$, for $\hbar\omega \ll k_BT \ll E_F$, is proportional to

$$A(\omega,T) \propto P(\omega,T) - P'(\omega,T) \propto \int_0^\infty dE f(E,\hbar\omega)\Big\{n_F(E/k_BT) - n_F([E+\hbar\omega]/k_BT)\Big\}, \tag{C.21}$$

and it can be approximated as

$$\begin{aligned} A(\omega,T) &\propto f(E_F,0)\int_0^\infty dE\Big\{n_F(E/k_BT) - n_F([E+\hbar\omega]/k_BT)\Big\} \\ &= f(E_F,0) \times k_BT \times \int_{-E_F/k_BT}^{-(E_F-\hbar\omega)/k_BT} dx\, n_F(x) \\ &\approx f(E_F,0) \times \frac{1}{1+e^{-E_F/k_BT}} \times \hbar\omega \sim \omega \end{aligned} \tag{C.22}$$

The net absorption of energy due to pairs of frequency ω is therefore to a first approximation proportional to ω and independent of T.

C.2.3 Extension to a generic system + bath

Suppose that the subsystem subject of study, characterized by the index $\tilde{\mathbf{k}}$, is coupled linearly to a bath of excitations,

$$H_{int} \propto (c^\dagger_{\tilde{\mathbf{k}}} + c_{\tilde{\mathbf{k}}}) \times \sum_{\tilde{\mathbf{q}}} \lambda_{\tilde{\mathbf{q}}} (b^\dagger_{\tilde{\mathbf{q}}} + b_{\tilde{\mathbf{q}}}), \tag{C.23}$$

where $c^\dagger_{\tilde{\mathbf{k}}}$ and $b^\dagger_{\tilde{\mathbf{q}}}$ represent subsystem and bath creation operators, respectively. We can calculate at $T = 0$

$$J_{gen}(\omega) = \int_{-\infty}^{\infty} dt\, e^{i\omega t} \langle H_{int}(t) H_{int}(0) \rangle \sim \omega^s \ , \tag{C.24}$$

which as we saw in Appendix B.2 reflects the evolution as a function of ω, up to second order in perturbation theory, of the amount of possible transitions (fluctuations) from a starting initial state (at $T = 0$ the ground state) to all final states for whom an energy $\hbar\omega$ has been exchanged between our subsystem and the bath. As temperature grows, for $T \gg \omega$, the amount of accessible transitions thanks to the thermal energy present in the system will consequently grow as T^s, so that $\mathrm{Im}\chi(T), Q^{-1}(T) \sim T^s$, at least when the perturbation H_{int} is not too strong.

C.3 Charge impurity density in SiO_2 and the SiO_2-Si interface

From refs. [Sze81, NB82]. In ref. [Sze81] they speak of four types of interface trapped charges:

1. Just in the interface, due to the interruption of the periodic lattice structure, there is the so-called *interface-trapped charge* Q_{it}. Densities as low as $Q_{it} \sim 10^{10}$ cm^{-2} are achieved by low-temperature (450°C) hydrogen annealing. These charges are associated to traps, called interface traps, which change occupancy with gate bias changes and have energy levels distributed throughout the bandgap. Interface traps characteristic of thermal oxidation are *donor* type in the upper half of the bandgap.

2. Close to the Si-SiO_2 interface there are also charge centers called *oxide fixed charge*, Q_{fc}, predominantly positive, immobile and with fixed charge when a gate voltage is applied. Experiments locate it within 30 Å of the interface.

3. There are *positive mobile ionic charges*, Q_m, related to trace contamination by alkali metal ions, causing reliability problems in semiconductor devices operated at high temperatures and voltages. Films impervious to mobile ions, such as

Si_3N_4 can prevent mobile ionic charge contamination of the oxide during device life, but there is no such film in our case. Effective densities $Q_m \sim 10^{10}$ cm^{-2} can be achieved without films.

4. There are oxide traps associated with defects in SiO_2, which are usually electrically neutral, and are charged by introducing electrons and holes into the oxide, originating *oxide trapped charge*.

5. During the diffusion of oxigen creating the oxide layer, if the process is fast enough, a considerable amount of dopant impurities (B, P, As or Sb) may be left in the oxide, although their diffusion coefficients in silicon dioxide are very small compared to the ones in silicon. In [YOTT79] experiments were made where up to 20% of the phosphorous was trapped inside the oxide during the oxidation in wet oxygen process at temperatures between 750 and 900°C.

These charges give rise to a charge density in the oxide layer, ρ_{ox}. Unfortunately, the published literature lacks the information on this quantity for oxides used in MEMS applications. What has been extracted from high-frequency capacitance-voltage curves of MOS capacitors is the *effective interface charge density* Q_f, which corresponds to

$$Q_f = \int_0^{t_{ox}} \frac{x}{t_{ox}} \rho_{ox} dx + Q_{it} \tag{C.25}$$

In [FKDB02] they mention that the breakdown field value for SiO_2 is $\sim$ 1 V/nm. This means that in typical graphene experiments, where the potentials are about 100 V applied through an oxide layer 300 nm thick, the field is 1/3 of the breakdown field, so most probably all the potentially chargeable impurities within the oxide will be charged. Indeed, in [KHDS02] a field of about 0.03 V/nm was sufficient to polarize the SiO_2 dielectric, and in [RFTJ02] they mention that the bulk oxide traps become charged with injection of electrons from the nanotube at gate fields above 0.03 V/nm.

C.3.1 Estimate of the charge concentration, and comparison with numbers given in other references to fit experiments

From the experimental Q_f values in [AP87], where a MOS setup with a 200 nm oxide layer, and p-type silicon (the most common choice for mass-produced chips) with doping $N_A = 4 \cdot 10^{15}$ cm^{-3} was the subject of the measurements, the authors in [WS04] extract the value of the quantity

$$Q_{ox} = \int_0^{t_{ox}} \rho_{ox} dx + Q_{it}, \tag{C.26}$$

where t_{ox} is the thickness of the oxide layer, assuming several distributions of charge in the oxide. If one chooses the charges to be concentrated in a layer of 20 nm starting from the interface and $Q_{it} = 0$, the result is

$$\rho_{ox} \sim 1.5 \cdot 10^{16} \text{ charges/cm}^3 \tag{C.27}$$

If instead of that one assumes a uniform distribution of charge throughout the oxide, the result is

$$\rho_{ox} \sim 3 \cdot 10^{15} \text{ charges/cm}^3 \tag{C.28}$$

C.3.2 Thickness of the charged layer in the doped Si gate

From [Sze81]. When one applies a voltage between the graphene and the p-doped Si electrode, the first effect at low voltages ($\sim$ 1 V) is to populate the intergap states associated with the impurities, creating a region of a certain thickness where all impurities are charged, so there the charge density is just the doping N_A, which for a typical low-doped Si wafer is $N_A \sim 10^{15} - 10^{16}\text{cm}^{-3}$. For that scale of voltages the thickness soon reaches a maximum value W_m before the complete depletion regime is reached. This value can be calculated as

$$W_m = \sqrt{\frac{4\epsilon_s k_B T \ln(N_A/n_i)}{q^2 N_A}}, \tag{C.29}$$

where $\epsilon_s \sim 11.9\epsilon_0$ is the dielectric constant of Si, $n_i \sim 10^{10}$ cm^{-3} its intrinsic doping (everything at room temperature), and q the electron charge. For a low-doped Si wafer one has $W_m \sim 450$ nm. The complete depletion regime is reached when the voltages applied are enough to curve the bands close to the Si-SiO_2 interface until the Fermi level reaches the bottom of the conduction band. Due to the high density of states of the band the charge density will increase dramatically in a narrow region $\sim$ 10 nm thick as the voltage is further raised, overwhelming the amount of charge corresponding to the intergap states, so for high voltages (for example typical values $V \sim 100$ V) the approximation of a 2D charged Si layer is reasonable for typical oxide thicknesses $t_{SiO_2} \sim 300$ nm.

The voltage that really matters is the one at the Si-SiO_2 interface, which can be safely taken as of the order of the potential applied between the electrodes.

C.3.3 Information about the SiO_2 surface and structure. Conclusions from experiments with carbon nanotubes

The strong adherence of the graphene layer to the SiO_2 substrate is probably due to the presence of Hydroxyl groups in the surface of the latter, which form hydrogen bonds with the carbon layer. When setting the graphene sheet into periodic motion,

a repeated breaking and healing of some these bonds (like a Velcro) can be a source of short-wavelength phonons which carry away part of the energy initially stored in the resonator, thus damping its motion. How many OH's are there? In ref. [SG95] they analyze Hydroxyl groups on a well-defined silica surface, and mention that isolated Si-OH will survive anneals at over 1000 ^{o}C, presumably because there is nowhere for the hydrogen to go: it needs to find another hydrogen to be removed as H_2 or even H_2O. As the concentration of H at the surface is reduced this becomes increasingly improbable. Adding hydrogen atoms from e.g. a hydrogen plasma helps desorb the remaining isolated Si-OH, but in any case the surface density of a previously fully hydroxylated surface after high-temperature annealing is ~ 1 OH/nm$^2 = 10^{14}$OH/cm^2. This is in agreement with another experiment [DPX98], which estimates a surface density of isolated silanol groups on a flat silica surface of about $9 \cdot 10^{13}$silanol/cm^2, thus supporting the idea of either a simultaneous breaking of a great number hydrogen bonds, for a resonator $\sim 1\mu$m wide, or no breaking of bonds at all.

The presence of oxide trapped charges within the SiO_2 and of other surface impurities has attracted the attention in several studies where its influence and possible use in carbon nanotube field-effect transistors has been contemplated [FKDB02, RFTJ02, KJV$^+$03, FTK$^+$06]. The most interesting conclusion for us is the one of [KJV$^+$03], where they show after systematic studies that there is a monolayer or submonolayer of water molecules hydrogen bonded to the Si-OH silanol groups all over the SiO_2 surface, which cannot be removed by pumping in vacuum over extended periods of time at room temperature. These molecules can store charge when a voltage is applied between the CNT and the underlying p-doped Si backgate, and are the main cause of hysteresis in I-V cycles, much more than the underlying oxide trapped charges within the SiO_2 substrate. These bulk charges were invoked incorrectly in [FKDB02, RFTJ02] as the main cause of hysteresis.

Returning to the surface water molecules, they manage in [KJV$^+$03] to estimate the charging per H_2O to be roughly $0.1|e|$ per molecule.

They also suggest ways to get rid of the molecules by combining i) thermal annealing in a dry atmosphere with simultaneous passivation of the surface with PMMA, which links strongly to the silanol groups and is also hydrophobic, ii) the permanent immersion of the passivated surfaces in dry oxygen atmosphere. In [FTK$^+$06] they also point out that a PMMA coating of the oxide surface changes locally the dielectric constant (it is 3.3-3.9 at 60 KHz, and 2.2-3.2 at 1 MHz, a bit smaller than the one of the oxide, 3.9).

In [FTK$^+$06] they say that logically the regions in the oxide which will be first charged will be those subject to the highest fields, which in the case of nanotubes will be close to the nanotube. They also estimate that trapped charges close to the CNT are expected to produce potential fluctuations on the length scale of the screening length $\lambda_{scr} \sim \sqrt{\frac{\epsilon_{CNT}}{\epsilon_{ox}} t_{CNT} t_{ox}} \sim 40$ nm ($\epsilon_{CNT} \sim 20$, $t_{CNT} \sim 3$ nm is the diameter of

the CNT and $t_{ox} = 100$ nm is the oxide thickness in their case). This formula for estimating the screening length is derived in [YOL92].

C.4 Screening of the potentials at the graphene sheet and Si gate

The equations for the selfconsistent potentials $v_{scr}(z, \tilde{\mathbf{r}} - \tilde{\mathbf{r}}', \omega)$ as a function of the bare potentials $v_0^j(z, \tilde{\mathbf{r}} - \tilde{\mathbf{r}}', \omega)$ are given by

$$\begin{aligned}
v_{scr}(d, \tilde{\mathbf{r}} - \tilde{\mathbf{r}}', \omega) &= v_0^C(d, \tilde{\mathbf{r}} - \tilde{\mathbf{r}}', \omega) + v_0^G(d, \tilde{\mathbf{r}} - \tilde{\mathbf{r}}', \omega) \\
&+ \int_C d\tilde{\mathbf{r}}_1 \int_C d\tilde{\mathbf{r}}_2 v_{\text{Coul}}(d, \tilde{\mathbf{r}} - \tilde{\mathbf{r}}_1, \omega) \chi^C(\tilde{\mathbf{r}}_1 - \tilde{\mathbf{r}}_2, \omega) v_{scr}(d, \tilde{\mathbf{r}}_2 - \tilde{\mathbf{r}}', \omega) \\
&+ \int_G d\tilde{\mathbf{r}}_3 \int_G d\tilde{\mathbf{r}}_4 v_{\text{Coul}}(d, \tilde{\mathbf{r}} - \tilde{\mathbf{r}}_3, \omega) \chi^G(\tilde{\mathbf{r}}_3 - \tilde{\mathbf{r}}_4, \omega) v_{scr}(0, \tilde{\mathbf{r}}_4 - \tilde{\mathbf{r}}', \omega) \\
v_{scr}(0, \tilde{\mathbf{r}} - \tilde{\mathbf{r}}', \omega) &= v_0^G(0, \tilde{\mathbf{r}} - \tilde{\mathbf{r}}', \omega) + v_0^C(0, \tilde{\mathbf{r}} - \tilde{\mathbf{r}}', \omega) \\
&+ \int_G d\tilde{\mathbf{r}}_1 \int_G d\tilde{\mathbf{r}}_2 v_{\text{Coul}}(0, \tilde{\mathbf{r}} - \tilde{\mathbf{r}}_1, \omega) \chi^G(\tilde{\mathbf{r}}_1 - \tilde{\mathbf{r}}_2, \omega) v_{scr}(0, \tilde{\mathbf{r}}_2 - \tilde{\mathbf{r}}', \omega) \\
&+ \int_C d\tilde{\mathbf{r}}_3 \int_C d\tilde{\mathbf{r}}_4 v_{\text{Coul}}(0, \tilde{\mathbf{r}} - \tilde{\mathbf{r}}_3, \omega) \chi^C(\tilde{\mathbf{r}}_3 - \tilde{\mathbf{r}}_4, \omega) v_{scr}(d, \tilde{\mathbf{r}}_4 - \tilde{\mathbf{r}}', \omega) \ ,
\end{aligned} \tag{C.30}$$

where for example in the first equation $v_0^C(d, \tilde{\mathbf{r}} - \tilde{\mathbf{r}}', \omega)$ represents the bare potential experienced by a point charge e in the graphene layer due to the presence of charges in that same layer, while $v_0^G(d, \tilde{\mathbf{r}} - \tilde{\mathbf{r}}', \omega)$ is the bare potential experienced by a point charge e in the graphene layer due to the presence of charges in the Si plane. v_{Coul} is the two-dimensional bare Coulomb potential. These equations simplify considerably in the $\tilde{\mathbf{q}}$ space, assuming 2D translational invariance:

$$\begin{cases}
v_{scr}(d, \tilde{\mathbf{q}}, \omega) = v_0^C(d, \tilde{\mathbf{q}}, \omega) e^{qd} + v_0^G(d, \tilde{\mathbf{q}}, \omega) + \\
\qquad + v_q \chi^C(\tilde{\mathbf{q}}, \omega) v_{scr}(d, \tilde{\mathbf{q}}, \omega) + v_q e^{-qd} \chi^G(\tilde{\mathbf{q}}, \omega) v_{scr}(0, \tilde{\mathbf{q}}, \omega) \\
v_{scr}(0, \tilde{\mathbf{q}}, \omega) = v_0^C(0, \tilde{\mathbf{q}}, \omega) + v_0^G(d, \tilde{\mathbf{q}}, \omega) e^{qd} + \\
\qquad + v_q e^{-qd} \chi^C(\tilde{\mathbf{q}}, \omega) v_{scr}(d, \tilde{\mathbf{q}}, \omega) + v_q \chi^G(\tilde{\mathbf{q}}, \omega) v_{scr}(0, \tilde{\mathbf{q}}, \omega)
\end{cases} \tag{C.31}$$

, where $v_q = 2\pi e^2/|\tilde{\mathbf{q}}|$ is the Fourier transform of the Coulomb potential in two dimensions, and where $v_0^G(0, \tilde{\mathbf{q}}, \omega)$ and $v_0^C(d, \tilde{\mathbf{q}}, \omega)$ have been expressed in terms of $v_0^G(d, \tilde{\mathbf{q}}, \omega)$ and $v_0^C(0, \tilde{\mathbf{q}}, \omega)$. Now we can calculate $v_{scr}(d, \tilde{\mathbf{q}}, \omega)$ and $v_{scr}(0, \tilde{\mathbf{q}}, \omega)$ in

terms of the rest of the variables,

$$\begin{pmatrix} v_{scr}(d) \\ v_{scr}(0) \end{pmatrix} = \begin{pmatrix} 1 - v_q\chi^C & -v_q e^{-qd}\chi^G \\ -v_q e^{-qd}\chi^C & 1 - v_q\chi^G \end{pmatrix}^{-1} \times \begin{pmatrix} e^{qd} & 1 \\ 1 & e^{qd} \end{pmatrix} \begin{pmatrix} v_0^C(0) \\ v_0^G(d) \end{pmatrix} \quad \text{(C.32)}$$

The dependence on $\tilde{\mathbf{q}}$ and ω has been omitted for the sake of clarity. Now, if we are interested only in the long wavelenght limit $v_q\chi^C, v_q\chi^G \gg 1$, the last equation simplifies to

$$\begin{aligned} \begin{pmatrix} v_{scr}(d) \\ v_{scr}(0) \end{pmatrix} &= \frac{1}{v_q^2\chi^C\chi^G\Big(1 - e^{-2qd}\Big)} \times \\ &\times \begin{pmatrix} v_q\Big(\chi^C e^{-qd} - \chi^G e^{qd}\Big) & v_q\Big(-\chi^G + \chi^C\Big) \\ v_q\Big(-\chi^C + \chi^G\Big) & v_q\Big(\chi^G e^{-qd} - \chi^C e^{qd}\Big) \end{pmatrix} \begin{pmatrix} v_0^C(0) \\ v_0^G(d) \end{pmatrix} \end{aligned} \quad \text{(C.33)}$$

Values of $v_0^C(0, \tilde{\mathbf{q}}, \omega)$ and $v_0^G(d, \tilde{\mathbf{q}}, \omega)$

Now we will calculate the parts of these terms which will give rise to a coupling to the vibration. When the graphene layer is set into motion with a bending mode of wavevector $\tilde{\mathbf{q}}$ and amplitude $A_{\tilde{\mathbf{q}}}$, the potential $v_0^C(0, \tilde{\mathbf{r}}, t)$ of a point charge e in the Si plane due to the charge in the graphene layer is

$$\begin{aligned} v_0^C(0, \tilde{\mathbf{r}}, t) &= \frac{1}{2}\int_C d\tilde{\mathbf{r}}' v_{\text{Coul}}(\tilde{\mathbf{r}} - \tilde{\mathbf{r}}', z')\rho(\tilde{\mathbf{r}}', z', t) \\ &= \frac{1}{2}\int_C d\tilde{\mathbf{r}}' \frac{2\pi e^2\rho_0}{\sqrt{(\tilde{\mathbf{r}} - \tilde{\mathbf{r}}')^2 + (d + A_{\tilde{\mathbf{q}}}e^{i(\tilde{\mathbf{q}}\tilde{\mathbf{r}}' - \omega_{\tilde{\mathbf{q}}}t)})^2}} \\ &\approx \frac{1}{2}\int_C d\tilde{\mathbf{r}}' \frac{2\pi e^2\rho_0}{\sqrt{(\tilde{\mathbf{r}} - \tilde{\mathbf{r}}')^2 + d^2}} + \frac{1}{2}\int_C d\tilde{\mathbf{r}}' \frac{2\pi e^2\rho_0 A_{\tilde{\mathbf{q}}}e^{i(\tilde{\mathbf{q}}\tilde{\mathbf{r}}' - \omega_{\tilde{\mathbf{q}}}t)}d}{\Big((\tilde{\mathbf{r}} - \tilde{\mathbf{r}}')^2 + d^2\Big)^{3/2}} \\ &\approx f(\tilde{\mathbf{r}}) + \pi e^2\rho_0 A_{\tilde{\mathbf{q}}}e^{-dq}e^{i(\tilde{\mathbf{q}}\tilde{\mathbf{r}} - \omega_{\tilde{\mathbf{q}}}t)} \end{aligned} \quad \text{(C.34)}$$

where in the third line an expansion for small $A_{\tilde{\mathbf{q}}}$ has been performed. The Fourier transform for $\omega \neq 0$ is

$$v_0^C(0, \tilde{\mathbf{k}}, \omega') = \pi e^2\rho_0 A_{\tilde{\mathbf{q}}}e^{-dq}\delta(\tilde{\mathbf{k}} - \tilde{\mathbf{q}})\delta(\omega' - \omega_{\tilde{\mathbf{q}}}) \quad , \quad |\tilde{\mathbf{q}}| = 1/L \quad \text{(C.35)}$$

Similarly, the potential of a point charge in the oscillating graphene sheet due to the charge in the Si plane $v_0^G(d)$, is

$$v_0^G(d, \tilde{\mathbf{r}}, t) = \frac{1}{2}\int_G d\tilde{\mathbf{r}}' \frac{2\pi e^2\rho_0}{\sqrt{(\tilde{\mathbf{r}} - \tilde{\mathbf{r}}')^2 + (d + A_{\tilde{\mathbf{q}}}e^{i(\tilde{\mathbf{q}}\tilde{\mathbf{r}} - \omega_{\tilde{\mathbf{q}}}t)})^2}} \approx f(\tilde{\mathbf{r}}) + \pi e^2\rho_0 A_{\tilde{\mathbf{q}}}e^{i(\tilde{\mathbf{q}}\tilde{\mathbf{r}} - \omega_{\tilde{\mathbf{q}}}t)} \quad \text{(C.36)}$$

leading to the same expression as eq.(C.35) but without the factor e^{-qd}

$$v_0^G(d,\tilde{\mathbf{k}},\omega') = v_0^C(0,\tilde{\mathbf{k}},\omega')e^{qd} \tag{C.37}$$

Substituting (C.35,C.37) in eq.(C.33), one obtains eq.(4.17).

C.5 Dissipation due to two-level systems in graphene resonators

C.5.1 Model and vibrating modes of a 2D sheet

The hamiltonian describing the coupling of the effective TLS's and the oscillating graphene sheet is given by [SGC07a]

$$H = \epsilon\,\sigma_x + \gamma\frac{\Delta_0^x}{\epsilon}\sigma_z\sum_{\mathbf{k}}\lambda_{\mathbf{k}}(b_{\mathbf{k}}+b_{\text{-}\mathbf{k}}^\dagger) + \sum_{\mathbf{k}}\hbar\omega_{\mathbf{k}}b_{\mathbf{k}}^\dagger b_{\mathbf{k}} \tag{C.38}$$

where $\epsilon = \sqrt{(\Delta_0^x)^2+(\Delta_0^z)^2}$, $b_{\mathbf{k}}^\dagger$ represent the phonon creation operators associated to the different vibrational modes of a sheet, and $\sum_{\mathbf{k}}\lambda_{\mathbf{k}}(b_{\mathbf{k}}+b_{\text{-}\mathbf{k}}^\dagger)$ represents the coupling to the strain tensor u_{ik}. There are two types, compression modes (longitudinal waves) and bending modes. The equations governing the former are [LL59]

$$\left\{\begin{array}{l} \frac{\rho}{E}\frac{\partial^2 u_x}{\partial t^2} = \frac{1}{1-\nu^2}\frac{\partial^2 u_x}{\partial x^2} + \frac{1}{2(1+\nu)}\frac{\partial^2 u_x}{\partial y^2} + \frac{1}{2(1-\nu)}\frac{\partial^2 u_y}{\partial x\partial y} \\ \frac{\rho}{E}\frac{\partial^2 u_y}{\partial t^2} = \frac{1}{1-\nu^2}\frac{\partial^2 u_y}{\partial y^2} + \frac{1}{2(1+\nu)}\frac{\partial^2 u_y}{\partial x^2} + \frac{1}{2(1-\nu)}\frac{\partial^2 u_x}{\partial x\partial y} \end{array}\right. \tag{C.39}$$

Choosing a solution $e^{ik_x x-\omega t}$ the equations simplify to wave equations:

$$\frac{\partial^2 u_x}{\partial t^2} - \frac{E}{\rho(1-\nu^2)}\frac{\partial^2 u_x}{\partial x^2} = 0 \quad , \quad \frac{\partial^2 u_y}{\partial t^2} - \frac{E}{2\rho(1+\nu)}\frac{\partial^2 u_y}{\partial x^2} = 0 \tag{C.40}$$

so that the speed of the longitudinal ($v_l = \sqrt{E/\rho(1-\nu^2)}$) and transversal ($v_t = \sqrt{E/2\rho(1+\nu)}$) waves are different. Therefore we will have two types of compression modes, longitudinal and transversal, each parametrized with a vector $\mathbf{k}$ in the plane. The expression for the local deformations associated to the longitudinal component in second quantization is

$$u^l(0) = \sum_{\mathbf{k}}\sqrt{\frac{\hbar}{2\rho twL\omega_{\mathbf{k}}}}(b_{\mathbf{k}}^l + b_{\text{-}\mathbf{k}}^{\dagger,l}) \quad , \quad \partial u^l = \sqrt{\frac{\hbar}{2\rho twL}}\sum_{\mathbf{k}}\frac{k^l}{\sqrt{\omega_{\mathbf{k}}}}(b_{\mathbf{k}}^l + b_{\text{-}\mathbf{k}}^{\dagger,l}) \tag{C.41}$$

and similarly for the transversal one. They give rise to an interaction hamiltonian

$$\begin{aligned} H_{int} &= \hbar\sigma_z\sum_{j=x,y}\sum_{i=l,t}\sum_k\Big[\gamma\frac{\Delta_0^x}{\epsilon}\sqrt{\frac{1}{2\hbar\rho twL}}\frac{k_j^i}{\sqrt{\omega_{k_j}^i}}\Big](a_{-k_j}^{\dagger,i} + a_{k_j}^i) \\ &= \hbar\sigma_z\sum_{j=x,y}\sum_{i=l,t}\sum_k\gamma_{eff}\frac{k_j^i}{\sqrt{\omega_{k_j}^i}}(a_{-k_j}^{\dagger,i} + a_{k_j}^i) \end{aligned} \tag{C.42}$$

which has an associated **superohmic** spectral function

$$J(\omega) = \sum_{j=x,y} \sum_{i=l,t} \sum_{k} \gamma_{eff}^2 \frac{(k_j^i)^2}{\omega_{k_j}^i} \delta(\omega - \omega_{k_j}^i) = \alpha_c \, \omega^2 \ , \tag{C.43}$$

with α_c given by

$$\alpha_c = \frac{Lw}{(2\pi)^2} \gamma_{eff}^2 \Big[\frac{1}{v_l^4} + \frac{1}{v_t^4} \Big] = \frac{1}{(2\pi)^2} \Big(\gamma \frac{\Delta_0^x}{\epsilon} \Big)^2 \frac{1}{2\hbar\rho t} \Big[\Big(\frac{\rho(1-\nu^2)}{E} \Big)^2 + \Big(\frac{2\rho(1+\nu)}{E} \Big)^2 \Big] \ . \tag{C.44}$$

In the case of the bending modes the governing equation is

$$\rho t w \frac{\partial^2 z}{\partial t^2} + \frac{Et^2}{12(1-\nu^2)} \triangle^2 z = 0 \tag{C.45}$$

so there is a non-linear dispersion relation, $\omega = k^2 \sqrt{Et^2/12\rho(1-\nu^2)}$. To obtain the approximate relation between the coordinate z which will have the bosonic operators associated, and the strain tensor u_{ik} appearing in the interaction part of the hamiltonian, we equate two expressions for the elastic free energy,

$$\begin{aligned} F_{sheet} &= \frac{Et^3}{24(1-\nu^2)} \int dxdy \Big[\Big(\frac{\partial^2 z}{\partial x^2} + \frac{\partial^2 z}{\partial y^2} \Big)^2 + 2(1-\nu) \Big\{ \Big(\frac{\partial^2 z}{\partial x \partial y} \Big)^2 - \frac{\partial^2 z}{\partial x^2} \frac{\partial^2 z}{\partial y^2} \Big\} \Big] \\ &= \frac{Et}{2(1+\nu)} \int dxdy \Big[u_{ik}^2 + \frac{\nu}{1-2\nu} u_{ll} \Big] \end{aligned} \tag{C.46}$$

and obtain an average relation

$$\langle u_{ij} \rangle \approx t \sqrt{\frac{1}{3(1-\nu)(9+\frac{3\nu}{1-2\nu})}} \langle \frac{\partial^2 z}{\partial x^2} \rangle \ . \tag{C.47}$$

With this information H_{int} reads

$$H_{int} = \hbar \sigma_z \sum_{j=x,y} \sum_{l,m=1,2,3} \sum_{k} \Big[\gamma \frac{\Delta_0^x}{\epsilon} \frac{t}{\sqrt{3(1-\nu)(9+\frac{3\nu}{1-2\nu})}} \frac{1}{\sqrt{2\hbar t w L \rho}} \frac{(k_j^{lm})^2}{\sqrt{\omega_{k_j}^{lm}}} \Big] (a_{-k_j}^{\dagger,lm} + a_{k_j}^{lm}) \ . \tag{C.48}$$

Proceeding as with the previous modes, the spectral function associated turns out to be **ohmic**:

$$J(\omega) = \alpha \, \omega \quad , \quad \alpha = \frac{9\sqrt{3}}{\pi} \Big(\gamma \frac{\Delta_0^x}{\epsilon} \Big)^2 \frac{\rho^{1/2}(1+\nu)^{3/2}(1-\nu)^{1/2}}{\hbar t^2 E^{3/2}(9+\frac{3\nu}{1-2\nu})} \tag{C.49}$$

We will restrict ourselves to the study of dissipation caused by the ohmic bath of bending modes, which will prevail at low temperatures over the superohmic bath of compression modes.

	1 layer	$t = 10$ nm
ω_{inf}	$7 \cdot 10^7$	$2.5 \cdot 10^9$
ω_{co}	$8 \cdot 10^{14}$	$3 \cdot 10^{13}$
α	~ 0.03	$\sim 3 \cdot 10^{-5}$

Table C.1: Estimate of the parameters of the bath, for $\gamma \sim 1$ eV.

C.5.2 Losses due to the ohmic bath. Temperature dependence

An estimate is given of the properties of the bath, namely α, ω_{inf} and ω_{co}, for two cases, the one of a single layer graphene sheet (whose thickness we take to be $t \sim 3$ Å), and a stack of layers 10 nm thick, using the value $\gamma \sim 1$ eV, in table (C.1). This value of γ is a big overestimate, since it corresponds to the value of the coupling of TLS's embedded in a vibrating amorphous structure to the oscillations, and as stated previously this is not our case, and the coupling will be reduced by some power of the factor $(a/d) \sim 10^{-4}$. We thus conclude that α is extremely small, and there is no appreciable renormalization of the tunneling amplitude, $\Delta_r = \Delta_0^x \cdot (\Delta_0^x/\omega_{co})^{\alpha/(1-\alpha)} \simeq \Delta_0^x$ [LCD+87]. In ref. [Wei99] an extensive analysis of the correlation function $C(t) = \langle \sigma_z(t)\sigma_z(0)\rangle$ of a TLS in presence of an ohmic bath is carried out, and for the cases we consider ($\alpha \ll 1$, biased TLS) the following results are obtained for the quasielastic (relaxational) peak around $\omega = 0$:

1. For $\epsilon < \pi\alpha kT$:

$$C_{rel}(\omega) = \frac{2\gamma_r}{\omega^2 + \gamma_r^2} \quad , \quad \gamma_r = \frac{\hbar\Delta_r^2}{2\pi\alpha kT}\frac{1}{1 + (\Delta_0^z/2\pi\alpha kT)^2} \approx \frac{\hbar\Delta_r^2}{2\pi\alpha kT} \tag{C.50}$$

2. For $\pi\alpha kT < \epsilon \leq kT$:

$$C_{rel}(\omega) = 2\Big(\frac{(\Delta_0^z)^2}{\epsilon^2} - \tanh^2\Big(\frac{\epsilon}{2kT}\Big)\Big)\frac{\gamma_r}{\omega^2 + \gamma_r^2} \approx 2\frac{(\Delta_0^z)^2}{\epsilon^2}\frac{\gamma_r}{\omega^2 + \gamma_r^2} \quad , \tag{C.51}$$

with

$$\gamma_r = 2\pi\alpha\frac{kT}{\hbar}\frac{\Delta_r^2}{(\Delta_0^z)^2 + \Delta_r^2} \tag{C.52}$$

3. For $\epsilon \geq kT$:

$$C_{rel}(\omega) = 2\frac{(\Delta_0^z)^2/\epsilon^2}{\cosh^2\Big(\frac{\epsilon}{2kT}\Big)}\frac{\gamma_r}{\omega^2 + \gamma_r^2} \approx 4e^{-\epsilon/kT}(\Delta_0^z)^2/\epsilon^2\frac{\gamma_r}{\omega^2 + \gamma_r^2} \quad , \tag{C.53}$$

with

$$\gamma_r = \pi\alpha\coth\Big(\frac{\epsilon}{2kT}\Big)\Delta_r^2/\hbar\epsilon \approx \pi\alpha\Delta_r^2/\hbar\epsilon \tag{C.54}$$

These expressions for $C_{rel}(\omega)$ substitute the one found usually in the context of sound attenuation in amorphous solids due to 3D acoustic modes, $C_{rel}^{3D}(\omega) = \frac{(\Delta_0^z)^2/\epsilon^2}{\cosh^2(\epsilon/2kT)} \frac{\Gamma}{\omega^2+\Gamma^2}$, and they will enter into the expression for the dissipation as follows:

$$Q^{-1}(\omega, T) = \frac{P\gamma^2}{EkT} \int_0^{\epsilon_{max}} d\epsilon \int_{u_{min}}^1 du \frac{1}{u\sqrt{1-u^2}} \omega C(\omega) \tag{C.55}$$

where $u = \Delta_r/\epsilon$, $\epsilon_{max} \sim 5$ K, and $(u\sqrt{1-u^2})^{-1}$ comes from the probability density of TLS's in an amorphous solid, like SiO_2.
When $kT > \epsilon_{max}$ there will be TLS's only in the regimes of eqs. (C.50) and (C.51), and moreover, thanks to the very low value of α and the range of ω typical of experiments we will have $\gamma_r < \omega$ for all values of u, so that $\gamma_r/(\omega^2+\gamma_r^2) \approx \gamma_r/\omega^2$, and

$$\begin{aligned} Q^{-1}(\omega, T) &= \frac{P\gamma^2}{EkT}\Big\{ \int_0^{\pi\alpha kT} d\epsilon \int_{u_{min}}^1 du \frac{1}{u\sqrt{1-u^2}} \frac{2\epsilon^2 u^2}{2\pi\hbar\omega\alpha kT} \\ &\qquad + \int_{\pi\alpha kT}^{\epsilon_{max}} d\epsilon \int_{u_{min}}^1 du \frac{1}{u\sqrt{1-u^2}} 2(1-u^2) \frac{2\pi\alpha kT u^2}{\hbar\omega} \Big\} \\ &\approx \frac{P\gamma^2}{E\hbar\omega}\Big\{ \frac{4\pi}{3}\alpha\epsilon_{max} + \frac{\pi^2}{3}\alpha^2 kT \Big\} \end{aligned} \tag{C.56}$$

So for high temperatures it will give a constant contribution to dissipation, plus a weak (due to the prefactor α^2) linear T dependence.
In the case of lower temperatures, $kT < \epsilon_{max}$, there are some TLS's in the regime corresponding to eq. (C.53), and again one can approximate $\gamma_r/(\omega^2+\gamma_r^2) \approx \gamma_r/\omega^2$ thanks to the low α, leading to

$$\begin{aligned} Q^{-1}(\omega, T) &= \frac{P\gamma^2}{EkT}\Big\{ \int_0^{\pi\alpha kT} d\epsilon \int_{u_{min}}^1 du \frac{1}{u\sqrt{1-u^2}} \frac{2\epsilon^2 u^2}{2\pi\hbar\omega\alpha kT} \\ &\qquad + \int_{\pi\alpha kT}^{kT} d\epsilon \int_{u_{min}}^1 du \frac{1}{u\sqrt{1-u^2}} 2(1-u^2) \frac{2\pi\alpha kT u^2}{\hbar\omega} \\ &\qquad + \int_{kT}^{\epsilon_{max}} d\epsilon \int_{u_{min}}^1 du \frac{1}{u\sqrt{1-u^2}} 4(1-u^2) e^{-\epsilon/kT} \frac{\pi\alpha u^2 \epsilon}{\hbar\omega} \Big\} \\ &\approx \frac{P\gamma^2}{E\hbar\omega}\Big\{ \frac{4\pi}{3}\alpha kT + \frac{\pi^2}{3}\alpha^2 kT + \frac{8\pi}{\sqrt{e}}\alpha kT \Big\} \\ &\approx \frac{P\gamma^2\alpha}{E\hbar\omega}\Big\{ \frac{4\pi}{3} + \frac{8\pi}{\sqrt{e}} \Big\} kT \end{aligned} \tag{C.57}$$

Thus, at low temperatures the contribution from TLS's to attenuation is linear in T. These tendencies come basically from the ohmic character of the vibrational bath and the probability density function of the TLS's. In case the TLS's resided in a crystalline material, or for some other reason their distribution function differed from the one of amorphous solids, changes in the behavior of $Q^{-1}(T, \omega)$ are to be expected.

Appendix D

Appendix to Chapter 6

D.1 Dipole matrix element from single-particle mean-field states

The derivation given in this section is borrowed from [Wei06]. We want to calculate the dipole matrix element $d_{\alpha\beta}$ defined in (6.14)

$$d_{\alpha\beta} = \langle\alpha|\Big[z\Theta(a-r) + \frac{za^3}{r^3}\Theta(r-a)\Big]|\beta\rangle \tag{D.1}$$

For that sake we need a description of the eigenstates $|\alpha\rangle$ of the mean-field Hamiltonian (6.11). The TDLDA numerical calculations briefly presented in Sec. 6.2inform us on the shape of the self-consistent mean field potential $V(r)$, as shown in Fig. 6.1. It suggests that for analytical calculations, $V(r)$ can be approximated by a spherical well of radius a and finite height V_0, $V(r) = V_0\Theta(r-a)$, where $V_0 = \epsilon_F + W$, ϵ_F and W being the Fermi energy and the work function of the considered nanoparticle, respectively.

Because of the spherical symmetry of the problem, the one-particle wave functions

$$\psi_{\epsilon lm}(\mathbf{r}) = \frac{u_{\epsilon l}(r)}{r}Y_l^m(\theta,\phi) \tag{D.2}$$

decompose into radial and angular parts given by the spherical harmonics $Y_l^m(\theta,\phi)$, where l and m are the angular momentum quantum numbers. The radial wave functions $u_{\epsilon l}(r)$ satisfy the reduced Schrödinger equation

$$\Big[-\frac{\hbar^2}{2m_e}\frac{d^2}{dr^2} + \frac{\hbar^2 l(l+1)}{2m_e r^2} + V(r)\Big]u_{\epsilon l}(r) = \epsilon u_{\epsilon l}(r) \tag{D.3}$$

with the conditions $u_{\epsilon l}(0) = 0$ and $\lim_{r\to\infty}[u_{\epsilon l}(r)/r] = 0$. This yields the single-particle eigenenergies ϵ in the mean-field potential $V(r)$. Thus, the matrix elements

$d_{\alpha\beta}$ can be separated into an angular part $\mathcal{A}_{l_\alpha l_\beta}^{m_\alpha m_\beta}$ and a radial part $\mathcal{R}_{l_\alpha l_\beta}(\varepsilon_\alpha, \varepsilon_\beta)$,

$$d_{ph} = \mathcal{A}_{l_\alpha l_\beta}^{m_\alpha m_\beta} \mathcal{R}_{l_\alpha l_\beta}(\varepsilon_\alpha, \varepsilon_\beta)\,. \tag{D.4}$$

With (D.1), we have

$$\mathcal{A}_{l_\alpha l_\beta}^{m_\alpha m_\beta} = \int_0^\pi d\theta \sin\theta \int_0^{2\pi} d\phi Y_{l_\alpha}^{m_\alpha\,*}(\theta,\phi) \cos\theta Y_{l_\beta}^{m_\beta}(\theta,\phi) \tag{D.5}$$

which can be expressed in terms of Wigner-3j symbols [Edm60] as

$$\mathcal{A}_{l_\alpha l_\beta}^{m_\alpha m_\beta} = (-1)^{m_\alpha} \sqrt{(2l_\alpha+1)(2l_\beta+1)} \times \begin{pmatrix} l_\alpha & l_\beta & 1 \\ 0 & 0 & 0 \end{pmatrix} \begin{pmatrix} l_\alpha & l_\beta & 1 \\ -m_\alpha & m_\beta & 0 \end{pmatrix}. \tag{D.6}$$

The Wigner-3j symbols contain the dipole selection rules $l_\alpha = l_\beta \pm 1$ and $m_\alpha = m_\beta$.

Concerning $\mathcal{R}_{l_\alpha l_\beta}(\varepsilon_\alpha, \varepsilon_\beta)$, in the limit of strong electronic confinement $V_0 \gg \epsilon_F$, the single-particle wave function vanishes outside the nanoparticle, enabling us to take the following approximation

$$\mathcal{R}_{l_\alpha l_\beta}(\varepsilon_\alpha, \varepsilon_\beta) \simeq \int_0^a dr u_{\varepsilon_\alpha l_\alpha}^*(r) r u_{\varepsilon_\beta l_\beta}(r) \tag{D.7}$$

The commutator of r with the self-consistent Hamiltonian $H_{sc} = \mathbf{p}^2/2m_e + V(r)$ reads

$$[r, H_{sc}] = \frac{i\hbar}{m_e} p_r\,, \tag{D.8}$$

where p_r is the conjugated momentum to the variable r. Calculating the matrix element of this commutator between two single-particle eigenstates $|\alpha\rangle$ and $|\beta\rangle$ of H_{sc} then allows to write

$$\langle\alpha|r|\beta\rangle = \frac{i\hbar}{m_e(\varepsilon_\beta - \varepsilon_\alpha)} \langle\alpha|p_r|\beta\rangle\,. \tag{D.9}$$

Now we use $[p_r, H_{sc}] = -i\hbar\, dV/dr$ to obtain

$$\langle\alpha|p_r|\beta\rangle = -\frac{i\hbar}{\varepsilon_\beta - \varepsilon_\alpha} \langle\alpha|\frac{dV}{dr}|\beta\rangle\,, \tag{D.10}$$

and substituting in (D.9) one gets

$$\langle\alpha|r|\beta\rangle = \frac{\hbar^2}{m_e(\varepsilon_\beta - \varepsilon_\alpha)^2} \langle\alpha|\frac{dV}{dr}|\beta\rangle\,, \tag{D.11}$$

so that the radial part of the dipole matrix element can be reexpressed as a function of dV/dr as

$$\mathcal{R}_{l_\alpha l_\beta}(\varepsilon_\alpha, \varepsilon_\beta) \simeq \frac{\hbar^2}{m_e(\varepsilon_\beta - \varepsilon_\alpha)^2} \int_0^a dr u_{\varepsilon_\alpha l_\alpha}^*(r) \frac{dV}{dr} u_{\varepsilon_\beta l_\beta}(r)\,, \tag{D.12}$$

which for an approximate step potential such as ours, $V(r) = V_0\Theta(r-a)$, leads to

$$\mathcal{R}_{l_\alpha l_\beta}(\varepsilon_\alpha, \varepsilon_\beta) \simeq \frac{\hbar^2}{m_e(\varepsilon_\beta - \varepsilon_\alpha)^2} V_0 u^*_{\varepsilon_\alpha l_\alpha}(a) u_{\varepsilon_\beta l_\beta}(a)\,. \tag{D.13}$$

For $V_0 \to \infty$ and $r \leq a$, the regular solutions of (D.3) satisfying $u_{\epsilon l}(a) = 0$ are given by

$$u_{\epsilon l}(r) = \frac{\sqrt{2}}{a^{3/2}} \frac{r j_l(kr)}{j_{l+1}(ka)}\,, \tag{D.14}$$

where $j_\nu(z)$ are spherical Bessel functions of the first kind [AIS70], and $k = \sqrt{2m_e\epsilon}/\hbar$. The condition $j_l(ka) = 0$ yields the quantization of the single-particle states in the infinitely deep spherical well. Inserting now the radial wave function (D.14) into (D.13),

$$\mathcal{R}_{l_\alpha l_\beta}(\varepsilon_\alpha, \varepsilon_\beta) = \frac{\hbar^2}{m_e a(\varepsilon_\beta - \varepsilon_\alpha)^2} V_0 \frac{j_{l_\alpha}(k_\alpha a)}{j_{l_\alpha+1}(k_\alpha a)} \frac{j_{l_\beta}(k_\beta a)}{j_{l_\beta+1}(k_\beta a)}\,. \tag{D.15}$$

Now, for $r \to a^+$, $u_{\epsilon l}(r) \to 0$ and $V(r) = V_0 \to \infty$, so that the radial Schrödinger equation (D.3) takes the form

$$\Big[-\frac{\hbar^2}{2m_e}\frac{d^2}{dr^2} + V_0\Big] u_{\epsilon l}(r) = 0\,. \tag{D.16}$$

With $k_0 = \sqrt{2m_e V_0}/\hbar$, the physical solution of this equation is

$$u_{\epsilon l}(r \to a^+) \sim e^{-k_0 r}\,. \tag{D.17}$$

Then

$$\frac{du_{\epsilon l}}{dr}\Big|_{r\to a^+} = -k_0 u_{\epsilon l}(r \to a^+)\,, \tag{D.18}$$

and imposing the continuity of the radial wave function and of its derivative with respect to r at $r = a$, we obtain

$$\frac{du_{\epsilon l}}{dr}\Big|_{r\to a^-} = -k_0 u_{\epsilon l}(r \to a^-)\,. \tag{D.19}$$

Therefore, using (D.14)

$$\lim_{V_0\to\infty}\Big[\frac{\sqrt{2m_e V_0}}{\hbar} j_l(ka)\Big] = -\frac{dj_l(kr)}{dr}\Big|_{r=a} = -k\frac{dj_l(\eta)}{d\eta}\Big|_{\eta=ka}\,. \tag{D.20}$$

Using the recurrence relation [AIS70]

$$\frac{l}{\eta} j_l(\eta) - \frac{dj_l}{d\eta} = j_{l+1}(\eta) \tag{D.21}$$

and the fact that $j_l(\eta) = j_l(ka) = 0$, we reach the final result for the radial matrix element [YB92]

$$\mathcal{R}_{l_\alpha l_\beta}(\varepsilon_\alpha, \varepsilon_\beta) = \frac{2\hbar^2}{m_\mathrm{e} a} \frac{\sqrt{\varepsilon_\alpha \varepsilon_\beta}}{(\varepsilon_\alpha - \varepsilon_\beta)^2} \,. \tag{D.22}$$

Note that the dipole selection rule $l_\alpha = l_\beta \pm 1$ appearing in the angluar matrix element (D.6) implies that $\varepsilon_\alpha \neq \varepsilon_\beta$, and thus (D.22) does not diverge. Furthermore, it decreases with increasing energy $|\varepsilon_\alpha - \varepsilon_\beta|$ of the dipole transition $|\alpha\rangle \to |\beta\rangle$.

D.2 Lowest energy of the particle-hole spectrum

Using the large ka expansion of (D.14) (semiclassical high-energy limit), the quantisation condition reads

$$ka = \pi \left(\frac{l}{2} + n \right) \tag{D.23}$$

with l and n non-negative integers. The energy of a single-particle (hole) state is related to its wavevector $k_{p(h)}$, its total angular momentum $l_{p(h)}$, and its radial quantum number $n_{p(h)}$ as

$$\varepsilon_{p(h)} = \frac{\hbar^2 k_{p(h)}^2}{2m_\mathrm{e}} = \varepsilon_\mathrm{F} \left(\frac{\pi}{k_\mathrm{F} a} \right)^2 \left(\frac{l_{p(h)}}{2} + n_{p(h)} \right)^2 \,. \tag{D.24}$$

Thus, the energy of a p-h excitation entering the RPA sum (6.48) is

$$\Delta\varepsilon_{ph} = \varepsilon_\mathrm{F} \left(\frac{\pi}{k_\mathrm{F} a} \right)^2 \left(\frac{l_p - l_h}{2} + n_p - n_h \right) \times \left(\frac{l_p + l_h}{2} + n_p + n_h \right) \,. \tag{D.25}$$

Notice that using the exact quantum mechanical spectrum in (6.48) would not change significantly the result depicted in Figure 6.4, since the approximation (D.23) is very reliable for states close to the Fermi energy. We have also checked that generating the p-h excitation energies randomly in the RPA sum (6.43) does not affect the physical picture of Figure 6.4. Indeed, the main ingredient to understand such a picture is the fast decay of the dipole matrix element with the p-h energy.

The expressions for the dipole matrix element (6.47) as well as for the typical dipole matrix element (6.57) diverge in the limit of a small p-h energy. It is therefore crucial for our analysis to determine the appropriate minimal p-h energy $\Delta\varepsilon_\mathrm{min}$ that renders this divergence unphysical.

This can be achieved by imposing the dipole selection rules in (D.25) and that the energy difference is minimal. The first condition dictates that $l_h = l_p \pm 1$ and $m_h = m_p$. Therefore there are two ways of obtaining the minimal energy difference: $n_p = n_h$ with $l_p = l_h + 1$ and $n_p = n_h + 1$ with $l_p = l_h - 1$. In both cases we have

$$\Delta\varepsilon_\mathrm{min} \simeq \frac{\varepsilon_\mathrm{F}}{k_\mathrm{F} a/\pi} \frac{k_h}{k_\mathrm{F}} \,. \tag{D.26}$$

Since we are interested in states close to the Fermi level, we can simplify (D.26) to expression (6.49).

If we consider sodium clusters with $k_{\rm F}a = 30$ ($a = 3.3\,$nm and $N \simeq 4000$ conduction electrons per spin direction), we have $\Delta\varepsilon_{\rm min} \approx \varepsilon_{\rm F}/10$. This is a much larger energy than the lowest one we can observe in the numerically generated excitation spectrum (see Fig. 1 in Ref. [MWJ02]). However, the two results are reconciled once we take into account the large degeneracy yielded by our approximate quantisation condition (D.23).

The degeneracy of p-h excitations with minimal energy is given by twice the number of pairs (l_h, n_h) compatible with $k_h = k_{\rm F}$ and $\Delta\varepsilon_{ph} = \Delta\varepsilon_{\rm min}$. Indeed, we have seen that there are two possible particle states p starting from h and verifying the above-mentioned conditions. For each n between 1 and $k_{\rm F}a/\pi$, there is a value of $l = 2(k_{\rm F}a/\pi - n)$ and therefore the number of degenerate p-h excitations with energy $\Delta\varepsilon_{\rm min}$ is

$$\mathcal{N} = 2\sum_{n=0}^{k_{\rm F}a/\pi}(2l+1) = 2\sum_{n=0}^{k_{\rm F}a/\pi}\left[4\left(\frac{k_{\rm F}a}{\pi} - n\right) + 1\right] \simeq 4\left(\frac{k_{\rm F}a}{\pi}\right)^2 . \tag{D.27}$$

This degeneracy factor has to be included in Figure 6.4, and it is crucial for the determination of the collective excitation.

D.3 Density of states at a fixed angular momentum l, $\rho_l(\varepsilon)$

For our derivations we need to have an estimate for the l-fixed density of states, which we will call $\rho_l(\varepsilon)$. It corresponds to the number of eigenstates per energy unit whose radial part $u_{kl}(r)$ satisfy (D.3) with the conditions $u_{\epsilon l}(0) = 0$ and $\lim_{r\to\infty}[u_{\epsilon l}(r)/r] = 0$. It is important to notice that the variable r is limited to positive values and that the centrifugal potential possesses a singularity at $r = 0$. This prevents us from a naïve application of the WKB approximation [Mer70] to treat this radial problem, as would be done for a standard 1D Schrödinger equation. First we have to rewrite (D.3) in terms of a variable where such a singularity is absent, and then we will apply WKB. The change of variables is

$$x = \ln r, \quad , \quad \chi_{kl}(x) = e^{x/2}u_{kl}(r)\,, \tag{D.28}$$

and (D.3) becomes non-singular

$$\left[\frac{d^2}{dx^2} + \Pi_l^2(x)\right]\chi_{kl}(x) = 0\,, \tag{D.29}$$

with

$$\Pi_l^2(x) = \frac{2m_e}{\hbar^2}e^{2x}[\varepsilon_{kl} V(e^x)] - \left(l + \frac{1}{2}\right)^2 . \tag{D.30}$$

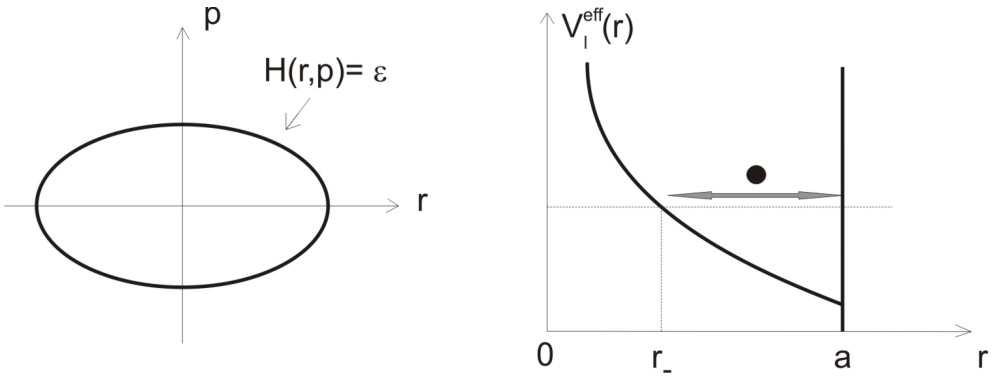

Figure D.1: Left: Phase-space trajectory of a periodic motion of energy ε in a confining potential. Right: Radial potential V_l^{eff} for fixed l, of the spherical cavity as a function of the radial coordinate r.

Using now the WKB approximation for $\chi_{kl}(x)$ amounts to change the centrifugal potential in (D.3) according to the Langer modification [Lan37, BM72]

$$l(l+1) \Rightarrow \left(l+\frac{1}{2}\right)^2 . \tag{D.31}$$

Therefore the modified effective radial potential becomes

$$V_l^{eff}(r) = \frac{\hbar^2(l+1/2)^2}{2m_e r^2} + V(r)\,, \tag{D.32}$$

where in our case $V(r)$ is the spherical billiard potential

$$V(r) = \begin{cases} 0, & r < a\,, \\ \infty, & r \geq a\,, \end{cases} \tag{D.33}$$

A plot of $V_l^{eff}(r)$ is provided in fig.(D.1). A semiclassical theory can be developed to calculate $\rho_l(\varepsilon)$, obtaining an expression whose first corrections lead to an extra oscillatory component $\rho_l^{osc}(\varepsilon)$ added to the Thomas-Fermi result for $\rho_l(\varepsilon)$ [WMWJ05, Wei06], $\rho_l^0(\varepsilon)$:

$$\rho_l^0(\varepsilon) = \frac{1}{h}\int dp\, dr \delta(\varepsilon - H_l(r,p)) \tag{D.34}$$

where $H_l(r,p)$ is the hamiltonian with potential (D.32). But for our purposes in this thesis the Thomas-Fermi result suffices, because the quantities we want to calculate will be integrals whose integrands include products of the kind $\rho_l(\varepsilon)\rho_{l\pm1}(\varepsilon)$, where the effects of the oscillating corrections are strongly suppressed.

To calculate (D.34) we start showing that the phase space integral on the right hand side equals the period of the classical trajectory of energy ε of the particle

confined in the $V_l^{eff}(r)$ shown in fig.(D.1)

$$\int dp\, dr \delta(\varepsilon - H_l(r,p)) = \tau_l(\varepsilon) \tag{D.35}$$

The delta function can be expressed as

$$\delta(\varepsilon - H_l(r,p)) = \sum_{\substack{(r',p') \text{ such that} \\ H(r',p')=\varepsilon}} \frac{\delta(r-r', p-p')}{|\nabla H(r',p')|}\,, \tag{D.36}$$

where $\delta(r-r', p-p')$ fulfills $\int dp\, dr \delta(r-r', p-p') f(r,p) = f(r',p')$, for a generic function $f(r,p)$. Therefore the surface integral (D.35) is converted by the sum over delta functions into a line integral over the trajectory in phase space whose energy is fixed at the value ε. The denominator can be reexpressed with the aid of the Hamilton equations satisfied by the classical trajectory:

$$\frac{dp}{dt} = -\frac{\partial H}{\partial r} \quad , \quad \frac{dr}{dt} = \frac{\partial H}{\partial p}\,, \tag{D.37}$$

so that $|\nabla H(r',p')| = \sqrt{[\partial H/\partial r]^2 + [\partial H/\partial p]^2}$ becomes $\sqrt{dr^2+dp^2}/dt = dl/dt$. Substituting in (D.35):

$$\int dp\, dr \sum_{\substack{(r',p') \text{ such that} \\ H(r',p')=\varepsilon}} \frac{\delta(r-r', p-p')}{|\nabla H(r',p')|} = \oint dl \frac{1}{dl/dt} = \oint dt = \tau_l(\varepsilon)\,. \tag{D.38}$$

The next step is to calculate $\tau_l(\varepsilon)$. For that sake we use the classical action functional

$$S[\varepsilon, \tau_l] = \int_0^{\tau_l} \Big[\frac{p^2}{2m} - V_l^{eff}(r)\Big] dt + \varepsilon\tau_l = \int_{r(t=0)}^{r(t=\tau_l)} dr \cdot p\,, \tag{D.39}$$

which satisfies $\partial S/\partial\varepsilon = \tau_l$. We will calculate S using its last form in terms of r and p, recalling the fact that for a trajectory of fixed energy

$$\frac{p^2}{2m} + V_l^{eff}(r) = \varepsilon \quad \to \quad p = \sqrt{2m(\varepsilon - V_l^{eff}(r))} \tag{D.40}$$

The value of S can then be calculated as

$$S[\varepsilon, \tau_l] = \int_{r(t=0)}^{r(t=\tau)} dr \cdot p = 2\int_{r_-(\varepsilon)}^{r=a} dr \sqrt{2m(\varepsilon - V_l^{eff}(r))}\,. \tag{D.41}$$

The value of the turning point $r_-(\varepsilon)$ on the left of the classically allowed region is given by the condition $V_l^{eff}(r_-(\varepsilon)) = \varepsilon$, i.e., $r_-(\varepsilon) = \hbar(l+1/2)/\sqrt{2m_e\varepsilon}$, see fig.(D.1).

Substituting the form of the potential $V_l^{eff}(r)$ in the integral (D.41), after a straighforward calculation we get

$$S[\varepsilon,\tau_l] = 2\hbar\Big[\sqrt{(2m\varepsilon a^2/\hbar^2) - \Big(l+\frac{1}{2}\Big)^2} - \Big(l+\frac{1}{2}\Big)\arccos\Big(\frac{l+1/2}{\sqrt{(2m\varepsilon a^2/\hbar^2)}}\Big)\Big], \quad \text{(D.42)}$$

and the period τ_l is obtained performing the partial derivative with respect to ε, obtaining in this way the desired Thomas-Fermi estimate for the partial density of states:

$$\tau_l(\varepsilon) = \frac{\hbar\sqrt{(2m\varepsilon a^2/\hbar^2) - \Big(l+\frac{1}{2}\Big)^2}}{\varepsilon} \quad \rightarrow \quad \rho_l(\varepsilon) \simeq \rho_l^0(\varepsilon) = \frac{\sqrt{(2m\varepsilon a^2/\hbar^2) - \Big(l+\frac{1}{2}\Big)^2}}{2\pi\varepsilon} \quad \text{(D.43)}$$

D.4 Local density of the dipole matrix element

Equation (6.51) defines the local density of dipole matrix elements connecting states at energies ε and $\varepsilon + \Delta\varepsilon$. We used particle and hole states in our definition, since this is the main interest of our work. But note that the calculation presented in this appendix is not restricted to that case and can be easily extended to any states. The result would be of course unchanged.

Local densities of matrix elements of arbitrary operators have been thoroughly studied as they can be easily connected with physical properties, ranging from far-infrared absorption in small particles [MR97] to electronic lifetimes of quantum dots [GJS04]. A semiclassical theory for the local density of matrix elements has been developed [FP86, Wil87, EFMW92], where (6.51) can be expressed as a smooth part given by correlations along classical trajectories plus a periodic orbit expansion. We will not follow here this general procedure, but continue to use the simple form of the dipole matrix elements (6.44) for states confined in a hard-wall sphere and the semiclassical approximation applied to the radial (fixed l) problem [MWJ02, MWJ03, WMWJ05].

Using the l-fixed density of states (D.43) we can write with the help of equations (D.4, D.6, D.22)

$$\begin{aligned}
\mathcal{C}(\varepsilon,\Delta\varepsilon) &= \sum_{\alpha\beta}\Big(A_{l_\alpha l_\beta}^{m_\alpha m_\beta}\Big)^2\Big(R_{l_\alpha l_\beta}(\epsilon_\alpha,\epsilon_\beta)\Big)^2\delta(\epsilon-\epsilon_\alpha)\delta(\epsilon+\Delta\epsilon-\epsilon_\beta) \\
&= \int_0^\infty d\epsilon_\alpha \sum_{l_\alpha m_\alpha}\rho_{l_\alpha}(\epsilon_\alpha)\int_0^\infty d\epsilon_\beta \sum_{l_\beta m_\beta}\rho_{l_\beta}(\epsilon_\beta)\Big(A_{l_\alpha l_\beta}^{m_\alpha m_\beta}\Big)^2\Big(R_{l_\alpha l_\beta}(\epsilon_\alpha,\epsilon_\beta)\Big)^2\delta(\epsilon-\epsilon_\alpha)\delta(\epsilon+\Delta\epsilon-\epsilon_\beta) \\
&= \sum_{l_\alpha m_\alpha, l_\beta m_\beta}\rho_{l_\alpha}(\epsilon)\rho_{l_\beta}(\epsilon+\Delta\epsilon)\Big(A_{l_\alpha l_\beta}^{m_\alpha m_\beta}\Big)^2\Big(R_{l_\alpha l_\beta}(\epsilon_\alpha,\epsilon_\beta)\Big)^2 \qquad \text{(D.44)}
\end{aligned}$$

$A^{m_\alpha m_\beta}_{l_\alpha l_\beta} \neq 0$ only if $m_\alpha = m_\beta$ and $l_\alpha = l_\beta \pm 1$, therefore

$$C(\epsilon,\Delta\epsilon) = \Big(\frac{2\hbar^2}{ma}\Big)^2 \frac{\epsilon(\epsilon+\Delta\epsilon)}{\Delta\epsilon^4} \sum_{l_\alpha,m_\alpha,l_\beta=l_\alpha\pm1} \rho_{l_\alpha}(\epsilon)\rho_{l_\beta}(\epsilon+\Delta\epsilon)\Big(A^{m_\alpha m_\alpha}_{l_\alpha l_\beta}\Big)^2 \qquad \text{(D.45)}$$

We first perform the sum over l_β:

$$\sum_{l_\beta=l_\alpha\pm1}\Big(A^{m_\alpha m_\alpha}_{l_\alpha l_\beta}\Big)^2\rho_{l_\beta}(\epsilon+\Delta\epsilon) = \Big(A^{m_\alpha m_\alpha}_{l_\alpha l_\alpha+1}\Big)^2\rho_{l_\alpha+1}(\epsilon+\Delta\epsilon) + \Big(A^{m_\alpha m_\alpha}_{l_\alpha l_\alpha-1}\Big)^2\rho_{l_\alpha-1}(\epsilon+\Delta\epsilon)$$

$$= \frac{(l_\alpha+1-m_\alpha)(l_\alpha+1+m_\alpha)}{(2l_\alpha+1)(2l_\alpha+3)}\rho_{l_\alpha+1}(\epsilon+\Delta\epsilon) + \frac{(l_\alpha-m_\alpha)(l_\alpha+m_\alpha)}{(2l_\alpha-1)(2l_\alpha+1)}\rho_{l_\alpha-1}(\epsilon+\Delta\epsilon) \qquad \text{(D.46)}$$

and then over m_α:

$$\sum_{m_\alpha=-l_\alpha}^{l_\alpha}(l_\alpha+1-m_\alpha)(l_\alpha+1+m_\alpha) = \frac{1}{3}(l_\alpha+1)(2l_\alpha+1)(2l_\alpha+3),$$

$$\sum_{m_\alpha=-l_\alpha}^{l_\alpha}(l_\alpha-m_\alpha)(l_\alpha+m_\alpha) = \frac{1}{3}l_\alpha(2l_\alpha-1)(2l_\alpha+1), \qquad \text{(D.47)}$$

yielding

$$\mathcal{C}(\varepsilon,\Delta\varepsilon) = \left(\frac{2\hbar^2}{m_e a}\right)^2 \frac{\varepsilon\varepsilon'}{3\Delta\varepsilon^4} \times \sum_{l_h=0}^{l_{\max}} \varrho_{l_h}(\varepsilon)\left[(l_h+1)\varrho_{l_h+1}(\varepsilon') + l_h\varrho_{l_h-1}(\varepsilon')\right] \qquad \text{(D.48)}$$

where $l_{\max}$ is the maximum allowed l_h for an energy ε, while $\varepsilon' = \varepsilon + \Delta\varepsilon$. In the semiclassical limit we can take $l_h \simeq l_h + 1 \gg 1$ and convert the sum into an integral. Thus,

$$C(\epsilon,\Delta\epsilon) = \frac{2}{3}\Big(\frac{2\hbar^2}{ma}\Big)^2\frac{\epsilon(\epsilon+\Delta\epsilon)}{\Delta\epsilon^4}\int_0^{l_{max}} dl\, l\frac{\sqrt{2m\epsilon a^2/\hbar^2-l^2}}{2\pi\epsilon}\frac{\sqrt{2m(\epsilon+\Delta\epsilon)a^2/\hbar^2-l^2}}{2\pi(\epsilon+\Delta\epsilon)}$$

$$= \frac{1}{6\pi^2}\Big(\frac{2\hbar^2}{ma}\Big)^2\frac{1}{\Delta\epsilon^4}\int_0^y dl\, l\sqrt{y^2-l^2}\sqrt{y'^2-l^2} \qquad \text{(D.49)}$$

where $y^2 = 2m\epsilon\, a^2/\hbar^2$ and $y'^2 = y^2 + 2m\Delta\epsilon\, a^2/\hbar^2$.Changing variables now to $u = l^2$, $du = 2ldl$, we get

$$C(\epsilon,\Delta\epsilon) = \frac{1}{12\pi^2}\Big(\frac{2\hbar^2}{ma}\Big)^2\frac{1}{\Delta\epsilon^4}\int_0^{y^2} du\sqrt{y^2-u}\sqrt{y'^2-u} \qquad \text{(D.50)}$$

Using the results of ref. [GR00] we obtain

$$\int_0^{y^2} du\sqrt{y^2-u}\sqrt{y'^2-u} = \frac{(y'^2-y^2)^2}{8}\ln\Big[\Big|\frac{y'-y}{y'+y}\Big|\Big] + \frac{(y'^2+y^2)yy'}{4} \qquad \text{(D.51)}$$

And substituting the values of y and y' one arrives at the desired expression (6.52).

D.5 Density of particle-hole excitations

The density of p-h excitations with energy $\Delta\varepsilon$ is defined in (6.55) and can be written as

$$\rho^{\text{p-h}}(\Delta\varepsilon) = \int_{\varepsilon_\text{F}-\Delta\varepsilon}^{\varepsilon_\text{F}} \mathrm{d}\varepsilon_h \sum_{l_h} (2l_h+1)\varrho_{l_h}(\varepsilon_h) \times \left[\varrho_{l_h+1}(\varepsilon_h+\Delta\varepsilon) + \varrho_{l_h-1}(\varepsilon_h+\Delta\varepsilon)\right] . \tag{D.52}$$

Using the semiclassical density of states (D.43) and performing the sum in the limit $l_h \gg 1$, we obtain

$$\rho^{\text{p-h}}(\Delta\varepsilon) \simeq \frac{\Delta\varepsilon^2}{8\pi^2}\left(\frac{2m_\text{e}a^2}{\hbar^2}\right)^2 \int_{\varepsilon_\text{F}-\Delta\varepsilon}^{\varepsilon_\text{F}} \mathrm{d}\varepsilon_h \frac{F(\varepsilon_h/\Delta\varepsilon)}{\varepsilon_h(\varepsilon_h+\Delta\varepsilon)} , \tag{D.53}$$

where the function F has been defined in (6.53). Performing the remaining integral over the hole energy in the limit $\Delta\varepsilon \ll \varepsilon_\text{F}$ is straightforward and leads to the result (6.56).

Bibliography

[ABV07] F. B. Anders, R. Bulla, and M. Vojta, *Equilibrium and non-equilibrium dynamics of the sub-ohmic spin-boson model*, Phys. Rev. Lett. **98** (2007), 210402.

[AHSD74] W. Arnold, S. Hunklinger, S. Stein, and K. Dransfeld, *Nonlinear ultrasonic attenuation in glasses*, J. Non Cryst. Sol. **14** (1974), 192.

[AHV72] P.W. Anderson, B.I. Halperin, and C.M. Varma, *Anomalous low-temperature thermal properties of glasses and spin glasses. (ultrasonic attenuation and magnetic impurity systems)*, Philos. Mag. **25** (1972), 1.

[AIS70] M. Abramowitz and eds. I.A. Stegun, *Handbook of mathematical functions, 9th ed.*, Dover, New York, 1970.

[AM76] N.W. Ashcroft and N.D. Mermin, *Solid state physics*, Harcourt, Orlando, 1976.

[AM03] K.-H. Ahn and P. Mohanty, *Quantum friction of micromechanical resonators at low temperatures*, Phys. Rev. Lett. **90** (2003), 085504.

[And86] A.C. Anderson, *On the coupling between two-level states and strains in amorphous solids*, J. Non-Crys. Solids **85** (1986), 211.

[ANVA$^+$99] M. Arndt, O. Nairz, J. Voss-Andreae, C. Keller, G. van der Zouw, and A. Zeilinger, *Wave-particle duality of* C_{60}, Nature **401** (1999), 680.

[AP87] A.I. Akinwande and J.D. Plummer, *Quantitative modeling of si/sio$_2$ interface fixed charge: I. experimental results*, J. Electrochem. Soc. **134** (1987), 2565.

[AS06] A. Altland and B. Simons, *Condensed matter field theory*, Cambridge University Press, 2006.

[BB75] A. Bohr and B.R.Mottelson, *Nuclear structure, vol. ii*, Benjamin, New York, 1975.

[BB94] G.F. Bertsch and R.A. Broglia, *Oscillations in finite quantum systems*, Cambridge University Press, 1994.

[BCLS93] C. Bréchignac, P. Cahuzac, J. Leygnier, and A. Sarfati, *Optical response of large lithium clusters: Evolution toward the bulk*, Phys. Rev. Lett. **70** (1993), 2036.

[BF04] H. Bruus and K. Flensberg, *Many-body quantum theory in condensed matter physics : An introduction*, Oxford University Press, 2004.

[BH77] J.L. Black and B.I. Halperin, *Spectral diffusion, phonon echoes, and saturation recovery in glasses at low temperatures*, Phys. Rev. B **16** (1977), 2879.

[BHMD00] J.-Y. Bigot, V. Halté, J.-C. Merle, and A. Daunois, *Electron dynamics in metallic nanoparticles*, Chem. Phys. **251** (2000), 181.

[Ble99] M.P. Blencowe, *Quantum energy flow in mesoscopic dielectric structures*, Phys. Rev. B **59** (1999), 4994.

[Ble04] M. Blencowe, *Quantum electromechanical systems*, Phys. Rep. **395** (2004), 159.

[Bli05] R.H. Blick *et al.*, *Focus on nano-electromechanical systems*, New J. Phys. **7** (2005), Editorial.

[BLTV05] R. Bulla, H. Lee, N. Tong, and M. Vojta, *Numerical renormalization group for quantum impurities in a bosonic bath*, Phys. Rev. B **71** (2005), 045122.

[BM72] M.V. Berry and K.E. Mount, *Semiclassical approximations in wave mechanics*, Rep. Prog. Phys. **35** (1972), 315.

[BM05] R. L. Badzey and P. Mohanty, *Coherent signal amplification in bistable nanomechanical oscillators by stochastic resonance*, Nature **437** (2005), 995.

[BMCD95] J.-Y. Bigot, J.-C. Merle, O. Cregut, and A. Daunois, *Electron dynamics in copper metallic nanoparticles probed with femtosecond optical pulses*, Phys. Rev. Lett. **75** (1995), 4702.

[BOS+07] A. Bostwick, T. Ohta, T. Seyller, K. Horn, and E. Rotenberg, *Quasiparticle dynamics in graphene*, Nature Physics **3** (2007), 36.

[BQKM07] R. H. Blick, H. Qin, H.-S. Kim, and R. Marsland, *A nanomechanical computer-exploring new avenues of computing*, New J. Phys. **9** (2007), 241.

[Bra93] M. Brack, *The physics of simple metal clusters: self-consistent jellium model and semiclassical approaches*, Rev. Mod. Phys. **65** (1993), 677.

[BRS+04] T. M. Buehler, D.J. Reilly, R.P. Starrett, V.C. Chan, A.R. Hamilton, A.S. Dzurak, and R.G. Clark, *Observing sub-microsecond telegraph noise with the radio frequency single electron transistor.*

[BS89] M. Barma and V. Subrahmanyam, *Optical absorption in small metal particles*, J. Phys.: Condens. Matter **1** (1989), 7681.

[BSS+99] A. Bachtold, C. Strunk, J.-P. Salvetat, J.-M. Bonard, L. Forró, T. Nussbaumer, and C. Schönenberger, *Aharonov bohm oscillations in carbon nanotubes*, Nature **397** (1999), 673.

[BTM+02] D. Boyer, P. Tamarat, A. Maali, B. Lounis, and M. Orrit, *Photothermal imaging of nanometer-sized metal particles among scatterers*, Science **297** (2002), 1160.

[BTV03] R. Bulla, N.-H. Tong, and M. Vojta, *Numerical renormalization group for bosonic systems and application to the sub-ohmic spin-boson model*, Phys. Rev. Lett. **91** (2003), 170601.

[BvdZV+07] J. Scott Bunch, Arend M. van der Zande, Scott S. Verbridge, Ian W. Frank, David M. Tanenbaum, Jeevak M. Parpia, Harold G. Craighead, and Paul L. McEuen, *Electromechanical resonators from graphene sheets*, Science **315** (2007), 490.

[BW04] R. B. Bhiladvala and Z. J. Wang, *Effect of fluids on the q factor and resonance frequency of oscillating micrometer and nanometer scale beams*, Phys. Rev. E **69** (2004), 036307.

[CGP+07] A.H. Castro Neto, F. Guinea, N.M.R. Peres, K.S. Novoselov, and A.K. Geim, *The electronic properties of graphene*, Rev. Mod. Phys. (to appear) (2007).

[CL00] P.M. Chaikin and T.C. Lubensky, *Principles of condensed matter physics*, Cambridge University Press, Cambridge, 2000.

[Cle02] A. N. Cleland, *Foundations of nanomechanics*, Springer (Berlin), 2002.

[CLW01] S. M. Carr, W. E. Lawrence, and M. N. Wybourne, *Accessibility of quantum efects in mesomechanical systems*, Phys. Rev. B **64** (2001), 220101(R).

[CR99] A. N. Cleland and M. L. Roukes, *External control of dissipation in a nanometer-scale radiofrequency mechanical resonator*, Sens. Actuators A **72** (1999), 256.

[CR02] ———, *Noise processes in nanomechanical resonators*, J. Appl. Phys. **92** (2002), 2758.

[Cra00] H. G. Craighead, *Nanoelectromechanical systems*, Science **250** (2000), 1532.

[CRB07] M. Chu, R. E. Rudd, and M. P. Blencowe, *The role of reconstructed surfaces in the intrinsic dissipative dynamics of silicon nanoresonators.*

[CRSU00] F. Calvayrfac, P.-G. Reinhard, E. Suraud, and C.A. Ullrich, *Nonlinear electron dynamics in metal clusters*, Phys. Rep. **337** (2000), 493.

[CT06] A. Chin and M. Turlakov, *Coherent-incoherent transition in the sub-ohmic spin-boson model*, Phys. Rev. B **73** (2006), 075311.

[CTB+03] L. Cognet, C. Tardin, D. Boyer, D. Choquet, P. Tamarat, and B. Lounis, *Single metallic nanoparticle imaging for protein detection in cells*, Proc. Natl. Acad. Sci. U.S.A. **100** (2003), 11350.

[DDA01] M.S. Dresselhaus, G. Dresselhaus, and Ph. Avouris, *Carbon nanotubes*, Springer Verlag, 2001.

[DDE96] M.S. Dresselhaus, G. Dresselhaus, and P.C. Eklund, *Science of fullerenes and carbon nanotubes*, Academic Press, 1996.

[DH81] P. Dutta and P.M. Horn, *Low-frequency fluctuations in solids: 1 / f noise*, Rev. Mod. Phys. **53** (1981), 497.

[dH93] W.A. de Heer, *The physics of simple metal clusters: experimental aspects and simple models*, Rev. Mod. Phys. **65** (1993), 611.

[DHT07] S. Das Sarma, E.H. Hwang, and W.-K. Tse, *Many-body interaction effects in doped and undoped graphene: Fermi liquid versus non-fermi liquid*, Phys. Rev. B **75** (2007), 121406(R).

[DKEM06] J. Dorignac, A. Kalinowski, S. Erramilli, and P. Mohanty, *Dynamical response of nanomechanical oscillators in immiscible viscous fluid for in vitro biomolecular recognition*, Phys. Rev. Lett. **96** (2006), 186105.

[DLC+05] R. S. Decca, D. López, H. B. Chan, E. Fischbach, D. E. Krause, and C. R. Jamell, *Constraining new forces in the casimir regime using the isoelectronic technique*, Phys. Rev. Lett. **94** (2005), 240401.

[Dor65] R.H. Doremus, *Optical properties of small silver particles*, J. Chem. Phys. **42** (1965), 414.

[DPX98] Y. Dong, S.V. Pappu, and Z. Xu, *Detection of local density distribution of isolated silanol groups on planar silica surfaces using nonlinear optical molecular probes*, Anal. Chem. **70** (1998), 4730.

[DYN+99] Z. Dai, S. Yamamoto, K. Narumi, A. Miyashita, and H. Naramoto, *Gold nanoparticle fabrication in single crystal* SiO_2 *by* MeV Au *ion implantation and subsequent thermal annealing*, Nucl. Instr. and Meth. B **149** (1999), 108.

[EBF+01] R. Egger, A. Bachtold, M.S. Fuhrer, M. Bockrath, D.H. Cobden, and P.L. McEuen, *Luttinger liquid behavior in metallic carbon nanotubes*, Lecture Notes in Physics, vol. 579, Springer Verlag, 2001.

[Edm60] A.R. Edmonds, *Angular momentum in quantum mechanics (second edition)*, Princeton University Press, Princeton, 1960.

[EFMW92] B. Eckhardt, S. Fishman, K. Müller, and D. Wintgen, *Semiclassical matrix elements from periodic orbits*, Phys. Rev. A **45** (1992), 3531.

[Eka84a] W. Ekardt, *Dynamical polarizability of small metal particles: Self-consistent spherical jellium background model*, Phys. Rev. Lett. **52** (1984), 1925.

[Eka84b] ———, *Work function of small metallic particles: Self-consistent spherical jellium-background model*, Phys. Rev. B **29** (1984), 1558.

[EOS+00] S. Evoy, A. Olkhovets, L. Sekaric, J. M. Parpia, H. G. Craighead, and D. W. Carr, *Temperature-dependent internal friction in silicon nanoelectromechanical systems*, Appl. Phys. Lett. **77** (2000), 2397.

[ER05] K. L. Ekinci and M. L. Roukes, *Nanoelectromechanical systems*, Rev. Sci. Inst. **76** (2005), 061101.

[ERK04] P. Esquinazi, M. A. Ramos, and R. König, *Acoustic properties of amorphous solids at very low temperatures: The quest for interacting tunneling states*, J. Low Temp. Phys. **135** (2004), 27.

[Esq98] P. Esquinazi (ed.), *Tunneling systems in amorphous and crystalline solids*, Springer (Berlin), 1998.

[ETB06] J.W. Evans, P.A. Thiel, and M.C. Bartelt, *Morphological evolution during epitaxial thin film growth: Formation of 2d islands and 3d mounds*, Sur. Sci. Rep. **61** (2006), 1.

[EW92] R. Egger and U. Weiss, *Quantum monte carlo simulation of the dynamics of the spin-boson model*, Z. Phys. B - Condensed Matter **89** (1992), 97.

[EWZB01] A. Erbe, C. Weiss, W. Zwerger, and R. H. Blick, *Nanomechanical resonator shuttling single electrons at radio frequencies*, Phys. Rev. Lett. **87** (2001), 096106.

[Fey48] R. P. Feynman, *Space-time approach to non-relativistic quantum mechanics*, Rev. Mod. Phys. **20** (1948), 367.

[FH65] R. P. Feynman and A. R. Hibbs, *Quantum physics and path integrals*, McGraw-Hill, New York, 1965.

[FKDB02] M. S. Fuhrer, B. M. Kim, T. Du1rkop, and T. Brintlinger, *High-mobility nanotube transistor memory*, Nano Lett. **2** (2002), 755.

[FP86] M. Feingold and A. Peres, *Distribution of matrix elements of chaotic systems*, Phys. Rev. A **34** (1986), 591.

[FS01] L. Forró and C. Schönenberger, *Carbon nanotubes, materials for the future*, Europhys. News. **32** (2001), 86.

[FTK+06] M. Freitag, J.C. Tsang, J. Kirtley, A. Carlsen, J.Chen, A. Troeman, H. Hilgenkamp, and Ph. Avouris, *Electrically excited, localized infrared emission from single carbon nanotubes*, Nano Lett. **6** (2006), 1425.

[FV63] R. P. Feynman and F. L. Vernon, Jr., *The theory of a general quantum system interacting with a linear dissipative system*, Ann. Phys. (N.Y.) **24** (1963), 118.

[FVF+00] N. Del Fatti, F. Vallée, C. Flytzanis, Y. Hamanaka, and A. Nakamura, *Electron dynamics and surface plasmon resonance nonlinearities in metal nanoparticles*, Chem. Phys. **251** (2000), 215.

[FZMR06] X. L. Feng, C. A. Zorman, M. Mehregany, and M. L. Roukes, *Dissipation in single-crystal 3c-sic ultra-high frequency nanomechanical resonators.*

[GC05] M. R. Geller and A. N. Cleland, *Superconducting qubits coupled to nanoelectromechanical resonators: An architecture for solid-state quantum-information processing*, Phys. Rev. A **71** (2005), 032311.

[GCP06] F. Guinea, A. H. Castro Neto, and N. M. R. Peres, *Electronic states and landau levels in graphene stacks*, Phys. Rev. B **73** (2006), 245426.

[GDP96] E.K.U. Gross, J.F. Dobson, and M. Petersilka, *Density functional theory of time-dependent phenomena*, Topics in Current Chemistry, vol. 181, Springer, Berlin, 1996.

[GGI02] L.G. Gerchikov, C. Guet, and A.N. Ipatov, *Multiple plasmons and anharmonic effects in small metallic clusters*, Phys. Rev. A **66** (2002), 053202.

[GGV99] J. González, F. Guinea, and M. A. H. Vozmediano, *Marginal-fermi-liquid behavior from two-dimensional coulomb interaction*, Phys. Rev. B **59** (1999), R2474.

[GH98] M. Grifoni and P. Hänggi, *Driven quantum tunneling*, Phys. Rep. **304** (1998), 229.

[GJS04] F. Guinea, R. A. Jalabert, and F. Sols, *Electronic lifetimes in ballistic quantum dots electrostatically coupled to metallic environments*, Phys. Rev. B **70** (2004), 085310.

[GK85] E.K.U. Gross and W. Kohn, *Local density-functional theory of frequency-dependent linear response*, Phys. Rev. Lett. **55** (1985), 2850.

[GMM06] F. Guinea, M.P. López-Sancho, and M.A.H. Vozmediano, *Carbon based materials magnetism*, ch. 15, p. 353, Elsevier Science, 2006.

[GN07] A. K. Geim and K. S. Novoselov, *The rise of graphene*, Nature Materials **6** (2007), 183.

[GR00] Gradshteyn and Ryzhik, *Table of integrals, series, and products*, Academic Press, 2000.

[GSSW93] M. Grifoni, M. Sassetti, J. Stockburger, and U. Weiss, *Nonlinear response of a periodically driven damped two-state system*, Phys. Rev. E **48** (1993), 3497.

[Gui84] F. Guinea, *Friction and particle-hole pairs*, Phys. Rev. Lett. **53** (1984), 1268.

[Gui85] ———, *Dynamics of simple dissipative systems*, Phys. Rev. B **32** (1985), 4486.

[Gui05] ———, *Electronic dephasing in wires due to metallic gates*, Phys. Rev. B **71** (2005), 045424.

[GW88] R. Görlich and U. Weiss, *Specific heat of the dissipative two level system*, Phys. Rev. B **38** (1988), 5245.

[Had91] R.C. Haddon *et. al.*, *Conducting films of* C_{60} *and* C_{70} *by alkali-metal doping*, Nature **350** (1991), 320.

[HAS+72] S. Hunklinger, W. Arnold, St. Stein, R. Nava, and K. Dransfeld, *Saturation of the ultrasonic absorption in vitreous silica at low temperatures*, Phys. Lett. A **42** (1972), 256.

[HAS06] E. H. Hwang, S. Adam, and S. Das Sarma, *Carrier transport in 2d graphene layers*, Phys. Rev. Lett. **98** (2006), 186806.

[HFZ+05] X. M. H. Huang, X. L. Feng, C. A. Zorman, M. Mehregany, and M. Roukes, *Vhf, uhf and microwave frequency nanomechanical resonators*, New J. Phys. **7** (2005), 247.

[HHP+03] A. Husain, J. Hone, H. W. C. Postma, X. M. H. Huang, T. Drake, M. Barbic, A. Scherer, and M. L. Roukes, *Nanowire-based very-high-frequency electromechanical resonator*, Appl. Phys. Lett. **83** (2003), 1240.

[HKC+07] M. A. Hopcroft, B. Kim, S. Chandorkar, R. Melamud, M. Agarwal, C. M. Jha, G. Bahl, J. Salvia, H. Mehta, H. K. Lee, R. N. Candler, and T. W. Kenny, *Using the temperature dependence of resonator quality factor as a thermometer*, Appl. Phys. Lett. **91** (2007), 013505.

[Iji91] S. Ijima, *Helical microtubules of graphitic carbon*, Nature **354** (1991), 56.

[IN92] G. L. Ingold and Yu. V. Nazarov, *Single charge tunneling*, Plenum Press (New York), 1992.

[J¨72] J. Jäckle, *On the ultrasonic attenuation in glasses at low temperatures*, Z. Physik **257** (1972), 212.

[Jac75] J.D. Jackson, *Classical electrodynamics (second edition)*, John Wiley & Sons, New York, 1975.

[Jac07] K. Jacobs, *Engineering quantum states of a nanoresonator via a simple auxiliary system*, Phys. Rev. Lett. **99** (2007), 117203.

[JG88] M. P. Sheetz J. Gelles, B. J. Schnapp, *Tracking kinesin-driven movements with nanometre-scale precision*, Nature **331** (1988), 450.

[JI68] Y. Jimbo and K. Itao, J. Horological Inst. Jpn. **47** (1968), 1.

[JLB07] K. Jacobs, P. Lougovski, and M. Blencowe, *Continuous measurement of the energy eigenstates of a nanomechanical resonator without a nondemolition probe*, Phys. Rev. Lett. **98** (2007), 147201.

[JPAH76] J. Jäckle, L. Piché, W. Arnold, and S. Hunklinger, *Elastic effects of structural relaxation in glasses at low temperatures*, J. Non-Crys. Solids **20** (1976), 365.

[JT37] H.A. Jahn and E. Teller, *Stability of polyatomic molecules in degenerate electronic state. i. orbital degeneracy*, Proc. R. Soc. London A **161** (1937), 220.

[KB06] Y. Kurzweil and R. Baer, *Quantum memory effects in the dynamics of electrons in gold clusters*, Phys. Rev. B **73** (2006), 075413.

[KC03] R.G. Knobel and A.N. Cleland, *Nanometre-scale displacement sensing using a single-electron transistor*, Nature **424** (2003), 291.

[KCdH$^+$84] W.D. Knight, K. Clemenger, W.A. de Heer, W.A. Saunders, and M.Y. Chou, *Electronic shell structure and abundances of sodium clusters*, Phys. Rev. Lett. **52** (1984), 2141.

[KCdHS85] W.D. Knight, K. Clemenger, W.A. de Heer, and W.A. Saunders, *Polarizability of alkali clusters*, Phys. Rev. B **31** (1985), 2539.

[KHDS02] H.E. Katz, X.M. Hong, A. Dodabalapur, and R. Sarpeshkar, *Organic field-effect transistors with polarizable gate insulators*, J. Appl. Phys. **91** (2002), 1572.

[KHO$^+$85] H.W. Kroto, J.R. Heath, S.C. O'Brien, R.F. Curl, and R.E. Smalley, *C60: Buckminsterfullerene*, Nature **318** (1985), 162.

[Khv04] D. V. Khveshchenko, *Quantum impurity models of noisy qubits*, Phys. Rev. B **69** (2004), 153311.

[KJV$^+$03] W. Kim, A. Javey, O. Vermesh, Q. Wang, Y. Li, and H. Dai, *Hysteresis caused by water molecules in carbon nanotube field-effect transistors*, Nano Lett. **3** (2003), 193.

[KK66] A. Kawabata and R. Kubo, *Electronic properties of fine metallic particles. ii. plasma resonance absorption*, J. Phys. Soc. Jpn. **21** (1966), 1765.

[KKS82] M.M. Kappes, R.W. Kunz, and E. Schumacher, *Production of large sodium clusters ($\mathrm{Na}_x, x < 65$) by seeded beam expansions*, Chem. Phys. Lett. **91** (1982), 413.

[KLER04] X. M. H. Huang K. L. Ekinci and M. L. Roukes, *Ultrasensitive nanoelectromechanical mass detection*, Appl. Phys. Lett. **84** (2004), 4469.

[KM96] S. Kehrein and A. Mielke, *On the spin-boson model with a sub-ohmic bath*, Phys. Lett. A **219** (1996), 313.

[KRSL07] I. Katz, A. Retzker, R. Straub, and R. Lifshitz, *Signatures for a classical to quantum transition of a driven nonlinear nanomechanical resonator*, Phys. Rev. Lett. **99** (2007), 040404.

[Kub57] R. Kubo, *Statistical-mechanical theory of irreversible processes. i. general theory and simple applications to magnetic and conduction problems*, J. Phys. Soc. Japan **12** (1957), 570.

[KV95] U. Kreibig and M. Vollmer, *Optical properties of metal clusters*, Springer-Verlag, Berlin, 1995.

[Lan37] R.E. Langer, *On the connection formulas and the solutions of the wave equation*, Phys. Rep. **51** (1937), 669.

[Lan80] Landau & Lifshitz, *Statistical physics, part i*, Pergamon, Oxford, 1980.

[LB99] X. Li and B. Bhushan, *Micro/nanomechanical characterization of ceramic films for microdevices*, Thin Solid Films **340** (1999), 210.

[LBCS04] M. D. LaHaye, O. Buu, B. Camarota, and K. C. Schwab, *Approaching the quantum limit of a nanomechanical resonator*, Science **304** (2004), 74.

[LBT+03] X. Li, B. Bhushan, K. Takashima, C.W. Baek, and Y.K. Kim, *Mechanical characterization of micro/nanoscale structures for mems/nems applications using nanoindentation techniques*, Ultramicroscopy **97** (2003), 481.

[LCD+87] A. J. Leggett, S. Chakravarty, A. T. Dorsey, M. P. A. Fisher, A. Garg, and W. Zwerger, *Dynamics of the dissipative two-state system*, Rev. Mod. Phys. **59** (1987), 1.

[Leg02] A. J. Leggett, *Testing the limits of quantum mechanics: motivation, state of play, prospects*, J. Phys: Condens. Matter **14** (2002), R415.

[LKLA99] B. Lamprecht, J.R. Krenn, A. Leitner, and F.R. Aussenegg, *Resonant and off-resonant light-driven plasmons in metal nanoparticles studied by femtosecond-resolution third-harmonic generation*, Phys. Rev. Lett. **83** (1999), 4421.

[LL59] L. D. Landau and E. M. Lifshitz, *Theory of elasticity*, Pergamon Press (London), 1959.

[LR00] R. Lifshitz and M.L. Roukes, *Thermoelastic damping in micro- and nanomechanical systems*, Phys. Rev. B **61** (2000), 5600.

[LS91] E. Lipparini and S. Stringari, *Collective excitations in deformed alkali metal clusters*, Z. Phys. D **18** (1991), 193.

[LTBP99] X. Liu, E. J. Thompson, B. E. White Jr., and R. O. Pohl, *Low-temperature internal friction in metal films and in plastically deformed bulk aluminum*, Phys. Rev. B **59** (1999), 11767.

[LUCS01] Y.-H. Liau, A.N. Unterreiner, Q. Chang, and N.F. Scherer, *Ultrafast dephasing of single nanoparticles studied by two-pulse second-order interferometry*, J. Phys. Chem. B **105** (2001), 2135.

[LVS+05] X. Liu, J. F. Vignola, H. J. Simpson, B. R. Lemon, B. H. Houston, and D. M. Photiadis, *A loss mechanism study of a very high q silicon micromechanical oscillator*, J. Appl. Phys. **97** (2005), 023524.

[LWW98] A. Lück, M. Winterstetter, and Ulrich Weiss, *Quantum monte carlo simulations of driven spin-boson systems*, Phys. Rev. E **58** (1998), 5565.

[MAU+07] J. Martin, N. Akerman, G. Ulbricht, T. Lohmann, J. H. Smet, K. von Klitzing, and A. Yacoby, *Observation of electron-hole puddles in graphene using a scanning single electron transistor*.

[Mer68] N.D. Mermin, *Crystalline order in two dimensions*, Phys. Rev. **176** (1968), 250.

[Mer70] E. Merzbacher, *Quantum mechanics*, John Wiley & Sons, New York, 1970.

[MGK+07] J. C. Meyer, A. K. Geim, M. I. Katsnelson, K. S. Novoselov, T. J. Booth, and S. Roth, *The structure of suspended graphene sheets*, Nature **446** (2007), 60.

[MGM06] M.P. López-Sancho, F. Guinea, and M.A.H. Vozmediano, *Nuevas formas de carbono*, 100@cias UNED **9** (2006), 64.

[MH07] M. J. Martin and B. H. Houston, *Gas damping of carbon nanotube oscillators*, Appl. Phys. Lett. **91** (2007), 103116.

[MHE+02] P. Mohanty, D. A. Harrington, K. L. Ekinci, Y. T. Yang, M. J. Murphy, and M. L. Roukes, *Intrinsic dissipation in high-frequency micromechanical resonators*, Phys. Rev. B **66** (2002), 085416.

[Mie08] G. Mie, *Beiträge zur optik trüber medien, speziell kolloidaler metallösungen*, Ann. Phys. (Leipzig) **25** (1908), 377.

[MM90] B.A. Morrow and A.J. McFarlan, *Chemical reactions at silica surfaces*, J. Non-Crys. Sol. **120** (90), 61.

[MP06] T. Makarova and F. Palacio (eds.), *Carbon based materials magnetism*, Elsevier Science, 2006.

[MR97] B. Mehlig and K. Richter, *Semiclassical linear response: Far-infrared absorption in ballistic quantum systems*, Phys. Rev. Lett. **80** (1997), 1936.

[MR01] H. J. Mamin and D. Rugar, *Sub-attonewton force detection at millikelvin temperatures*, Appl. Phys. Lett. **79** (2001), 3358.

[MSL+05] R. Mukhopadhyay, V. V. Sumbayev, M. Lorentzen, J. Kjems, P. A. Andreasen, and F. Besenbacher, *Cantilever sensor for nanomechanical detection of specific protein conformations*, Nano Lett. **5** (2005), 2385.

[MWJ02] R. Molina, D. Weinmann, and R.A. Jalabert, *Oscillatory size dependence of the surface plasmon linewidth in metallic nanoparticles*, Phys. Rev. B **65** (2002), 155427.

[MWJ03] R.A. Molina, D. Weinmann, and R.A. Jalabert, *Oscillatory behavior and enhancement of the surface plasmon linewidth in embedded noble metal nanoparticles*, Eur. Phys. J. D **24** (2003), 127.

[MZ07] I. Martin and W. H. Zurek, *Measurement of energy eigenstates by a slow detector*, Phys. Rev. Lett. **98** (2007), 120401.

[NB82] E.H. Nicollian and J.R. Brews, *Mos physics and technology*, Wiley-Interscience (New York), 1982.

[NBL+06] A. Naik, O. Buu, M. D. LaHaye, A. D. Armour, A. A. Clerk, M. P. Blencowe, and K. C. Schwab, *Cooling a nanomechanical resonator with quantum back-action*, Nature **443** (2006), 193.

[NGM+04] K. S. Novoselov, A. K. Geim, S. V. Morozov, D. Jiang, Y. Zhang, S. V. Dubonos, I. V. Grigorieva, and A. A. Firsov, *Electric field effect in atomically thin carbon films*, Science **306** (2004), 666.

[NGM+05] K. S. Novoselov, A. K. Geim, S. V. Morozov, D. Jiang, M. I. Katsnelson, I. V. Grigorieva, S. V. Dubonos, and A. A. Firsov, *Two-dimensional gas of massless dirac fermions in graphene*, Nature **438** (2005), 197.

[NM07] K. Nomura and A.H. MacDonald, *Quantum transport of massless dirac fermions in graphene*, Phys. Rev. Lett. **98** (2007), 076602.

[NMM+06] K.S. Novoselov, E. McCann, S.V. Morozov, V.I. Falko, M.I. Katsnelson, U. Zeitler, D. Jiang, F. Schedin, and A.K. Geim, *Unconventional quantum hall effect and berry's phase of 2pi in bilayer graphene*, Nature Physics **2** (2006), 177.

[NP99] P. Nozieres and D. Pines, *The theory of quantum liquids (third edition)*, Perseus Books (Cambridge, Massachusets), 1999.

[OKNS00] T. Oku, T. Kusunose, K. Niihara, and K. Suganuma, *Chemical synthesis of silver nanoparticles encapsulated in boron nitride nanocages*, J. Mater. Chem. **10** (2000), 255.

[Pei35] R.E. Peierls, *Quelques proprietes typiques des corpses solides*, Ann. I. H. Poincare **5** (1935), 177.

[PFFF02] E. Paladino, L. Faoro, G. Falci, and R. Fazio, *Decoherence and 1/f noise in josephson qubits*, Phys. Rev. Lett. **88** (2002), 228304.

[Phi72] W.A. Phillips, *Tunneling states in amorphous solids*, J. Low Temp. Phys. **7** (1972), 351.

[Phi87] W. A. Phillips, *Two-level states in glasses*, Rep. Prog. Phys. **50** (1987), 1657.

[Phi88] W.A. Phillips, *Comment on "two-level systems observed in the mechanical properties of single-crystal silicon at low temperatures"*, Phys. Rev. Lett. **61** (1988), 2632.

[Pie93] H.O. Pierson, *Handbook of carbon, graphite, diamond and fullerenes - properties, processing and applications*, William Andrew Publishing/Noyes, New York, 1993.

[PIW] http : //en.wikipedia.org/wiki/Path_integral_formulation

[PJ04] D. M. Photiadis and J. A. Judge, *Attachment losses of high q oscillators*, Applied Physics Letters **85** (2004), 482.

[PP06] B. Partoens and F.M. Peeters, *From graphene to graphite: Electronic structure around the k point*, Phys. Rev. B **74** (2006), 075404.

[RBMC04] D. Rugar, R. Budakian, H.J. Mamin, and B.W. Chui, *Single spin detection by magnetic resonance force microscopy*, Nature **430** (2004), 329.

[RFTJ02] M. Radosavljevic, M. Freitag, K. V. Thadani, and A. T. Johnson, *Nonvolatile molecular memory elements based on ambipolar nanotube field effect transistors*, Nano Lett. **2** (2002), 761.

[RS80] P. Ring and P. Schuck, *The nuclear many-body problem*, Springer-Verlag, Berlin, 1980.

[RSK05a] R. Ruskov, K. Schwab, and A. N. Korotkov, *Quantum nondemolition squeezing of a nanomechanical resonator*, IEEE transactions on nanotechnology **4** (2005), 132.

[RSK05b] ———, *Squeezing of a nanomechanical resonator by quantum nondemolition measurement and feedback*, Phys. Rev. B **71** (2005), 235407.

[SB98] S. Sundararajan and B. Bhushan, *Micro/nanotribological studies of polysilicon and sic films for mems applications*, Wear **217** (1998), 251.

[SB02] ———, *Development of afm-based techniques to measure mechanical properties of nanoscale structures*, Sens. Actuators A **101** (2002), 338.

[SB04] D. V. Scheible and R. H. Blick, *Silicon nanopillars for mechanical single-electron transport*, Appl. Phys. Lett. **84** (2004), 4632.

[SBNI02] S. Sundararajan, B. Bhushan, T. Namazu, and Y. Isono, *Mechanical property measurements of nanoscale structures using an atomic force microscope*, Ultramicroscopy **91** (2002), 111.

[Sch02] K. Schwab, *Spring constant and damping constant tuning of nanomechanical resonators using a single-electron transistor*, Appl. Phys. Lett. **80** (2002), 1276.

[SCK+07] S.-B. Shim, J. S. Chun, S. W. Kang, S. W. Cho, S. W. Cho, Y. D. Park, P. Mohanty, N. Kim, and J. Kim, *Micromechanical resonators fabricated from lattice-matched and etch-selective gaas/ingap/gaas heterostructures*, Appl. Phys. Lett. **91** (2007), 133505.

[SD85] H. Spohn and R. Dümcke, *Quantum tunneling with dissipation and the ising model over R*, J. Stat. Phys. **41** (1985), no. 389.

[SDC04] D. H. Santamore, A. C. Doherty, and M. C. Cross, *Quantum nondemolition measurement of fock states of mesoscopic mechanical oscillators*, Phys. Rev. B **70** (2004), 144301.

[SG95] O. Sneh and S.M. George, *Thermal stability of hydroxyl groups on a well-defined silica surface*, J. Phys. Chem. **99** (1995), 4639.

[SG06] T. Stauber and F. Guinea, *Entanglement and dephasing of quantum dissipative systems*, Phys. Rev. A **73** (2006), 042110.

[SGC07a] C. Seoanez, F. Guinea, and A. H. Castro Neto, *Dissipation due to two-level systems in nano-mechanical devices*, Europhys. Lett. **78** (2007), 60002.

[SGC07b] ———, *Surface dissipation in nems: Unified description with the standard tunneling model, and effects of metallic electrodes.*

[SGH+00] C. Sönnichsen, S. Geier, N. E. Hecker, G. von Plessen, J. Feldmann, H. Ditlbacher, B. Lamprecht, J. R. Krenn, F. R. Aussenegg, V. Z-H. Chan, J. P. Spatz, and M. Möller, *Spectroscopy of single metallic nanoparticles using total internal reflection microscopy*, Appl. Phys. Lett. **77** (2000), 2949.

[SGM+07] F. Schedin, A.K. Geim, S.V. Morozov, D. Jiang, E.H. Hill, P. Blake, and K.S. Novoselov, *Detection of individual gas molecules absorbed on graphene*, Nature Materials **6** (2007), 652.

[SHN06] S. Savel'ev, X. Hu, and F. Nori, *Quantum electromechanics: qubits from buckling nanobars*, New J. Phys. **8** (2006), 105.

[SHWR00] K. Schwab, E. A. Henriksen, J. M. Worlock, and M. L. Roukes, *Measurement of the quantum of thermal conductance*, Nature **404** (2000), 974.

[Sim05] B. Simmons, *Quantum condensed matter field theory*, 2005, http : //www.tcm.phy.cam.ac.uk/ bds10/tp3.html.

[SIM07] S.-B. Shim, M. Imboden, and P. Mohanty, *Synchronized oscillation in coupled nanomechanical oscillators*, Science **316** (2007), 95.

[SKM+91] K. Selby, V. Kresin, J. Masui, M. Vollmer, W.A. de Heer, A. Scheidemann, and W.D. Knight, *Photoabsorption spectra of sodium clusters*, Phys. Rev. B **43** (1991), 4565.

[SR05] K. C. Schwab and M. L. Roukes, *Putting mechanics into quantum mechanics*, Phys. Today **July** (2005), 36.

[SRCR04] L.B. Sharos, A. Raman, S. Crittenden, and R. Reifenberger, *Enhanced mass sensing using torsional and lateral resonances in microcantilevers*, Appl. Phys. Lett. **84** (2004), 4638.

[SSMM07] A. Shnirman, G. Schön, I. Martin, and Y. Makhlin, *1/f noise and two-level systems in josephson qubits*, vol. Electron Correlation in New Materials and Nanosystems, Nato Science Series, no. 241, p. 343, Springer Netherlands, 2007.

[SSMS00] S. Schultz, D. R. Smith, J. J. Mock, and D. A. Schultz, *Single-target molecule detection with nonbleaching multicolor optical immunolabels*, Proc. Natl. Acad. Sci. U.S.A. **97** (2000), 996.

[Sta03] T. Stauber, *Universal asymptotic behavior in flow equations of dissipative systems*, Phys. Rev. B **68** (2003), 125102.

[SYU+04] V. Sazonova, Y. Yaish, H. Ustunel, D. Roundy, T. A. Arias, and P. L. McEuen, *A tunable carbon nanotube electromechanical oscillator*, Nature **431** (2004), 284.

[Sze81] S.M. Sze, *Physics of semiconductor devices*, Wiley-Interscience (New York), 1981.

[Tho06] J. Thomas, *Research highlights: Graphene: Through thick and thin*, Nature Nanotechnology **doi:10.1038/nnano.2006.143** (December 2006).

[Ü06] H. Üstunel, *Quantitative prediction of the elastic and anelastic phenomena on the nanometer scale*, Ph.D. thesis, Cornell University, Ithaca NY, 2006.

[URA04] H. Ustunel, D. Roundy, and T. A. Arias, *Modelling a suspended nanotube oscillator*.

[VTB05] M. Vojta, N. H. Tong, and R. Bulla, *Quantum phase transitions in the sub-ohmic spin-boson model: Failure of the quantum-classical mapping*, Phys. Rev. Lett. **94** (2005), 070604.

[VZ0] A. M. Van Der Zande, private communication.

[Wal47] P.R. Wallace, *The band theory of graphite*, Phys. Rev. **71** (1947), 622.

[Wei88] M.B. Weissman, *1/f noise and other slow, nonexponential kinetics in condensed matter*, Rev. Mod. Phys. **60** (1988), 537.

[Wei99] U. Weiss, *Quantum dissipative systems*, World Scientific (Singapore), 1999.

[Wei06] G. Weick, *Quantum dissipation and decoherence of collective excitations in metallic nanoparticles*, Ph.D. thesis, Université Louis Pasteur, Strasbourg and Universität Augsburg,

2006, http : //deposit.ddb.de/cgi − bin/dokserv?idn = 981745679 &dok_var = d1&dok_ext = pdf&filename = 981745679.pdf.

[WIJW06] G. Weick, G. Ingold, R.A. Jalabert, and D. Weinmann, *Surface plasmon in metallic nanoparticles: Renormalization effects due to electron-hole excitations*, Phys. Rev. B **74** (2006), 165421.

[Wil87] M. Wilkinson, *A semiclassical sum rule for matrix elements of classically chaotic systems*, J. Phys. A **20** (1987), 2415.

[Wil06] M. Wilson, *Electrons in atomically thin carbon sheets behave like massless particles*, Physics Today **January** (2006), 21.

[WIWJ07] G. Weick, G.-L. Ingold, D. Weinmann, and R.A. Jalabert, *Sidebands in the light absorption of driven metallic nanoparticles*, Eur. Phys. J. D **44** (2007), 359.

[WMWJ05] G. Weick, R. Molina, D. Weinmann, and R.A. Jalabert, *Lifetime of the first and second collective excitations in metallic nanoparticles*, Phys. Rev. B **72** (2005), 115410.

[WOE04] D.F. Wang, T. Ono, and M. Esashi, *Thermal treatments and gas adsorption influences on nanomechanics of ultra-thin silicon resonators for ultimate sensing*, Nanotechnology **15** (2004), 1851.

[WP95] B. E. White Jr. and R. O. Pohl, *Elastic properties of thin films*, Mat. Res. Soc. Symp., vol. 356, 1995, p. 567.

[WS54] R.D. Woods and D. Saxon, *Diffuse surface optical model for nucleon-nuclei scattering*, Phys. Rev. **95** (1954), 577.

[WS04] Y. Wu and M.A. Shannon, *Theoretical analysis of the effect of static charges in silicon-based dielectric thin films on micro- to nanoscale electrostatic actuation*, J. Micromech. Microeng. **14** (2004), 989.

[WSSG06] B. Wunsch, T. Stauber, F. Sols, and F. Guinea, *Dynamical polarization of graphene at finite doping*, New. Journ. Phys. **8** (2006), 318.

[Wv07] A. Weichselbaum and J. von Delft, *Sum-rule conserving spectral functions from the numerical renormalization group*, Phys. Rev. Lett. **99** (2007), 076402.

[WWIJ07] G. Weick, D. Weinmann, G.-L. Ingold, and R.A. Jalabert, *Anomaly in the relaxation dynamics close to the surface plasmon resonance*, Europhys. Lett. **78** (2007), 27002.

[XWS+06] F. Xue, Y.D Wang, C.P. Sun, H. Okamoto, H. Yamaguchi, and K. Semba, *Controllable coupling between flux qubit and nanomechanical resonator by magnetic field*.

[YB91] C. Yannouleas and R.A. Broglia, *Collective and single-particle aspects in the optical response of metal microclusters*, Phys. Rev. A **44** (1991), 5793.

[YB92] C. Yannouleas and R. A. Broglia, *Landau damping and wall dissipation in large metal clusters*, Ann. Phys. **217** (1992), 105.

[YDG82] C. Yannouleas, M. Dworzecka, and J.J. Griffin, *Nuclear dissipation as damping of collective motion in the time-dependent rpa : (i). the microscopic model*, Nucl. Phys. A **379** (1982), 256.

[YL88] C. C. Yu and A. J. Leggett, Comm. Cond. Mat. Phys. **14** (1988), 231.

[YOE00] J. Yang, T. Ono, and M. Esashi, *Surface effects and high quality factors in ultrathin single-crystal silicon cantilevers*, Appl. Phys. Lett. **77** (2000), 3860.

[YOE02] J. L. Yang, T. Ono, and M. Esashi, *Energy dissipation in submicrometer thick single-crystal silicon cantilevers*, J. Microelectromech. Syst. **11** (2002), 775.

[YOL92] R-H Yan, A. Ourmazd, and K.F. Lee, *Scaling the si mosfet: From bulk to so1 to bulk*, IEEE Trans. Elec. Dev. **39** (1992), 1704.

[YOTT79] K. Yagi, K. Oyu, M. Tamura, and T. Tokuyama, *Carrier-concentration reduction in high-dose phosphorus-implanted silicon caused by wet-oxygen oxidation*, Appl. Phys. Lett. **35** (1979), 275.

[YSC+00] K. Y. Yasumura, T. D. Stowe, E. M. Chow, T. Pfafman, T. W. Kenny, B. C. Stipe, and D. Rugar, *Quality factors in micron- and submicron-thick cantilevers*, J. Microelectromech. Syst. **9** (2000), 117.

[Zal98] R. Zallen, *The physics of amorphous solids*, Wiley, New York, 1998.

[Zen38] C. Zener, *Internal friction in solids ii. general theory of thermoelastic internal friction*, Phys. Rev. **53** (1938), 90.

[Zen48] ———, *Elasticity and anelasticity of metals*, The University of Chicago Press (Chicago), 1948.

[ZGF+07] S.Y. Zhou, G.-H. Gweon, A.V. Fedorov, P.N. First, W.A. de Heer, D.-H. Lee, F. Guinea, A.H. Castro Neto, and A. Lanzara, *Substrate-induced band gap opening in epitaxial graphene*, Nature Materials **October** (2007).

[ZGS+05] G. Zolfagharkhani, A. Gaidarzhy, S.-B. Shim, R.L. Badzey, and P. Mohanty, *Quantum friction in nanomechanical oscillators at millikelvin temperatures*, Phys. Rev. B **72** (2005), 224101.

[ZP71] R. C. Zeller and R. O. Pohl, *Thermal conductivity and specific heat of noncrystalline solids*, Phys. Rev. B **4** (1971), 2029.

[ZTSK05] Y. Zhang, Y.-W. Tan, H.L. Stormer, and P. Kim, *Experimental observation of the quantum hall effect and berry's phase in graphene*, Nature **438** (2005), 201.